

ISSN 0288-4534
CODEN: KONA E7

粉

KONA

POWDER AND PARTICLE

No. 8 (1990)

Published by The Party of Powder Technology (JAPAN)

Special issue for global exchange of
information about powder technology

TIME 1:26 0895°C

TIME 1:29 0873°C

TIME 1:32 0846°C

TIME 1:34 0830°C

Announcement of New Editorial Policy of KONA Journal

KONA has been issued annually by the Party of Powder Technology, Japan since 1983. According to the decision by the Editorial Board, some alterations to the editorial policy of KONA have been made for further strengthening of its international character with this issue No. 8 (1990) as follows.

The editorial board will 1) ensure not only the republication of the English version of selected research reports or general comments originally published in Japanese but also the publication of original monographs or articles written in English for the advancement of powder science and technology in the world through KONA. The articles would cover recent notable results or technical reports dealing with powder science and technology which are to be collected from all over the

world. The editorial board will also 2) promote the international communication of these developments by appropriate distribution of KONA.

KONA is distributed free of charge to senior researchers of universities and laboratories as well as to institutions and libraries in this field throughout the world under the sponsorship of Hosokawa Micron Corporation. Within these limits, the publisher is always glad to consider the addition of names of those who wish to obtain this journal regularly to the mailing list.

Explanation of the Cover

“粉”; This Chinese character is pronounced as “KONA” in Japanese and means “Powder”.

“粉” on the front page was written by the late Mr. Eiichi Hosokawa, founder of Hosokawa Micron Corporation.

Editorial Board

G. Jimbo Editor in Chief
(Nagoya Univ., JAPAN)

Asian Block

Y. Kousaka Block Vice Chairman
(Univ. of Osaka Prefecture, JAPAN)

N. Yoshioka (Okayama Univ. of Science, JAPAN)

M. Arakawa (Former Kyoto Institute of Tech., JAPAN)

T. Oshima (Himeji Institute of Tech., JAPAN)

K. Miyanami (Univ. of Osaka Prefecture, JAPAN)

H. Emi (Kanazawa Univ., JAPAN)

Y. Kuwahara (Government Industrial Research Institute, Nagoya, JAPAN)

T. Yoshida (Hosokawa Micron Corp., JAPAN)

T. Yokoyama (Hosokawa Micron Corp., JAPAN)

Secretariat

T. Suzuki (Hosokawa Micron Corp., JAPAN)

F. Nakagawa (Hosokawa Micron Corp., JAPAN)

European Block

J. Schwedes Block Chairman
(Institut für Mechanisch Verfahrenstechnik, GERMANY)

B. Scarlett Block Vice Chairman
(Delft Univ. of Technology, NETHERLAND)

K. Schönert (Technische Univ. Clausthal, GERMANY)

F. Löffler (Univ. Karlsruhe, GERMANY)

H. Schubert (Bergakademie Freiberg, GERMANY)

E. Forssberg (Univ. Lulea, SWEDEN)

S. R. de Silva (Postec-Research, NORWAY)

D. Ocepek (Univ. Ljubljana, YUGOSLAVIA)

Secretariat

D. Schwechten (Alpine AG, GERMANY)

Americas Block

M. McLaren Block Chairman
(State Univ. of Rutgers, U.S.A.)

T. P. Meloy Block Vice Chairman
(West Virginia Univ., U.S.A.)

J. P. Clark (Massachusetts Institute of Tech., U.S.A.)

R. K. Rajamani (Univ. of Utah, U.S.A.)

H. Herman (State Univ. of New York, U.S.A.)

B. H. Kaye (Laurentian Univ., CANADA)

L. Hixon (Hosokawa Micron Inter., U.S.A.)

W. Gregg (Hosokawa Micron Inter., U.S.A.)

Secretariat

J. Van Cleef (Hosokawa Micron Inter., U.S.A.)



Hosokawa Micron Corporation and its R&D Center

Publication Office and Owner of Copyright

The Party of Powder Technology (Japan)
in Hosokawa Micron Corporation

No.9, 1-chome, Shoudai Tajika, Hirakata-shi, Osaka 573 Japan

(Complimentary Copy)

Contents

• Letter from editor	<i>G. Jimbo</i>	3
< Original Report >		
• Preparation of Fine Particles of Superconducting Oxide by Aerosol Reactor	<i>K. Okuyama, K. Arai, Y. Kousaka, N. Tohge, M. Tatsumisago, T. Minami and M. Adachi</i> . .	4
• Electrostatic Formation of a Ceramic Membrane with Fine Pores	<i>H. Yamamoto, T. Nomura and S. Masuda</i> . . .	12
• The Relationship between the Flocculation State of Particles and the Packing Structure on the Surface of Gypsum Mold	<i>M. Arakawa, H. Kobayashi, K. Hirado and K. Inoue</i>	18
• Wear of Media during Ultra-fine Grinding	<i>K. Suzuki, Y. Kuwahara and T. Ishizuka</i>	24
• The Release of Enzymes and Proteins from Baker's Yeast Disrupted by a Agitator Bead Mill	<i>K. Matsumoto, H. Ohya, S. Ito and M. Naito</i>	31
• Deposition of Aerosol Particles on Surface Composed of Different Kinds of Materials	<i>H. Yoshida, M. Minooka and H. Masuda</i>	39
• Controlling the Moisture Content within a Product of the Continuous Dryer	<i>I. Shishido, T. Fujimoto, S. Matsumoto and S. Ohtani</i>	48
• An Assessment of the Mechanism of Particle Shape Separation by a Rotating Conical Disk with a Spiral Scraper	<i>K. Yamamoto, T. Tsukada and M. Sugimoto</i>	55
• The Dynamic Measurement of the Physical Properties of Powders Using Vibration – the Mixing Effect of a Small Amount of Fine Powder	<i>M. Satoh, T. Fujimoto, T. Shigemura, F. Hamano and K. Miyanami</i>	67
< Review >		
• Current Status of the Mechanofusion Process for Producing Composite Particles	<i>K. Tanno</i>	74
• Fundamentals of Aerosol Filtration	<i>H. Emi</i>	83
< Original Report >		
• Motion Analysis in Tumbling Mills by the Discrete Element Method	<i>B. K. Mishra and R. K. Rajamani</i>	92
• An XPS Investigation of Hydrothermal and Commercial Barium Titanate Powders	<i>C. C. Hung and R. E. Riman</i>	99
• Competition between Powder Metallurgy and Other Near Net Shape Processes: Case Studies in the Automotive and Aerospace Industries	<i>N. V. Nallicheri and J. P. Clark</i>	105
• Compositional Variation in Multiphasic Compacted Powders	<i>T. P. Meloy and S. Drescher</i>	119
• Ultrafine Grinding in an Annular Ball Mill	<i>O. A. Orumwense and E. Forssberg</i>	126
• Experimental Investigation of Silo Stresses under Consideration of the Influence of Hopper/Feeder Interface	<i>D. Schulze and J. Schwedes</i>	134
• Chemical Vapour Precipitation of Silicon Nitride Powders in a Laser Reactor	<i>R. A. Bouer, F. E. Kruis, P. van der Put, B. Scarlett and J. Schoonman</i>	145
• Emission Control of Particles and Gaseous Pollutants with a High-Temperature Granular Bed Filter	<i>W. Peukert and F. Löffler</i>	155
• Information Article		160

See page 11 for description of the cover photograph.

I am writing this letter just in the season of Christmas and New Year greetings, the time of looking back the passing year of 1990. This year might have a special meaning for Japanese powder scientists and also for this KONA journal.

We have organized the Second World Congress PARTICLE TECHNOLOGY in Kyoto, and it was, I believe, very successful by attracting over seven hundred attendants, including one hundred sixty from overseas countries, all with excellent scientific contributions. In that Congress the word of KONA also played an important role by naming a newly launched academic award as KONA award, which was presented by Mr. M. Hosokawa. The celebrating meeting of its presentation to Dr. C. S. Campbell of Southern California University organized by Hosokawa Micron Corp. was also very successful with the attendance of nearly almost all world-widely famed powder scientists.

I was very much impressed by these facts, which, I believe, clearly reveal the new phase of internationalization of Japanese powder science and technology. KONA journal can not stay out of such a big flow.

The first general meeting of the newly organized editorial committee of this journal, which is announced in this issue, was held on the occasion of the World Congress with the attendance of many foreign members. It was confirmed there that three editorial committees had already been established in three regions and the new system had smoothly started, the fruit of which you can see in this issue.

Indeed this journal still keeps its original function of introducing annually research achievement of Japanese powder technology to foreign countries. But at the same time, this journal now has added a new function of introducing the tendencies of this field of technology of all over the world both with reviews and original papers.

I hope these new criterion and character of this journal will be accepted widely in the new phase of internationalization of Japanese powder science and technology, which was revealed in 1990 and will be revealed more clearly in the coming new year.

A handwritten signature in black ink, appearing to read "G. Jimbo", with a long, sweeping horizontal line underneath it.

Genji Jimbo
Editor in chief

Preparation of Fine Particles of Superconducting Oxide by Aerosol Reactor[†]

Kikuo Okuyama

*Faculty of Engineering
Hiroshima University**

Kouji Arai and Yasuo Kousaka

*Department of Chemical Engineering
University of Osaka Prefecture***

**Noboru Tohge, Masahiro Tatsumisago
and Tsutomu Minami**

*Department of Applied Chemistry
University of Osaka Prefecture***

Motoaki Adachi

*Osaka Prefectural Radiation Research Institute****

Abstract

A new process for preparing particles of superconducting oxides was developed by using an aerosol flow reactor in which aqueous solutions of corresponding metal nitrates are atomized and their droplets are evaporated and thermally decomposed. The particles obtained from this process are spherical and their size can be controlled by changing the concentration of the aqueous solutions. For the Y-Ba-Cu-O system, the particles having an orthorhombic $YBa_2Cu_3O_{7-x}$ phase can be formed directly at the decomposition temperatures from 900 to 1000°C. The bodies sintered from these particles show the offset temperature of the superconducting transition at 87 K. For the Bi-Ca-Sr-Cu-O system, the superconducting particles of the $Bi_2Ca_2Sr_2Cu_3O_x$ and $Bi_{1.8}Pb_{0.2}Ca_2Sr_2Cu_3O_x$ compounds were prepared directly. The crystalline phases of the particles were found to be very sensitive to oxygen pressure in the carrier gas as well as to the decomposition temperature. The sintered bodies from the powders of $Bi_{1.8}Pb_{0.2}Ca_2Sr_2Cu_3O_x$ had onset temperature of 110 K and offset temperature of 80 K.

1. Introduction

Oxide ceramic preparations have been studied intensively ever since the high critical transition temperatures T_c were reported in the La-M-Cu-O (M=Ba, Sr, Ca) ($T_c = 40$ K)^{1,2)}, the Y-Ba-Cu-O ($T_c = 90$ K)^{3,4,5)} and the Bi-Ca-Sr-Cu-O ($T_c = 110$ K)⁶⁾ systems. The sintering powders are usually prepared through the solid-state reac-

tion of the corresponding metal oxides, hydroxides and/or carbonates^{2~6)}. To achieve their homogeneity, however, the calcination and grinding processes must be repeated several times.

The authors have shown that the aerosol flow reactor is an excellent process to produce fine oxide powders, such as TiO_2 , SiO_2 , Al_2O_3 and $\alpha-Fe_2O_3$ ^{7,8)}. This technique has the following advantages: (1) the particles produced are ultrafine, several hundreds of a nm or less, (2) the distribution of their diameters is uniform and easy to control, and (3) highly pure oxide particles can be synthesized directly from appropriate vapors in a short time. In this study, the aerosol flow reactor using spray pyrolysis technique was applied to the preparation of fine powders of high T_c superconductors in Y-

* 1-4-1, Kagamiyama, Higashi-hiroshima, 724
TEL. 0824-22-7111

** Mozu-umemachi 4-804, Sakai 591
TEL. 0722-52-1161

*** Shinke-cho 174-16, Sakai 593
TEL. 0722-36-2221

[†] This report was originally printed in *J. Soc. Powder Technology, Japan*, 26, 146-150 (1989) in Japanese, before being translated into English with the permission of the editorial committee of the Soc. Powder Technology, Japan.

Ba-Cu-O and Bi-Ca-Sr-Cu-O systems.

2. Experimental Procedure

2. 1 Aqueous solution preparation

In the Y-Ba-Cu-O system, the aqueous solution to be sprayed is prepared by dissolving appropriate amounts of the corresponding metal nitrates in ultrapure water; the ratio of nitrates is $\text{Y}(\text{NO}_3)_3 \cdot 6\text{H}_2\text{O} : \text{Ba}(\text{NO}_3)_2 : \text{Cu}(\text{NO}_3)_2 \cdot 2\text{H}_2\text{O} = 1:2:3$. The concentrations of the solution vary from 0.0072 to 0.36 mol/l.

In the Bi-Ca-Sr-Cu-O system, the corresponding metal nitrates are dissolved in water containing nitric acid (14%) at the ratio of $\text{Bi}(\text{NO}_3)_3 \cdot 5\text{H}_2\text{O} : \text{Ca}(\text{NO}_3)_2 \cdot 4\text{H}_2\text{O} : \text{Sr}(\text{NO}_3)_2 : \text{Cu}(\text{NO}_3)_2 \cdot 3\text{H}_2\text{O} = 2:2:2:3$. And another Bi-Pb-Ca-Sr-Cu-O sample is also prepared by adding $\text{Pb}(\text{NO}_3)_2 \cdot 5\text{H}_2\text{O}$ to the above nitrate mixture with the cation ratio of $\text{Bi}:\text{Pb}:\text{Ca}:\text{Sr}:\text{Cu} = 1.8:0.2:2:2:3$. The concentrations of the solution vary from 0.006 to 0.48 mol/l.

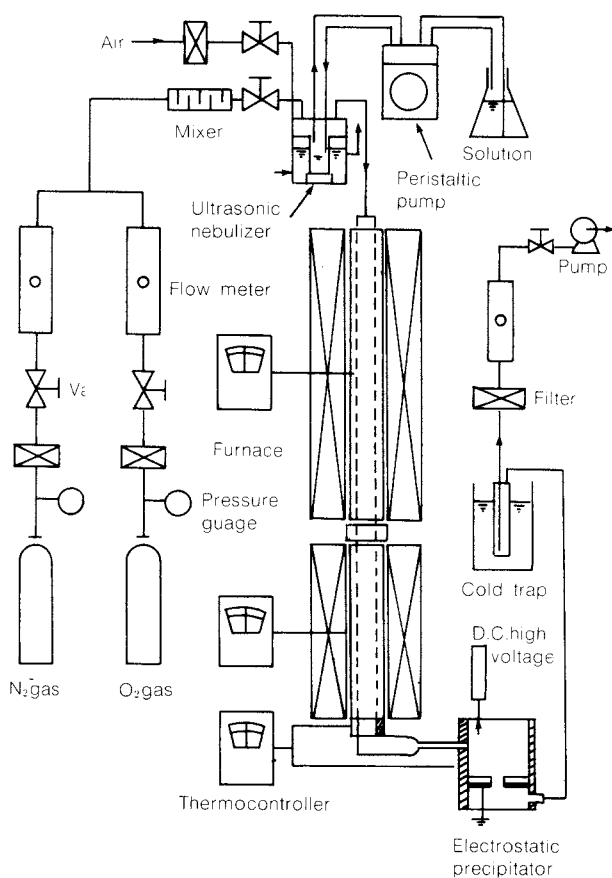


Fig. 1 Experimental system for producing fine particles of superconducting oxides.

2. 2 Aerosol flow reactor

Figure 1 is a schematic diagram of the aerosol flow reactor system used in this study^{9,10}. The system consists of an ultrasonic nebulizer, a reaction furnace and an electrostatic precipitator. The aqueous solution was atomized with the ultrasonic nebulizer, which was operated at 1.7 MHz. The droplets generated were led to the reaction furnace (30 mm in inner diameter and 940 mm long) with carrier gas, and thermally decomposed at various temperatures. The flow rate of the carrier gas varied from 0.7 to 2.6 l/min. The powders produced were collected using an electrostatic precipitator. In the Y-Ba-Cu-O system, air was used as the carrier gas. In the Bi-Ca-Sr-Cu-O system, a mixture gas of the nitrogen and oxygen at various mixing ratios was used as the carrier gas to examine the effect of oxygen pressure on the particles' crystal structure.

The crystalline phase and shape of the powders obtained were examined using an x-ray diffraction ($\text{CuK}\alpha$) and a scanning electron microscope (SEM), respectively. The temperature dependence of the resistivity of the sintered bodies was measured using the conventional four-probe method where silver paste was used for the electrodes.

3. Experimental Results and Discussion

3. 1 Y-Ba-Cu-O system

Figure 2 shows the x-ray diffraction patterns of the powders obtained at various decomposition temperatures. In the pattern of the powders obtained at 800°C, most of the peaks can be assigned to BaCO_3 and $\text{Y}_2\text{Cu}_2\text{O}_5$, indicating that the temperature is insufficient to form the compound $\text{YBa}_2\text{Cu}_3\text{O}_{7-x}$; the formation of the carbonate is possible when air is the carrier gas. However, the patterns of the powders prepared at 900° and 1000°C show that the compound $\text{YBa}_2\text{Cu}_3\text{O}_{7-x}$ is produced. Moreover, it was noted that the crystallinity of these powders develops with an increasing decomposition temperature; the powders obtained at 1000°C are indeed of the orthorhombic single phase, as can be seen from the shape of the peak at $2\theta = 32^\circ$ and the relative intensity of the two peaks at around $2\theta = 47^\circ$ ¹¹. On the other hand, when the decomposition temperature exceeds 1000°C, the BaCu_2O_3 and Y_2BaCuO_5 phases appear

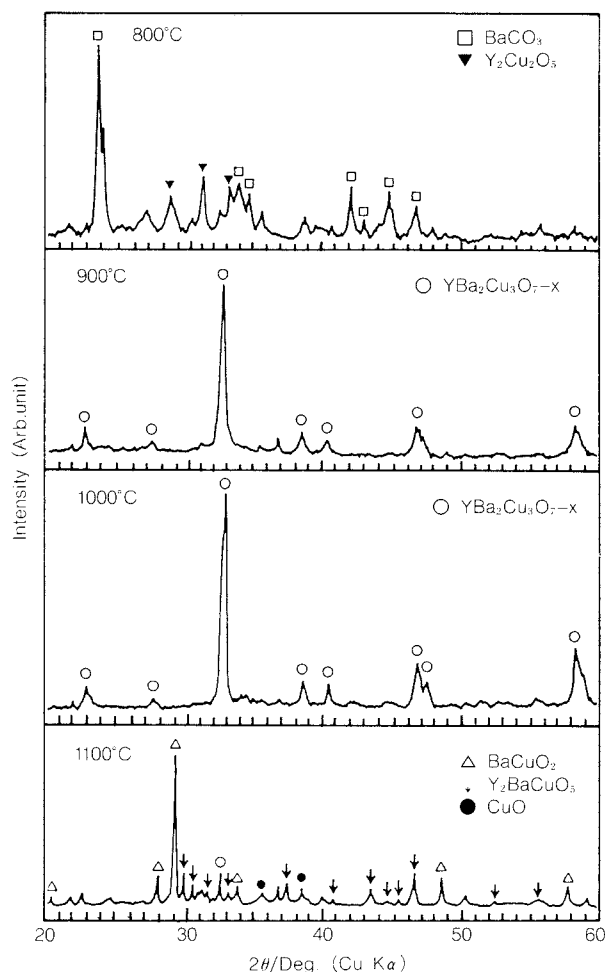


Fig. 2 X-ray diffraction patterns of $\text{YBa}_2\text{Cu}_3\text{O}_{7-x}$ particles obtained at various decomposition temperatures: 800°C, 900°C, 1000°C, and 1100°C

with the other minor phases: $\text{YBa}_2\text{Cu}_3\text{O}_{7-x}$ and CuO . This means that the decomposition temperature in this range is too high to produce the compound $\text{YBa}_2\text{Cu}_3\text{O}_{7-x}$, since these phases have been reported for ceramics sintered above 950°C and in the samples quenched from the melts at 1400°C^{12,13}. The results show that the $\text{YBa}_2\text{Cu}_3\text{O}_{7-x}$ powders, even in an orthorhombic form, can be synthesized directly by the thermal decomposition of the appropriate metal nitrates from 900° to 1000°C, using air as the carrier gas.

The flow rate of the carrier gas was changed from 0.65 to 2.6 l/min to examine the effect of the flow rate on the crystal structure at 900° and 1000°C. The x-ray diffraction patterns of the particles generated under these conditions showed the $\text{YBa}_2\text{Cu}_3\text{O}_{7-x}$ single

phase. It was found that the crystalline phase was greatly affected by the decomposition temperature, but not by the retention time in the furnace.

Figure 3 shows the SEM photographs of the $\text{YBa}_2\text{Cu}_3\text{O}_{7-x}$ powders prepared at 1000°C and flow rate of 1.3 l/min, where concentra-

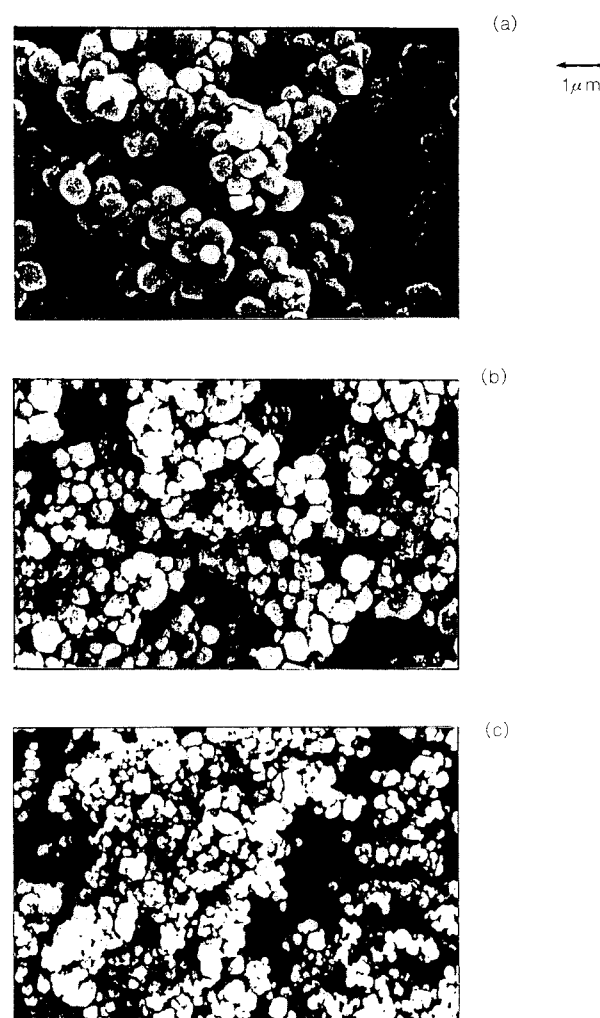


Fig. 3 SEM photographs of the $\text{YBa}_2\text{Cu}_3\text{O}_{7-x}$ particles generated from solutions of three different concentrations: 0.36 mol/l(a), 0.036 mol/l(b), and 0.0072 mol/l(c)

tions of the solution are 0.36, 0.036 and 0.0072 mol/l. Their size distribution measured from the photographs are shown in Fig. 4. The geometric mean diameters of these particles are 0.57, 0.36 and 0.15 μm and the geometric standard deviations are 1.36, 1.60 and 1.99, respectively. The mean size and the width of distribution increases and decreases, respectively, with the concentration of the solution. It

was found that the particles obtained were spherical and their size can be controlled by changing the concentration of the aqueous solution.

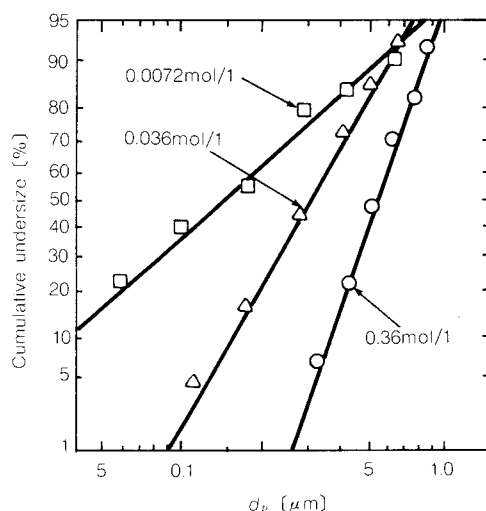


Fig. 4 Size distribution of $\text{YBa}_2\text{Cu}_3\text{O}_{7-x}$ particles obtained from SEM photographs

The powders which were obtained from the solution of 0.36 mol/l at 1000°C were pressed into a pellet mold 13 mm in diameter and 0.5 mm in depth. The obtained pellet was sintered at 900°C for 4 h in air, followed by annealing at 500°C for 5 h in O_2 . Figure 5 shows the x-ray diffraction pattern of the sintered body. The shapes of the peaks at $2\theta = 32^\circ$ and 47° show that the sintered body is the orthorhombic single phase of $\text{YBa}_2\text{Cu}_3\text{O}_{7-x}$.

Figure 6 shows the typical temperature dependence of the resistivity for the sintered body. The resistivity of the sample shows metallic behavior down to around 90 K and it begins to drop abruptly at 88 K, with the offset temperature of 84 K.

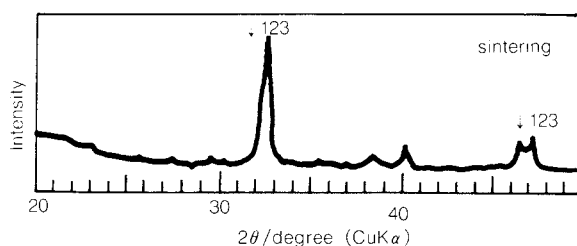


Fig. 5 X-ray diffraction pattern of the sintered body from $\text{YBa}_2\text{Cu}_3\text{O}_{7-x}$ particles

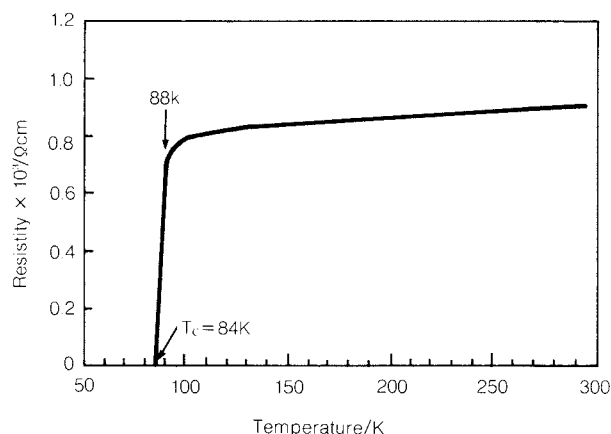


Fig. 6 Temperature dependence of the resistivity for the sintered body; $\text{YBa}_2\text{Cu}_3\text{O}_{7-x}$ powder as produced at 1000°C , sintered at 900°C for 4 h in air and annealed at 500°C for 5 h in O_2

3. 2 Bi-Ca-Sr-Cu-O system

The Bi-Ca-Sr-Cu-O system discovered by Maeda *et al.*⁶⁾ has three main superconducting phases with different transition temperatures around 10, 80, and 110 K, which have the respective c-axis values of 24, 39 and 37 Å. It was found that the crystalline phase of the particles obtained in this system is greatly affected by the oxygen partial pressure in the carrier gas as well as the decomposition temperature.

Figure 7 shows the SEM photograph of synthesized particles of $\text{Bi}_2\text{Ca}_2\text{Sr}_2\text{Cu}_3\text{O}_x$ prepared at 800°C in a nitrogen gas stream, where concentrations of the solution are 0.48, 0.06 and 0.06 mol/l. The average diameters of the particles were about 1.4, 0.8 and 0.4 μm, respectively. It was found that the particles obtained are spherical and their sizes increase with the concentration of the aqueous solution which is the same as the case of $\text{YBa}_2\text{Cu}_3\text{O}_{7-x}$ particles. These features meet the requirements needed not only for the standard samples of superconductive particles but also for the starting powders used in sintering.

Figure 8 shows the x-ray diffraction patterns of the particles obtained at various decomposition temperatures in the nitrogen gas stream. In the pattern, the 770° and 780°C , peaks can be assigned to both the 80 and 10 K phases, indicating that the temperature is not sufficient to form the superconducting compound. However, the patterns of the particles prepared at

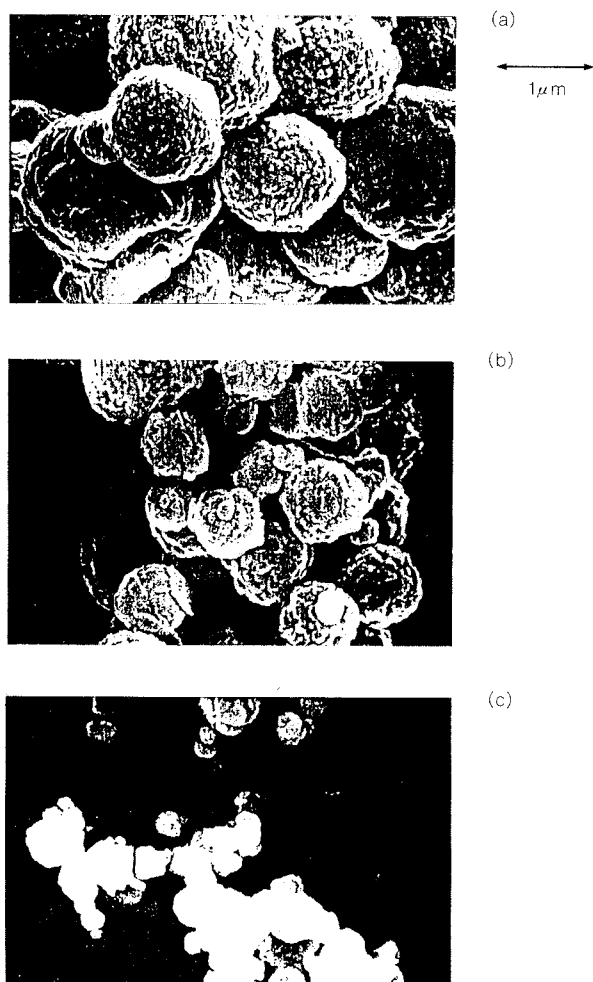


Fig. 7 SEM photographs of $\text{Bi}_2\text{Ca}_2\text{Sr}_2\text{Cu}_3\text{O}_x$ particles generated from solutions of three different concentrations: 0.48 mol/l(a), 0.06 mol/l(b), and 0.006 mol/l(c)

800°C show that the 80 K phase superconducting oxide particles are produced directly in the Bi-Ca-Sr-Cu-O system. The SEM photograph of Fig. 7 shows particles prepared under these conditions. On the other hand, when the decomposition temperature exceeds 800°C, the 10 K phase (c-axis 24 Å) appears again with other minor phases. This means that the decomposition temperature in this range is too high to produce the compound in the 80 K phase, and the particles have melted as discussed in the previous study¹⁰.

Figure 9 shows the x-ray diffraction patterns of particles obtained using the nitrogen carrier gas with the oxygen gas pressure of 1/13 atm. The 80 K superconducting phase can be seen under the decomposition temperature of 840°C,

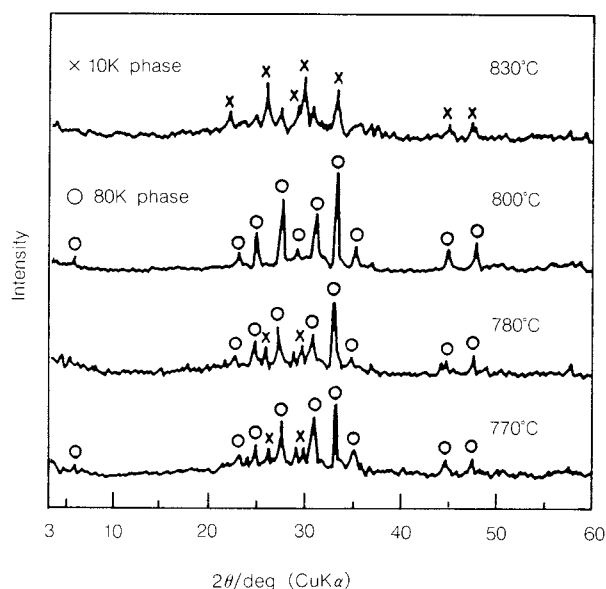


Fig. 8 X-ray diffraction patterns of $\text{Bi}_2\text{Ca}_2\text{Sr}_2\text{Cu}_3\text{O}_x$ particles obtained at different temperatures in a nitrogen stream

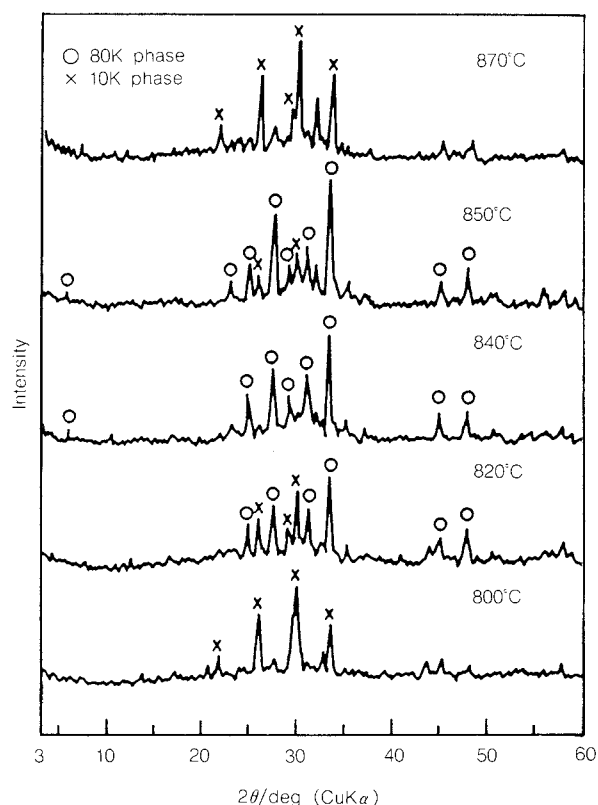


Fig. 9 X-ray diffraction patterns of $\text{Bi}_2\text{Ca}_2\text{Sr}_2\text{Cu}_3\text{O}_x$ particles obtained at different temperatures in oxygen at a partial pressure of 1/13 atm

which is higher than that in the case of nitrogen gas only as shown in Fig. 8. Under oxygen par-

tial pressures above 1/5 atm, the particles produced were found to have only the 10 K phase, irrespective of any decomposition temperatures.

The above results show that the 80 K phase particles can be synthesized directly under the limited conditions according to the decomposition temperature and oxygen pressure. Figure 10 shows the crystal structure's dependence on the decomposition temperature and oxygen pressure. In the figure, the circles indicate that the 80 K superconductive phase can only be formed, the triangles; the mixture of 80 K and 10 K phase, and crosses; the 10 K phase only. When the oxygen pressure in the carrier gas is increased, the decomposition temperature where the 80 K phase can be obtained was seen to increase as well. This figure indicates the necessary operating condition to directly ob-

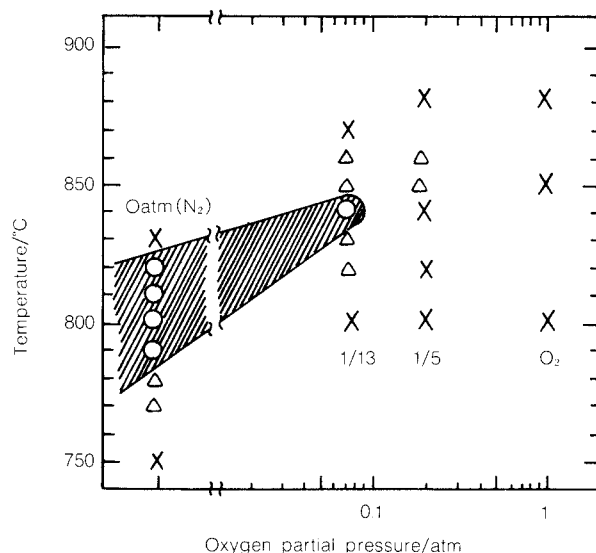


Fig. 10 Relationship of the crystalline phase of $\text{Bi}_2\text{Ca}_2\text{Sr}_2\text{Cu}_3\text{O}_x$ particles to the oxygen partial pressure and decomposition temperature

tain the 80 K phase particles. As a result, the 110 K phase has not appeared over a wide range of oxygen pressures and decomposition temperatures. The result is similar to that obtained for the preparation of $\text{BiCaSrCu}_2\text{O}_x$ particles¹⁰.

Figure 11 shows the x-ray diffraction patterns of the particles obtained in the $\text{Bi}_{1.8}\text{Pb}_{0.2}\text{Ca}_2\text{Sr}_2\text{Cu}_3\text{O}_x$ compound at various decomposition temperatures in a nitrogen stream. In the patterns of the particles ob-

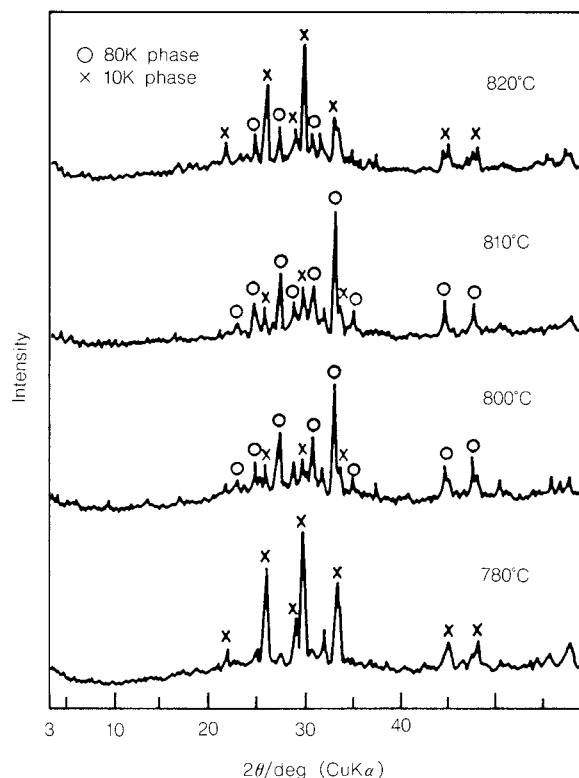


Fig. 11 X-ray diffraction patterns of $\text{Bi}_{1.8}\text{Pb}_{0.2}\text{Ca}_2\text{Sr}_2\text{Cu}_3\text{O}_x$ particles obtained at different temperatures in a nitrogen gas stream

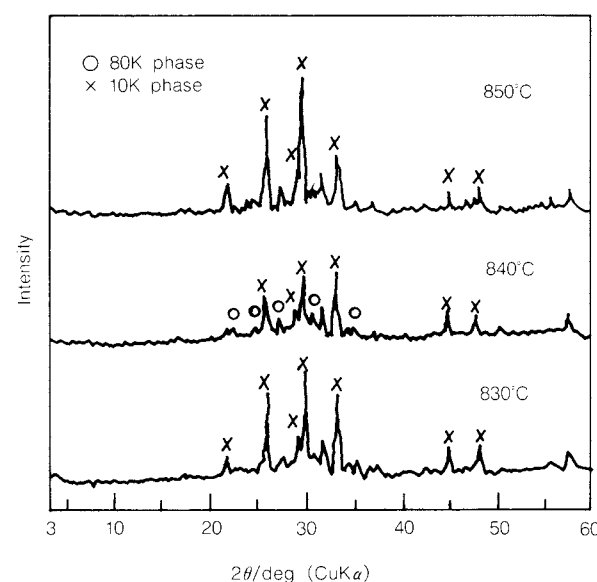


Fig. 12 X-ray diffraction patterns of $\text{Bi}_{1.8}\text{Pb}_{0.2}\text{Ca}_2\text{Sr}_2\text{Cu}_3\text{O}_x$ particles obtained at different temperatures in oxygen at a partial pressure of 1/13 atm

tained at 800°C, the peaks can be assigned to the 80 and 10 K phases. When 10% of Bi is re-

placed by Pb, it was seen that the 10 K phase appears. The x-ray diffraction patterns of particles obtained at an oxygen partial pressure of 1/13 atm are shown in Fig. 12. In the patterns, the 10 K phase appears as well. As seen from the comparison of these results with those for the $\text{Bi}_2\text{Ca}_2\text{Sr}_2\text{Cu}_3\text{O}_x$ compound, the 80 K superconductive phase tends to weaken with the addition of Pb, which will be explained after additional research.

The $\text{Bi}_2\text{Ca}_2\text{Sr}_2\text{Cu}_3\text{O}_x$ and $\text{Bi}_{1.8}\text{Pb}_{0.2}\text{Ca}_2\text{Sr}_2\text{Cu}_3\text{O}_x$ particles obtained at 840°C in the carrier gas with an oxygen partial pressure of 1/13 atm, followed by annealing at 845°C for 1 h in air, were pressed into pellets by same method as described in the Y-Ba-Cu-O system. After the pellets were sintered at 845°C for 20 h in air, the resistivity of the samples was measured. Figure 13 shows the temperature dependence of the resistivity for the sintered body. It was seen that the resistivities of both sintered bodies of $\text{Bi}_2\text{Ca}_2\text{Sr}_2\text{Cu}_3\text{O}_x$ and $\text{Bi}_{1.8}\text{Pb}_{0.2}\text{Ca}_2\text{Sr}_2\text{Cu}_3\text{O}_x$ particles show metallic behavior, and that the sample with Pb indicates the transition with an onset temperature of 100 K and an offset temperature of 80 K. Since the optimum condition for sintering has not yet been determined, it can be expected that the superconductive properties of the sintered bodies may be further improved by examining the sintering and subsequent annealing processes in detail.

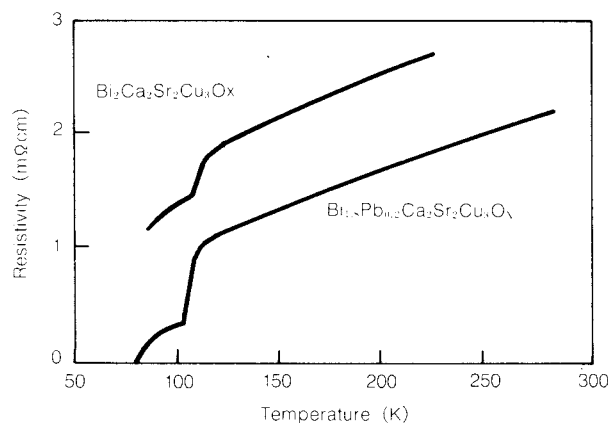


Fig. 13 Temperature dependence of the resistivity for sintered bodies of $\text{Bi}_2\text{Ca}_2\text{Sr}_2\text{Cu}_3\text{O}_x$ and $\text{Bi}_{1.8}\text{Pb}_{0.2}\text{Ca}_2\text{Sr}_2\text{Cu}_3\text{O}_x$ particles

Conclusions

A new process using the aerosol flow reactor was developed to prepare superconducting par-

ticles in the Y-Ba-Cu-O and Bi-Ca-Sr-Cu-O systems. In the process, aqueous solutions of the corresponding metal nitrates are atomized and their droplets are evaporated and thermally decomposed. The particles generated are spherical and their size can be controlled by the concentration of the aqueous solutions. In the Y-Ba-Cu-O system, the uniformly-distributed fine powders of the $\text{YBa}_2\text{Cu}_3\text{O}_{7-x}$ compound, even in an orthorhombic single phase, are directly produced by the process. The powders give the superconducting ceramics with offset T_c at around 84 K. For Bi-Ca-Sr-Cu-O system, the superconducting particles of $\text{Bi}_2\text{Ca}_2\text{Sr}_2\text{Cu}_3\text{O}_x$ and $\text{Bi}_{1.8}\text{Pb}_{0.2}\text{Ca}_2\text{Sr}_2\text{Cu}_3\text{O}_x$ compounds are prepared directly. The crystalline phases of the particles are found to be very sensitive to the oxygen pressure in the carrier gas as well as the decomposition temperature. The sintered bodies from the powders of $\text{Bi}_{1.8}\text{Pb}_{0.2}\text{Ca}_2\text{Sr}_2\text{Cu}_3\text{O}_x$ show the superconducting phase with an onset temperature of 110 K and an offset temperature of 80 K.

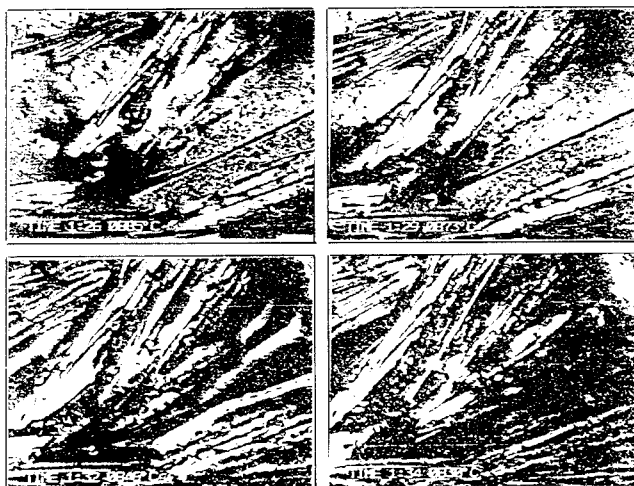
References

- 1) Bednorz, J. G. and K. A. Muller: *Z. Phys.*, **B64**, 189 (1986).
- 2) Chu, C.W. P.H. Hor, R. L. Meng, L. Gao, Z. J. Huang and Y. Q. Wang: *Phys. Rev. Lett.*, **58**, 405 (1987).
- 3) Wu, M. K., J. R. Ashburn, C. J. Torng, P. H. Hor, R. L. Meg, L. Gao, Z. J. Huang, Y. Q. Wang and C. W. Chu: *Phys. Rev. Lett.*, **58**, 908 (1987).
- 4) Hikami, S. T., T. Hirai and S. Kagoshima: *Jpn. J. Appl. Phys.*, **26**, L314 (1987).
- 5) Takagi, H., S. Uchida, H. Sato, H. Ishii, K. Kishio, K. Kitazawa, K. Fueki and S. Tanaka: *Jpn. J. Appl. Phys.*, **26**, L601 (1987).
- 6) Maeda, H., Y. Tanaka, M. Fukutomi and T. Asano: *Jpn. J. Appl. Phys.*, **27**, L209 (1988).
- 7) Okuyama, K., Y. Kousaka, N. Tohge, S. Yamamoto, J. J. Wu, R. C. Flagam and J. H. Seinfeld: *AIChE J.*, **32**, 2010 (1986).
- 8) Okuyama, K., Y. Kousaka, N. Tohge and M. Adachi: *J. Mater. Sci. Lett.*, **6**, 1466 (1987).
- 9) Tohge, N., M. Tatsumisago, T. Minami, K. Okuyama, M. Adachi and Y. Kousaka: *Jpn. J. Appl. Phys.*, **27**, L1086 (1988).
- 10) Tohge, N., M. Tatsumisago, T. Minami, K. Okuyama, K. Arai and Y. Kousaka: *Jpn. J. Appl. Phys.*, **28**, L1175 (1989).
- 11) Takayama-Muromachi, E., Y. Uchida, K. Yukino, T. Tanaka and K. Kato: *Jpn. J. Appl. Phys.*, **26**, L665 (1987).

12) Komatsu, T., K. Imai, K. Matsushita, M. Ishii, M. Tanaka, T. Yamashita: *Jpn. J. Appl. Phys.*, **26**, L1272 (1987).

13) Ishii, M., T. Maeda, M. Matsuda, M. Takata and T. Yamashita: *Jpn. J. Appl. Phys.*, **26**, L1959 (1987).

Explanation of the cover photograph



The partial melting state of the Bi-based superconducting oxide ($\text{Bi}_2\text{Sr}_2\text{Ca}_1\text{Cu}_2\text{O}_x$) has been directly observed using a microscope high temperature heating system (ULVAC MS-E1R). The sample was prepared by the conventional solid state reaction and packed into an alumina cell. The sample was heated up to 1000°C in a gold image furnace with an infrared heater. The melting and crystallization behavior during the heating and cooling process were observed by means of the optical microscope.

The cover photographs are optical microscope images of the partial melting state and crystallization from the molten oxide during the cooling process. The growth of the needlelike crystals are observed. These crystals are $(\text{Ca}, \text{Sr})\text{CuO}_x$ which is not superconducting phase.

Presented by:

Yoshiaki TANAKA, *Tsuginori HASEBE
National Research Institute for Metals,
Tsukuba Laboratories,
1-2-1, Sengen Tsukuba, Ibaraki 305

*On leave from

Sumitomo Heavy Industries Co., Ltd.
Hiratsuka Research Laboratory,
63-30, Yuuhigaoka Hiratsuka, Kanagawa 254

Electrostatic Formation of a Ceramic Membrane with Fine Pores[†]

Hideo Yamamoto, Tsuyoshi Nomura
and Senichi Masuda

*Institute of Industrial Science,
University of Tokyo**

Abstract

A new method for forming a ceramic membrane was devised. Ultra-fine particles synthesized by thermally activated CVD (Chemical Vapor Deposition) were deposited on the surface of a porous ceramic supporter by electrostatic force and sintered in an inert gas atmosphere. The ceramic membrane made by this method is available for ultrafiltration because it has very fine pores of about 0.04 micro-meter in diameter but a large porosity.

1. Introduction

A new process for producing ceramic membranes with fine pores, using ultra-fine particles prepared by a vapor-phase reaction (thermal CVD process) has been developed, with studies on its effectiveness being carried out^{1~3)}.

The principle of this method is as follows: CVD ultra-fine particles are electrically charged directly after being produced, deposited onto a surface of a porous ceramic substrate in the DC-field to form a particle layer, and are sintered to form a membrane with fine pores. This new method was named "Electrostatic Formation of a Ceramic Membrane (EFCM)", and it is being investigated further.

It is very important to successfully develop this method of forming ceramic membranes with fine pores because of its extensive applications, including water treatment under high pressure and high temperature, separation or condensation of organic solutions, cleaning of high temperature gases containing corrosive components, etc., while the present polymer membranes are not always suited to these specific processes.

This paper describes the principle of the

Electrostatic Formation of a Ceramic Membrane (EFCM), the structure and results of basic performance tests of the membrane as a separation membrane in the case of forming a membrane from silicon nitride ultra-fine particle coating on the outside of porous ceramic tubes.

2. Experimental Apparatus and Principles of Electrostatic Formation of a Ceramic Membrane (EFCM)

Figure 1 shows a schematic diagram of the

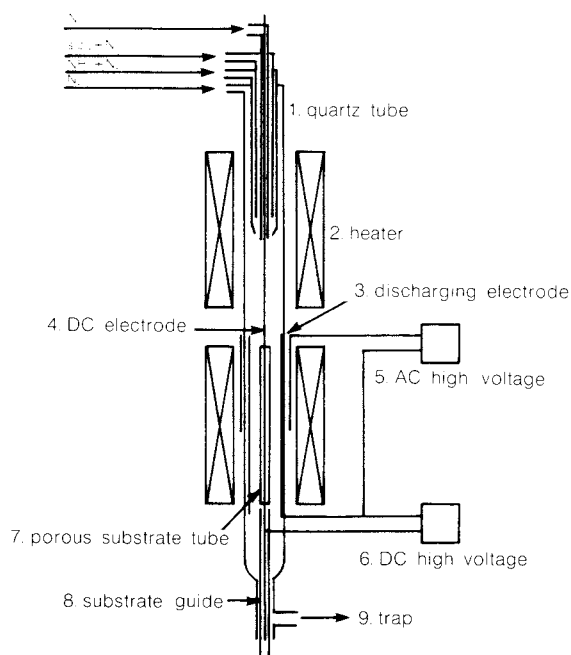


Fig. 1 Schematic diagram of experimental apparatus

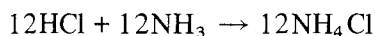
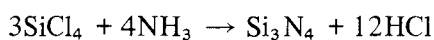
* Roppongi, Minato-ku, Tokyo 106, Japan
TEL. 03-402-6231

† This report was originally printed in *J. Soc. Powder Technology, Japan*, 26, 169-173 (1989) in Japanese, before being translated into English with the permission of the editorial Committee of the Soc. Powder Technology, Japan.

experimental apparatus for producing a membrane from ultra-fine silicon nitride particles. It consists of a reactor and membrane-forming section, with a quartz tube (1) contained within (42mm ID). The reactor consists of four coaxial quartz tubes within a quartz tube (1). In a membrane-forming section, a corona-discharging electrode (3) and a DC electrode (4) are installed to charge the ultra-fine particles from the reactor and make them migrate. Power supplies (5) and (6) supply high-frequency high voltage (about 20 kHz, 20 kV) and high DC voltage (about 5 kV), respectively. An AC-corona discharging system is adopted for stable corona generation even under high temperature and in a complex gas composition, and mono-polar ions are produced by supplying the DC voltage to this system.

The ultra-fine particles prepared in the reactor are carried down like a thin cylinder with sheath gas (inert gas such as nitrogen or argon) which flows from the inner and outer inlet. Reaching the forming section, they are charged with the same polarity in the corona area close to the discharging electrode, migrate toward the center electrostatically in the supplied DC-field, deposit on the outer wall of the substrate (a porous ceramic tube) installed on the central axis and form a layer of the accumulated particles. The substrate can be moved up or down and rotating slowly to be coated with a uniform layer. The particle layer is then sintered directly into an asymmetric ceramic membrane without being taken out of the apparatus. The porous substrate used in this study is sintered alumina tubes with an outer and inner diameter of 10 and 7 mm, respectively, and its nominal mean pore size is 10 μm .

For preparing the ultra-fine particles of silicon nitride as the forming material of the membrane, silicon-tetrachloride and ammonia gas are used. This reaction is carried under excess ammonia; therefore, ammonium-chloride deposits as the by-product following the reactions:



Ammonium-chloride, however, does not deposit on the substrate surface when the membrane forming section is kept above its sublimation temperature of 340°C⁴⁾.

The ultra-fine particles of silicon nitride prepared at 1200°C are considered to be amorphous like⁴⁾.

3. Membrane Formation

3. 1 Size and size distribution of the particles prepared by CVD

It is expected that the pore size of the membrane prepared by sintering the deposited particle layer would depend on the size of the constituent silicon nitride particles, and it is necessary to prepare particles as fine as possible for forming a membrane with fine pores. The size of the particles prepared by thermal CVD process depends on the concentration of the reactive gases and the reaction temperature essentially; therefore, it is necessary to select the optimum condition for preparing particles.

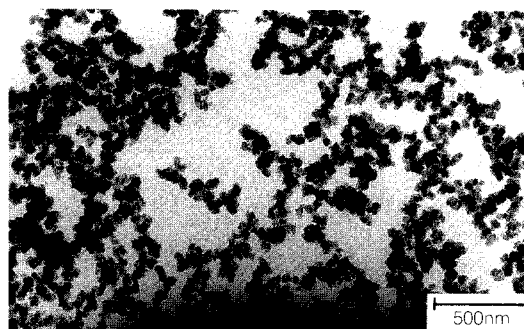


Fig. 2 TEM photograph of Si_3N_4 particles synthesized by thermally activated CVD (temperature; 1200°C, concentration of SiCl_4 ; 1.4%, $\text{NH}_3/\text{SiCl}_4 = 6$)

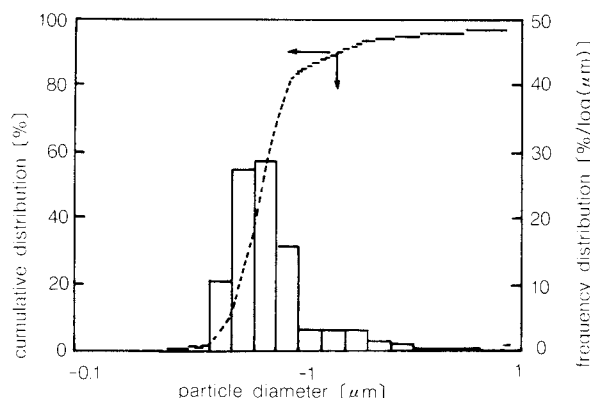


Fig. 3 Size distribution of the particles of Fig. 2 measured with centrifugal photo extinction method

Figures 2 and 3 show a TEM photo of the silicon nitride particles prepared in these experiments and the size distribution of these particles measured by the photo extinction centrifugal sedimentation method, respectively. These

particles were synthesized under the following reactive conditions: the concentration of silicon-tetrachloride in the reactor was 1.4% by volume, the ratio of ammonia to silicon-tetrachloride was 6 and the reaction temperature was 1200°C. As being observed in Fig. 2, the particles are of uniform diameter of several tens of nm, and the weight medium diameter is 0.07 μm according to Fig. 3. It should be noted that the photo extinction centrifugal sedimentation method does not give an absolutely correct size distribution, because it has some problems remaining to be solved including several factors such as the extinction coefficient, but we can get a significant information regarding the relative size distributions of the

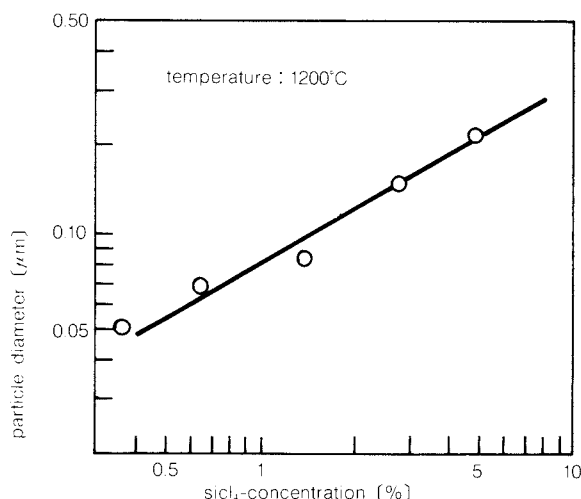


Fig. 4 Effect of SiCl_4 concentration at reaction zone on average particle size ($\text{NH}_3/\text{SiCl}_4 = 6$)

other particle groups. Figure 4 shows the effects of the silicon-tetrachloride concentration on the average particle size determined by the photo extinction centrifugal sedimentation method, where the weight-average particle size is plotted against the silicon-tetrachloride concentration in the reaction zone (the ratio of ammonia to silicon-tetrachloride was fixed at 6). It is shown that the average particle size decreases as the silicon-tetrachloride concentration decreases.

3. 2 Electrostatic deposition

Figure 5 presents a photo of the substrate coated with the electrostatically deposited particles before sintering. The upper photo is the alumina substrate coated with the particles; it is difficult to be observed because both the par-

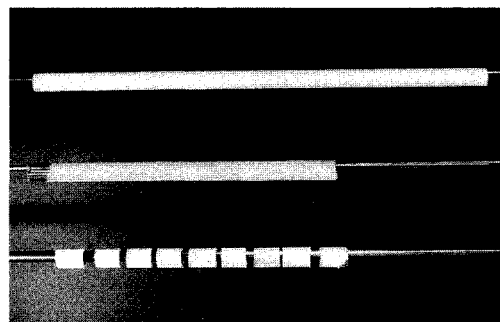


Fig. 5 Photograph of ceramic tubes with particle deposits

ticles and substrate were white in color. To avoid this difficulty, the middle one shows the particles which are deposited on a quartz tube. The lower one shows the test pieces for the electromicroscope. The white part is the deposit layer in the middle one. It is observed that the particles are deposited uniformly over the tube's surface. The length and thickness of the deposited particle layer can be controlled by the movement distance of the substrate, and the velocity of movement of the substrate and the concentration of the particles prepared, respectively.

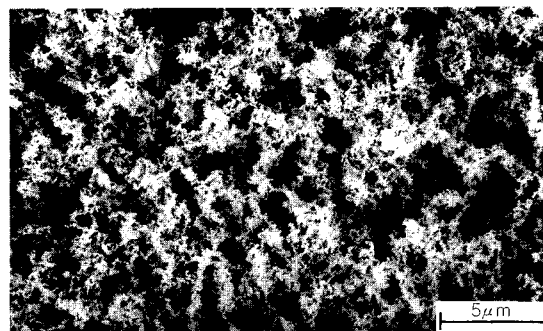


Fig. 6 SEM photograph of particle deposits on a ceramic tube by electrostatic force (before being sintered)

Figure 6 shows a SEM photo of the surface of the particle layer deposited by electrophoresis. It shows a structure peculiar to the electrostatic deposit, and this structure is supposed to reflect the membrane structure as discussed in the following section. The deposit structures expected to be controlled by the intensity of the DC-field and quantity of charge on each particle.

3. 3 Structure of the sintered membrane

To form a better membrane, it is necessary to sinter the particle layer to provide as a

porous layer as possible, with larger voids. In sintering ceramic materials, the temperature, time of reaction, rate of temperature rise, the atmosphere and the sintering aids must be controlled. In these experiments, the deposits were sintered under various trial and error conditions and the membrane structures examined by SEM analysis mainly. The silicon nitride particles prepared in these experiments could be sintered at $1200 \sim 1300^{\circ}\text{C}$ in nitrogen. This is a much lower temperature than that normally associated with production of the structural silicon nitride materials. For this reason, these particles are considered very small and amorphous, or the deposit layer is very thin. As this is a very interesting phenomenon, it is necessary to study it in more depth in future.



Fig. 7 Sectional photograph (SEM) of the ceramic membrane

Figure 7 presents a cross-sectional SEM photo of the membrane. It is an asymmetric, dense membrane with a thickness of approximately $20 \mu\text{m}$, covering the 1.5 mm thick alumina substrate. Figure 8 shows a SEM photo of the membrane with its surface structures. This membrane was sintered at 1200°C for 2 hr in nitrogen. A very peculiar membrane with a three-dimensional network is observed. Such structures have resulted presumably from the characteristic structures of the electrostatically deposited particle layer shown in Fig. 6. A membrane with this structure has a large porosity similar to a fiber filter; therefore, is advantageous in keeping the pressure drop very low when it is utilized as the separation membrane.

The pore size of the membrane shown in Fig. 8 is several micrometers, determined from the photo, and can be directly applied for various industrial purposes including microfiltra-

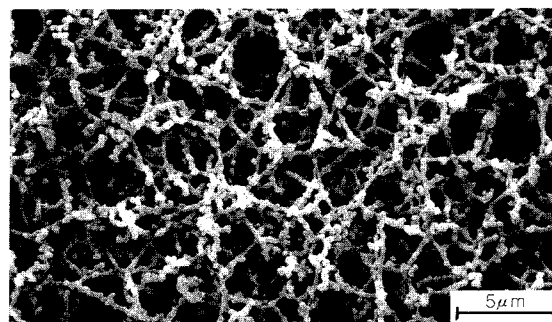


Fig. 8 SEM photograph of ceramic membrane surface

tion (MF). On the other hand, there is also a strong need for a membrane with smaller pores. To control the size of the ultra-fine particles synthesized as the material for the membrane is one of the major factors that can be used to control the pore size in this membrane forming method. One of the factors to control the particle size is the reactant gas concentration as shown in Fig. 4. The membrane shown in Fig. 8 is made from the particles prepared with a silicon-tetrachloride concentration of 1.4%, while with a fairly reduced concentration of 0.21% in Fig. 9. The pore size of the membrane

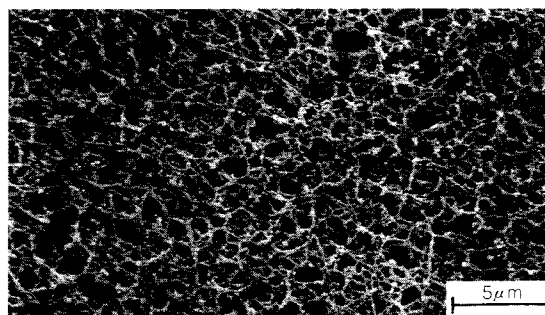


Fig. 9 SEM photograph of ceramic membrane surface

shown in Fig. 9, determined from the micro-photo, is $1 \mu\text{m}$ or less, and it is about one-tenth of the membrane shown in Fig. 8. Although the size of these particles is not measured, it is considered to be much smaller than that of the particles in Fig. 8, and estimated to be $0.04 \mu\text{m}$ from Fig. 4. (It has to be noted that this particle size is characterized using the photo extinction centrifugal sedimentation method.) These results have indicated that the pore size of the membrane can be controlled to some extent by controlling the size of the

deposited (or prepared) particles. On the other hand, in these experiments, decreasing the reactant gas concentration with change the number concentrations of the produced particles; therefore, the concentration of the depositing particles is expected to be one of the factors to control the pore size of the membrane. It is, however, not known how the structures of the deposited particle layer are affected by these factors, nor how the structures of the sintered membrane are affected by that of the deposited particle layer. At present, the effects of reactant gas concentration, reaction temperature, electrostatic depositing conditions and sintering conditions are being quantitatively investigated.

4. Basic Characteristics of the Membranes

The membranes prepared by the method "Electrostatic Formation of a Ceramic Membrane (EFCM)" have characteristic structures; therefore, they are expected to be used for a wide variety of industrial applications. These ceramic membranes are highly heat- and chemical-resistant, and they are sufficiently porous to allow fluids to pass at a very low pressure drop. Some of the expected applications of these membrane are, therefore, utilizing them as the filters for high-temperature gas cleaning and for the separation of organic solutions.

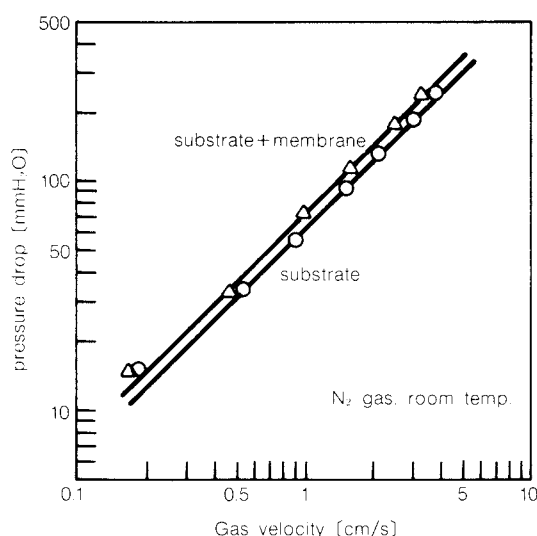


Fig. 10 Gas pressure drop of the ceramic membrane

Figure 10 shows the gas pressure drops across the substrate and that coated with the

membrane shown in Fig. 8. They have almost the same magnitude of resistance to gas permeation, though the pore size of the membrane is about 1/10th the size of the alumina substrate (nominal pore size is 10 μm). This is due to the fact that the ceramic membrane layer is much thinner than the substrate (20 to 1500 μm), and the membrane has a porous and three-dimensional network structure.

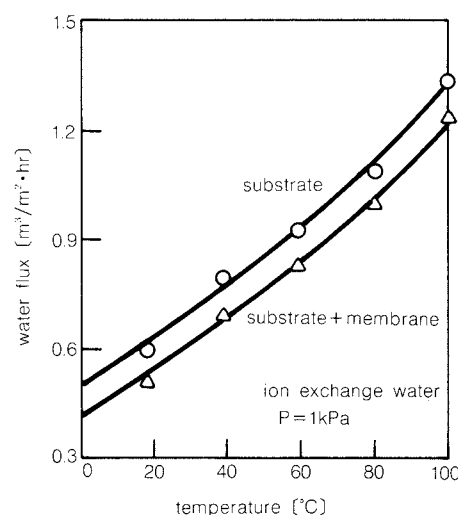


Fig. 11 Water flux of the ceramic membrane

Figure 11 shows similar experimental results in case of water flow at various temperatures. The decrease in the water flux caused by forming the membrane is about 10%, and its resistance may be seen to be very low. It is also noted that water flux increases with temperature, these membranes are suitable for treatment of water as well as for separation of organic solutions at high temperatures.

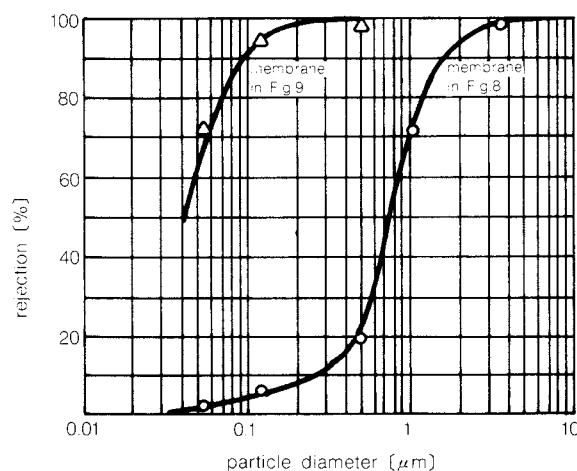


Fig. 12 Rejection of the ceramic membrane

Figure 12 shows the results of the separation tests of the membranes shown in Figs. 8 and 9 using the mono-dispersed polystyrene latex systems of various particle sizes (latex concentration is 100 ppm or less). The separation capacity corresponds to the pore size distribution of each membrane and agrees well with the results of observing by SEM photos. Both membranes have a sharp separation efficiency; in particular, the efficiency of the membrane shown in Fig. 9 is 0.04 μm at a 50% rejection, and this is high enough to be used for ultrafiltration (UF).

4. Conclusions

This paper has discussed the principle of the Electrostatic Formation of a Ceramic Membrane (EFCM), and the characteristics and basic properties of the ceramic membranes prepared by this method.

The membranes prepared by this newly developed process are characterized by a three-dimensional network structure and very high porosity; therefore, they allow various fluids to pass through them at a very low pressure drop. These characteristics are unique for these membranes.

The pore size of the membrane can be controlled to some extent by controlling the size of the ultra-fine particles used as the material of the membrane. One membrane prepared in this study has micropores of 0.04 μm on the

average.

The separation efficiency of the membrane (this corresponds to its micropore distribution) is fairly sharp, it is suitable for various applications including ultra-filtration (UF), and now other application areas are under studying. We are also investigating the effectiveness of the electrostatic formation of a ceramic membrane applying for ultra-fine particles of materials other than silicon nitride, such as titanium dioxide and alumina.

Acknowledgment

The authors wish to thank Japan Synthetic Rubber Co., Ltd. for proving the polystyrene latex particles for the mono-dispersal systems, and Mr. T. Iketani for his valuable suggestions on the measurement of the membrane separation efficiency.

References

- 1) Yamamoto, H., T. Nomura and K. Shindou: Preprints of 20th Autumn Meeting of Soc. of Chem. Engrs., Japan, p. 175, Himeji (1987).
- 2) Nomura, T., H. Yamamoto, K. Shindou and H. Ookubo: Preprints of 53rd Annual Meeting of Soc. of Chem. Engrs., Japan, p. 402, Sendai (1988).
- 3) Yamamoto, H. and T. Nomura: *SEISAN-KENKYU*, **40**, 407 (1988).
- 4) Yamamoto, H.: *J. Soc. of Powder Tech., Japan*, **26**, 163 (1989).

The Relationship between the Flocculation State of Particles and the Packing Structure on the Surface of Gypsum Mold[†]

Masafumi Arakawa, Hideki Kobayashi,
Kei-ichiro Hirado and Keikichi Inoue

Faculty of Engineering and Design,
Kyoto Institute of Technology*

Abstract

Generally a slip-casting process is closely related to the flocculation state of particles. The present investigation was undertaken in order to understand the relationship between the flocculation state of the particles and the packing structure on the surface of gypsum mold.

The flocculation state of particles in an Al_2O_3 -slurry was discussed on the basis of rheological and sedimentation behavior as a function of dispersant concentration. It was found that these properties could be classified into three modes.

On the slurries, the rate and pressure in the absorption of water, the increase in the packing layer thickness, and the porosity and permeability of the packing layer were measured in order to explain the packing structure on the surface of mold.

From these measurements, the relationship between the flocculation state of the particles and the packing structure could be modelled.

1. Introduction

Slip casting process is the method for obtaining a green body by pouring a slurry into a gypsum mold and making the water absorb into the mold. In this molding, the slurry should be sufficiently fluid to permit complicated shape to be formed and have a densely packed casting layer.

The present study investigated the flocculation state of particles in a slurry consisting of an sinterable alumina water system using the rheological properties and the sedimentation behaviors by adding dispersants. In addition, the casting mechanism of particles in the slurry was considered from the solvent absorbing rate of the gypsum mold, water absorbing pressures, the thicknesses of casting layer, the variation of the porosity and permeability of casting layers.

2. Experimental Methods

2. 1 Samples

* Goshokaido-cho, Matsugasaki, Sakyo-ku, Kyoto 606
TEL. 075-791-3211

[†] This report was originally printed in *J. Soc. Powder Technology, Japan*, **25**, 585-590 (1988) in Japanese, before being translated into English with the permission of the editorial committee of the Soc. Powder Technology, Japan.

The powder sample used in the experiment is sinterable low sodium alumina powder (density 3.93 g/cm^3 , mean particle size $0.4 \mu\text{m}$, specific surface area $5.5 \text{ m}^2/\text{g}$), the same as the sample used in the previous report¹⁾. An ammonium polycarbonate is used the dispersion agent. The slurry was prepared by the solution comprising 35g of ion-exchanged water to which the dispersant added, and by adding 100g of alumina.

2. 2 Experiments

2. 2. 1 Measurements of slurry characteristics

The apparent viscosity and flow curves of the prepared slurry were measured using a rotational viscometer.

ζ -potential was calculated from measured results using the microscopic electrophoresis method.

As the high concentrated slurry used in the experiment is required for a natural sedimentation for a long hour, here the changes in sedimentation volume in the field of the same centrifugal force ($1.19 \times 10^3 \text{ N}$) were measured by a centrifugal particle size distribution measuring method²⁾ using a balancing machine. Also, the sedimentation process in this apparatus is

able to continuously detect the movement of gravity in the slurry according to sedimentation. With the measurement of sedimentation volume at the time where the moving quantity of gravity becomes constant, this was defined as the sedimentation volume of flocculated particle layer.

2. 2. 2 Measurements of characteristics of gypsum mold

The measurement of the water absorbing pressure of gypsum is carried out in the equipment the same as that in the previous report¹⁾.

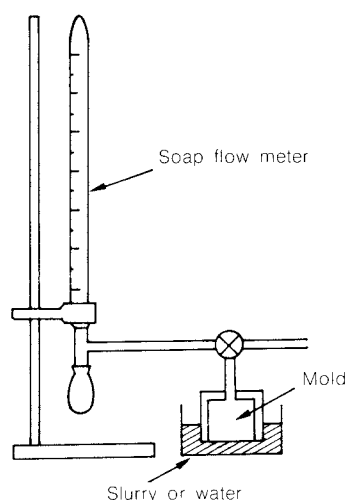


Fig. 1 Apparatus for measurement of water absorbing rate

The apparatus, shown in Fig. 1, is used for the measurement of the water absorbing rate of gypsum. With gypsum in the slurry dipping, the air volume pushed out from the mold by the absorbing water of gypsum is measured by a soap film flow meter. The absorbing rate was obtained from the water absorbing volume per unit time.

2. 2. 3 Measurements of characteristics of casting layers

The changes in the thickness of the casting layers were measured directly by a vernier caliper after dipping the gypsum mold into the slurry.

The measurement of porosity was carried out in following manner. With the gypsum mold having a cross-sectional area of $4.0 \times 10^{-3} \text{ m}^2$ dipped in slurries which have different conditions, and with the casting layers produced in them after a setting time for picking out, the

layers are measured instantaneously.

After they were dried, their weights were measured and their porosities were calculated from initial volumes and the density of alumina.

Next, the permeability of casting layers were measured using the device shown Fig. 1. Initially, with the gypsum mold sealed its side surface dipped in the slurry, the casting layer is produced by picking out the mold after a setting time. After that, this is dipped quickly into the water, the water volume permeating the casting layer was measured and the permeability was calculated from the result obtained.

Furthermore, a SEM observation was carried out on the drain sides of dried plastic solid obtained.

3. Experiment Results and Consideration

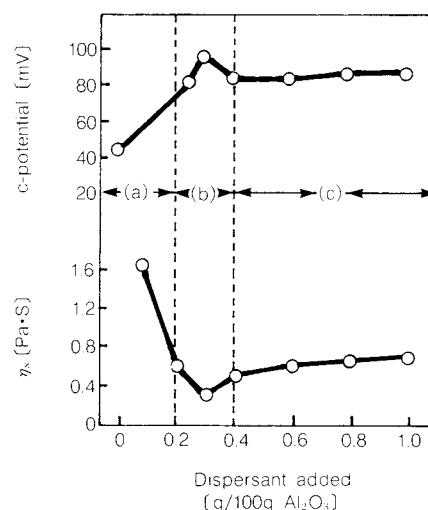


Fig. 2 Relation between apparent viscosity (η_s), ζ -potential and concentration of dispersant

Figure 2 shows the relationship between the added quantity of the dispersant, the viscosity of slurry and the ζ -potential. Here, the added quantity of dispersant is represented by added weight in g to 100g of alumina. The slurry can be divided roughly into three ranges from the figure. (a) is a system having a high viscosity, reducing its viscosity abruptly by adding a quantity of the dispersant, and its ζ -potential. (b) is considered that the resiliency between particles is the largest in three systems. ζ -potential is hardly changed in (c), though the viscosity increases with the added quantity of the dispersant. Three representative kinds of slurry were prepared with the added quantities of dispersant to alumina 100g; (a) 0.18g, (b) 0.30g

and (c) 100g. Hereafter, in the experiment, these are called as (a), (b) and (c).

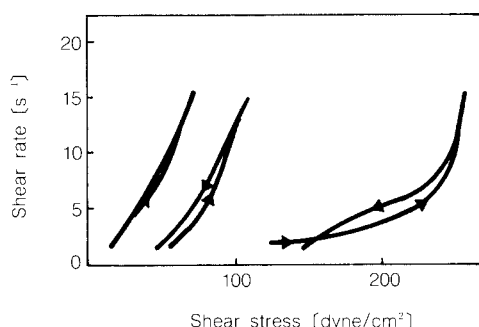


Fig. 3 Flow curves for sample slurries

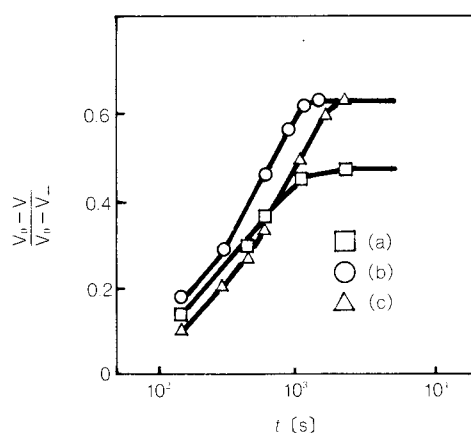


Fig. 4 Change of sedimentation volume as sedimentation time

Figure 3 shows the flow curves of three kinds of slurry, (a), (b) and (c). From Figs. 2 and 3, it is considered that slurry (b) has a behavior close to the Newtonian flow and its particles are well dispersed. In (a), it is presumed that there is an aggregate structure having a strong interparticle force, with a flow behavior for a strong agitation. Slurry (c) is considered to have a medium structure between them.

The same results are obtained from the sedimentation behavior in the centrifugal sedimentation method. Figure 4 shows the relationship between sedimentation times and the volume compressibility obtained from the detected moving quantity of gravity and actual sedimentation volumes. Here, the volume compressibility is defined as follows.

Assuming the packing of particles by the centrifugal force of concentrated slurry is the same as the compaction of the powder, the relationship between the aggregate state of the particles and the packing mechanism³⁾ is to

appear in the compressibility of particles added by the centrifugal force. Copper⁴⁾ considered that the compressive process of the powder consists of the packing of particle groups and the elimination of voids by deforming each particle, and be proposed Eq. (1).

$$\frac{V_0 - V}{V_0 - V_\infty} = \alpha_1 e^{k_1/F} + \alpha_2 e^{k_2/F} \quad (1)$$

V_0 and V are the apparent volume of the powder before compression and at pressure P respectively, and α_1 , α_2 , k_1 and k_2 are the constants obtained experimentally. V_∞ is the volume of the particles compacted and deformed to a solid having no void, that is, a specific volume of the material. Since the deformation of the particles is difficult to produce under general conditions of compaction of inorganic powder, here an apparent volume in the closest packing of the uniform sphere particle group (porosity = 0.26) was adopted.

In systems (b) and (c), the volume compressibility at the acceleration is approximately 60% of the closest packing for each, and is approximately 50% for system (a). With the same inclination of straight lines and different yield values in (b) and (c), it appears that the packing structures are similar, but the aggregate states are different in the two systems. It was considered that differences between system (a) and system (b), (c) are due to the aggregate structures.

As described above, to explain the relationship between rheological properties and sedimenting behaviors of the slurries, the yield values of each system are obtained from the flow curves in Fig. 3, and its values are converted to the aggregating force per one contact of particle is obtained with the assumption, wherein the diameter of alumina is a uniform globular particle of $0.4 \mu\text{m}$, dispersing uniformly on the surface of the rotor of the viscometer. From the values in Table 1, it can be assumed that system (a) has an apparent aggregating

Table 1 Flocculation state of particles in sample slurries

	Yield value [dyne/cm ²]	F_f [N]
(a)	230.6	5.71×10^{-13}
(b)	17.4	0.43×10^{-13}
(c)	58.3	1.45×10^{-13}

force 13 times than that of system (b), and system (c) has the apparent aggregating force three times that of system (b). Then, for example, assuming that there is hardly any difference in the motive force of each particle, it is considered that the differences between the apparent aggregating forces relate to the interacting strength forming an aggregating body in the slurries. Previous changing behaviors of volume compressibility are considered to be derived from both size of the aggregate and its structural strength.

3. 2 Casting mechanisms to gypsum mold

Generally, casting progress with the flow generated by absorbing a solvent into gypsum mold.

Also, it is known that the water absorption is affected by two factors; the wettability of the mold itself and the permeability of water to the just formed casting layer⁵⁾, and that from the previous report¹⁾ a factor relating to the permeability of casting layer is more dominant than a factor relating to the permeability of gypsum mold. Figure 5 shows, as shown in previous report¹⁾, the relationship between the reciprocals of the water absorbing rates measured in the three kinds of slurry and the square roots of time. The intercept shows the factor relating to the permeability of gypsum mold, and the inclination shows the factor relating to the permeability of casting layer. From Fig. 5, it is also clear that the permeability of casting

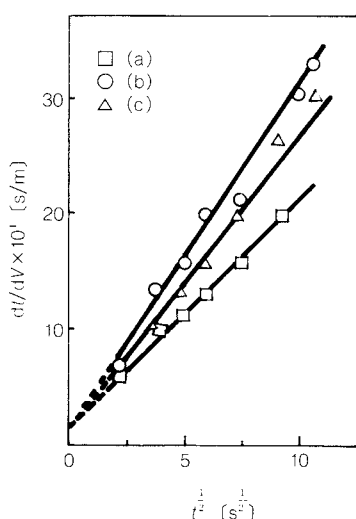


Fig. 5 Flow resistance of the casting layer/gypsum mold system as a function of the square root of the casting time

layer is more dominant than that of the gypsum mold. Furthermore, the magnitude of the permeability of the particle packing layers formed is ordered by its inclinations from large to small; (b), (c), (a). This order shows the density of the casting layers. The ratio between the square of the thickness of the casting layers and the casting time in the forming state of casting layer in a uniform packing structure is reported to be constant depending on time^{5,7)}; but, as shown in Fig. 6, in this experiment, the relationship was not always established and its linear relationship did not occur except for dispersoid (b). Namely, in systems

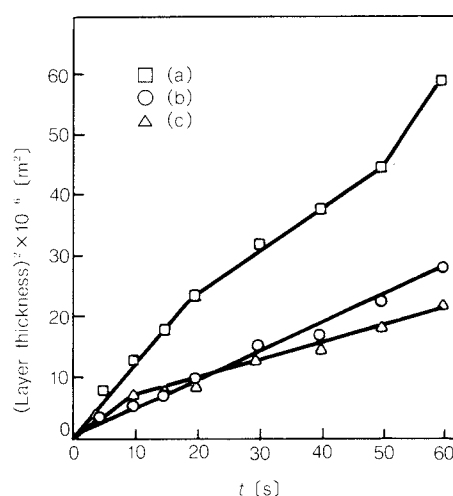


Fig. 6 Relation between the square of layer thickness and the casting time

(a) and (c), initially with a porous casting layer forming in the state of flocculating particles, the packing layer is more densely compacted disintegrating itself by the permeant pressure in

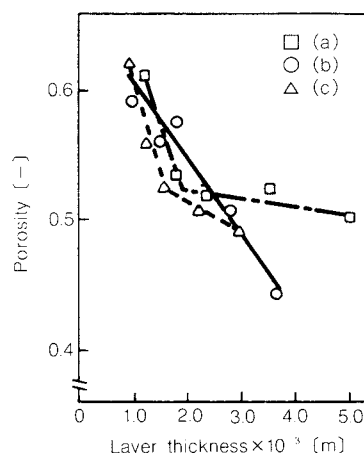


Fig. 7 Relation between the porosity of casting layer and the layer thickness

between the layers. It suggests that there is a periodical layer forming process repeating the porous layer formation of the flocculating particles due to the reduction in the permeating water quantity. In the mechanism, it is clearly recognized that the first disintegrating compaction has a decisive effect in Fig. 7, and the porosity of the casting layer becomes almost constant and its thickness is approximately 2 mm. Against this, in sample (b), the porosity decreases and its particle packing structure densifies with its thickness. In addition, in system (b) a type of periodicity is recognized; hence, it is presumed to be not a perfect dispersion, but a type of flocculation forming structure. However, the packing of particles was deemed to be a linearly and uniformly progressing change due to its small change.

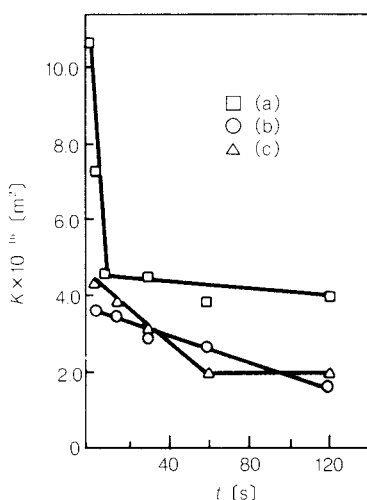


Fig. 8 Relation between the permeability (K) of casting layer and the casting time

Figure 8 shows the changes of permeability of the casting layers in the three systems^{7~9)}. In Fig. 8, the abscissa the casting time to the gypsum mold, and the ordinate is the values of permeability obtained from the D'arcy's equation¹⁰⁾ shown in Eq. (2).

$$\frac{dv}{dt} = \frac{K \Delta P}{\eta L} \quad (2)$$

dv/dt is the water absorbing rate per unit cross-sectional area, K the permeability of casting layers, L the thickness of casting layers, ΔP is water absorbing pressure and η is viscosity of water.

Since in the previous report¹⁾ the permeability of the gypsum mold is deemed to be sufficiently negligible in comparison with that of the casing layers, here the permeant pressure of casting layers was set to be equal for the water absorbing pressure of the gypsum mold. The water absorbing pressure obtained from the previous measurement was 0.046 MPa.

In Fig. 8, the permeability in system (a) drops drastically after casting until ca. 10 sec, but its change goes almost flat after that, and in system (c) its change becomes constant after ca. 60 sec. Against this, in system (b) the permeability of casting layer formed decreases almost at a constant rate. Like the above-described changes of porosity, it is presumed that in systems (a) and (c) the packing structure of particles in the casting layer is changed within the above-said time, and in system (b) the packing progresses at a constant state.

In observing plastic solids of the three sys-

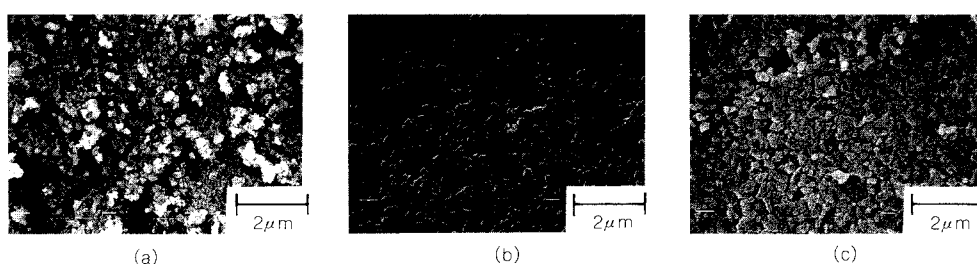


Fig. 9

tems using SEM, there are few differences for the drain sides of systems (b) and (c) as shown in Fig. 9, but system (a) has a rough structure and an uneven surface. It is considered that the flat and dense states in systems (b) and (c) were produced by the rearrangement of parti-

cles during the drying after draining. On the other hand, system (a) had a considerably strong aggregate state, because it had a rough state.

3. 3 Models of casting mechanisms

The aggregate structures of particles in the slurries as stated above and the casting mechanisms having changes in porosity and permeability of the formed casting layers are represented by models as shown in Fig. 10.

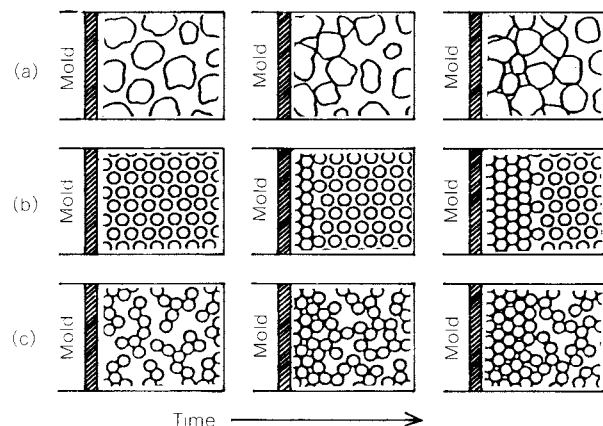


Fig. 10 Schematic diagram of casting process

In the slurry of system (a), with a large flocculated body making, at the beginning the casting progresses with the disintegration of the flocculated body by the water absorbing pressure. The disintegration stops in the flocculated body in a short time and after that the casting in an aggregate state begins. In system (b), with the porosity and permeability uniformly reducing, hence, with the assumption that the compression of casting layer and the packing of particles are progressing uniformly, the casting layer grows slowly with a totally dense structure. In system (c), beginning with a disintegrating structure of flocculated body progressing to casting like system (a), after that, the casting progresses with the aggregate body. The difference in the casting between system (a) and (c) was considered that it depends on the differences of aggregate size and its bending strength.

4. Conclusion

The aggregate state of slurry and its casting mechanism in the slip casting considered.

The characteristics of prepared slurries could be divided roughly into three systems by measuring ζ -potential, apparent viscosity, flow curves and centrifugal sedimentation, etc., that is;

- (a) a system wherein particles has a large size and comparatively strong aggregate

structure,

- (b) an uniformly dispersed system, and

- (c) a system forming a weak and network aggregate structure.

The casting mechanism of three kinds of slurries could be represented by the models as shown in Fig. 10 from the measuring results of casting thickness, permeability and porosity. In dispersoid slurry, with each particle sequentially going to casting, the formed layers become dense, and thereby, its growing speed slows down. On the contrary, the casting forming an aggregate structure in the slurry has a higher casting speed than that of dispersoid due to its casting with a large aggregate unit. With the casting comparatively close to gypsum mold disintegrating its aggregate body, after that, the casting progresses gradually in the aggregate state.

Nomenclature

K	: permeability of casting layer	[m ²]
P	: pressure	[Pa]
ΔP	: pressure drop of particle layer	[Pa]
k_1, k_2	: constants	[—]
V	: powder volume	[m ³]
V_0	: initial volume	[m ³]
V_∞	: volume of the most close packing	[m ³]
L	: layer thickness	[m]
α_1, α_2	: constants	[—]
η	: viscosity	[poise]

References

- 1) Arakawa, M. and H. Kobayashi: *J. Soc. Mat. Sci. Japan*, **36**, 1172 (1987).
- 2) Arakawa, M. and G. Shimomura: *J. Soc. Powder Technol., Japan*, **21**, 12 (1984).
- 3) Arakawa, M.: *J. Soc. Mat. Sci. Japan*, **34**, 1245 (1985).
- 4) Copper, A.R. and L.E. Eaton: *J. Am. Ceram. Soc.*, **45**, 97 (1962).
- 5) Leenaars, A.F.M. and A.J. Burggraaf: *J. Colloid and Interface Sci.*, **105**, 27 (1985).
- 6) Yogyokyokai: "Ceramic Processing", p. 158, Gihodo (1984).
- 7) Adcock, D.S. and I.C. McDowall: *J. Am. Ceram. Soc.*, **40**, 355 (1957).
- 8) Li Jiutu and B. Rand: *Brit. Ceram. Trans. J.*, **83**, 186 (1984).
- 9) Tiller, F.M. and Chun-Der Tsai: *J. Am. Ceram. Soc.*, **69**, 882 (1986).
- 10) Shirato, M.: "Shinpan Roka no Mekanizumu", p. 89, Tanin Syokan (1978).

Wear of Media during Ultra-fine Grinding[†]

Kazuo Suzuki, Yoshitaka Kuwahara
and Toshio Ishizuka

Government Industrial Research Institute, Nagoya
Agency of Industrial Science and Technology, M.I.T.I.*

Abstract

Contamination during fine grinding is an important problem for a raw powder of newly developed materials. Wear behaviors of grinding media, which were made of steel, alumina and zirconia, were examined during fine grinding using a vibration ball mill. Ball wear was nearly proportional to a specific surface area of ground products. It was supposed that the wear in wet grinding is more than in dry grinding, because wet grinding is more effective for fine grinding. Wear was effected by the materials of the grinding media. Ball wear, which was made of zirconia, was the least of three kinds of balls, that were used. Linear wear was not as much as ball wear.

Introduction

Powder is rarely a final product, but is handled, much more frequently, as an intermediate product, as is the case with starting material for the newly developed materials. It is increasingly required that powders be finer as the starting material for the new materials, and its particle and surface characteristics, chemical composition, crystalline phase have been attracting more attention. Grinding is a common procedure to reduce particle size in the production of preparation of powders, which are increasingly required to be finer.

In grinding operation, a physical and mechanical energy supplies to the powder. It decreases the particle size and, at the same time, produces new surface. However, it wears down the grinding media because of the frequently applied contact force. The grinding procedure is invariably accompanied by this type of problem and causes the powder to be contaminated with fine solids from the grinding components. The extent of contamination tends to increase as the size of the grinding particle decreases.

This problem is more pronounced in the fine grinding operation.

It is accepted that the wear mechanisms fall into four general categories¹⁾; (1) adhesive, (2) abrasion, (3) corrosive wear and (4) surface fatigue. Each mechanism rarely appears by itself but in combination with the others. Furthermore, the extent of the actual wear varies greatly and depends on many factors, such as the atmosphere and operating conditions to which it is exposed.

Abrasive is one type of powder. Abrasion is distinguished from wear, but these may be regarded as the same phenomenon in that an abrasive causes volume reduction (or dimensional change) in materials it contacts. An abrasive consists of hard particles of which efficiently grind something or remove foreign matter therefrom. Extensive wear may result if the ground particles are harder than the grinding medium.

Wear caused by ball milling was extensively studied in 1940's, from the respective of controlling operations²⁾. As a result, the mechanisms of the ball wear are considered to fall into the three general categories³⁾: The first and the second are based on the concepts that wear rate is proportional to the ball surface area (d^2) and the ball mass (d^3), respectively, and the third is intermediate between the two, assuming that the wear rate is proportional to d^n ($2 < n < 3$), where d stands for the ball diame-

* 1-1 Hirate-cho, Kita-ku, Nagoya 462 Japan
TEL. 052-911-2111

† This report was originally printed in *J. Soc. Powder Technology, Japan*, 26, 411-416 (1989) in Japanese, before being translated into English with the permission of the editorial committee of the Soc. Powder Technology, Japan.

ter. These studies were carried out with steel balls and mainly directed at controlling the grinding speed to understand the relationships between ball size reduction and the ball make-up methods. The wear phenomena results were analyzed in which abrasive wear played a predominant role yet contamination of the powder was not discussed.

This study investigated the wear of media both for dry and wet grinding using a vibration ball mill, with emphasis on powder contamination. Silica sand served as the sample powder and three different materials were used for the grinding medium.

2. Experimental Procedure and Sample

The grinding apparatus used in this study was a high-vibration, high amplitude mill (nano-VMILL with two containers, Chuo Kakoki Co., Ltd.), whose amplitude (total amplitude) (from 4 to 19 mm and whose frequency varied up to 3400 c.p.m. by an inverter. In this study, the amplitude and frequency were set up at 10 mm and 1200 c.p.m., respectively, and its vibration strength was 8.06 relative to the acceleration of gravity. The grinding media (balls) were of HD alumina (3, 5 and 10 mm in diameter, Nippon Kagaku Togyo Co., Ltd.), YTZ zirconia (3, 5 and 10 mm in diameter, Tosoh Co., Ltd. – Nippon Kagaku Togyo Co., Ltd.), and carbon steel (3 mm (1/8") and 5 mm (3/16") in diame-

ter, Tsubakimoto Seiki Co., Ltd.). The charged quantity of each grinding medium was set up at $J = 0.7$. Two types of mill containers were used; one was lined with HD alumina (Nippon Kagaku Togyo Co., Ltd.) for the ceramic balls, and the other was of steel for the steel balls. These were 170 mm ϕ \times 200 mm (4.5 ℓ) and 200 mm ϕ \times 195.6 mm (6.1 ℓ), respectively, in size.

The sample powder was of silica sand (SiO_2 : 99.85%, #200, Kyoritsu Yougyo Genryo Co., Ltd.), ground by both the dry and wet processes, the latter was performed in the presence of water. The charged quantity of the sample powder was set at $U = 1.14$. For the wet grinding, the concentration and charged quantity of slurry were set at 40 wt% and 114%, respectively. These conditions are summarized in Table 1.

The grinding time was as much as 100 hours for wet grinding and 50 hours for dry grinding. A small quantity was sampled at given time intervals, to monitor the wear rate and specific surface area changing with time. The same quantity of water was made up in wet grinding.

The wear rate was followed in two ways; chemical analysis of sampled powder and weight loss of the grinding balls. The ball was weighted before and after the test; it was thoroughly washed with pure water to recover the ground product and dried before being measured after the test. The chemical analysis

Table 1 Experimental conditions

Mill container	Ball	Powder	
		Dry grinding	Wet grinding
Alumina lining pot Internal volume : 4.5 ℓ	Alumina or zirconia (3, 5, 10 mm) Weight of ball : 6.20 kg (Alumina) : 10.50 kg (Zirconia) ($J = 0.70$)	Weight of powder : 1.70 kg ($U = 1.14$)	Weight of powder : 0.75 kg Weight of water : 1.12 kg Concent. of slurry: : 40 wt% ($U = 1.14$ in slurry)
Steel pot Internal volume : 6.1 ℓ	Steel (3, 5 mm) Weight of ball : 19.70 kg ($J = 0.70$)	Weight of powder : 2.30 kg ($U = 1.14$)	Weight of powder : 1.00 kg Weight of water : 1.50 kg Concent. of slurry : 40 wt % ($U = 1.14$ in slurry)

was performed by means of an ICP luminescence analyzer (ICPA-100S, Nippon Jarrell Ash Co., Ltd.), with Al as the trace element for the alumina balls, Zr for the zirconia balls (Al was used simultaneously for the liner), and Fe for the steel balls. Figure 1 shows sample preparation procedure for ICP analysis. The analytical conditions were: ICP output: 1.4 kW, carrier gas rate: 0.52 l/min, plasma gas rate: 14 l/min, auxiliary gas rate: 0.52 l/min, measurement wavelength: AlI 396.15 nm for the alumina balls. AlI 394.40 nm for alumina liner, FeII 238.20 nm and ZrII 348.82 nm.

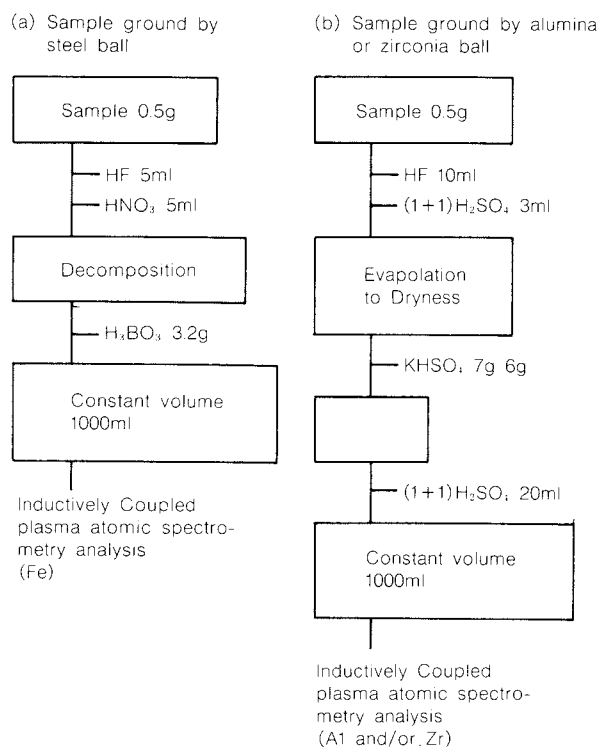


Fig. 1 Analytical procedures of Fe, Al and Zr in ground SiO_2 powder

The specific surface area was determined by the N_2 gas absorption type BET methods (Carlo Elba, Sorptomatic 1800).

3. Results and Discussions

Figure 2 shows the parity plot, where the wear debris fraction in SiO_2 powder determined by the chemical analysis is plotted against that determined by the weight balance of the ball on a log-log graph. The solid line represents the 1:1 relationship between them. It is only natural that the values for the zirconia ball case are the same, because only the ZrO_2

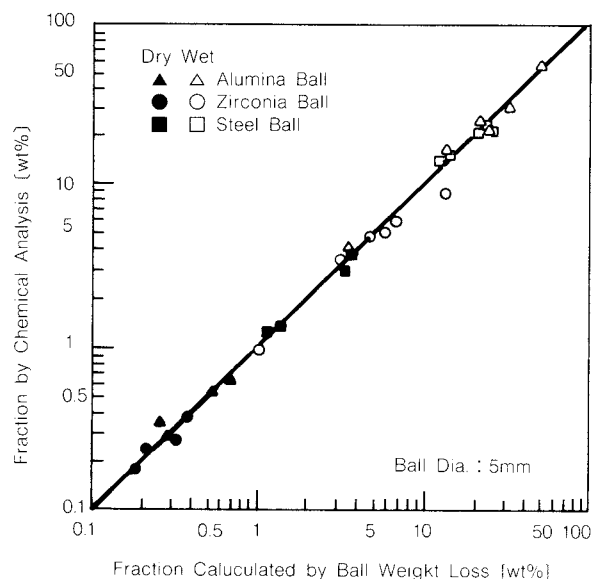


Fig. 2 Comparison of measured wear debris fraction in SiO_2 powder between two methods

concentration resulting from the balls was chemically analyzed (concentration of alumina as the wall material was analyzed separately). For the steel and alumina ball case, however, the chemically analyzed value should be higher, with respect to the wear debris from the walls. Nevertheless, they coincided well with each other, suggesting that the quantities of debris from the walls were very small and, at the same time, the chemical analysis results were reliable.

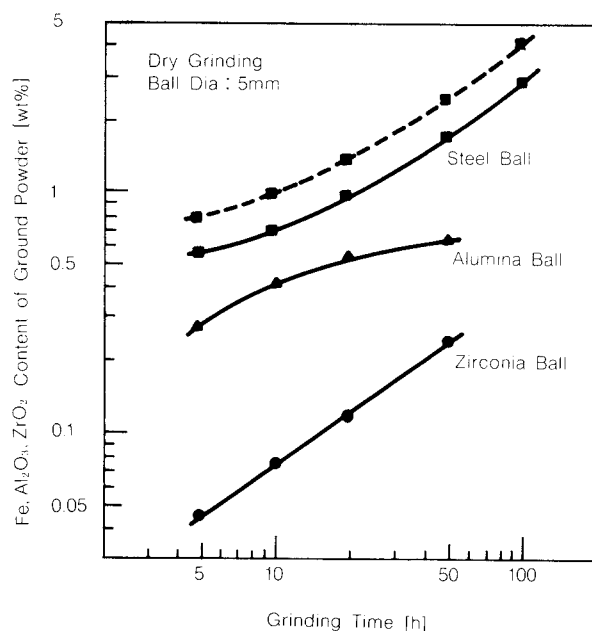


Fig. 3 Ball wear behaviors under dry grinding

Figure 3 shows Fe, Al₂O₃ and ZrO₂ concentrations in the ground powder over time for the dry grinding case. The broken line presents the Fe₂O₃ concentration in the powder ground by the steel balls. It serves as a comparison for the later presented wet grinding results, which discuss Fe₂O₃ concentration. The wear of the balls, is presented by Fe quantity, which, however, is in all likelihood oxidized into Fe₂O₃ when present in the ground powder. Of the 5 mm-diameter balls tested, the steel ball produced the largest quantity of the wear debris, followed by the alumina and then the zirconia ball. Wear is often associated with relative hardness of the materials involved. In general, hardness of steel, alumina and zirconia are Hv 400, 2000 and 1300, respectively, while that of silica sand is Hv 800. Thus, steel satisfies the condition that causes abrasive wear by the ground silica sand powder. It was observed, however, that the wear debris quantity was not proportional to the grinding time, meaning that the wear, even if abrasive wear predominated, was affected by ground powder characteristics (extent of size reduction during the process), in addition to the ball size (surface area or mass), and that the wear could not be explained by abrasive wear alone, because the vibration ball mill used in this study used impact force as grinding mechanism. The relationship between

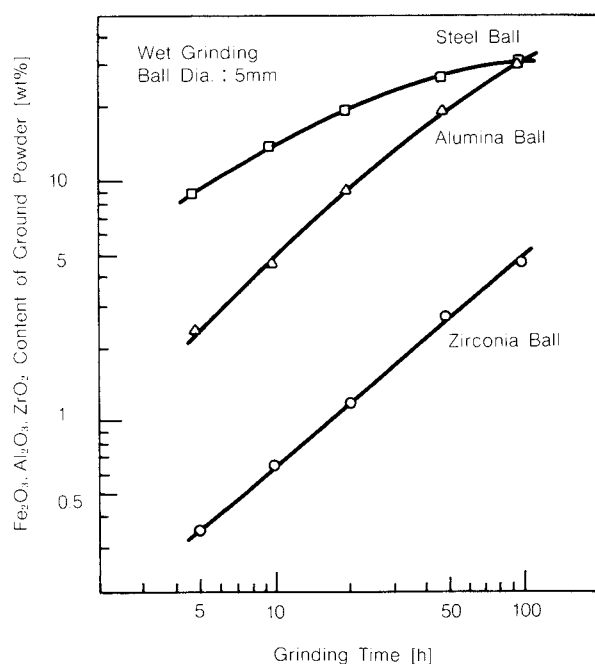


Fig. 4 Ball wear behaviors under wet grinding

wear rate and hardness was reversed for the results with the alumina and zirconia balls.

Figure 4 presents the wet grinding results, where the balls had the same diameter as those used for the dry grinding and where the debris from the steel balls was represented by iron oxide (Fe₂O₃), estimated from the elementary Fe concentration in the powder, because Fe was considered to be oxidized. As for the wet grinding, the zirconia balls demonstrated the smallest wear rate. Comparing the results shown in Fig. 4 with those in Fig. 3 revealed that the debris produced by the wet grinding was approximately one order of magnitude greater than that by the dry grinding.

As described earlier, grinding with the zirconia balls was performed in the alumina lined container. Analysis of Zr and Al concentrations in the ground powder, therefore, gave the

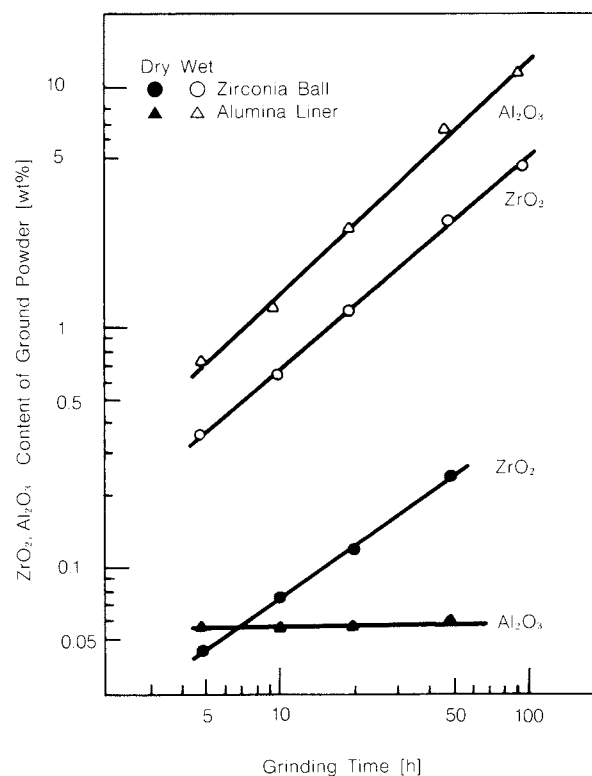


Fig. 5 Wear behaviors of alumina vessel and zirconia ball

quantities of the balls and the lining worn during the grinding process. Figure 5 shows the analytical results, indicating that the lining was worn quite differently during the dry and wet grinding process. During wet grinding impact of the balls were directly applied continuously to

the alumina walls, because the powder was dispersed in the grinding fluids, with the result that quantity of worn alumina increased with grinding time. During dry grinding, on the other hand, the extent of wear of the alumina walls was limited, except during the first grinding stage before the walls were coated with a layer of ground powder. An increase in the worn quantity with time was not observed. It is possible that the ground powder coating the walls greatly absorbed the impact of the balls and protected the walls. The balls were also coated with the powder, but the layer was probably thin as it repeatedly exfoliated from, and reattached to, the balls were continuously worn, though their wear rate was approximately one order of magnitude lower than that observed during wet grinding.

The wear of alumina and zirconia balls and the alumina walls during wet grinding was further investigated by the other test. It was conducted for 50 hours under almost the same conditions, except that no powder was used. The same diameter (5 mm) balls, in 1.5 l of water were used to measure the wear of balls. During the test, the slurry samples containing the worn powder were collected after 5 and 20 hours. The quantity of worn balls during 50 hours was measured by balance. The quantity of liner worn during the 50 hours grinding was estimated from the measured slurry density and the quantity of worn balls. The quantities of the balls and liner worn by 5 and 20 hours were also estimated.

Table 2 Results of wear test without powder in water

Materials	Ball wear	Liner wear	Total wear
Alumina			
5h	36.8 (48.5)	16.9 (5.0)	53.7 (53.5)
20h	147.0 (155.5)	24.6 (16.0)	171.6 (171.5)
50h	367.5	37.8	404.3
Zirconia			
5h	2.4 (2.7)	8.5 (8.2)	10.9 (10.9)
20h	9.6 (9.6)	29.5 (29.6)	39.1 (39.2)
50h	24.1	74.1	98.2

(g)

The results are shown in Table 2, where the slurry concentrations estimates are based on the assumption that the balls were worn at a constant rate. The estimated results in paren-

theses are based on the assumption that the ratio of wear quantity between balls and liner was constant. Densities of the alumina ball and liner are described later. The specific surface areas measured 26.1 (5 hours) to 45.1 (50 hours) m^2/g with the powder from the worn alumina balls, and 12.9 (5 hours) to 34.0 (50 hours) m^2/g with the worn zirconia balls (including the worn alumina powder from the liner). This indicates that they were fairly fine. It was therefore considered that all closed pores in the sintered body surfaced in the worn powders and that their densities were slightly higher than those provided by manufacturer (alumina: 3.60, zirconia: 6.00). The manufacturer's values were used in the calculation however.

As shown in Table 2, the wear rate of the liner was fairly low, approximately 10% the anticipated results as shown in Fig. 2. This and the results shown in Fig. 2 (except for the zirconia ball results), showed that the liner was less worn than the ball, when similar materials were used as the grinding media. When the balls of dissimilar materials (zirconia balls and alumina liner in this case) were used, on the other hand, the alumina liner was worn significantly more, and great care must be taken in such case. It should be noted, however, that the wear rate in the presence of ground powder (Alumina: 193.4 g, Zirconia: 21.6 g (Alumina: 56.6 g)) was lower in each case, as revealed by the 50 hours grinding tests. It is possible that the ground powder dampened the balls' impact on the liner walls, even during the wet grinding.

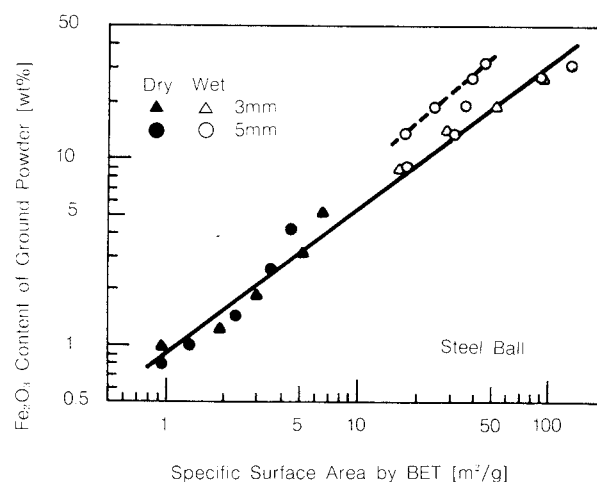


Fig. 6 Relation between specific surface area and contamination of powder ground by steel ball

The densities of the alumina ball and liner, provided by manufacturer were 3.60 and 3.50, respectively, which are considerably lower than well-densified alumina at 3.98. The alumina ball consisted of sintered Al_2O_3 (91%), SiO_2 (7%) and unknowns (2%), and may have contained 10% or more of glassy and spinel phases in the grain boundaries and a number of pores. Both the glassy and spinel phases were low in hardness and strength, and the presence of large quantities of the grain boundaries diminished the inherent characteristics of alumina therefore aggravating the wear of the alumina products. The zirconia ball had a density of 6.00, which was very close to the theoretical density of 6.05. Zirconia, though not very strong, its toughness helps reduce its wear.

Figure 6 through 8 show the relationships between the specific surface area of ground powder and contents of Fe_2O_3 , Al_2O_3 and ZrO_2 , respectively, where the specific surface area is the value of the ground powder containing the wear debris. Figure 6 shows the steel ball results. The broken line represents the wet grinding results (marked with o's) with the 5 mm-diameter balls, where the samples were treated with an acid to remove the Fe_2O_3 wear debris. The relationship with the wear debris-containing powder is represented by a straight line on a log-log plot, indicating that the wear debris content was closely related to the specific surface of the ground powder and that the

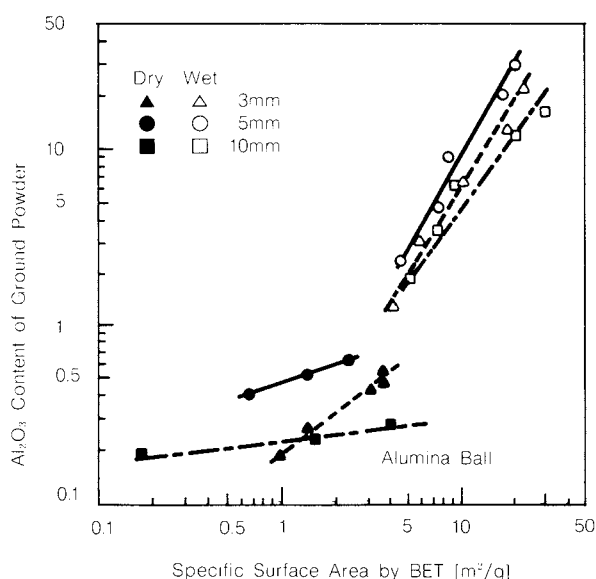


Fig. 7 Relation between specific surface area and contamination of powder ground by alumina ball

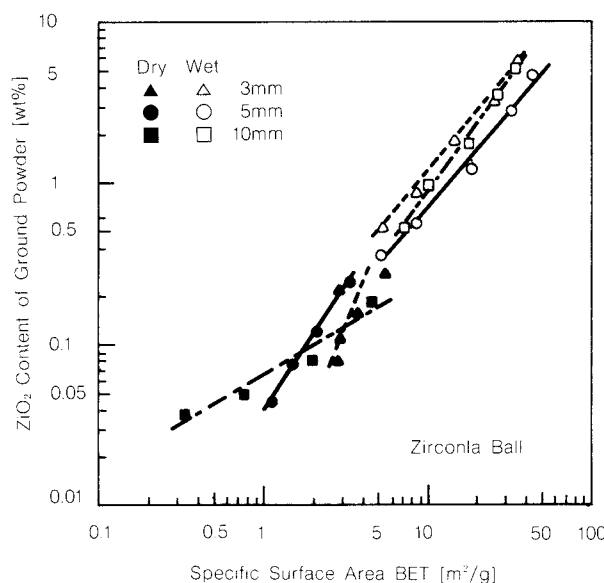


Fig. 8 Relation between specific surface area and contamination of powder ground by zirconia ball

grinding methods whether dry or wet had no effect on the relationship, though they produced very different amounts of wear debris.

The acid-treated powder had a significantly reduced specific surface area, which means that the wear debris of steel was somewhat finer. Figure 7 and 8 present the results with the alumina and zirconia balls, respectively. Unlike the case with the steel balls, the dry grinding produced smaller quantities of wear debris, and caused the content to be less sensitive to the specific surface of the powder than the wet grinding. In any case, no significant increase in specific surface area is expected from dry grinding.

The effects of the ball size were hidden by the effects of the mechanical properties of the different materials. During wet grinding, the wear debris quantity tended to increase as specific surface area of ground powder increased. It is therefore believed that the ground powder is somewhat contaminated with the wear debris when making a very fine powder.

4. Conclusions

Three types of grinding media were used both for dry and wet grinding in a vibration ball mill, to investigate extent of wear debris contamination in the ground powder.

- (1) The extent of contamination was essentially proportional to the specific surface area

of the ground powder in any case of what grinding medium material was used. Wet grinding, which grinds powder at a higher rate than dry grinding, will cause the ground powder more contamination.

- (2) Of the ball types used in the tests, the zirconia ball produced the least amount of debris, followed by the alumina ball and then the steel ball.
- (3) The liner was generally less worn than the balls. However, care must be taken if the liner and the ball are of dissimilar materials.
- (4) Wear of the grinding medium in the impact mechanism seems to be more affected by the materials' strength than the ball size (mass or surface area).

Acknowledgements

The authors thank Mr. Fumisaku Maruyama, president of Chuo Kakoki Co., Ltd., for his support in this study, and Messrs. Kazumitsu Murakami and Tatsuyoshi Ito for their co-operation.

Nomenclature

J : ball filling of mill (ratio of volume of balls plus space between balls to volume of mill) [—]

U : powder fraction (ratio of volume of powder particles plus space between particles to volume of space between balls) [—]

References

- 1) Hashimoto K.: "Funtaimamou no Taisaku", p.2, Nikkan Kougyou Shinbunsha (1981).
- 2) Prentice T.K.: *J. Chem. Met. Min. Soc., South Africa*, Jan. 99 (1943), White H. A.: *Trans. AIME*, **153**, 116 (1943), Garms W. I. and J. L. Stevener: *Trans. AIME*, **169**, 133 (1943), Norman T. E. and C. M. Leob: *Mining Tech.*, AIME Tech. Pub. No. 2319, 1 (1948), Norman T. E. and C. M. Leob: *Trans. AIME*, **183**, 330 (1943), Norquist D. E. and J. E. Moeller: *Trans. AIME*, **187**, 721 (1950), Rose H. E. and R. M. E. Sullivan, "A Treatise on the Internal Mechanics of Ball, Tube and Rod Mills", Constable London, 1957, Lorenzetti J. J.: Proc. 3rd Symp. on Grinding, Armco Chile, S.A.M.I. Vina del Mar 284 (1980), Davis E. W. *Trans. AIME*, **61**, 250 (1919), Longmore E. L.: *Trans. Inst. Min. Met.*, **46**, 569 (1937), Crocker B. S.: *J. Chem. Met. Min. Soc. South Africa*, Feb. 133 (1944), Bond F. C.: *Trans. AIME*, **153**, 373 (1943), Bond F. C.: *J. Chem. Met. Min. Soc. South Africa*, Jan. 131 (1944), Vermeulen L. A. and D. D. Howat: *Mintek Report*, **M201**, 1 (1985).
- 3) Menacho J. and F. Concha: *Powder Tech.*, **47**, 87 (1986).

The Release of Enzymes and Proteins from Baker's Yeast Disrupted by a Agitator Bead Mill[†]

Kanji Matsumoto and Haruhiko Ohya

*Dept. of Material Science and Chemical Engineering,
Faculty of Engineering
Yokohama National University**

Sadam Ito

*Mitsubishi Heavy Industries Co., Ltd.***

Makio Naito

*R & D Center, Hosokawa Micron Corp.****

Abstract

Baker's yeast suspended in pure water was disintegrated by the agitator bead mill using glass beads having a diameter of 0.5 to 2.0 mm. ADH (alcohol dehydrogenase) was released faster than protein and G-6-PDH (glucose-6-phosphate dehydrogenase), and a concept of the selective release of enzyme was defined. The final weight of the protein released and the activities of enzymes, the release rate constant for protein and ADH, and the release selectivity between the protein and ADH were dependent on the bead size, the weight of beads and the agitation speed. The optimum condition for release existed for each operation parameter. The electrical conductivity of the yeast slurry had good correlation with the amount of G-6-PDH and protein released. This result indicated that the degree of release for these substances could be estimated from the measurement of electric conductivity.

1. Introduction

The release of intracellular materials (such as enzymes) after cells have been disrupted or crushed is an important downstream process that can be effected either chemically or mechanically^{1,2)}. Mass production schemes frequently depend on the available mechanical facilities, such as high-pressure homogenizers³⁾ and bead mills⁴⁾, the characteristics of which have been previously compared^{3,4)}.

The high-speed agitator bead mill, which is widely used to disrupt bacteria, quickly disintegrates cells into fine pieces. Disintegrating cells into fine pieces is a good method for releasing a sufficient quantity of intracellular materials. At the same time, however, disintegration

tends to cause various problems in post-treatment processes, such as the separation of solids from liquids in the disrupted bacteria materials⁷⁾, which increases the amount of impurities present.

Overtreating is therefore unnecessary to destroy cytoplasm if the target materials can be sufficiently released by a milder disintegration process that selectively disrupts cell walls. For materials that cannot be sufficiently released unless the cells are thoroughly disrupted, their subsequent separation and purification may be performed more efficiently in a two-stage process. First the cells are mildly disrupted to destroy cell walls selectively, and second, the cells are disrupted thoroughly after releasing and removing the separable materials produced in the first stage.

Intracellular materials such as enzymes and proteins can be selectively released depending on the morphologies and locations of the target materials. The similar concept of chemically disrupting the cells is called "biochemical cell refining" by Asenjo⁸⁾. For mechanical disruption, the possibility of selectively releasing

* 156, Tokiwadai, Hodogaya-ku, Yokohama 240
TEL. 045 (335) 1451

** 1-1-1, Wadasaki-cho, Hyogo-ku, Kobe 652
TEL. 078 (672) 3111

*** No. 9, Shoudai Tajika 1-chome, Hirakata, Osaka 573
TEL. 0720 (55) 2220

† This report was originally printed in *J. Soc. Powder Technology, Japan*, 26, 424-429 (1989) in Japanese, before being translated into English with the permission of the editorial committee of the Soc. Powder Technology, Japan.

yeast enzymes has been demonstrated using a high-speed agitator bead mill^{9,10}.

A low-speed bead mill, which disrupts cells at a lower rate than a high-speed bead mill, has the following advantages: continuous cell disruption with a separation of released materials, a lower rate of temperature increase, controlled deactivation of the released enzymes caused by a high shear rate¹¹, and low levels of contamination and impurities caused by wear.

In this study, the authors have investigated the release characteristics (i.e., release quantity, release rate and selectivity) of enzymes and proteins that are separated in batches from baker's yeast by a low-speed agitator bead mill, and the effects of the operating parameters (i.e., bead size, bead quantity, and agitation rate) on these characteristics.

2. Experimental Apparatus and Procedure

2. 1 Bead mill and beads

The bead mill used in this study was crusher (Aquamizer AQ 5), equipped with a rotor and six agitation rods (15 mm in diameter) vertically arranged on the same periphery. Each agitation rod was 0.06 m away from the mill center. The agitation tank was 0.20 m in diameter and 0.25 m high. Both the agitation rods and the tank were made of stainless steel (SUS 304).

Three types of beads (glass spheres with a density of $2.48 \times 10^3 \text{ kg/cm}^3$, Union Co., Ltd.) were used with average diameters of 0.5, 1.0 and 2.0 mm, respectively.

2. 2 Experimental procedure

Ionized water was added to 0.5 kg of wet baker's yeast (*S. cerevisiae*, Oriental Yeast Co., Ltd.) to $2 \times 10^{-3} \text{ cm}^3$, and the mixture was charged into the agitation tank. As pretreatment, it was agitated at 100 rpm, and then agitated at a given speed after a given quantity of the glass beads was added to the tank. A small quantity of a silicon-base defoaming agent was used when the agitation was accompanied by an excessive amount of foaming. The defoaming agent produced no adverse effects on the released yeast. The yeast slurry was kept at approximately 297 K by circulating cooling water through the jacket surrounding the agitation tank.

The bead mill was stopped periodically to

collect the samples (approximately 10^{-5} m^3 each). Each sample was then separated centrifugally (operating conditions: 15,000 rpm, 30 min) immediately after it was collected, and the supernatant liquid was removed and analyzed for enzyme activity, water-soluble protein content, pH level, and electric conductivity. The enzymes analyzed for activity were ADH (alcohol dehydrogenase) and G-6-PDH (glucose-6-phosphate dehydrogenase), which were analyzed in accordance with the methods described in the Oriental Yeast Co., Ltd.'s biochemicals catalog (p. 9 and p. 45). The water-soluble proteins were measured according to the Lowry method, with bovine serum albumin as the standard¹². The particle size distribution of the disrupted yeast was determined by a Coulter counter (aperture diameter: 30 μm).

3. Results and Discussion

3. 1 Rate of release of ADH, G-6-PDH and protein

Figure 1 shows the effects of agitation time on the quantity of released ADH, G-6-PDH and proteins. Most ADH was released during the

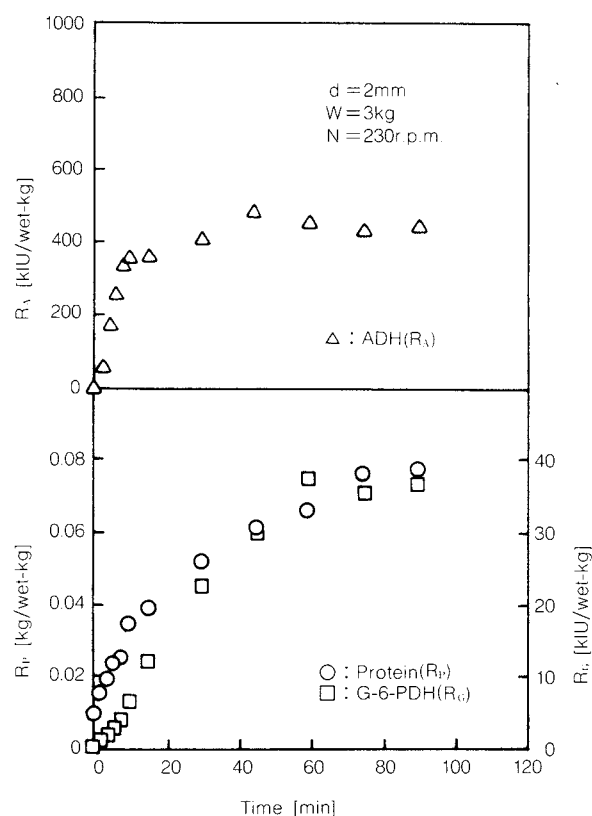


Fig. 1 Rate of release of ADH, G-6-PDH and protein

initial stage of agitation, as it is located close to the cell walls¹³. The quantity of released G-6-PDH and proteins, mainly present in cytoplasm, increased with time. The release curves for G-6-PDH and proteins are quite similar, and the selectivity characteristics are discussed mainly with respect to ADH and proteins.

The results shown in Fig. 1 were replotted in Fig. 2 to show the relationship between $R_m / (R_m - R)$ and time. As shown, the released quantity of both ADH and proteins correlates fairly well with agitation time according to the equation:¹⁴⁾

$$\ln [R_{mi} / (R_{mi} - R_i)] = K_i t \quad (1)$$

$i = A$ (for ADH) or P (for proteins)

where, R_m is the maximum released quantity, K is a constant given by the inclination of the curve shown in Fig. 2, and t is the agitation time.

3. 2 Selectivity of enzyme release

As illustrated schematically in Fig. 3, R_A reaches a constant level in a shorter time than R_P . The time at which the sharp increase in R_A stops is defined as T_C , which corresponds to the release rate of ADH. Figure 4 shows the relationship between K_A and T_C under various

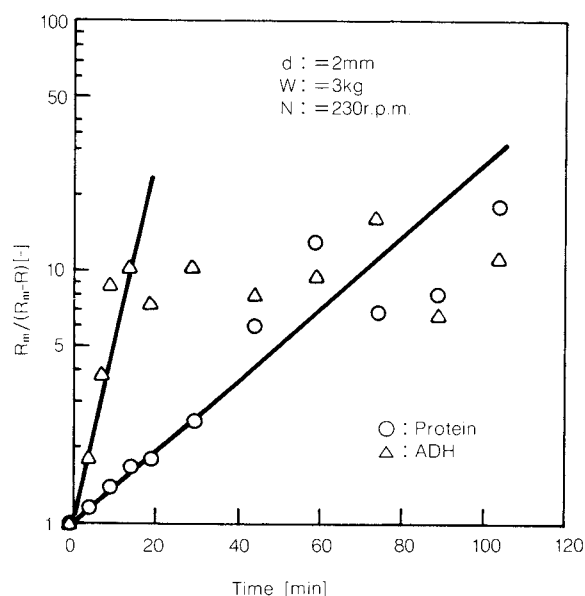


Fig. 2 Plot of $\ln [R_m / (R_m - R)]$ against t

conditions and indicates that K_A is almost inversely proportional to T_C .

Next, the ratios K_A / K_P and X_A / X_P ($X_i = R_i$

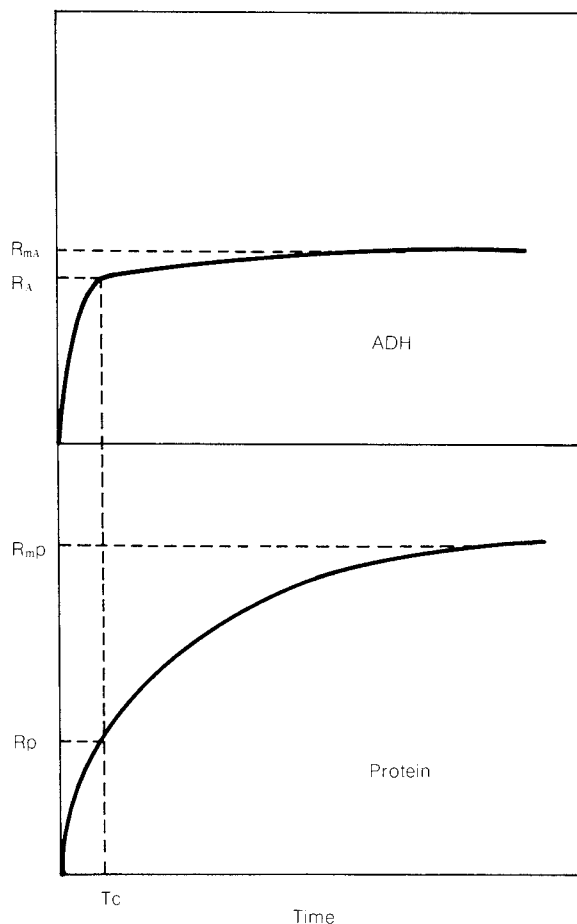


Fig. 3 Definition of a release selectivity between ADH and protein

at $t = T_C / R_{mi}$) were introduced as criteria to assess the effects of each operating parameter on the selectivity of enzyme release. K_A / K_P and X_A / X_P represent the ratio of the release rate constant and the ADH release rate at $t = T_C$ to those of proteins during the initial stage of agitation. A higher ratio indicates a higher selectivity of release.

The effects of each parameter on these selectivity criteria are discussed below. It should be noted, however, that the data was scattered fairly widely, probably as a results of uneven yeast production conditions, experimental conditions, and the conditions under which the yeast was preserved. The results reported herein are the average values for 2 to 4 data items obtained under the same conditions.

3. 3 Bead size

Table 1 (A) summarizes the effects of bead size (diameter) on the release characteristics of materials separated from yeast when using 3 kg

Table 1 Characteristics of substances released from disrupted baker's yeast

			R_{mA} ($\frac{KIU}{wet\text{-}kg}$)	R_{mP} ($\frac{kg}{wet\text{-}kg}$)	K_A (min^{-1})	K_P (min^{-1})	K_A/K_P (—)	X_A/X_P (—)
A	$d[mm]$	0.5	460	0.10	5.0	1.4	3.6	2.6
	$W=3\text{ kg}$	1.0	660	0.12	18.3	3.3	5.5	2.6
	$N=230\text{ rpm}$	2.0	480	0.08	17.0	3.5	4.9	2.0
B	$W[kg]$	2.5	470	0.08	14.0	2.8	5.0	1.8
	$d=2\text{ mm}$	3.0	480	0.08	17.0	3.5	4.9	2.0
	$N=230\text{ rpm}$	4.5	530	0.09	21.3	4.6	4.7	1.9
		6.0	740	0.08	30.8	9.5	3.2	1.9
C	$N[rpm]$	120	600	0.08	7.6	2.0	3.8	1.9
	$d=2\text{ mm}$	230	480	0.08	17.0	3.5	4.9	2.0
	$W=3\text{ kg}$	320	600	0.08	23.2	4.3	5.4	2.4
		460	370	0.08	13.0	5.4	2.4	1.1

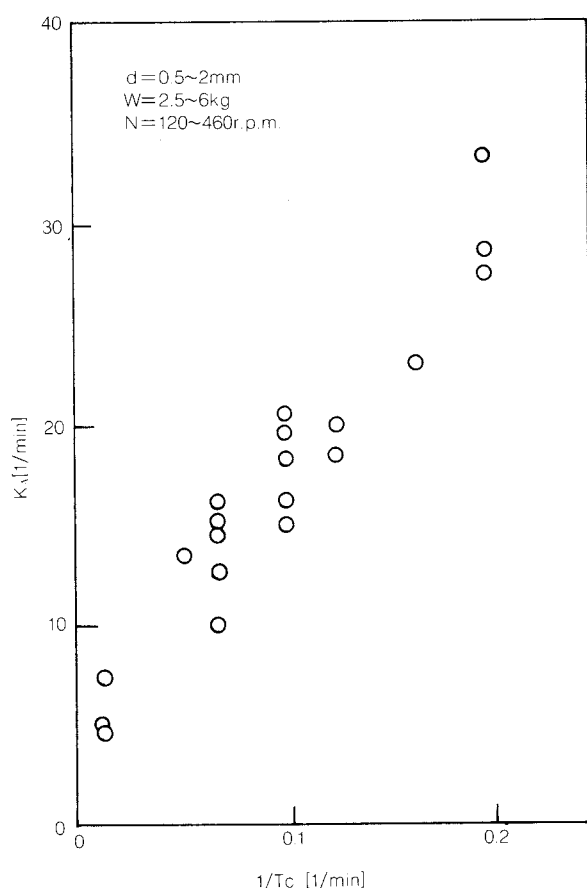


Fig. 4 Relationship between K_A and $1/T_C$

of beads and an agitator speed of 230 rpm. Both R_{mA} and R_{mP} attained their maximum levels at a bead diameter (d) of 1 mm. Schutte, *et al.*, disrupted yeast with glass beads of $d = 0.5$ to 1.0 mm in a horizontal continuous bead mill (Netzsch LME 20), and demonstrated that

R_m attains a maximum at $d = 1$ mm for the enzymes present near the cell walls and at $d = 0.75$ mm for those present in the cytoplasm⁴⁾. Their results also show optimum bead size for producing a maximum R_m value varies depending on the location of the target enzyme in the cell.

The K_A and K_P values agreed with each other when beads of $d = 1$ to 2 mm, but the beads of $d = 0.5$ mm produced the lowest K_A and K_P values used in this study. Currie, *et al.*, observe that the K_P value increases as bead size diameter decreases from 0.5 to 3 mm (glass beads for a Netzsch Molinex KE 5 unit)¹⁵⁾. Marffy, *et al.*, on the other hand, have tested glass beads of $d = 0.1$ to 1 mm in a Dyno-Mill unit and observed that the K_P value attains a maximum at $d = 0.5$ mm⁹⁾.

As discussed above, the effects of bead size on the K_A and K_P levels vary depending on the type of apparatus used. It is expected that in a closed-type mill, such as a horizontal bead mill, the rate of bead collision necessary for disruption is not decreased much by using small beads because their movement is restricted by the surface of the walls. In an open-type bead mill (such as the apparatus used in this study), on the other hand, lightweight beads are affected more by the flowing liquid, with the result that the rate of bead collision decreases, thus decreasing the K values.

Beads of $d = 0.5$ mm produced the highest K_A/K_P ratio, followed by those of $d = 2$ mm and then $d = 1$ mm. The X_A/X_P ratio was almost the same for beads of $d = 0.5$ and 1 mm, while

that for beads of $d = 2$ mm was slightly lower.

We therefore conclude that beads of $d = 1$ mm produce the optimum release results under the conditions used in this study. However, it was still unknown whether these beads would produce optimum release results under different operating conditions. Therefore the effects of bead quantity and agitation rate on the release characteristics were investigated using beads of $d = 2$ mm, which are heavy enough to remain unaffected by the flowing liquid.

3. 4 Bead quantity

Table 1 (B) summarizes the results of the effects of bead quantity (W) on the release characteristics at an agitator speed of 230 rpm. A given quantity of beads was added to $2 \times 10^{-3} \text{ m}^3$ of the slurry containing the yeast, and hence the height of the liquid varied with the quantity of beads. Before agitation, the height of the liquid was approximately 0.11 m at $W = 3$ kg and 0.14 m at $W = 6$ kg, which corresponds to the distance of approximately 0.05 m and 0.02 m between the bead surface and the liquid surface.

The R_{mA} and R_{mP} values were constant

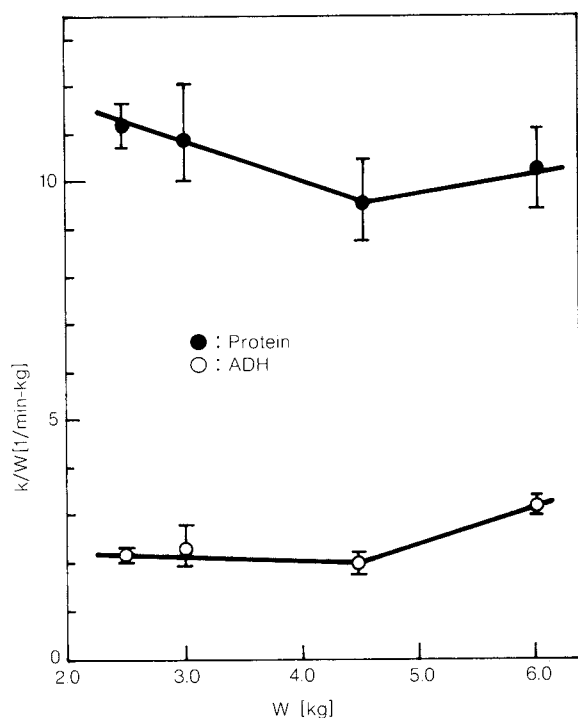


Fig. 5 Effect of the weight of glass beads on the release rate constant of ADH and protein

with respect to bead quantity, except that the R_{mA} level at $W = 6$ kg was slightly higher than the others.

Figure 5 shows the effects of bead quantity W on the K_A/W and K_P/W ratios. As shown, these ratios are almost independent of W , except for K_P/W at $W = 6$ kg; i.e., K_A and K_P are almost proportional to W . It was observed that the release rate constant of proteins was almost proportional to W^2 during the disintegrating of yeast in a vertical bead mill¹⁵⁾.

The possible reasons cited for the higher R_{mA} and K_P/W values at $W = 6$ kg than those at lower W levels were (a) the increased apparent density of those beads in the lower portion of the tank and (b) the changed pattern of movement of the beads that from the increased bead load. The K_A/K_P and X_A/X_P ratios were constant with respect to bead quantity, except for those at $W = 6$ kg.

3. 5 Agitation speed

Table 1 (C) summarizes the results on the effects of agitator speed (N) on the release characteristics. As shown, R_{mA} changed with N , but R_{mP} was almost independent of N . The reasons for the irregular changes in R_{mA} are unknown.

Figure 6 shows the effects of agitator speed N on the K_A/N and K_P/N ratios. The K_A/N ratio is almost constant, irrespective of N in a range from 100 to 320 rpm, but drops sharply at $N = 460$ rpm. In contrast, the K_P/N ratio decreases gradually with N . Therefore, each of the K_A/K_P and X_A/X_P ratios attains a maxi-

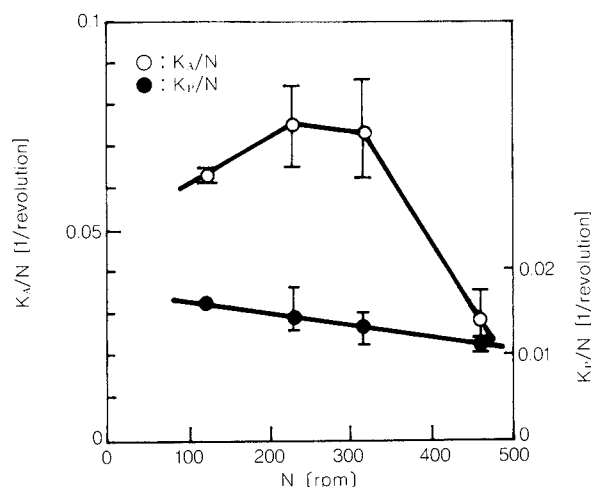


Fig. 6 Effect of the agitator speed on the release rate constant of ADH and protein

mum at around 320 rpm, and drops sharply at around 460 rpm.

These result indicate that K_A and K_P are affected by N differently, and that there is an optimum N level, above which release selectivity decreases as a result of the decreased K_A .

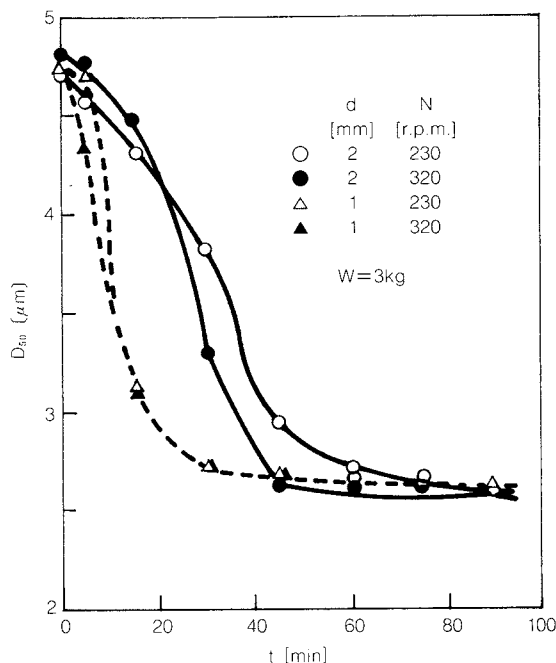
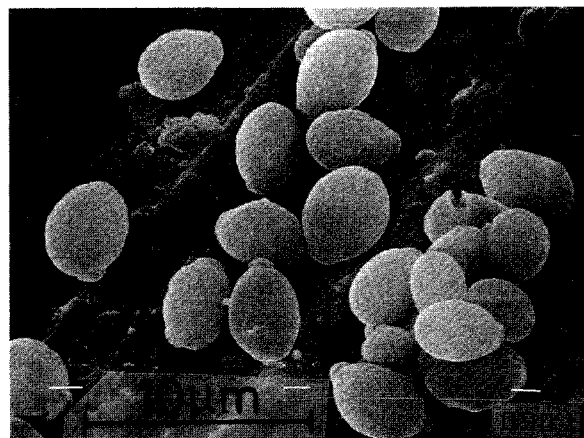


Fig. 7 Relationship between t and D_{50}

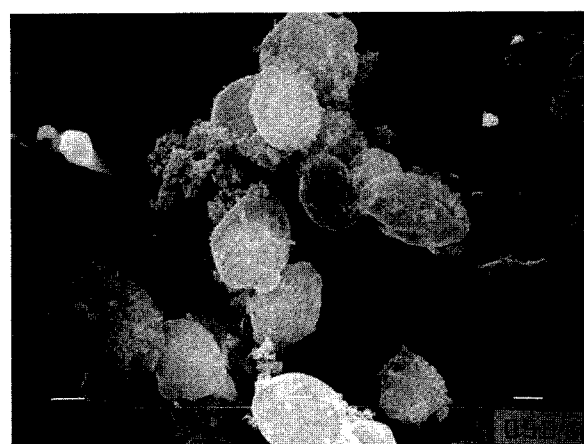
3. 6 Size of disrupted yeast and release characteristics

Figure 7 shows the relationship between the disruption time and the 50% particle size (D_{50}) of yeast disrupted under varying conditions. The attainable size of disrupted yeast is approximately $2.6 \mu\text{m}$, irrespective of the size of the beads with which it was disrupted, although disruption speed is fastest with 1 mm beads. Figure 8 presents the SEM photographs of intact and disrupted yeast, where yeast is disrupted using the beads of 1 mm for 5 min. (b) and 15 min. (c). These photographs indicate that the yeast was not disrupted by the beads into small pieces; instead, the cell walls were partially deformed and disrupted by the beads, thus allowing the intracellular materials (mainly cytoplasm) to escape through the broken cell walls. Therefore, both partially disrupted yeast and the released materials were counted with a Coulter counter.

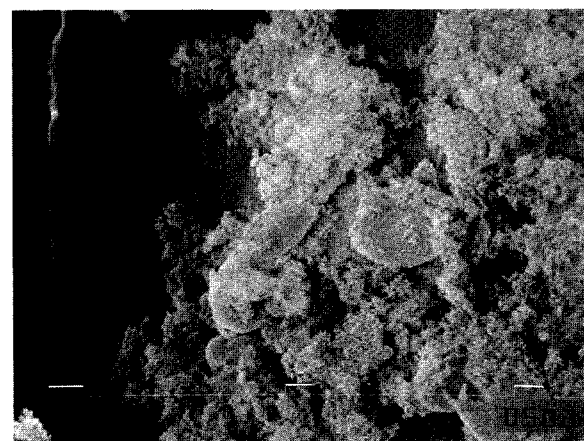
Figure 9 shows the relationship between the protein release rate ($r_p = R_p/R_{mP}$) and the size



a) $t = 0$ [min]



b) $t = 5$ [min]



c) $t = 15$ [min]

Fig. 8 SEM photos of disrupted yeast using the glass beads of $d=1$

of disrupted yeast (D_{50}). As shown, almost 50% of R_{mP} was attained by slightly decreasing the yeast size by disruption. In other words, partial disruption can cause the release of intracellular

materials.

3. 7 Yeast slurry pH level and electric conductivity

Schutte, *et al.*, found that the electric conductivity (λ) of the yeast slurry, which was disrupted in batches using a planetary mill, is proportional to the amount of nucleic acids released¹⁶⁾. They also observed in this study that the slurry pH and electric conductivity

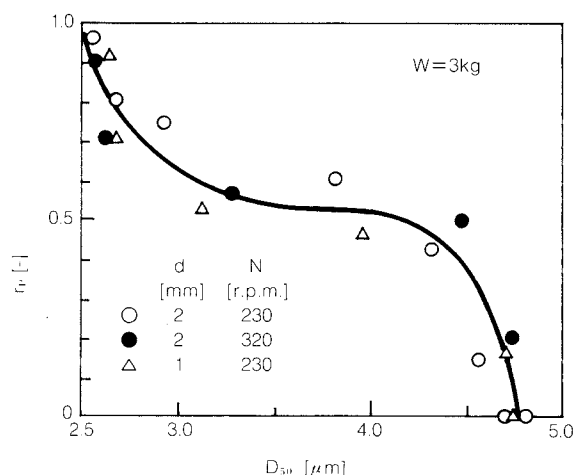


Fig. 9 Relationship between D_{50} and r_p

changed with the disruption time with electric conductivity having a higher repeatability. Figure 10 plots $E (= (\lambda - \lambda_0)/(\lambda_\infty - \lambda_0))$ and $r_G (= R_G/R_{mG})$ against r_p , where λ_∞ and λ_0 are the λ value at $t = 0$ and $t = 90$ min, respectively. As shown, E has a strong correlation with r_G and r_p indicating that the extent of

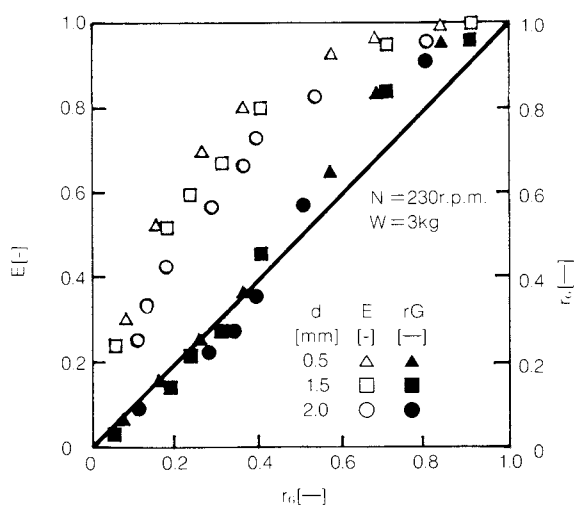


Fig. 10 Correlations among r_p , r_G and E

release from disrupted yeast can be estimated by measuring the λ value. No correlation was observed with $r_A (= R_A/R_{mA})$.

4. Conclusions

Baker's yeast dispersed in pure water was disrupted in batches by using glass beads in order to investigate the release characteristics of ADH, G-6-PDH and proteins. The following results were obtained under the conditions of this study:

- (1) The maximum release rate and selective release characteristics of the materials present in yeast were dependent on the agitator speed on the size and quantity of the beads with which yeast was disrupted. There was an optimum set of operating conditions for each parameter. The indices that represent the release characteristics tended to decrease when the bead size was excessively small or when the agitator speed was excessively high.
- (2) The electric conductivity of the disrupted yeast slurry was correlated with the released quantity of G-6-PDH or proteins, allowing us to estimate the released quantities of these materials by measuring the electric conductivity of the slurry.

Nomenclature

d	: diameter of glass beads	[mm]
D_{50}	: 50% particle size of disrupted yeast	[μ m]
E	: reduced electric conductivity of yeast slurry	[-]
K	: release rate constant of enzyme or protein	[ℓ /min]
N	: agitator speed	[rpm]
r	: ratio of R to R_m	[-]
R	: enzymes activity or weight of protein per unit weight of packed yeast at t	[KIU/wet-kg or kg/wet-kg]
R_m	: final value of R	[KIU/wet-kg or kg/wet-kg]
t	: disruption time	[min]
T_C	: time when the release rate of ADH suddenly decreases	[min]
X	: value of r at $t = T_C$	[-]
W	: weight of glass beads	[kg]
λ	: electric conductivity of yeast slurry	[S]

< Subscript >

A	: ADH (alcohol dehydrogenase)
G	: G-6-PDH (glucose-6-phosphate dehydrogenase)
P	: Protein

References

- 1) Wimpenny, J.W.T.: *Process Biochemistry*, **2**, 41 (1967).
- 2) Matsumoto, K.: *J. Soc. Powder Technol.*, **25**, 303 (1988).
- 3) Hetherrington, P.J., J.M. Follows, P. Dunnill and M.D. Lilly: *Trans. Instn. Chem. Engrs.*, **49**, 142 (1971).
- 4) Schutte, H., K.H. Kroner, H. Hustedt and M.R. Kula: *Enzyme Microb. Technol.*, **5**, 143 (1983).
- 5) Kula, M.-R. and H. Schutte: *Biotech, Progress*, **3**, 31 (1987).
- 6) Chisti, Y. and M. Moo-young: *Enzyme Microb. Technol.*, **8**, 194 (1986).
- 7) Quirk, A.V. and J.R. Woodrow: *Enzyme Microb. Technol.*, **6**, 201 (1984).
- 8) Asenjo, J.A., B.A. Andrews, J.B. Hunter and S. Lecorre: *Process Biochemistry*, **59**, 158 (1985).
- 9) Marffy, F. and M.-R. Kula: *Biotechnol. Bioeng.*, **16**, 623 (1974).
- 10) Shetty, J. and J. Kinsella: *Biotechnol. Bioeng.*, **20**, 755 (1978).
- 11) Belter, P.A., E.L. Cussler and W.S. Hu: "Bioseparations", p.89, John Wiley & Sons (1988).
- 12) Lowry, O.H., N.J. Rosenbrough, A.L. Farr and R.J. Randall: *J. Biol. Chem.*, **193**, 265 (1951).
- 13) Schutte, H. and M.-R. Kula: *Ger. Chem. Eng.*, **9**, 149 (1986).
- 14) Lason, J.L., M. Hoare, C.B. Orsborn, D.J. Doyle and P. Dunnill: *Biotechnol. Bioeng.*, **21**, 745 (1979).
- 15) Currie, J.A., P. Dunnill and M. D. Lilly: *Biotechnol. Bioeng.*, **14**, 725 (1972).
- 16) Luter, H.: *Die Nahrung*, **24**, 265 (1980).

Deposition of Aerosol Particles on Surface Composed of Different Kinds of Materials[†]

Hideto Yoshida

*Dept. of Chemical Engineering,
Hiroshima University**

Makoto Minooka

Maruo Calcium Co., Ltd.

Hiroaki Masuda

*Dept. of Chemical Engineering,
Kyoto University****

Abstract

Experimental and theoretical studies of particle deposition on a surface composed of different materials (copper and polyethylene) were conducted. Deposition of charged aerosol particles was affected by a localized electrostatic field created by the contact potential difference between the metal (copper) and the dielectric material (polyethylene), and the particles charged with positive polarity deposited mainly on the polyethylene surface, which was charged with negative polarity. This fact suggests that the deposition is caused by the Coulombic force between the surface and the particles. The deposition flux was larger for smaller particles because of the larger effect of the electrostatic field.

Aerosol particles with negative polarity do not deposit on the polyethylene surface because the surface charge is negative. The deposition is, however, enhanced on the neighboring copper surface. This is explained by the fact that the electrostatic field vector directs to the main stream.

It is found that the agreement between calculated results and experimental data is better for the case of assuming intrusion of the electric charge into the polyethylene than for that of assuming fixed interface charge.

Introduction

Recently, reliable techniques to prevent the deposition of fine particles on wafers in a superclean room have been in increasing demand to use in producing high-quality integrated circuits during the LSI manufacturing process. There are a number of dielectric (SiO₂) — metal (Cu or Al) contacts on a wafer constituting an LSI, and even fine particles less than 0.1 μm, when deposited on the wafer surface, may prove to be major cause of a defec-

tive product. It is essential, therefore, to analyze the quantity and distribution of aerosol particles deposited on a surface consisting of different kinds of materials and the deposition mechanisms involved, in order to develop a method for electively preventing the particle deposition. Few studies, except for Rosinsky, *et al.*⁶⁾, Emi, *et al.*²⁾, and Ikumi, *et al.*³⁾, have discussed the effects of the wall surface materials on the deposition of fine particles. Rosinsky, *et al.*⁶⁾, and Ikumi, *et al.*³⁾, have investigated the distribution of fine particles deposited on dielectric surfaces, concluding that these particles are not distributed evenly, but instead form particle-islands, because the dielectric surfaces are not electrically uniform. Emi, *et al.*, have passed charged and non-charged particles through pipes made of different materials to obtain the penetration efficiency. They concluded that the deposition of particles on the inner dielectric walls was main-

* Shitami, Saijo, Higashi-Hiroshima, Hiroshima 724
TEL. 0824 (22) 7111

** 1455, Nishioka, Uozumi-cho, Akashi, Hyogo 674
TEL. 078 (942) 2112

*** Yoshida-honmachi, Sakyo-ku, Kyoto 724
TEL. 075 (753) 5565

† This report was originally printed in *Kagaku Kogaku Ronbun-shu*, 14, 655-661 (1988) in Japanese, before being translated into English with the permission of the editorial committee of the Soc. Chemical Engineers, Japan.

ly determined by the amount of electrostatic force²⁾.

The above results are related to the deposition of particles on relatively large surfaces, and provide little information regarding deposition of a aerosol particles on surfaces composed of dissimilar materials of fine patterns, where the dissimilarity between the surface materials serves as a major driving force for the deposition of particles onto the surfaces.

In this study, the authors have attempted to numerically investigate and analyze where and to what extent the aerosol particles are deposited on a surface composed of different kinds of materials (copper and polyethylene).

1. Experimental Equipment and Procedure

Figure 1 illustrates the experimental equip-

ment used in this study. The monodisperse latex aerosol particles (D_p : 0.17 μm , 0.33 μm and 0.62 μm) were used as test particles, which were generated by a nebulizer.

The aerosol particles generated by the nebulizer were electrically charged. In order to control the charge level of particle, the following three types of particles were used:

- (1) Particles which had not been controlled in charge level.
- (2) Particles which were neutralized, after passing through a charge neutralizer (using americium oxide) and a charged particle collector operating under a high voltage.
- (3) Particles with a charge level controlled to $+e$ or $-e$ (where, e means an elementary charge) by passing through the charge neutralizer

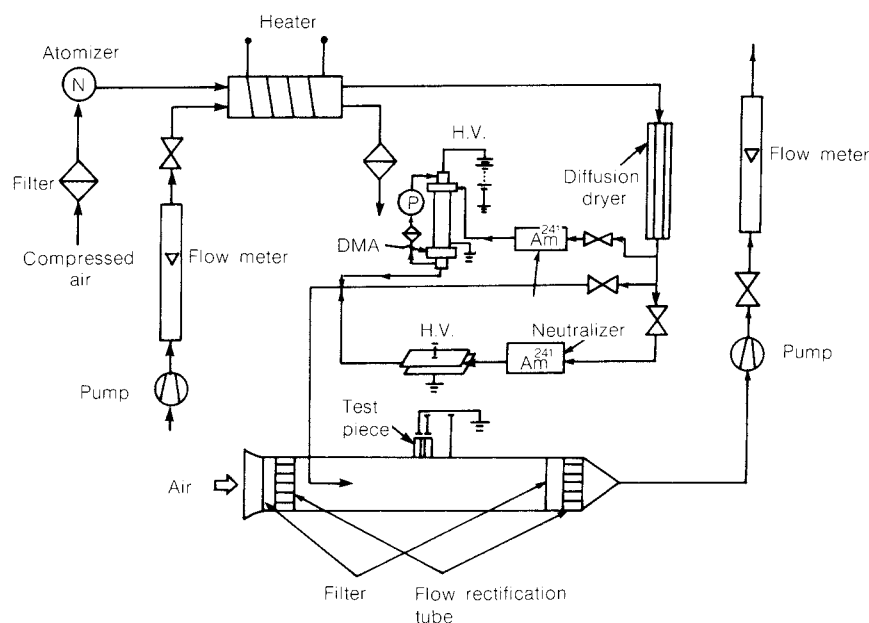


Fig. 1 Experimental apparatus

and a differential mobility analyzer (DMA)⁴⁾.

The air rate was set to a low level ($\bar{U}_x = 6$ cm/s), simulating the conditions of a clean room or work room. The area of test space was 50 cm long and 30 mm \times 120 mm. The test piece was set on the upper wall 20 cm downstream of the aerosol supply.

Figure 2 shows the test piece, which had a 0.3 mm thickness polyethylene sheet sandwiched by 1.5 mm thickness copper plates. The surface on which the particles were to be deposited was polished, and the copper plates were grounded for a long time before the test. The test period lasted from 15 to 20 hr, and

the particle distribution on the test piece was determined by using a scanning electron microscope (JSM-5200) to count the deposited particles.

2. Results and Discussion

2. 1 State of particle deposition

Figure 3 shows an SEM photograph of the latex particles (D_p : 0.33 μm) deposited on the dissimilar surface. The charge level of these particles was not controlled. They deposited more on the dielectric side than on the copper side.

In an attempt to clarify changes in the deposited quantity around the interface between these dissimilar materials, the deposition flux distributions were determined by counting the latex particles on the SEM photographs in different positions.

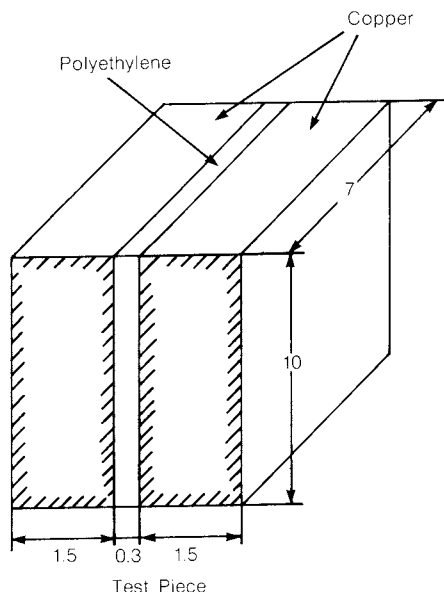
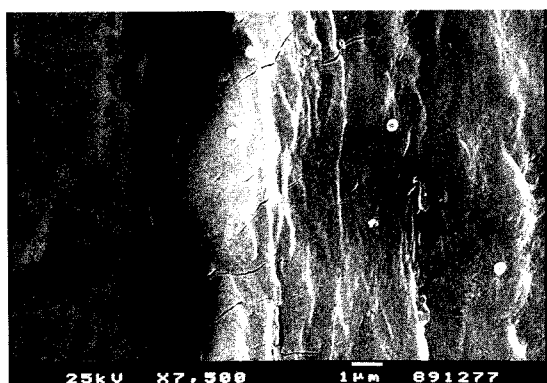


Fig. 2 Test piece composed of different materials



Copper → Polyethylene
 $D_p = 0.33 \mu\text{m}$

Fig. 3 Photograph of particle deposition
($D_p = 0.33 \mu\text{m}$)

Figure 4 shows the deposition flux distribution for the $0.33 \mu\text{m}$ particles. As shown, the deposition flux proved to be approximately 5 times greater on the dielectric than on copper, and attained a maximum level at the dielectric center while proving to be slightly lower on the interfaces. We also observed that the deposition flux was almost constant at a position about 1 mm or more from the dielectric.

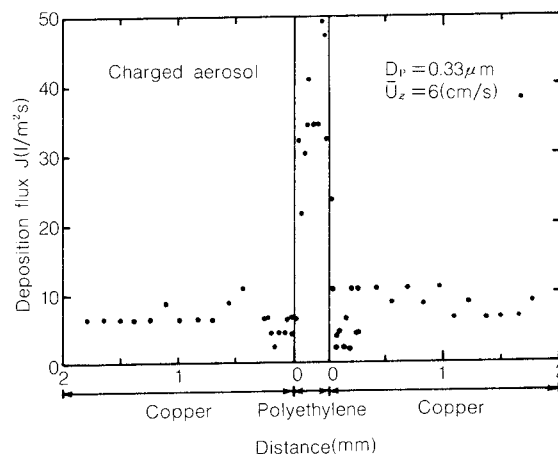


Fig. 4 Deposition flux distribution

The positively charged particles were deposited on the polyethylene surface, because the polyethylene charged negatively due to the contact potential difference between the copper and polyethylene. It was therefore necessary to understand the degree of the contact potential difference between the polyethylene and

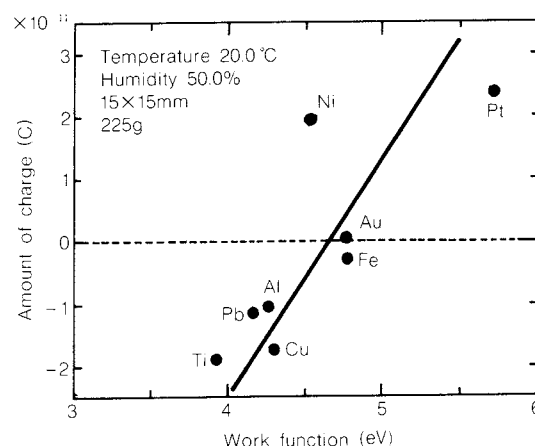


Fig. 5 Relation between amount of charge and work function

copper. The contact potential difference between dissimilar materials is well known, but that between a dielectric and a metal is still relatively unknown.

Tests were, therefore, performed, in which a polyethylene sheet was placed into contact with a variety of metals with different work functions. Thereafter, the charge level difference between them could be measured after they were separated, based on the concept that the work function which indicated zero charge

transfer was equivalent work function of the dielectric¹⁾.

Figure 5 shows the results. The very small charge generated was measured using a Faraday cage (Advantest, TR-8031) and a vibration-capacity electrometer (Advantest, TR-8411) in a chamber in which temperature and humidity were kept at constant levels. The polyethylene sheet measured was 15 mm square. The results were scattered, unless the sheet's charge was eliminated as far as possible. As Fig. 5 shows, the equivalent work function of the dielectric was 4.6 eV, and the contact potential difference between copper and polyethylene was approximately 0.3 V. Thus, the polyethylene sheet would have a negative charge relative to the copper plate, when these two came into contact.

As a matter of course polyethylene will become positively charged relative to platinum, when these two come into contact, since the work function of the platinum is larger than the polyethylene.

2. 2 Theoretical analysis

A numerical analysis was carried out to understand the contact potential difference created as a result of the contact between polyethylene and copper, and the resulting electrical field generated around the interfaces. The potential distribution in a space is provided by the following equation:

$$\frac{\partial^2 V}{\partial x^2} + \frac{\partial^2 V}{\partial y^2} = -\frac{\rho}{\epsilon} \quad (1)$$

where V represents the potential difference, ρ represents the space-charge density and ϵ represents the dielectric constant. The equation (1) may be reduced to a dimensionless Laplace's differential equation (2) without dimensions by use of the contact potential difference between the dissimilar materials, and assuming that the aerosol concentration is sufficiently low to create only a negligibly small space charge ($\rho = 0$).

$$\frac{\partial^2 \bar{V}}{\partial \bar{x}^2} + \frac{\partial^2 \bar{V}}{\partial \bar{y}^2} = 0 \quad (2)$$

$$\bar{V} = \frac{V}{\Delta V}, \bar{x} = \frac{x}{R}, \bar{y} = \frac{y}{R}$$

where $\bar{V} = V/\Delta V$, $\bar{x} = x/R$, $\bar{y} = y/R$, ΔV is the

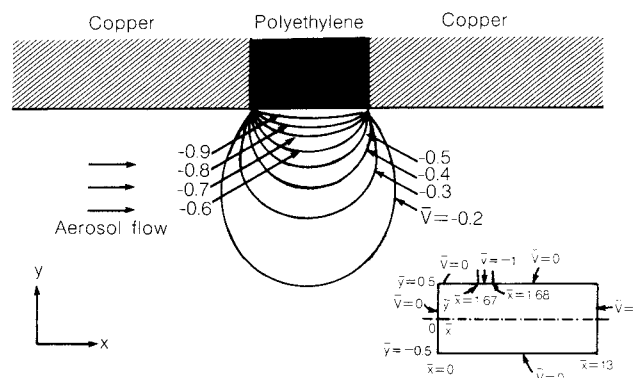


Fig. 6 Calculated electric potential distribution

contact potential difference, and R is the width of the rectangular area through which the aerosol particles pass.

Equation (2) was solved numerically by applying the relaxation method, with the boundary conditions of the dimensionless potentials, $\bar{V} = -1$ at the polyethylene surface and $\bar{V} = 0$ at the grounded copper section.

Figure 6 shows the calculated equivalent potential distributions, including those around the polyethylene-copper interfacial area. It also shows the detailed boundary conditions applied in solving Equation (2). The results suggest that the equivalent potential is symmetrically distributed, and that the potential abruptly changes around the interfacial area, decreasing sharply with the distance from the polyethylene section.

Next, the potential distribution was used to estimate the deposition flux on the wall surfaces. The convective diffusion equation (3) could be applied, by neglecting the inertial force acting on the particles, since the particle size and flow rate were sufficiently small:

$$\frac{\partial (cv_x)}{\partial x} + \frac{\partial (cv_y)}{\partial y} = D \left(\frac{\partial^2 c}{\partial x^2} + \frac{\partial^2 c}{\partial y^2} \right) \quad (3)$$

where v_x and v_y represent the particle velocity components in the x , y directions, c is the concentration, and D is the Brownian diffusion coefficient.

We considered the following three components of the electrostatic force applied to the particles:

- (1) Coulombic force
- (2) force generated by image charge
- (3) dielectric migration force

The particle velocity components in the x

and y directions can be obtained by the following equations, considering the electrostatic force, consisting of the above three components as well as gravity as the external forces applied to the particles:

$$\begin{aligned} v_x &= u_x + \frac{CqE_x}{3\pi\mu D_p} + \frac{\pi}{4} D_p^3 \epsilon_0 \left(\frac{\epsilon_p - \epsilon_0}{\epsilon_p + 2\epsilon_0} \right) \\ &\quad \times \left(\frac{\partial E_x^2}{\partial x} + \frac{\partial E_y^2}{\partial x} \right) \left(\frac{C}{3\pi\mu D_p} \right) \\ v_y &= u_y + \frac{CqE_y}{3\pi\mu D_p} + \left(\frac{q^2}{16\pi\epsilon_0 s^2} \right) \left(\frac{C}{3\pi\mu D_p} \right) \\ &\quad + \frac{\pi}{4} D_p^3 \epsilon_0 \left(\frac{\epsilon_p - \epsilon_0}{\epsilon_p + 2\epsilon_0} \right) \left(\frac{\partial E_x^2}{\partial y} + \frac{\partial E_y^2}{\partial y} \right) \\ &\quad \times \left(\frac{C}{3\pi\mu D_p} \right) - \frac{C\rho_p D_p^2 g}{18\mu} \end{aligned} \quad (4)$$

where E_x and E_y represent the strength of the electrical field in the x and y directions ($E_x = -\partial V/\partial x$, and $E_y = -\partial V/\partial y$), ϵ_p and ϵ_0 represent the dielectric constants of the particles and the air, q represents the charge of the particle, C represents Cunningham's slip correction factor, and u_x and u_y represent the fluid velocity components in the x and y directions respectively.

The particle velocity components, calculated by Equation (4), were substituted into Equation (3), to determine the concentration field by applying a numerical analysis with the relaxation method. The concentration at the wall surface was assumed to be zero (perfect absorption wall), as the boundary condition. For the differential expression of Equation (3), it is desirable to use the central difference for assessing the convection term near the wall and the windward difference for assessing the convection term at the duct center. This will improve the calculation accuracy because the particle velocity components are sufficiently small in the vicinity of the wall surface indicating that the diffusion term is not longer negligible. The exponential method⁵⁾, automatically taking the above into consideration, was used to carry out a numerical calculation.

The following equation was used to determine the particle deposition flux at the wall surface:

$$J = cv_y - D \frac{\partial c}{\partial y} \Big|_w \quad (5)$$

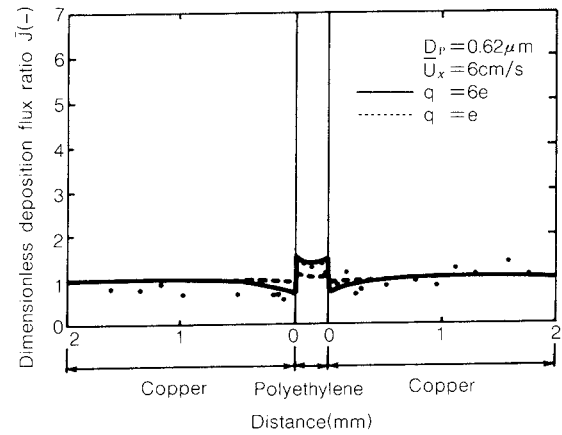


Fig. 7 Deposition flux distribution compared with calculated result ($D_p = 0.62 \mu\text{m}$)

2. 3 Distribution of the deposited particles

a) When the particle charge is not controlled:

The following is a discussion of the experimental results for the case in which the charge on the particles, generated by the nebulizer, is not controlled.

Figure 7 presents the results for $0.62 \mu\text{m}$ particles, in which the dimensionless deposition flux ratio represents the ratio of particles deposited by diffusion only to the particles deposited by both diffusion and electrostatic force. The following equation demonstrates this ratio:

$$\bar{J} = \frac{J_{D+E}}{J_D} \quad (6)$$

The experimental data are well represented by the calculated results (solid line) developed by

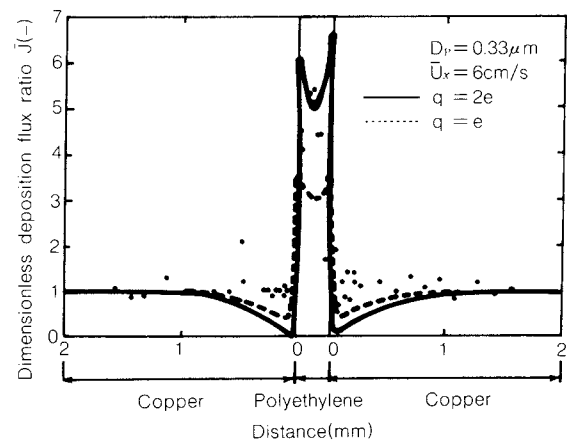


Fig. 8 Deposition flux distribution compared with calculated result ($D_p = 0.33 \mu\text{m}$)

assuming that each particle is charged with electricity of $q = 6e$. As shown, the amount of particles deposited on the polyethylene surface is higher than the amount deposited on the copper surface. The figure also shows the calculated results by assuming that $q = e$ (broken line); the deposited amount is smaller because of the reduced electrostatic effect.

Figure 8 presents similar results for the $0.33 \mu\text{m}$ particles, the number of $0.33 \mu\text{m}$ particles deposited on the polyethylene surface greatly increases compared with the $0.62 \mu\text{m}$ particles. This results are due to the increased electrostatic effect for the smaller particles, and the experimental results are well represented by the calculated results developed by assuming $q = 2e$ (solid line).

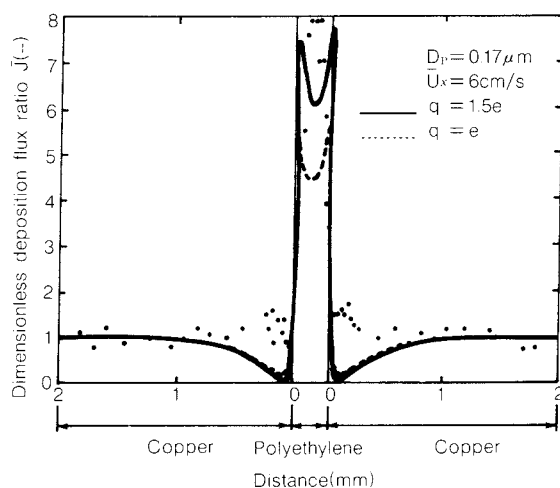


Fig. 9 Deposition flux distribution compared with calculated result ($D_p = 0.17 \mu\text{m}$)

Figure 9 provides the results for the $0.17 \mu\text{m}$ particles, the number of particles deposited on the polyethylene surface greatly increases in this case as well. The calculated results follow the same trend. The experimental results are well represented by the calculated results developed by assuming $q = 1.5e$. This, however, is not true for those particles around the interfaces. The calculated flux ratio decreases in the copper section near the interface vicinity, which is conceivably the result of the electrical field vector being directed locally to the upstream side, as illustrated in the equivalent potential chart (Fig. 6). The sharp increase in deposition flux at the dielectric surface near the interfaces is the result of the sharply changing potential

of these areas. There is a discrepancy between the experimental and calculated results of the copper surface in the vicinity of the interfaces because the calculation assumes that all the particles are positively charged, while some particles are actually negatively charged. Surface roughness was considered to somewhat affect the deposition flux. The effects, however, are negligible, since the interface thickness is sufficiently greater than the surface roughness. The experimental results presented by Shimada, *et al.*⁷⁾, support this proposition.

b) Non-charged particles:

The results shown in Fig. 7 through 9 indicate that the electrostatic force, generated by the particles' electricity is the major cause forcing them to deposit on the dielectric surface. This means that the number of non-charged particles deposited onto a surface should be constant, irrespective of the surface material. In order to confirm this, we conducted experiments with non-charged particles, in which the aerosol particles generated by the nebulizer were passed through a charge neutralizer and a high-voltage (3 kV) field between two parallel plates, to remove the charged particles. The distance between the plates and the size of the plates were designed to remove the charged particles completely.

Figure 10 compares the results of the charged $0.17 \mu\text{m}$ particles with the same size non-charged particles. The deposition flux of the non-charged particles is constant, irrespective of the surface material. In principle, even the

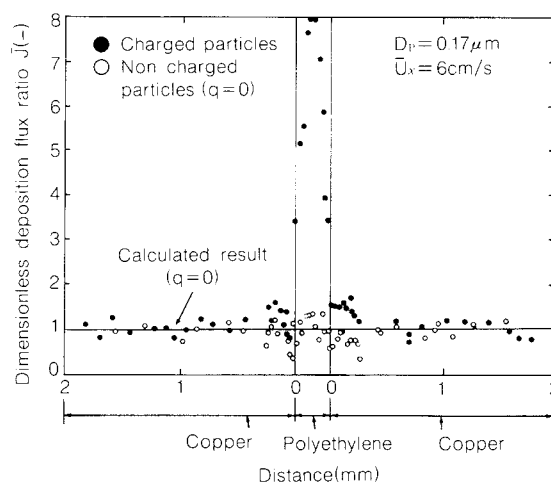


Fig. 10 Effect of particle charge on the deposition flux distribution

non-charged particles are affected by the dielectric migration force. This effect, however, proved to be very small under the conditions of this study (as indicated by the solid line representing the calculated results) because there was a very low contact potential difference of 0.3 V. These results have confirmed that the particles' electricity is the major cause of the differences in the extent of the deposits, depending on the surface material.

c) Particles with a known charge level:

When copper makes contact with polyethylene, the latter is negatively charged, as indicated by the work function relationship, which is shown in Fig. 5. Using particles of a known charge level, therefore, allows us to control the amount deposited on the polyethylene surface. In order to confirm the above proposition, we attempted to control the charge level of the particles by passing them through a differential mobility analyzer (DMA)⁴⁾. Figure 11 shows the results of the $0.17 \mu\text{m}$ particles, whose charge level was controlled at $q = e$. This figure also presents the corresponding calculated results. The experimental results agree well with

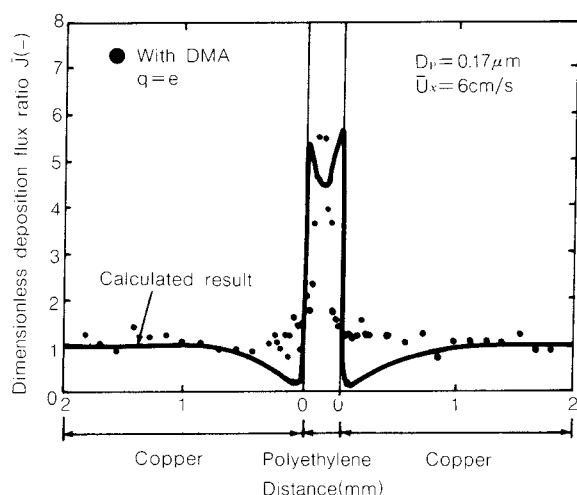


Fig. 11 Deposition flux distribution with particle charge equal to e

the calculated results, except for those results near the vicinity of the interfaces. Next, we carried out experiments with negatively charged particles ($q = -e$). The negatively charged particles are repulsed by the dielectric surface, which is also negatively charged. Figure 12 provides the results. As shown, there are no particles on the dielectric surface. The increased

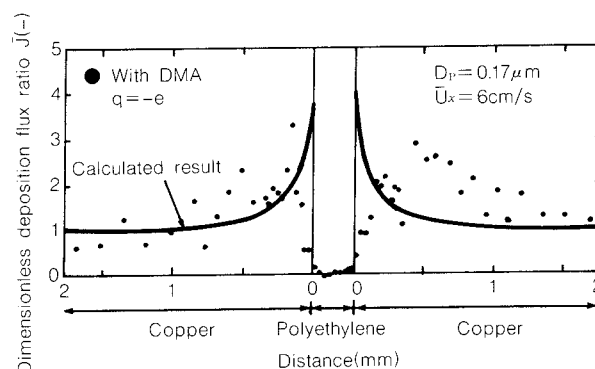


Fig. 12 Deposition flux distribution with particle charge equal to $-e$

deposition flux of the copper plates in the vicinity of the interfaces results because the electrical field vector around this region is directed to the central axis of the air flow, judging from the equivalent potential distribution shown in Fig. 6. This has the effect of repulsing part of the negatively charged particles. The experimental results generally match well with the calculated ones, except for the experimental flux on the copper plates in the vicinity of the interfaces, which slightly deviates from the calculated flux. The reasons for the discrepancy are not yet understood.

The next case considers the effect of the intrusion of an electrical charge into the dielectric material in the numerical calculation. The calculated deposition flux ratio shown in Fig. 11 increases sharply in the interfacial area on the polyethylene surface, while the experimental ratio attains its maximum at the polyethylene center. For the calculation, the potential on the dielectric surface was assumed to be constant, thus causing the potential to rapidly change in the vicinity of the interface. In actuality, however, some charge seemingly intrudes into the dielectric body¹⁾, with the result that the potential is not evenly distributed over the dielectric surface.

Assuming that the potential distribution on the dielectric surface is represented by the following equation¹⁾, the particle deposition flux is calculated, where the intrusion of a charge into the dielectric body is considered:

$$\bar{V} = -\alpha_1 - \alpha_2 (1 - \exp(-\frac{x}{\delta})), \alpha_1 + \alpha_2 = 1 \quad (7)$$

where x represents distance from the interface

and δ for the depth to which the charge intrudes. In the region of $x \gg \delta$, the potential (contact potential difference) is constant.

Figure 13 compares the calculated results to the experimental ones, where the potential distribution determined by equation (7) in the case of $q = e$. The calculated results still show a maximum flux at the interface with a low δ level of 0.02 mm, but the maximum appears at the dielectric center with a δ level of 0.04 mm, thus showing the same trend as the experimental results.

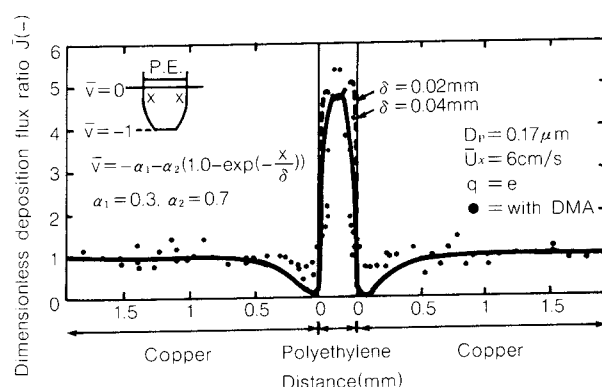


Fig. 13 Deposition flux distribution compared with modified calculated result

Conclusion

The deposition of aerosol particles on a surface composed of different kinds of materials (copper and polyethylene) was investigated both experimentally and theoretically, in order to determine where and to what extent the particles were deposited.

- (1) The electrically charged particles are affected by the electrical field, which is spontaneously generated when the metal comes into contact with the dielectric; the positively charged particles are deposited extensively onto the polyethylene surface, which is charged negatively in the copper-polyethylene system.
- (2) The extensive deposition of positively charged particles onto the dielectric surface is mainly caused by the coulombic force generated as a result of the interaction between the particles and the electrical field. Smaller particles are more affected by the electrical field, and, therefore, deposited

more extensively onto the surface.

- (3) The negatively charged particles are rarely deposited on a negatively charged dielectric, but are deposited extensively onto the copper section in the vicinity of the interfaces. This occurs because the electrical field vector is directed locally to the main stream flow in the vicinity of the interfaces.
- (4) The calculated results assuming that a charge intrudes into the dielectric body match better with the experimental results than in the case in which no charge intrusion is considered.

Acknowledgement

This study was financed in part by a grant from the Ministry of Education (General Research C, 62550703, 1987) in Japan.

Nomenclature

C	: Cunningham's slip correction factor	[-]
c	: particle concentration	[kg/m ³]
D_p	: particle diameter	[μm]
D	: Brownian diffusion coefficient	[m ² /s]
E_x, E_y	: electric field component of x and y directions, respectively	[V/m]
e	: elementary charge	[C]
J, \bar{J}	: particle deposition flux and dimensionless deposition flux defined by Eq. (6), respectively	[kg/m ² s], [-]
q	: particle charge	[C]
R	: width of two-dimensional test section (3.0cm)	[m]
s	: distance from wall	[m]
u_x, u_y	: fluid velocity component of x and y directions, respectively	[m/s]
\bar{u}_x	: average fluid velocity	[m/s]
v_x, v_y	: particle velocity component of x and y directions, respectively	[m/s]
$\bar{x}(=x/R), \bar{y}(=y/R)$: dimensionless co-ordinates	[-]
$V, \Delta V$: voltage, dimensionless voltage and contact potential difference, respectively	[V], [-], [V]
ρ	: space charge density	[C/m ³]
μ	: gas viscosity	[kg/m·s]
ϵ, ϵ_p	: permittivities of air and particle, respectively	[F/m]
α_1, α_2	: constants defined by Eq. (7)	[-]
δ	: effective Debye length	[m]

References

- 1) Asano, K.: "Seidenki Kougaku Ensyu", Asakura Syoten, Tokyo, 27 (1985)
- 2) Emi, H., C. Kanaoka, Y. Otani and S. Fujiya: *J. of Aerosol Research, Japan*, **2**, 4 (1987).
- 3) Ikumi, S.: *Thesis of Master Course, Hiroshima Univ.*, 78 (1983).
- 4) Kanaoka, C., Y. Otani and H. Emi: *J. Society of Powder Technology, Japan*, **21**, 12, 753 (1984).
- 5) Patankar, S.V.: "Numerical Heat Transfer and Fluid Flow", McGraw-Hill, 88 (1980).
- 6) Rosinski, J. and G. Langer: *Powder Technology*, **1**, 167 (1967).
- 7) Shimada, M., K. Okuyama, Y. Kousaka and K. Ohshima: *J. Chem. Eng. Japan*, **20**, 1, 57 (1987).

Controlling the Moisture Content within a Product of the Continuous Dryer[†]

Ikuro Shishido

*Miyagi Prefectural Institute of Technology**

Tadashi Fujimoto

*Nikkan Kogyo Shinbun***

Shigeru Matsumoto and Shigemori Ohtani

*Dept. of Bio-chemical Engineering,
Tohoku University****

Abstract

The control characteristics of the moisture content within a product (dried sardine powder called "fish meal") are investigated for an in-direct heating continuous dryer. The system is described by a state space model, and the controller is designed based on the discrete I-PD control scheme. State variable is estimated by applying the steady or extended Kalman filter because the moisture content measured by an infra-red hygrometer contains a large amount of random noise due to the rough surface of the powdery product. Satisfactory control performance is achieved for a pilot-scale continuous dryer.

Introduction

Most dryers used in various plants are in-direct heating dryers which employ steam as heat source. During operation, it is common practice to control only the amount of steam used and its pressure empirically without other control methods. From the standpoint of a dryer's energy consumption and product quality, dryer control should be important, yet no significant efforts have been made in this direction. One obstacle which may be preventing this movement could be the lack of high-performance moisture content sensors to measure the moisture content within a product.

One moisture content sensor currently in use is the infra-red hygrometer. The infra-red hygrometer is strongly influenced by surface conditions, in particular, of powdery products for example, fishmeal. That is to say, the infra-red hygrometer detects a large amount of noise

due to surface irregularities of a product, and indicates if there is a variation in the moisture content. The use of this output to control a dryer varies greatly and thus hinders stable control. For these reasons, we researched one method of moisture content control with a continuous dryer in which a product's moisture content was estimated after noise removal with a Kalman filter¹⁾. One of the digital filters in addition to a simple I-PD control law^{2,3)} was applied.

1. Control Model

1. 1 System's transfer function

A single input/output system with the input being the flow rate of steam, which is the dryer's heat source, and the output being the moisture content at the outlet of the dryer. Since most drying systems can be approximated by a dead time plus a first order lag, the system's transfer function can be expressed as :

$$G_p(s) = \frac{K \exp(-Ls)}{1 + Ts} \quad (1)$$

where T = time constant (min)

L = dead time (min)

K = proportional gain factor (—).

1. 2 System's space condition indication

The infra-red hygrometer output usually

* 8-7-20, Nagamachi, Sendai 982
TEL. 022 (248) 4386

** 1-8-10, Kudankita, Chiyoda-ku, Tokyo 102
TEL. 03 (222) 7111

*** Aoba, Aramaki, Sendai, Miyagi 980
TEL. 022 (222) 1800

† This report was originally printed in *J. Soc. Powder Technology, Japan*, **25**, 654-659 (1988) in Japanese, before being translated into English with the permission of the editorial committee of the Soc. Powder Technology, Japan.

contains a large amount of noise. Therefore, output feedback results in instability. Various filtering or smoothing treatments can be considered. We used a digital Kalman filter to estimate the space condition. A stochastic system model was designed on the assumption that a large amount of noise was added to the observation area. In this case, it was necessary to present the system model with space condition. However, because the dead time element is included in Eq. (1), the space condition is expressed in infinite degrees if no changes is made. So here approximation by the Taylor expansion was done as:

$$Y(s) = \frac{K \exp(-L_s)}{1 + T_s} U(s) \doteq \frac{K}{(1 + T_s)(1 + L_s)} U(s) \quad (2)$$

Thus,

$$TL_s^2 Y(s) + (L + T) s Y(s) + Y(s) = K U(s) \quad (3)$$

From this, if the state variables are changes in moisture content and time derivative

$$X_1 = Y, X_2 = dY/dt, y = Y \quad (4)$$

the following equations are obtained

$$\dot{\mathbf{x}} = \mathbf{A}\mathbf{x} + \mathbf{b}u \quad (5)$$

$$y = \mathbf{c}\mathbf{x} + w \quad (6)$$

$$\text{where } \mathbf{A} = \begin{bmatrix} 0 & 1 \\ -1/(TL) - (T+L)/(TL) & 1 \end{bmatrix} \quad (7)$$

(2 × 2 matrix)

$$\mathbf{x} = \begin{bmatrix} X_1 \\ X_2 \end{bmatrix} \quad (2 \times 1 \text{ vector})$$

$$\mathbf{b} = \begin{bmatrix} 0 \\ k/TL \end{bmatrix} \quad (2 \times 1 \text{ vector})$$

$$\mathbf{c} = [10] \quad (1 \times 2 \text{ vector})$$

and where u is the sum of \bar{u} , definitive input (dryer's steam flow percentage) and v , model error and other irregular elements (disturbances), as

$$u = \bar{u} + v \quad (8)$$

and w is observation noise. Here an assumption is made that the w and v noises are white random noise. In other words, the following equations are assumed

$$\begin{aligned} E(u) &= \bar{u}, \quad E(v^2) = Q \\ E(w) &= 0, \quad E(w^2) = R \end{aligned} \quad (9)$$

This space condition model is a continuous-time system. To express this with the discrete-time system

$$X_{k+1} = \mathbf{F}X_k + \mathbf{g}u_k \quad (10)$$

$$Y_k = \mathbf{C}X_k + W_k \quad (11)$$

\mathbf{F} and \mathbf{g} in the equation are obtained as follows:

$$\mathbf{F} = \exp(\mathbf{A}\tau), \quad (2 \times 2 \text{ matrix}) \quad (12)$$

$$\mathbf{g} = \int_0^\tau \exp(\mathbf{A}t) dt \cdot \mathbf{b}, \quad (2 \times 1 \text{ vector}) \quad (13)$$

where τ = sampling time.

1. 3 Kalman filter designs

1. 3 1 Steady Kalman filter

Assuming expected values for u_k , $(u_k - \bar{u}_k)^2$, w_k and w_k^2 in Eqs. (10) and (11) from Eq. (9) as follows:

$$E(U_k) = \bar{u}_k, \quad E\{(U_k - \bar{u}_k)^2\} = Q \quad (9')$$

$$E(W_k) = 0, \quad E(W_k^2) = R$$

the estimated condition vector $\hat{\mathbf{x}}$ by the discrete Kalman filter is obtained as follows:

$$\hat{\mathbf{x}}_k = \tilde{\mathbf{x}}_k + \mathbf{P}\mathbf{c}^T R^{-1} (y_k - \mathbf{c}\tilde{\mathbf{x}}_k), \quad (2 \times 1 \text{ vector}) \quad (14)$$

$$\tilde{\mathbf{x}}_k = \mathbf{F}\hat{\mathbf{x}}_{k-1} + \mathbf{g}u_k, \quad (2 \times 1 \text{ vector}) \quad (15)$$

where \mathbf{P} can be considered the convergent value of the following equations.

$$\mathbf{P}_k = (\mathbf{M}_k^{-1} + \mathbf{c}^T R^{-1} \mathbf{c})^{-1}, \quad (2 \times 2 \text{ matrix}) \quad (16)$$

$$\mathbf{M}_k = \mathbf{F}\mathbf{P}_{k-1}\mathbf{F}^T + \mathbf{g}\mathbf{Q}\mathbf{g}^T, \quad (2 \times 2 \text{ matrix}) \quad (17)$$

1. 3 2 Extended Kalman filter

The above-mentioned steady Kalman filter is considered especially effective when the system's transfer function is known, as shown in Eq. (1), however, when the processing quantity fluctuates or the material changes, the length between the surface evaporation section and the internal evaporation section within the dryer also changes. This causes the system to change, thereby changing the values of K , L and T in Eq. (1). Moreover, if this change occurs while the dryer is in use, it is expected that condition estimates with the steady Kalman filter are no longer possible. In such circumstances, the extended Kalman filter⁴⁾ can be applied to estimate the condition by making K , L and T unknown values. In other words, the assumption is made that the system can be expressed as:

$$\mathbf{x}_{k+1} = \mathbf{F}(\theta)\mathbf{x}_k + \mathbf{g}(\theta)u_k \quad (18)$$

$$y_k = \mathbf{c}\mathbf{x}_k + w_k \quad (19)$$

where θ is the parameter when \mathbf{F} and \mathbf{g} in Eqs. (12) and (13) respectively are considered unknown.

$$\begin{bmatrix} \mathbf{x}_{k+1} \\ \theta_{k+1} \end{bmatrix} = \begin{bmatrix} \mathbf{F}(\theta)\mathbf{x}_k + \mathbf{g}(\theta)u_k \\ \theta_k \end{bmatrix} \quad (20)$$

$$y_k = \mathbf{c}\mathbf{x}_k + w_k \quad (21)$$

From this, extending the state variable \mathbf{z}_k , the estimated value of the state variable \mathbf{z}_{k+1} is obtained as follows:

$$\mathbf{z}_k = \begin{bmatrix} \mathbf{x}_{k+1} \\ \theta_{k+1} \end{bmatrix}, (8 \times 1 \text{ vector}) \quad (22)$$

where

$$\mathbf{f}_k = \begin{bmatrix} \mathbf{F}(\theta)\mathbf{x}_k + \mathbf{g}(\theta)u_k \\ \theta_k \end{bmatrix}, (8 \times 1 \text{ vector}) \quad (24)$$

$$S_k = [\mathbf{H}\mathbf{P}_k\mathbf{H}^T + R]^{-1}, (\text{scalar}) \quad (25)$$

$$\mathbf{N}_k = \mathbf{J}_k\mathbf{P}_k\mathbf{H}^T S_k, (8 \times 1 \text{ vector}) \quad (26)$$

$$\mathbf{P}_{k+1} = \mathbf{J}_k\mathbf{P}_k\mathbf{J}_k^T + \mathbf{Q} - \mathbf{N}_k S_k^{-1} \mathbf{N}_k^T, (8 \times 8 \text{ matrix}) \quad (27)$$

$$\mathbf{J}_k = \begin{bmatrix} \mathbf{F}(\hat{\theta}_k) & \mathbf{L}_k \\ 0 & \mathbf{I} \end{bmatrix}, (8 \times 8 \text{ matrix}) \quad (28)$$

$$\mathbf{H} = [\mathbf{c} \ 0], \mathbf{Q} = \begin{bmatrix} \mathbf{Q}\mathbf{I}_2 & 0 \\ 0 & 0 \end{bmatrix} \quad (29)$$

(1 × 8 vector) (8 × 8 matrix)

Also, \mathbf{L}_k is given from the following equation.

$$\mathbf{L}_k = \frac{\partial}{\partial \theta} [\mathbf{F}(\theta)\hat{\mathbf{x}}_k + \mathbf{g}(\theta)u_k] |_{\theta=\hat{\theta}_k} \quad (30)$$

(2 × 6 matrix)

1. 4 Design of I-PD control law

The I-PD control can be designed with par-

tial knowledge of dynamic characteristics of the process and that even a system which has a relatively large dead time can be easily designed. According to Kitamori^{2,3)} with the transfer function of the material under control,

$$G_p(s) = \frac{b_0 + b_1s + b_2s^2 + \dots}{a_0 + a_1s + a_2s^2 + \dots} \quad (31)$$

with the transfer function of the feedback compensation element

$$G_f(s) = f_0 + f_1s + \dots \quad (32)$$

and with the transfer function of the controller,

$$G_c(s) = \frac{k}{s} \quad (33)$$

the denominator series of the closed loop system transfer functions from target value to control amount is expressed as:

$$G(s)^{-1} = a_0' + a_1's + a_2's^2 + a_3's^3 + \dots \quad (34)$$

then, k , f_0 and f_1 can be determined by corresponding coefficients at as high a level as possible to the following reference model:

$$G'(s)^{-1} = 1 + \alpha_1\delta_s + \alpha_2\delta^2s^2 + \alpha_3\delta^3s^3 \quad (35)$$

where

$$\{\alpha_i\} = \{1, 0.5, 0.15\} \quad (i = 1, 2, 3) \quad (36)$$

In practice, because of the discrete-time system, it is considered that the rise time δ , (when the PD action is used to compensate the dynamic characteristics), is obtained as the minimum root of the positive of the following equation (τ : sampling time)

$$\begin{aligned} & (a_2' + \tau a_1' + \tau^2 a_0')\alpha_4\delta^3 + \\ & (-a_3' + 7/12\tau^2 a_1' + 1/4\tau^3 a_0')\alpha_3\delta^2 + \\ & (-a_3' - 7/12\tau a_2' + 1/18\tau^3 a_0')\tau\alpha_2\delta + \\ & (-1/3a_3' - 1/4\tau a_2' - 1/18\tau^2 a_1')\tau^2 = 0 \end{aligned} \quad (37)$$

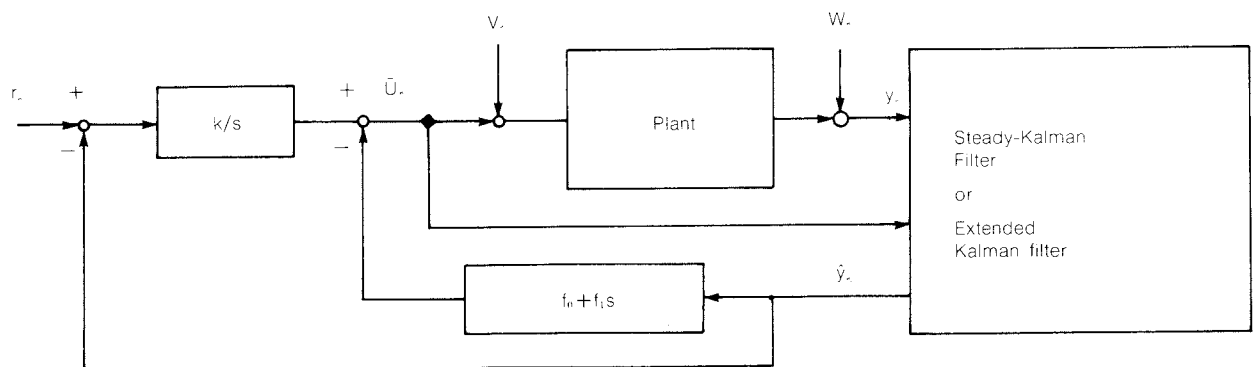


Fig. 1 Scheme of control system

and, k^2 ($=k$), f_0^* ($=f_0$), and f_1^* ($=f_1 + 0.5\tau f_0$) are respectively given from:

$$k^* = \frac{(a_2' + \tau a_1' + 1/3\tau^2 a_0')}{\delta(\alpha_3\delta^2 + \tau\alpha_2\delta + 1/3\tau^2)} \quad (38)$$

$$f_0^* = k^*\alpha_1\delta - a_0' \quad (39)$$

$$f_1^* = k^*\alpha_2\delta^2 - a_1' + 1/2\tau f_0^* \quad (40)$$

The block diagram of the entire system is shown in Fig. 1.

2. Simulation Results

2. 1 Influence of observation noise

Figure 2 shows the influence of noise on the controllability with one-minute sampling item when the Kalman filter was not used: (a) shows the ideal state, free of noise, and (b) and (c) show the standard variations of noise σ_n of 0.1 and 0.5, respectively. It can be predicted from the simulation result, as the figure indicates, that as the noise increases, the control input variation increases, and this system is controllable if the noise level is less than 0.1, however, a noise exceeding 0.1 would greatly fluctuate the steam flow rate, thereby increas-

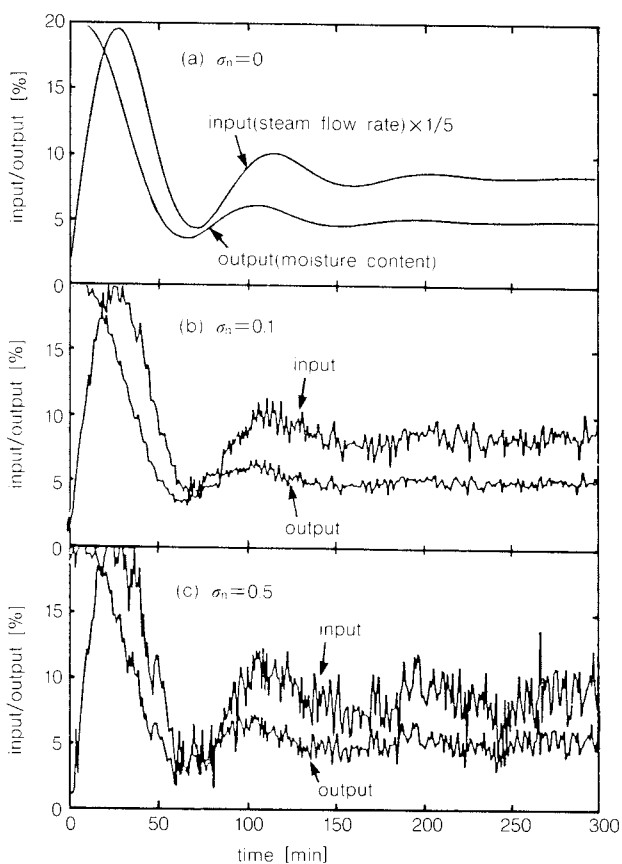


Fig. 2 Simulation result (influence of noise)

ing the influence on the upstream side, for example, of a boiler.

2. 2 Effect of the steady Kalman filter

Figure 3 shows the simulation result when

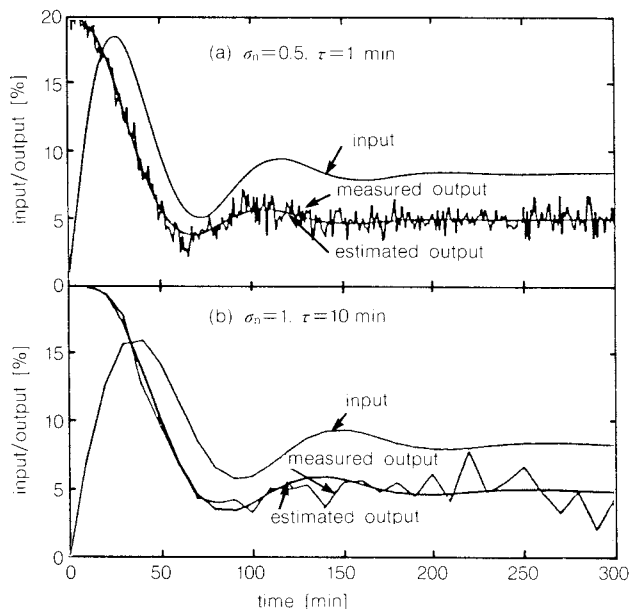


Fig. 3 Simulation result using Kalman Filter

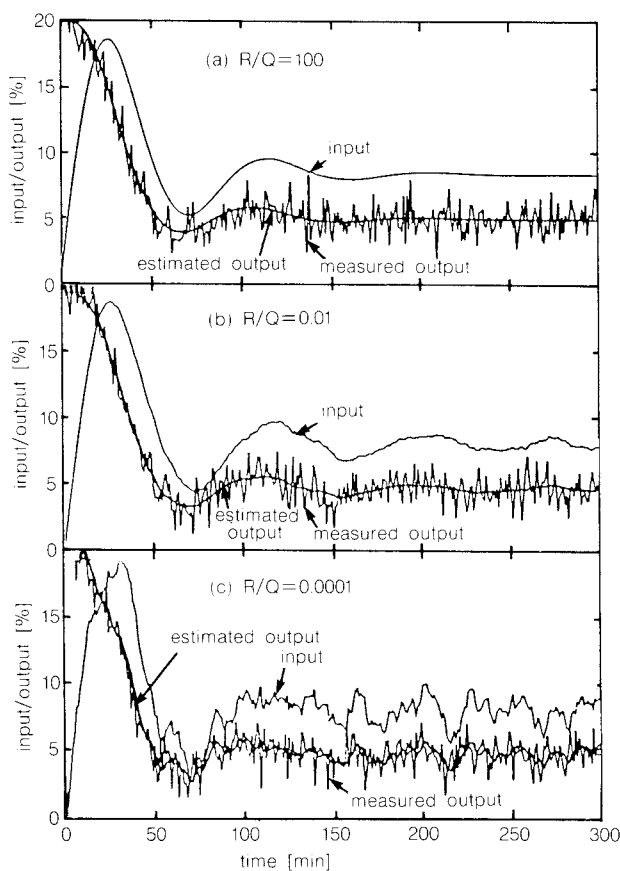


Fig. 4 Simulation result using Kalman Filter

the Kalman filter was used to remove noise: (a) shows the case when the standard variation of noise was 0.5 and a sampling time of one minute; (b) when the standard variation of noise was 1.0 and a sampling time of 10 minutes. Both cases indicate favorable controls, and the condition estimation using the Kalman filter produces satisfactory controls for relatively large noise during the varying sampling time from 0.5 to 60 minutes.

2. 3 Kalman filter R and Q

When designing the Kalman filter, it is necessary to obtain information about the system and noise to be observed. The values of R and Q were determined as a results of trial and error. That is to say, R and Q were randomly assumed as the change in the steam flow rate, which is a control variable, was investigated by simulation. Figure 4 shows this example. From the figure, it is known that if the R/Q ratio is more than 0.01, generally good control is possible. In the experiment, described later, $R = 0.1$ and $Q = 1$ were used, however, no further studies have been made to test whether these are optimal values.

2. 4 Effect of the extended Kalman filter

For system changes such as variation in processing quantity, it is necessary to study whether the extended Kalman filter can approximate the condition variable. Figure 5 shows the simulation result when the system started to change. For some reason, 30 minutes after the start of control and one hour later the system changed from its initial state (K and T in Eq. (1) changed from 0.355 and 40.7 to 0.2 and 60.0, respectively). According to (a), it is evident that the steady Kalman filter does not estimate the condition favorably. The application example (b) of the extended Kalman filter under the same conditions, clearly indicates favorable condition estimation. Here the system's information content was increased by shortening the sampling time to carry out condition estimation favorably and the controlling time was set at appropriate time intervals to suppress abrupt variations in the control input. The figure shows an example of one minute sampling time and 5-minute controlling time.

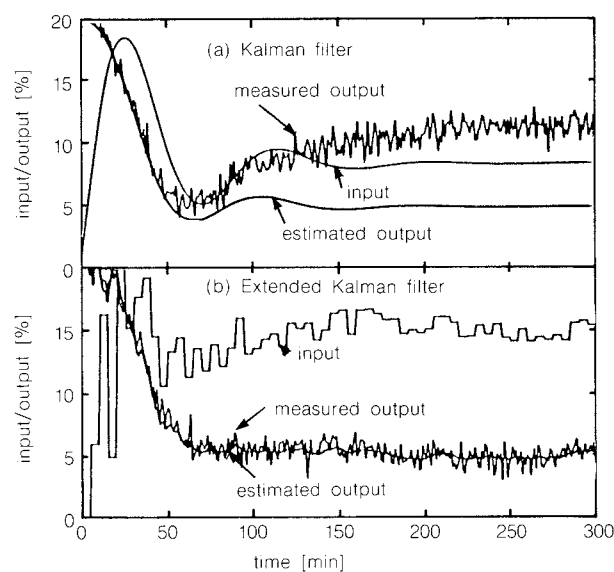


Fig. 5 Simulation result with system parameter change

3. Experiment

3. 1 Experimental equipment and method

Figure 6 shows a schematic drawing of the continuous dryer used in the experiment. The convection type dryer employs an indirect heating system which uses latent and sensible heat of steam as the heat source. Inside the dryer, there are five steam heated steel tubes, a rotor with blades attached to feed the product, and a steam heated jacket. The total length of the dryer is 2 m, and the inside diameter of the jacket is 20 cm. Samples are charged into the dryer by a screw conveyor. The product coming out of the dryer is transported outside the system on the final conveyor and there its final moisture content is measured by an infrared absorption colorimetric moisture meter (model IR-M, made by Chino Seisakusho). The sample in this case is the in-process product produced during fishmeal production, used mainly as stock feed from sardines and sardine residue. Since the fishmeal also contains a little oil, it is not possible to measure the moisture content accurately by only observing the strength of the absorption wave length on a single wave length zone on a general purpose infra-red adsorption hygrometer because infra-red is also absorbed by oils. Therefore, the absorption rate on the dual wave length zone was detected and two voltage outputs E_1 and E_2 , which are related to water and oil contents,

were obtained. It was assumed that the relationship between these outputs and moisture content can be expressed as follows from the results of the preliminary experiments:

$$y = 0.2328 + 2.653 \ln(1250E_1) - 2.4539 \ln(1250E_2) \quad (41)$$

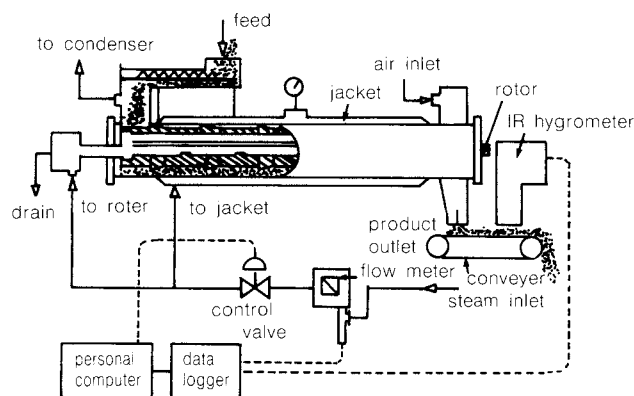


Fig 6 Schematic drawing of experimental continuous drying equipment

3. 2 Experimental result

In the preliminary experiment when no digital filter was used, no control was made because the control input varied because of the noise. Also, in the preliminary experiment when the steady Kalman filter was used, no control was made because the system could not follow the system parameter changes because the processing quality varied or the heat transfer surface of the experimental equipment was dirty. The formal experiment used the extended Kalman filter from the start. **Figure 7** shows the experimental result. Case (a) shows the initial moisture content of the material as 66% of the wet basis, 0.1 minute sampling time, 5 minute control cycle and 7% target moisture content. The moisture content at the dryer outlet shows the values per minute. According to the figure, the target value was obtained about one hour after the experiment start, thereby indicating favorable control regardless of the large amount of noise observed. Case (b) shows the target moisture content initially set at 5% but then changed to 7% 1.8 hours after the experiment started. As seen from the figure, the moisture content was slightly overshoot at the outlet, however, it becomes steady 1.4 hours after resetting the target moisture content.

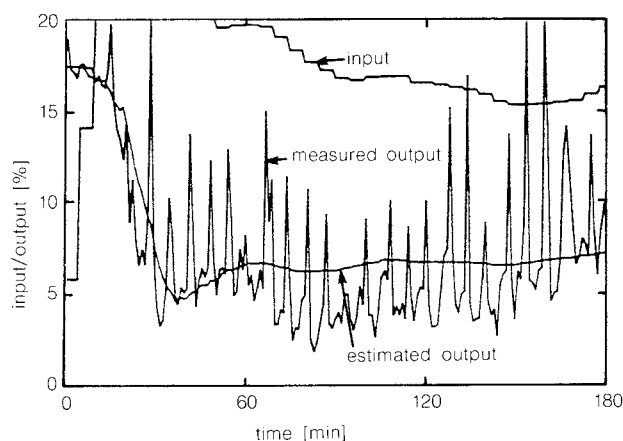


Fig. 7 Experimental result of controlled system (a) constant target moisture content

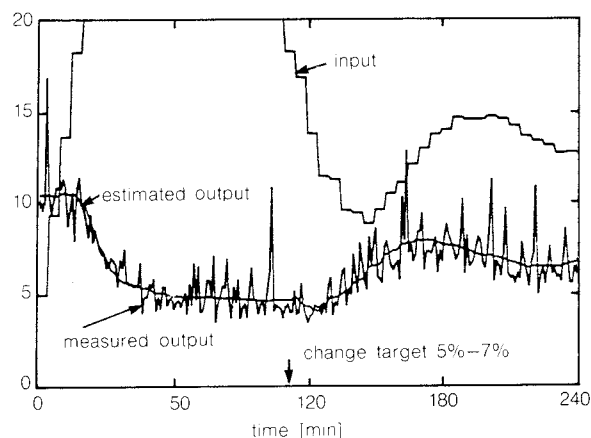


Fig. 7 Experimental result of controlled system (b) step change target moisture content

Conclusion

In this report, in order to control the product's moisture content in a continuous dryer, the system was first expressed in terms of the condition space model. Next the control system was constructed based on the I-PD control law. In this case, an observer is made up by the steady or extended Kalman filter to remove the influence of variations in product moisture content, which is measured by the infra-red absorption moisture meter. This shows that a product's moisture content can be favorably controlled by applying the extended Kalman filter even if the quantity of material to be processed varies to some extent.

Acknowledgments

We would like to thank the Ishinomaki Gyogyo Kogyo Company for letting us use its

continuous dryer to carry out this experiment. We would like to thank Mr. Junichiro Takahashi and Mr. Mikio Inai of the same company for their kindest cooperation in this experiment.

Nomenclature

A	: system matrix at continuous-time system	[-]
b	: control distribution vector at continuous-time system	[-]
c	: measurement vector	[-]
E	: output voltage from infra-red hygrometer	[V]
f	: feedback gain factor of I-PD controller	[-]
F	: system matrix at discrete-time system	[-]
g	: control distribution vector at discrete-time system	[-]
G	: transfer function	[-]
k	: gain factor of I-PD controller	[-]
K	: proportional gain factor	[-]
L	: dead time	[min]
Q	: covariance of system disturbance	[-]
R	: covariance of measurement disturbance	[-]
s	: the complex variable in Laplace domain	[-]

T	: time constant	[min]
u	: input variable	[-]
\bar{u}	: steady value of input variable	[-]
V	: system disturbance	[-]
W	: measurement disturbance	[-]
x	: state variable vector	[-]
\dot{x}	: time differential vector of x	[-]
\hat{x}	: estimated state vector	[-]
\tilde{x}	: state vector in Kalman filter theorem	[-]
y	: output variable	[-]
z	: extended state variable vector in extended Kalman filter theorem	[-]
σ_n	: standard variation of noise	[-]
τ	: sampling time	[min]

References

- 1) Arimoto, T.: "Kalman Filter", Sangyotsusyo (1977).
- 2) Kitamori, T.: *Trans. Soc. Instrum. & Control Engrs. Japan*, **15**, [4], 549 (1979)
- 3) Kitamori, T.: *ibid*, **15**, [5] 695 (1979).
- 4) Lennaratljung: *IEEE Trans. on Automatic Cntl.*, **AC-24**, [1], 36 (1979).

An Assessment of the Mechanism of Particle Shape Separation by a Rotating Conical Disk with a Spiral Scraper[†]

Kenichi Yamamoto, Tatsuo Tsukada
and Masunori Sugimoto

Dept. of Chemical Engineering,
Toyama University*

Abstract

To study the shape separation mechanism of solid particles of differing shapes on a rotating conical disk with a spiral scraper, the behaviors of particles travelling along the scraper wall were discussed by using some cylindroid particles differing in cross-sectional shape. In this paper, for the simulation of the particle's motion along the scraper, three types of the motion were proposed and combined each other.

Simulations were carried out under various operating conditions, and the values of θ_s (: the vectorial angle at which a particle leaves the scraper wall) were calculated for each particle.

The following results were obtained.

- (1) θ_s decreases with increase in the shape index k over a comparatively wide range of k , where k is the ratio of the semi-minor axis b to semi-major axis a of an ellipse at cross section of a cylindroid. The correlation between θ_s and k is considerably affected by the rotating speed of the disk n and inclination angle of the disk surface β .*
- (2) The particles of differing shapes could be effectively sorted along the scraper on the disk.*
- (3) θ_s values estimated by the simulation agree approximately with the ones observed for various cylindroid particles.*

Introduction

Various methods for continuously separating solid particles of different shapes have been proposed, such as the inclined rotating disk^{1~5)}, the inclined vibrating plate^{6,7)} and the inclined rotating cylinder⁸⁾ methods.

The authors have developed a device, which has a rotating conical disk with a spiral scraper serving as the key component for continuously separating solid particles of differing shapes. The authors have also investigated its separation characteristics by using solid particles with irregular shapes. As a result, it has been confirmed that the device is an effective solid shape separator, because of its wide shape-separation

zone along the scraper and its relatively high separation efficiency^{9,10)}.

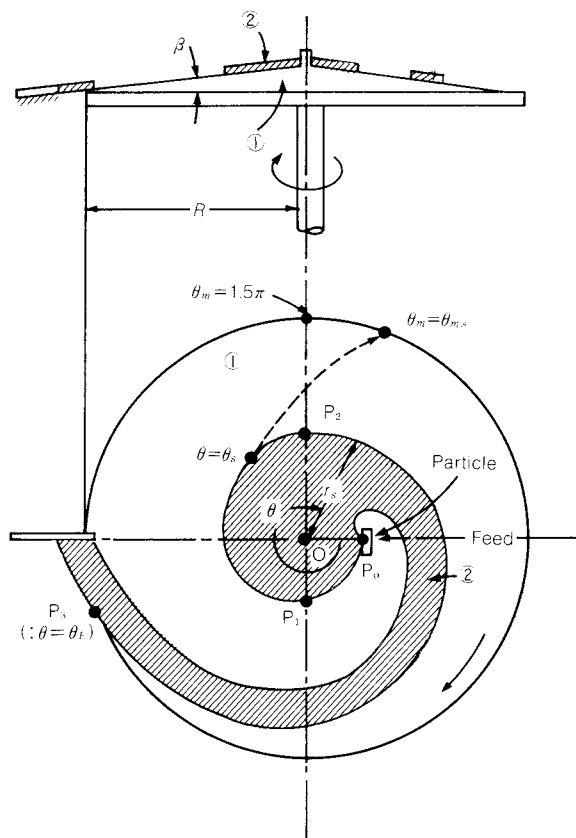
In this study, attempts were made to simulate the motion of the cylindroid particles along the scraper walls, in order to understand the basic separation mechanisms of the device. Using the results as a basis, we can discuss the effects of the operating conditions based on the relationship between the particle cross-section and the separation position on the scraper.

1. Separator

The previously described separator^{9,10)} was used in this study. **Figure 1** outlines the key parts of the device consisting of a rotating conical disk (1) (surface inclination: β , radius: R , speed of rotation: n [min^{-1}], hereinafter referred to as the disk) and the spiral scraper (2) set on the disk. The scraper was fixed by another table, and was stationary. The P_0 to P_3 section of the scraper (hereinafter referred to

* 3190, Gofuku, Toyama 930
TEL. 0764 (41) 1271

† This report was originally printed in *J. Soc. Powder Technology, Japan*, 26, 12-22 (1989) in Japanese, before being translated into English with the permission of the editorial committee of the Soc. Powder Technology, Japan.



- ① Rotating conical disk
- ② Spiral scraper fixed to holder

as the scraper wall) is represented by the following logarithmic spiral equation:

$$r_s = a_0 e^{p\theta} \quad (p = \tan \alpha = \text{const.}) \quad (1)$$

where, θ [rad] is the amplitude in a clockwise direction from point \mathbf{P}_0 , and r_s and a_0 are the radius vectors [m] at $\theta = \theta$ and point \mathbf{P}_0 , respectively.

2. Particle-shape Separation Mechanisms Based on the Simulated Motion of the Cylindroid Particles

2. 1 Assumptions for a motion model of the cylindroid particles

We assume that, as discussed previously¹⁰⁾, the shape separation characteristics of the particles collected along the outer periphery of the disk are greatly determined by the difference of the particles in a motion along the scraper wall, i.e., by the difference in mechanical sta-

bility, during the separation of irregularly shaped particles. In this subsection, the difference among these particles in the motion along the scraper was, therefore, simulated and discussed.

In this study, the motion of the cylindroid particles with different cross-sectional shapes were investigated, as shown in **Fig. 2**, where G - x' , G - y' and G - z' represent the axes of the rectangular coordinates with the particle centroid, G , serving as the origin, x' and z' representing the minor axis ($2b$) and the major axis ($2a$) of the cylindroid cross-section and y' representing the axis perpendicular to the G - x' - z' plane.

Assume that a cylindroid particle is supplied in such a way that it slowly makes the outer periphery of the $G-x'z'$ plane contact with the scraper wall at point P_0 , as shown in Fig. 1. Furthermore, consider the motion of a particle driven along the scraper by the rotating disk until it is dropped from the scraper wall onto the disk after losing its mechanical balance.

The analysis of the particle motion was simplified by the following two assumptions:

- (1) The y' axis of the cylindroid particle moving while making contact with the scraper wall is approximately horizontal, and perpendicular to the radius vector of the scraper.
- (2) The angular velocity of the particle centroid G around the disk center (point O) is the same as the angular velocity of the disk, ω [rad/s].

The position of the particle centroid, G , is therefore given the following equation:

$$\theta = \omega t \quad (2)$$

where, $\omega = \pi n/30$

Next, consider the particle motion on the two rectangular coordinates, $O\text{-}xz$ and $O\text{-}rh$ fixed to the rotating disk, as shown in Fig. 2. At $t = t$, the particle will make contact with the scraper wall and the disk at points E and C, respectively, on the outer periphery of the $G\text{-}x'z'$ (the elliptic plane) containing the centroid G. At the same time, it will make a two-dimensional motion parallel to the $O\text{-}xz$ coordinates plane (or $O\text{-}rh$ plane) on the rotating disk, while the scraper forces it to move in the r direction, according to the above assumptions.

2. 2 Basic equations for the position and attitude of the cylindroid particle

The angles of attitude ϕ , λ and δ [rad], shown in Fig. 2, of the cylindroid particle that

satisfies the conditions of Eq.(3) should also satisfy the relationships of Eqs. (4) and (5) at an amplitude $\theta = \theta$ ($t = t$):

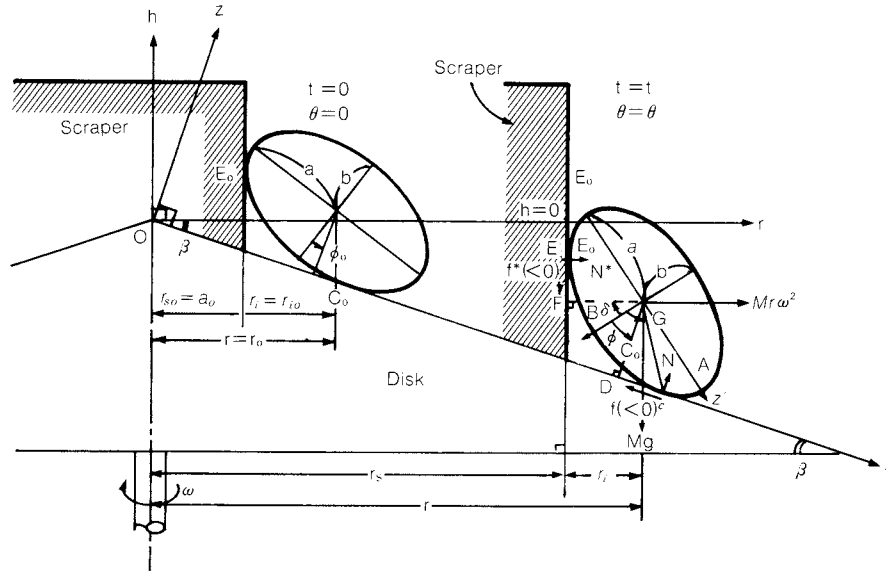


Fig. 2 Geometry, co-ordinate systems, forces acting on a cylindroid, and the motion of a cylindroid on the rotating conical disk with a spiral scraper

$$x'^2/b^2 + z'^2/a^2 = 1 \quad (3)$$

$$\delta = \phi + \beta - \pi/2 \quad (4)$$

$$\tan \lambda = (a^2/b^2) \tan \phi \quad (5)$$

where, ϕ , λ and δ are the angles in the counter-clockwise direction from the standard line GB to GD, GC and GF, respectively. Then, the distances \overline{GC} , \overline{GD} , \overline{GF} , \overline{CD} and \overline{EF} are given by Eqs. (6) through (10):

$$\overline{GC} = r_C' = \left(\frac{a^4 \sin^2 \phi + b^4 \cos^2 \phi}{a^2 \sin^2 \phi + b^2 \cos^2 \phi} \right)^{1/2} \quad (6)$$

$$\overline{GD} = z_G = (a^2 \sin^2 \phi + b^2 \cos^2 \phi)^{1/2} \quad (7)$$

$$\overline{GF} = r_i = (a^2 \sin^2 \delta + b^2 \cos^2 \delta)^{1/2} \quad (8)$$

$$\overline{CD} = x_{CD} = \frac{(a^2 - b^2) \sin \phi \cos \phi}{(a^2 \sin^2 \phi + b^2 \cos^2 \phi)^{1/2}} \quad (9)$$

$$\overline{EF} = h_{EF} = \frac{(b^2 - a^2) \sin \delta \cos \delta}{(a^2 \sin^2 \delta + b^2 \cos^2 \delta)^{1/2}} \quad (10)$$

The peripheral lengths for which the cylindroid particle makes contact with the disk and the scraper wall, S_x ($=C_0C$) and S_h ($=E_0E$), respectively, at $t=0$ to $t=t$ are given by Eqs. (11) and (12):

$$S_x = \int_{\phi_0}^{\phi} \frac{a^2 b^2}{(a^2 \sin^2 \phi + b^2 \cos^2 \phi)^{3/2}} d\phi \quad (11)$$

$$S_h = \int_{\delta_0}^{\delta} \frac{a^2 b^2}{(a^2 \sin^2 \delta + b^2 \cos^2 \delta)^{3/2}} d\delta \quad (12)$$

where, the subscript 0 stands for the value at $t = 0$.

Based on these relations, the position of the particle centroid, G, in the x and z directions (x, z) and its speed and acceleration are given by Eqs. (13) through (18). Also the rotary motion of the particle around the y' axis is given by Eqs. (19) and (20):

$$x = (r_s + r_i)/\cos \beta - z_G \tan \beta \quad (13)$$

$$\dot{x} = \left(\frac{dr_s}{dt} + \frac{dr_i}{d\phi} \dot{\phi} \right) / \cos \beta - \frac{dz_G}{d\phi} \dot{\phi} \tan \beta \quad (14)$$

$$\ddot{x} = \left(\frac{d^2 r_s}{dt^2} + \frac{d^2 r_i}{d\phi^2} \dot{\phi}^2 + \frac{dr_i}{d\phi} \ddot{\phi} \right) / \cos \beta - \left(\frac{d^2 z_G}{d\phi^2} \dot{\phi}^2 + \frac{dz_G}{d\phi} \ddot{\phi} \right) \tan \beta \quad (15)$$

$$z = z_G \quad (16)$$

$$\dot{z} = \frac{dz_G}{d\phi} \dot{\phi} \quad (17)$$

$$\ddot{z} = \frac{d^2 z_G}{d\phi^2} \dot{\phi}^2 + \frac{dz_G}{d\phi} \ddot{\phi} \quad (18)$$

$$\dot{\lambda} = \frac{d\lambda}{d\phi} \dot{\phi} \quad (19)$$

$$\ddot{\lambda} = \frac{d^2 \lambda}{d\phi^2} \dot{\phi}^2 + \frac{d\lambda}{d\phi} \ddot{\phi} \quad (20)$$

The r and h coordinates of the centroid, G , are given by Eqs. (21) and (22):

$$r = x \cos \beta + z \sin \beta = r_s + r_i \quad (21)$$

$$h = -x \sin \beta + z \cos \beta \\ = z_G / \cos \beta - (r_s + r_i) \tan \beta \quad (22)$$

Thus, Eqs. (5) and (13) through (22) can reveal the motion of the particle restricted by the scraper and the disk, if ϕ , $\dot{\phi}$ and $\ddot{\phi}$ at an arbitrary time $t = t$ are known. The motion of the particle will be discussed in detail in the following subsection.

2. 3 Changes in position and attitude of the particle over time

2. 3 1 Forms and equations of particle motion

Assuming that the position and the attitude angles of the particle change from $t = 0$ to $t = t$, as shown in Fig. 2, the slip velocity, v , at the contact point, C , of the particle in the x direction ($v > 0$, when the particle slips in the positive x direction) and the slip velocity, v^* , at the contact point, E , in the h direction ($v^* > 0$, when the particle slips in the positive h direction) are given by Eqs. (23) and (24), respectively.

$$v = \frac{dx}{dt} + \frac{dx_{CD}}{dt} - \frac{dS_x}{dt} \\ = \frac{a_0 p \omega e^{p\omega t}}{\cos \beta} - \left(\frac{h_{EF}}{\cos \beta} + x_{CD} \tan \beta + z_G \right) \dot{\phi} \quad (23)$$

$$v^* = \frac{dh}{dt} + \frac{dh_{EF}}{dt} + \frac{dS_h}{dt} \\ = -a_0 p \omega e^{p\omega t} \cdot \tan \beta \\ + \left(r_i + \frac{x_{CD}}{\cos \beta} + h_{EF} \tan \beta \right) \dot{\phi} \quad (24)$$

In this study, the motion forms of the particle moving while it is making contact with the scraper and disk surfaces are represented by the positive, negative or zero values of the slip velocities, v and v^* . The particle motion may be

classified into three general categories, case-1, -2 and -3, as shown in Fig. 3, depending on the characteristics of the device and the particle in motion; (1) the inclination, β , of the disk is relatively small, (2) the particle is slowly supplied to point, P_0 , and (3) the particle is continuously forced out by the scraper in the positive direction of the radius vector, r , of the disk. In Fig. 3, the v and v^* values (positive, negative or zero) are shown for each case, and at the same time, the frictional forces, f and f^* , at the disk and scraper surfaces are marked with the friction type (either stationary or dynamic), and furthermore, at the direction, where f_s and f_d are the stationary and the dynamic frictional forces at the disk surface and f_s^* and f_d^* are those at the scraper surface.

As Fig. 3 suggests, Case 1 represents a case in which the particle slips both on the disk and the scraper surfaces.

In Case 2, on the other hand, the particle moves without slipping on the disk surface, although it slips on the scraper surface in the positive h direction.

Case 3 represents a case in which the motion of the particle in Case 2 is reversed; the particle slips on the disk surface in the x direction and moves without slipping on the scraper surface in the h direction.

Case 1 will be further subdivided into Cases 1-1 and 1-2, depending on the direction of slip velocity v^* on the scraper surface, and Case 3 will be divided into Case 3-1 and 3-2, depending on the direction in which the stationary frictional force, f_s^* , works, where f_s^* is ≤ 0 in the former case and $f_s^* > 0$ in the latter case.

For all cases, the motion equations of the particle centroid G in the x and z directions and around the y' axis (the moment is positive in the clockwise direction) are given by Eqs. (25) through (27), respectively, in which the directions of the frictional forces, f and f^* , are positive in the positive x and h directions:

$$M\ddot{x} = Mg \sin \beta + Mr \omega^2 \cos \beta + f - f^* \sin \beta \\ + N^* \cos \beta \quad (25)$$

$$M\ddot{z} = -Mg \cos \beta + Mr \omega^2 \sin \beta + N + f^* \cos \beta \\ + N^* \sin \beta \quad (26)$$

$$I\ddot{\lambda} = -z_G f - x_{CD} N + r_i f^* + h_{EF} N^* \quad (27)$$

$$I = M(a^2 + b^2)/4 \quad (28)$$

where, M is mass of the particle, N and N^* are

normal reaction forces generated on the disk and scraper surface, respectively, g is the acceleration due to gravity, and I is the moment of inertia.

The dynamic frictional forces, f_d and f_d^* , are provided by Eqs. (29) and (30), respectively.

$$f_d = \mu_d N \quad (29)$$

$$f_d^* = \mu_d^* N^* \quad (30)$$

where, μ_d and μ_d^* are the coefficients of the dynamic friction between the particle and the disk surface, and between the particle and the scraper surface, respectively. These are constant, irrespective of the slip velocity.

Next, let's discuss the particle motion for each case.

2. 3 2 Motion equations, Case 1

Referring to Fig. 3, the direction of the dynamic frictional forces are $f = -f_d$ and $f^* = -f_d^*$ in Case 1-1, and $f = -f_d$ and $f^* = f_d^*$ in Case 1-2. This is based on which the Eqs. (25), (26), (29) and (30), are solved for the reaction and frictional forces in Case 1 (: subscript 1), as shown by Eqs. (31) through (34):

$$f_d^* = f_{d1}^* = \frac{-\mu_d^* M \{ (g + \mu_d r \omega^2) \sin \beta + (r \omega^2 - \mu_d g) \cos \beta - \ddot{x} - \mu_d \ddot{z} \}}{(\mu_d \pm \mu_d^*) \sin \beta + (1 \mp \mu_d \mu_d^*) \cos \beta} \quad (31)$$

$$f_d = f_{d1} = M (g \sin \beta + r \omega^2 \cos \beta - \ddot{x}) \pm f_{d1}^* (\sin \beta \pm \cos \beta / \mu_d^*) \quad (32)$$

$$N = N_1 = f_{d1} / \mu_d \quad (33)$$

$$N^* = N_1^* = f_{d1}^* / \mu_d^* \quad (34)$$

where, the upper side represents Case 1-1 and the lower side represents Case 1-2. Different signs (with respect to the positive and negative) are used for a term. Substituting Eqs. (31) and (32) for Eqs. (27), (29) and (30) will yield Eq. (35):

$$I \ddot{\lambda} = (z_G - \frac{x_{CD}}{\mu_d}) f_{d1} \mp (r_i \mp \frac{h_{EF}}{\mu_d^*}) f_{d1}^* \quad (35)$$

Substituting Eqs. (20), (15) and (18) for the $\ddot{\lambda}$, \ddot{x} and \ddot{z} values of the above equations will yield the following differential equation (Eq. (36)), hereinafter referred to as the basic motion equation:

$$\ddot{\phi}(\phi, \dot{\phi}, t) = \{ \dot{\phi}^2 \cdot f_{11}(\phi) + f_{12}(\phi, t) \} / f_{13}(\phi) \quad (36)$$

where,

$$f_{11}(\phi) = \frac{-a^2 + b^2}{4} \frac{d^2 \lambda}{d\phi^2} U_{11} \pm (\frac{d^2 r_i}{d\phi^2} \frac{1}{\cos \beta} - \frac{dx_{CD}}{d\phi} \tan \beta) U_{12} \pm \frac{dx_{CD}}{d\phi} U_{13}$$

$$f_{12}(\phi, t) = \pm p^2 \omega^2 a_0 e^{p\omega t} \cdot U_{12} / \cos \beta + (\mu_d z_G - x_{CD})(g \mp \mu_d^* r \omega^2) \pm (\mu_d^* r_i \mp h_{EF}) \{ (g + \mu_d r \omega^2) \sin \beta + (r \omega^2 - \mu_d g) \cos \beta \}$$

$$f_{13}(\phi) = \frac{a^2 + b^2}{4} \frac{d\lambda}{d\phi} U_{11} \pm (\frac{h_{EF}}{\cos \beta} + x_{CD} \tan \beta) U_{12} \mp x_{CD} U_{13}$$

$$\begin{cases} U_{11} = (\mu_d \pm \mu_d^*) \sin \beta + (1 \mp \mu_d \mu_d^*) \cos \beta \\ U_{12} = (\mu_d z_G - x_{CD})(\mu_d^* \cos \beta \mp \sin \beta) - \mu_d^* r_i \pm h_{EF} \\ U_{13} = (\mu_d z_G - x_{CD})(\mu_d^* \sin \beta \pm \cos \beta) - \mu_d \mu_d^* r_i \pm \mu_d h_{EF} \end{cases}$$

The motion form of Case 1-1 will be transferred into the motion form of Case 2, when $v = 0$, and Cases 1-1 and 1-2 into the Case 3 motion form, when $v^* = 0$ (refer to Fig. 3).

2. 3 3 Motion equations, Case 2

The reaction and frictional forces generated on each surface are provided by the following equations for Case 2 (: subscript 2) after substituting the relations, $f = -f_s$ and $f^* = -f_d^*$ into Eqs. (25) through (27):

$$N^* = N_2^* = \frac{[I \ddot{\lambda} - M \{ z_G (g \sin \beta + r \omega^2 \cos \beta - \ddot{x}) - x_{CD} (g \cos \beta - r \omega^2 \sin \beta + \ddot{z}) \}]}{z_G (\mu_d^* \sin \beta + \cos \beta) - x_{CD} (\mu_d^* \cos \beta - \sin \beta) - \mu_d^* r_i + h_{EF}} \quad (37)$$

$$N = N_2 = M (g \cos \beta - r \omega^2 \sin \beta + \ddot{z}) + (\mu_d^* \cos \beta - \sin \beta) N_2^* \quad (38)$$

$$f_s = f_{s2} = M (g \sin \beta + r \omega^2 \cos \beta - \ddot{x}) + (\mu_d^* \sin \beta + \cos \beta) N_2^* \quad (39)$$

$$f_d^* = f_{d2}^* = \mu_d^* N_2^* \quad (40)$$

Assuming that the slip velocity, v , is zero on the disk surface in the Case 2 motion form will reduce Eq. (23) into Eq. (41):

$$\dot{\phi} = L_2 / U_2 \quad \left\{ \begin{array}{l} L_2 = a_0 p \omega e^{p\omega t} / \cos \beta \\ U_2 = h_{EF} / \cos \beta + x_{CD} \tan \beta + z_G \end{array} \right\} \quad (41)$$

Differentiating Eq. (41) by t will yield the

basic motion equation for Case 2:

$$\ddot{\phi}(\phi, \dot{\phi}, t) = \left(\frac{dL_2}{dt} U_2 - L_2 \frac{dU_2}{dt} \right) / U_2^2$$

$$= \left\{ \left(\frac{a_0 p^2 \omega^2 e^{p\omega t}}{\cos\beta} \right) U_2 - L_2 \left(\frac{dh_{EF}}{d\delta} \frac{1}{\cos\beta} \right) \right.$$

$$\left. + \frac{dx_{CD}}{d\phi} \tan\beta + \frac{dz_G}{d\phi} \right\} \dot{\phi} / U_2^2 \quad (42)$$

In the Case 2 motion form, the particle will start to slip on the disk surface in the positive x direction, when its stationary frictional force, f_{s2} , exceeds the maximum stationary frictional force, $\mu_s N_2$, (μ_s : stationary friction coefficient on the disk surface), transferring itself into the Case 1-1 motion form, and into the Case 3 motion form, when the start of the slippery motion is accompanied by $v^* = 0$ (refer to Fig. 3).

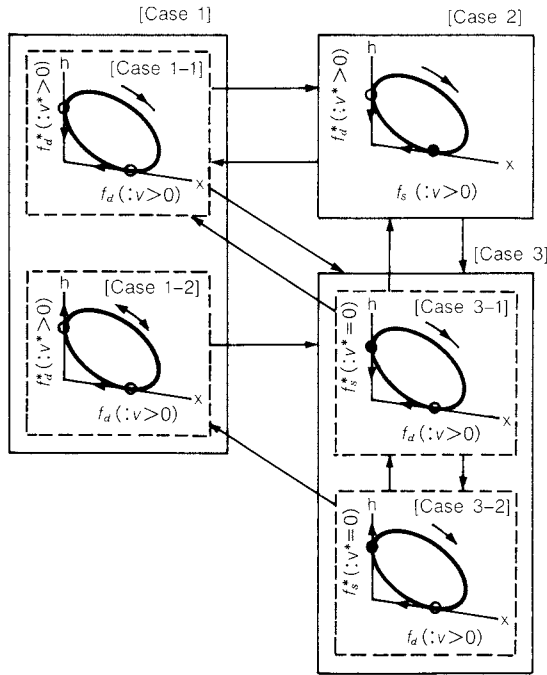


Fig. 3 The modes of particle's motion in the present simulation

2. 3 4 Motion equations, Case 3

The direction in which f_s^* works depends on the overall force balance acting on the particle, and may change in the Case 3 motion form. Assuming a negative f_s^* direction, the reaction and frictional forces generated on each surface are provided by the following equations for Case 3(: subscript 3) by solving Eqs. (25) through (27) and (29) with the relations, $f = -f_d$

and $f^* = -f_s^*$.

$$N^* = N_3^* = \frac{J_{31} - I\ddot{\lambda}(\sin\beta - \mu_d \cos\beta)}{(\mu_d z_G - x_{CD}) - r_i(\mu_d \sin\beta + \cos\beta) - h_{EF}(\sin\beta - \mu_d \cos\beta)} \quad (43)$$

$$J_{31} = M[gr_i(\sin\beta - \mu_d \cos\beta) - r\omega^2\{(\mu_d z_G - x_{CD}) - r_i(\cos\beta + \mu_d \sin\beta)\} + \ddot{x}\{(\mu_d z_G - x_{CD})\cos\beta - r_i\} + \ddot{z}\{(\mu_d z_G - x_{CD})\sin\beta - \mu_d r_i\}]$$

$$f_s^* = f_{s3}^* = J_{32} / (\mu_d \cos\beta - \sin\beta) \quad (44)$$

$$J_{32} = N_3^*(\mu_d \sin\beta + \cos\beta) + M\{g(\sin\beta - \mu_d \cos\beta) + r\omega^2(\cos\beta + \mu_d \sin\beta) - \ddot{x} - \mu_d \ddot{z}\}$$

$$f_d = f_{d3} = M(g\sin\beta + r\omega^2 \cos\beta - \ddot{x}) + f_{s3}^* \sin\beta + N_3^* \cos\beta \quad (45)$$

$$N = N_3 = f_{d3} / \mu_d \quad (46)$$

Assuming that $v^* = 0$ in the Case 3 motion form will reduce Eq. (24) into Eq. (47):

$$\dot{\phi} = L_3 / U_3$$

$$\left\{ \begin{array}{l} L_3 = a_0 p \omega e^{p\omega t} \cdot \tan\beta \\ U_3 = r_i + x_{CD} / \cos\beta + h_{EF} \tan\beta \end{array} \right\} \quad (47)$$

Differentiating Eq. (47) by t will yield the basic motion equation for Case 3.

$$\ddot{\phi}(\phi, \dot{\phi}, t) = \left(\frac{dL_3}{dt} U_3 - L_3 \frac{dU_3}{dt} \right) / U_3^2$$

$$= \left\{ (a_0 p^2 \omega^2 e^{p\omega t} \cdot \tan\beta) U_3 - L_3 \left(\frac{dr_i}{d\delta} + \frac{dx_{CD}}{d\phi} \frac{1}{\cos\beta} + \frac{dh_{EF}}{d\delta} \tan\beta \right) \dot{\phi} \right\} / U_3^2 \quad (48)$$

When $f_{s3}^* \geq 0$, the motion form of the particle will be represented by Case 3-1, in which the stationary frictional force works in the negative h direction. When $f_{s3}^* < 0$, it will be represented by Case 3-2, in which the stationary frictional force works in the reverse direction. When $|f_{s3}^*| > \mu_s^* N_3^*$ (where, μ_s^* : coefficient of the stationary friction of the particle on the scraper surface), the particle will start to slip on the scraper wall surface, in both the positive h direction in Case 3-1, and the negative h direction in Case 3-2. The Case 3-1 motion form is transferred into Case 1-1, or from Case 3-2 into Case 1-2, when the slip velocity $v > 0$, and from Case 3-1 into Case 2, when the start of the slippery motion is accompanied by $v = 0$

(refer to Fig. 3).

2. 4 Simulation of the cylindroid particle motion

2. 4. 1 Simulation procedure

The motion of the cylindroid particle until it leaves the scraper surface is simulated by the method illustrated in Fig. 4.

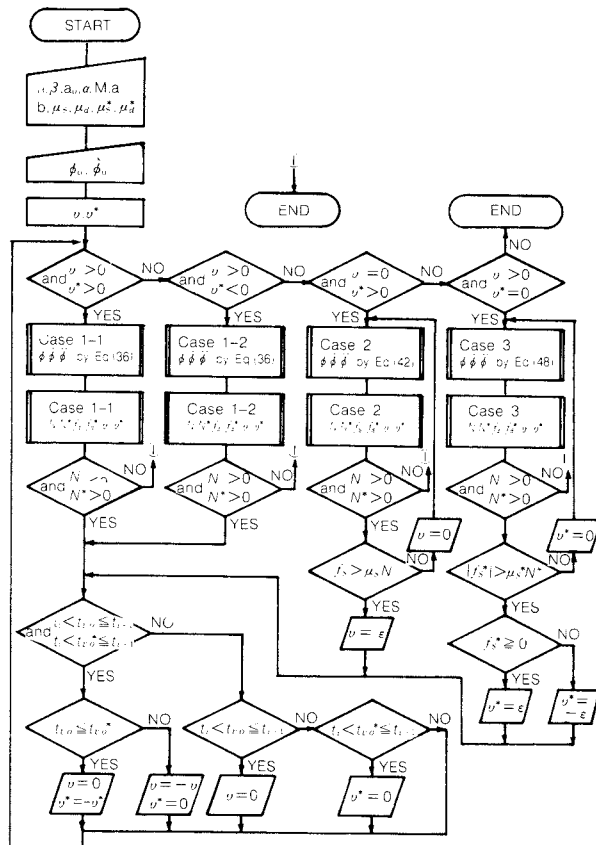


Fig. 4 Flow chart of calculation

(1) Initial conditions

It is assumed that the angle of the attitude of the particle at $t = 0$, i.e., $\phi = \phi_0$, will equal the angle of attitude, $\phi_0 = \phi'_0$, at which the particle is stationarily balanced at $\theta = 0$, immediately before it comes into contact with the scraper wall surface at Point P_0 .

In other words, the conditions under which the particle balanced on the assumption that it does not slip on the disk surface are provided by Eq. (49), which is derived from Eqs. (25) through (27) with N^* , f^* , \ddot{x} , \ddot{z} and $\ddot{\lambda}$ set at zero and with the relation of $f = -f_s$:

$$Y(\phi) = z_G (g \sin \beta + r_0 \omega^2 \cos \beta) - x_{CD} (g \cos \beta - r_0 \omega^2 \sin \beta) = 0 \quad (49)$$

where, r_0 is r (Eq. (21)) at $t = 0$.

The aforementioned ϕ'_0 is the value of ϕ sufficiently close to zero that satisfies the conditions given by Eq. (49), and is obtained by a numerical calculation (the Newtonian method).

The initial angular velocity, $\dot{\phi}_0$, on the other hand, is set to zero.

(2) The numerical analysis of basic motion equations

The form of motion at $t = 0$ may be determined from the v and v^* values, determined by substituting the operating conditions and the initial conditions ($\phi_0 = \phi'_0$, $\dot{\phi}_0 = 0$) into Eqs. (23) and (24). The basic equations for the motion forms (differential equations) are numerically analyzed by the Adams-Moulton method with increment $\Delta t = 1 \times 10^{-3}$ s, to find ϕ , $\dot{\phi}$ and $\ddot{\phi}$ at $t = t_1$ ($= 1 \times \Delta t$). These ϕ , $\dot{\phi}$ and $\ddot{\phi}$ values and the condition of $t = t_1$ will give the values of the reaction forces, N and N^* , the frictional forces, f and f^* , and the slip velocities, v and v^* . Determine the next form of the motion, by the method described below, after determining the signs of the slip velocities, v and v^* , (positive, negative or zero). Repeat the above procedure to find ϕ , $\dot{\phi}$ and $\ddot{\phi}$ at $t = t_1 + \Delta t$ to determine the next form of the motion, until the particle comes off the scraper (i.e., $N^* \leq 0$).

(3) Motion form transfer

1) Setting the slip velocity, when it changes its direction

When the direction of the slip velocity at $t = t_{i+1}$ ($= t_i + \Delta t$), determined by the motion form at $t = t_i$ ($i = 0, 1, 2, \dots$), is opposite to that at $t = t_i$, i.e., when it can be assumed that slip velocity becomes zero at $t_i < t \leq t_{i+1}$, the slip velocity at $t = t_{i+1}$ will be corrected by the method described later, and the corrected value will be used as the criterion to determine the motion form at $t = t_{i+1}$.

Assume that the slip velocities at $t = t_i$ are $v^* = v_i^*$ in the h direction and $v = v_i$ in the x direction, and that those at $t = t_{i+1}$, determined by the motion form at $t = t_i$, are $v^* = v_{i+1}^*$ and $v = v_{i+1}$, respectively.

Next, assume, for the sake of simplicity, that the v^*-t and $v-t$ relationships are represented by straight lines passing through points (t_i, v_i^*) and (t_{i+1}, v_{i+1}^*) , and (points t_i, v_i) and (t_{i+1}, v_{i+1}) , respectively. Then, the estimated time, $t = t_{v0}^*$

and $t = t_{v0}$, required for v^* and v to become zero is given by the following equations:

$$t_{v0}^* = -v_i^*(t_{i+1} - t_i)/(v_{i+1}^* - v_i^*) + t_i \quad (50)$$

$$t_{v0} = -v_i(t_{i+1} - t_i)/(v_{i+1} - v_i) + t_i \quad (51)$$

The conditions making the slip velocities zero at $t_i < t \leq t_{i+1}$ are; [Condition 1]: $t_i < t_{v0}^* \leq t_{i+1}$ on the scraper surface, and [Condition 2]: $t_i < t_{v0} \leq t_{i+1}$, based on a straight line approximation.

It can be assumed that, once the slip velocity becomes zero at $t_i < t \leq t_{i+1}$, the particle will not start to slip until the stationary frictional force on the contact face exceeds the maximum stationary frictional force. Therefore, the slip velocity at $t = t_{i+1}$ is assumed to be zero, when the slip velocity becomes zero at $t_i < t \leq t_{i+1}$. In other words, the slip velocity at $t = t_{i+1}$ is corrected to $v_{i+1}^* = 0$ when only [Condition 1] is satisfied, and to $v_{i+1} = 0$ when only [Condition 2] is satisfied.

When [Condition 1] and [Condition 2] are satisfied simultaneously, the slip velocities at $t = t_{i+1}$ are corrected in the following manner: In the test device used in this study, v^* and v cannot become zero simultaneously, because the particle is continuously forced to move in the r direction. Because of this, the slip velocity, v^* or v , is regarded as zero at $t = t_{i+1}$, which ever becomes zero faster in the time between t_i and t_{i+1} . In such as case, the other slip velocity at $t = t_{i+1}$ is corrected to a level which is the same in absolute value as the one at $t = t_{i+1}$ cited in Eq. (50) or (51), and which has the same sign (positive or negative) as the one at $t = t_i$.

2) Setting the slip velocity, when the particle starts to slip

When f_{s2} is greater than $\mu_s N_2$ in the Case 2 motion form, the particle will start to slip on the disk surface in the x direction. The slip velocity when the particle starts to slip on the disk surface in the x direction is set at $v_{i+1} = +\epsilon^*)$ ($= 1 \times 10^{-5}$ m/s).

In the Case 3 motion form, on the other hand, when $|f_{s3}^*|$ is larger than $\mu_s^* N_3^*$, the particle will start to slip on the scraper surface. Assuming that the slip velocities in the Cases 3-1 and 3-2 motion forms are opposite to each other in the direction in which slipping starts, they are set at $v_{i+1}^* = +\epsilon$ and $v_{i+1}^* = -\epsilon$, respec-

tively.

No correction of the slip velocity at $t = t_{i+1}$ is made in any cases other than the above 1) and 2), and the same motion form is assumed at $t = t_i$ and $t = t_{i+1}$. These criteria determine the slip velocities, v_{i+1}^* and v_{i+1} , and, hence, the motion form, at $t = t_{i+1}$ (refer to Fig. 4).

2. 4 2 Simulation results and discussion

The particle motion was simulated under various conditions in this study. Figure 5 presents some typical simulation results, showing the motion of the particle over time until the reaction force, N^* , is zero on the scraper surface. The particle will undergo different motion forms until it leaves the scraper at $t = t_s$ and $\theta = \theta_s$ (an amplitude determined by Eq. (2)). Simulation results have confirmed that the rotating motion of the particle in each form has the direction described in Fig. 3.

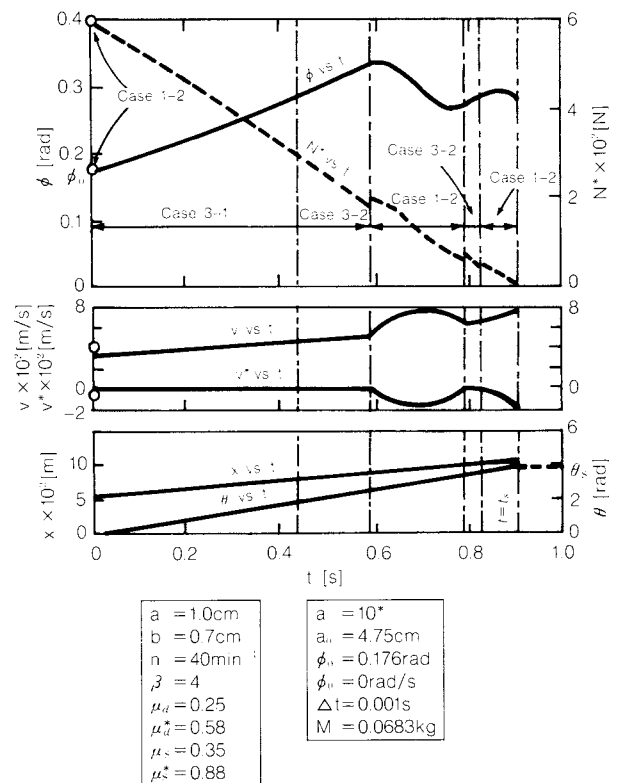


Fig. 5 Representative result of calculation. A particle leaves the scraper wall at $\theta = \theta_s$ ($N^* = 0$) undergoing various modes of motion

*) It has been confirmed that the slip velocity immediately before it becomes zero is of the order of 1×10^{-5} m/s within the range of the conditions adopted by this simulation work, serving as a basis for the slip velocity when the particle starts to slip.

Next, the relationship between the position at which the particle leaves the scraper ($\theta = \theta_s$) and the particle shape index, k ($= b/a$), is discussed, on the basis of simulated results.

Figure 6 shows the relationship between θ_s and k for the particles with the same density

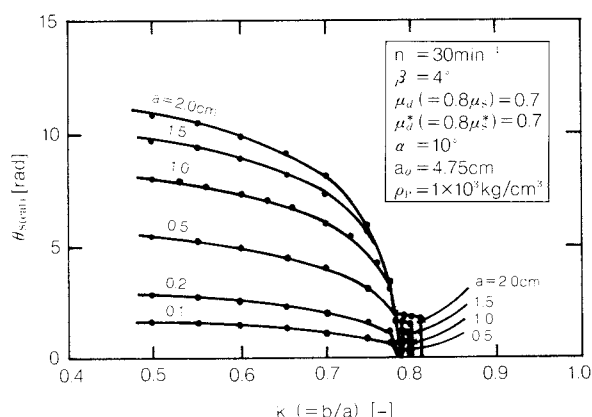


Fig. 6 Relationship between θ_s (cal) (calculated by simulation) and shape index k ($=b/a$) for various particle size a

but different sizes (a 's). The θ_s value varies with the k value for each particle size under the conditions used in the study, indicating that the particle with different k values ($: 0.5 \leq k \leq 0.8$) are possibly separated from each other along the scraper surface. Furthermore, the θ_s varies for the particles with the same shape, but different sizes (a 's). It is therefore necessary to make the size of the particles uniform before they are separated according to shape.

The simulation results have also indicated that the θ_s - k relationship is unchanged for the particles with different densities, when they are the same size.

Figure 7 gives the typical results for the effects of the inclination of the disk (angle β) on the θ_s - k relationship, indicating that the θ_s value tends to decrease as the β value increases for the particles with the same shape. It has also been observed that there are three distinctive regions with respect to the k value in the θ_s - k curve for any β level; (1) the region in which $\theta_s \approx 0$, (2) the region in which θ_s increases as k decreases, and (3) the region in which θ_s is kept at a relatively high level (e.g., $\theta_s = 14$ rad at $\beta = 6^\circ$). The separation according to the shape of the particles of differing shapes is possible in region (2) but not in regions (1) and (3). Notwithstanding separation according

to particle shape is possible among different regions.

Figure 7 also shows the motion form of the particle leaving the scraper at $t = t_s$. At $t = t_s$, the motion form is represented only by Case 2, in which the particle rolls over the disk surface, in region (1), by Case 2 for high k values and by Case 1-1 for low k values in region (2), and only by Case 1-2, where the particle slips on the disk surface while periodically changing its angel of attitude, ϕ , in region (3). This means that a particle with a sufficiently large k value (the cross-section is close to a circle) is rolling, whereas the particle with a smaller k value is slipping on the disk surface as it leaves the scraper wall. Based on these discussions, the position, θ_s , at which the particle leaves the scraper is mainly determined by its rolling or slipping characteristics (or its resistance to rolling or slipping) on the disk surface in regions (1) and (3), respectively, whereas it is determined by both characteristics in region (2). The different characteristics of these regions may distinguish them from each other in a step-by-step (or discontinuous) manner.

Viewed from the point of view of the characteristics of the device used in this study, it is safe to assume, that once the amplitude, $\theta = \theta_E$, at which the scraper intersects the outer periphery of the disk is determined, all particles of $\theta_s \geq \theta_E$ will leave the disk at $\theta_s = \theta_E$.

Figure 8 shows the typical results for the effects of rotation speed of the disk (n) on the

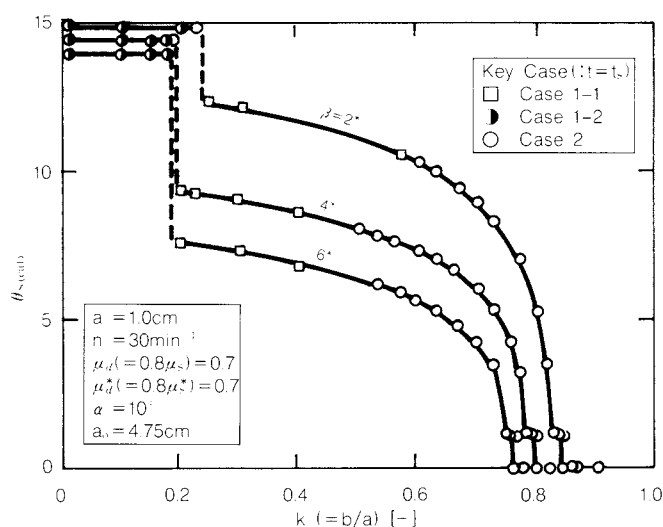


Fig. 7 Effects of inclination angle of the disk surface β on θ_s vs. k

θ_s - k relationship, indicating that θ_s decreases as n increases for the particles with the same shape within a k range of $0.4 \lesssim k \lesssim 0.9$, and the k range characterized by region (2) (refer to Fig. 7) narrows as n increases.

2. 4 3 Simulated and measured θ_s

In an attempt to assess the adequacy of the simulation results, the θ_s values were actually measured by the test device ($R = 23$ cm, $\beta = 4^\circ$, $a_0 = 4.75$ cm, and $\alpha = 10^\circ$), using cylindroid particles having various shapes and friction characteristics. Table 1 gives the measured properties of the cylindroid particles used for this study. These particles were slowly supplied to the device at point P_0 ($\theta = 0$) under the given initial conditions, so that θ_s values could be measured 10 times for each run.

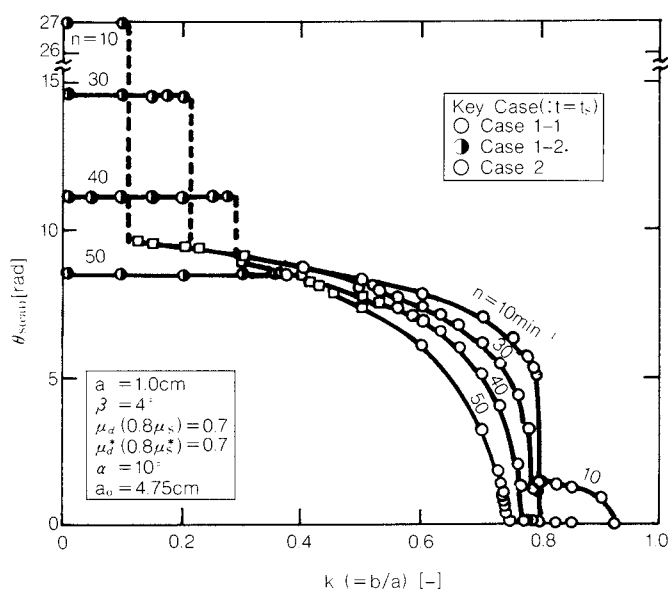


Fig. 8 Effects of rotating speed of disk n on θ_s vs. k

The simulated θ_s values matched well with the observed ones, as shown in Fig. 9. The observation of a cylindroid particle moving along the scraper revealed that (1) the direction of the y' axis almost coincided with the tangential line of the scraper wall, around which it changed periodically to some extent, and that (2) the particle was affected by a frictional force in the direction of the tangential line, resulting in that the angular speed of the particle around the disk centroid (point O) was smaller than that of the disk (ω). The observed θ_s values were, on the whole, larger than the simulated ones, as shown in Fig. 9, conceivably because of the differences between the assumptions of particle motion ((1) and (2), discussed in Section 2.1) and the above-mentioned, observed characteristics (1) and (2).

Conclusions

We investigate the basic mechanism involved in a rotating conical disk with a spiral scraper for separating particles according to shapes by considering the models of the particle motion along the scraper, simulating the particle motion on its basis.

We obtained the following conclusions from our investigations of the relationship between the cross-sectional shape, $k (=b/a)$, of the cylindroid particles and the position (amplitude), θ_s , at which each particle leaves the scraper: (1) the θ_s level tended to decrease as the k level increased (approaching a cylindrical shape) over a fairly wide k range, which suggested the possibility of separating the particles according to their shape along the scraper, and (2) the θ_s level tended to decrease as the rotation speed of the disk (n) and the inclination (β) of the

Table 1 Properties of particles used in the experiments

Particle*)	a [cm]	b [cm]	$l^{**})$ [cm]	$M \times 10^3$ [kg]	μ_s [-]	μ_d [-]	μ_s^* [-]	μ_d^* [-]
A	1.0	0.8	4.0	78.3	0.19	0.15	0.29	0.19
B	1.0	0.7	4.0	68.2	0.19	0.16	0.35	0.21
C	1.0	0.6	4.0	58.2	0.21	0.15	0.38	0.21
A'	1.0	0.8	4.0	78.3	0.35	0.25	0.88	0.58
B'	1.0	0.7	4.0	68.3	0.35	0.25	0.88	0.58
C'	1.0	0.6	4.0	58.3	0.35	0.25	0.88	0.58

*) A, B, C : Cylindroids made of iron

A', B', C' : Cylindroids made of iron, and coated with high polymer film

**) l : Longitudinal length of a cylindroid

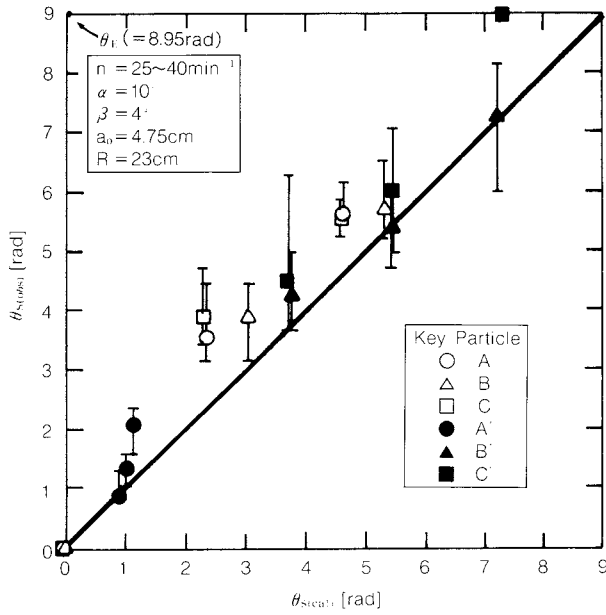


Fig. 9 Comparison of the experimental results $\theta_s(\text{obs})$ with calculated ones $\theta_s(\text{cal})$

disk surface increased, for a particle of a given shape.

The simulated θ_s values matched fairly well with the observed ones for the cylindroid particles.

The shape-separation characteristics along the scraper (the above-mentioned conclusion (1)) qualitatively coincided with the previously discussed shape-separation characteristics of the irregularly shaped particles observed along the disk's outer periphery of the same device (the collection position, θ_m , decreased as the particle shape approached a sphere)¹⁰⁾. We, therefore, conclude that the shape-separation characteristics along the disk's outer periphery are greatly affected by those along the scraper.

Nomenclature

a, b, r'_c	: radii of an ellipse at cross section of a cylindroid (see Fig. 2)	[m]
a_0	: constant of spiral curve in Eq. (1)	[m]
f, f^*	: friction force acting on a particle by disk and scraper, respectively	[N]
f_s, f_s^*	: static friction force by disk and scraper, resp.	[N]
f_d, f_d^*	: kinetic friction force by disk and scraper, resp.	[N]
g	: acceleration due to gravity	[m/s ²]
$G\text{-}x', y', z'$: fixed rectangular co-ordinate system located in a cylindroid	[m]
h, r, x, z	: co-ordinates of center of gravity	[m]

h_{EF}	: distance between point E and F (see Fig. 2)	[m]
I	: moment of inertia	[kg·m ²]
k	: shape index ($=b/a$)	[—]
l	: longitudinal length of a cylindroid	[m]
M	: mass of a cylindroid particle	[kg]
n	: rotating speed of disk	[1/min]
N, N^*	: normal reaction force by disk and scraper, resp.	[N]
$O\text{-}r, h,$: fixed rectangular co-ordinate systems located on the rotating conical disk, respectively (see Fig. 2)	[m]
$O\text{-}x, z$: located on the rotating conical disk, respectively (see Fig. 2)	[m]
p	: constant of spiral curve in Eq. (1)	[—]
r_i	: distance between scraper and center of gravity of a cylindroid	[m]
r_s	: radius vector of scraper	[m]
R	: radius of disk	[m]
S_h, S_x	: perimeter of a cylindroid calculated by Eqs. (12) and (11), resp.	[m]
t	: time	[s]
t_s	: time at which a particle leaves the scraper wall	[s]
t_{v0}, t_{v0}^*	: time at $v = 0$ and $v^* = 0$, resp.	[s]
v, v^*	: sliding velocity of a particle on the disk and scraper wall, resp.	[m/s]
x_{CD}	: distance between point C and D (see Fig. 2)	[m]
z_G	: distance between disk and center of gravity of a cylindroid	[m]
α	: constant of spiral curve in Eq. (1)	[rad]
β	: inclination angle of surface of the disk to the horizon	[rad]
δ, λ, ϕ	: counterclockwise angle from x' axis to each point of an ellipse (see Fig. 2)	[rad]
e	: set value of sliding velocity at the time when a particle slipped in simulation ($= 1 \times 10^{-5}$)	[m/s]
θ	: vectorial angle along the scraper	[rad]
θ_E	: vectorial angle at point P_3 (see Fig. 1)	[rad]
θ_m	: vectorial angle around the disk	[rad]
θ_{ms}	: θ_m at which a particle is sampled	[rad]
θ_s	: θ at which a particle leaves the scraper wall	[rad]
μ_d, μ_d^*	: coefficient of kinetic friction between particle and disk or scraper, resp.	[—]
μ_s, μ_s^*	: coefficient of static friction between particle and disk or scraper, resp.	[—]
ρ_p	: particle density	[kg/m ³]
ϕ_0	: ϕ satisfying Eq. (49) at $t = 0$	[rad]
ω	: angular velocity of the disk	[rad/s]

< Subscripts >

0 : initial

- 1, 2, 3 : Case 1, 2 and 3, resp.
i : number of iteration

References

- 1) Carpenter, F.G. and V.R. Deitz: *J. Research N.B. S.*, **47**, 139 (1951).
- 2) Sugimoto, M. and K. Yamamoto: *J. Res. Ass. of Powder Technol.*, **8**, 426 (1971).
- 3) Sugimoto, M., K. Yamamoto and J.C. Williams: *J. Chem. Eng., Japan*, **10**, 137 (1977).
- 4) Yamamoto, K. and M. Sugimoto: *J. Soc. Powder Technol., Japan*, **16**, 521 (1979).
- 5) Koga, J., S. Endoh, M. Sugimoto and K. Yamaguchi: *Kagaku Kogaku Ronbunshu*, **8**, 285 (1982).
- 6) Abe, E. and H. Hirose: *J. Chem. Eng., Japan*, **15**, 323 (1982).
- 7) Shinohara, K., T. Maenami and T. Tanaka: *Part. Sci. and Technol.*, **4**, 161 (1986).
- 8) Furuuchi, M. and K. Gotoh : *Powder Technol.*, **54**, 31 (1988).
- 9) Yamamoto, K. and M. Sugimoto: *J. Soc. Powder Technol., Japan*, **22**, 626 (1985).
- 10) Yamamoto, K. and M. Sugimoto: *ibid.*, **22**, 813 (1985).

The Dynamic Measurement of the Physical Properties of Powders Using Vibration – the Mixing Effect of a Small Amount of Fine Powder[†]

Munetake Satoh, Takashi Fujimoto,
Takashi Shigemura, Fumiaki Hamano
and Kei Miyanami

Department of Chemical Engineering
University of Osaka Prefecture*

Abstract

A vibrational tester for measuring the dynamic physical properties of powders has been developed. The tester system consists of an electromagnetic vibrator with a controller for frequency and acceleration, a solid sphere sensor attached to a load transducer, and a microcomputer.

It has been shown that the characteristic curves, when measured as the relationship between the frequency and the vertically transmitted force through the powder bed, are sensitive to changes in the physical properties of the powders. The mixing effect of a small amount of fine powder on the change in the peaks of the characteristic frequency has been measured using two different mixers.

1. Introduction

Some physical properties of powders, such as flowability and friction coefficients, are not solely the result of the physical and chemical properties of the particles themselves, but are also due to the dynamic conditions created by external forces such as gravity, vibration or electromagnetism. Vibration has been applied in practical processes (e.g., conveying, packing and distributing powders) and has also been used to study the fundamental characteristics of powder beds.

In previous work¹⁾, whose objective was to evaluate powder flowability as a function of applied vibrations, an apparatus for measuring the resistance acting on a solid sphere inserted into the powder bed and horizontally displaced while the bed is vibrated was developed and tested. The influence of the vibration frequency on the fluidization and packing characteristics of the powder bed was investigated, and, as an application, the optimum frequency to be used in vibration-aided mixers could be selected. The same paper also considered the

possibility of using this measuring apparatus to detect slight changes in the flowability of the powder by measuring simultaneously the powder's resistance to the horizontal movement of the solid sphere, and the vertical force transmitted through the vibrating bed onto the sphere. For this purpose, another load cell (for measuring the vertically transmitted force) has been included in the system. The horizontal motion of the sphere has also been improved by using a sliding plate to effect displacement.

With this new measuring system, experiments have been conducted first to obtain the relationship between the frequency of the applied vibration and the vertically transmitted force and, second, to study the effect that adding small amounts of fine powders will have on the peaks at the characteristic frequencies. For the latter, two different mixers were used and the resulting characteristic curves were compared.

2. Experimental Equipment and Method

Figure 1 is a schematic diagram of the vibratory powder tester. Basically, the tester consists of a cylindrical vessel (13) mounted on an electromagnetic vibrator (14) and a solid sphere sensor (11) suspended into the vessel by a supporting rod (12) attached to the upper part of the equipment. As described in the pre-

* 4-804, Mozu-Umemachi, Sakai, Osaka 591
TEL. 0722 (52) 1161

† This report was originally printed in *J. Soc. Powder Technology, Japan*, **25**, 609-614 (1988) in Japanese, before being translated into English with the permission of the editorial committee of the Soc. Powder Technology, Japan.

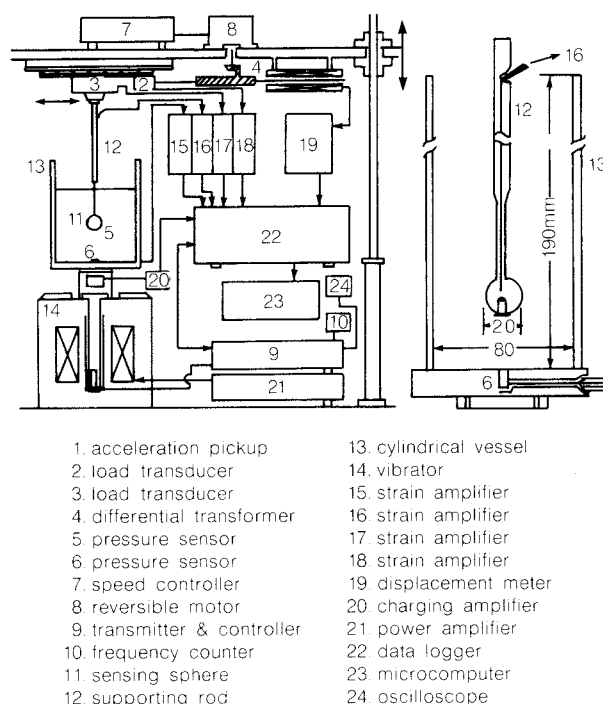


Fig. 1 Schematic diagram of the vibrational tester

vious publication, the vibrating system also includes a transmitter and controller (9), an acceleration sensor (10), and a power amplifier (21).

As the vibration frequency is varied, the acceleration is maintained at the desired value by controlling the vibration amplitude. The mechanical force exerted by the powder on the sphere is converted into DC potential by means of two load transducers placed under the sliding plate. One load transducer measures the vertical compression force and the other measures the horizontal compression force as the sphere is displaced.

In a previous evaluation of the relationship between the force and the corresponding output voltage, the measuring system was found to be able to follow up the frequency sweeping rate. By means of a variable-speed motor (8), the sphere can be moved along a distance of 0.05 m, and its displacement is measured by a differential transformer (4).

Two pressure sensors are also included in the equipment, one attached to the sphere, the other to the bottom wall of the vessel containing the sample. The sphere can be initially placed into the vessel at a depth of approximately 0.1 m. The data supplied by all the sensors is collected by a multichannel data logger

(22) (Brain IV, 12 bit, 16 ch) and processed by a microcomputer (23).

Some representative physical properties of the powders tested in this work are shown in Table 1. Before testing, the alumina powder was washed with acetone and dried.

The tested mixtures were prepared using two

Table 1 Physical properties of powders used in this work

material	symbol	average diameter [μm]	density [kg/m^3] true loose	angle of repose [deg]
Alumina	WA	130	3970 1988	37.3
Silicon carbide	SiC	130	3240 1482	37.0
Zircon sand	Zr	130	4650 2850	33.0
Toyoura sand	TS	200	2550 1590	34.1
Lactose	LA	74	1430 798	44.3
Glass bead No.02	GB	250	2690 1498	23.5
Polyvinylchloride	PVC	160	1540 494	37.0
Carnauba wax	wax	2~5	997 590	47.3
Boron Nitride	BN	2.5	2260 420	51.2

different mixers, namely, (I) a high-speed stirring mixer²⁾ (SFC-5, Kawata Ltd.) and (II) a rotary drum with simultaneous rocking motion³⁾ (RM-10G, Aichi Electric Co.). With mixer (I), three different mixtures were prepared: i) a wax with a low melting point was added to alumina and stirred until the frictional heat thus generated raised the temperature of the mixture above the wax's melting point, resulting in the adhesion of fine wax particles onto the surface of the alumina particles⁴⁾; ii) BN (boron nitride) was added to the mixture obtained in i); iii) BN was directly added to alumina. All these mixtures were prepared with an impeller agitation speed of 1500 rpm while the mixer was vibrated at 41.7 Hz.

With mixer (II), mixtures (of two components) were prepared by rotating the vessel at 63.3 rpm with a rocking speed of 10 min^{-1} (rocking angle 20°) for one hour.

Besides the measuring conditions, other factors likely to influence the vibrating state of the bed include the characteristics of the solid sphere and the vessel itself. By fixing the measurement conditions and using a reference powder for comparison, the method for evaluating the relative variation of the physical properties of different powders was tested.

The measuring conditions used in these experiments are listed in Table 2. For measure-

Table 2 Measuring conditions of the powder tester

Diameter of cylinder	0.08[m]
Height of cylinder	0.19[m]
Height of powder bed	0.08[m]
Diameter of sphere	0.02[m]
Position of sphere center	0.035[m] from the bottom center of the cross-section
Range of frequency	20 ~ 440 [Hz]
Sweeping rate	1.6 [Hz/s]
Magnitude of acceleration	1G

ments, a fixed quantity of the sample is introduced into the testing vessel, and the sensing sphere is inserted and placed at a prescribed position within the bed. Then, to fix the initial packing state for all samples, the particle bed is vibrated sinusoidally at 60 Hz and at an acceleration of 1G for 10 minutes. Once this preliminary conditioning of the bed is accomplished, the initial frequency is set, and the frequency range is swept at a fixed acceleration of 1G. At the same time, the vertically transmitted force F_V at each frequency is measured continuously.

3. Results and Discussion

3. 1 Relationship between the vertically transmitted force F_V and the frequency f

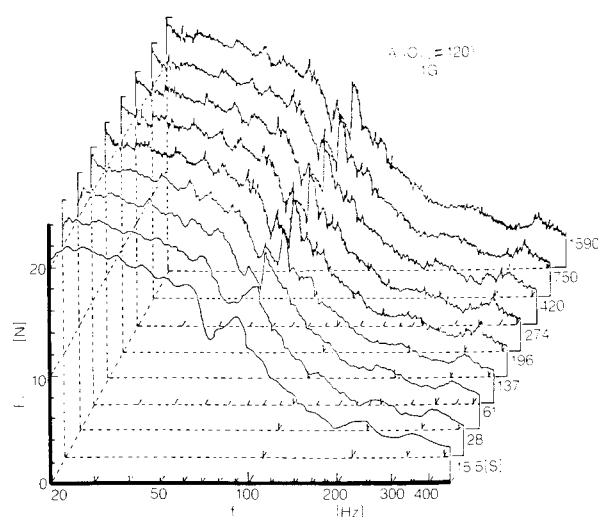


Fig. 2 Effect of the sweeping rate of frequency on the characteristics curve of vertically transmitted force, F_V

Figure 2 shows the output curves of the vertically transmitted force as a function of the frequency and the sweeping rate of the frequencies obtained for alumina at frequencies between 20 ~ 450 Hz. It can be seen that the fine details of the output curves are lost as the sweeping rate increases because it takes a finite time for the powder bed to attain a steady state when it is vibrating at a given frequency. If the sweeping rate is high before the bed reaches the steady motion corresponding to a certain frequency, the next frequency is set, and thus the response curve cannot exhibit the characteristic peaks clearly, i.e., a low resolution is attained. Mitigating the effect of these imbalanced stresses is just a matter of time. Using 397 cm³ samples, the output curves are clear and detailed for sweeping rates below 2.15 Hz/s and the basic pattern of the response curves is not affected by further decreases in the sweeping rate. The same behavior was exhibited by other powders and a sweeping rate of 1.6 Hz/s was chosen for the rest of the experiments.

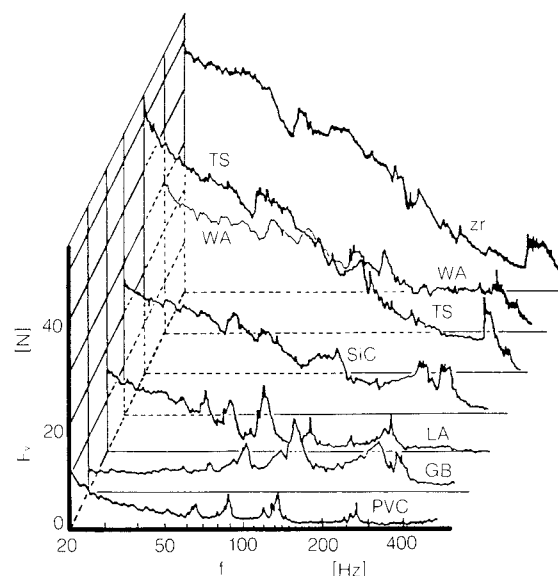


Fig. 3 Characteristics curves of F_V-f for various powder samples (constant sweeping rate and acceleration)

Figure 3 shows the $F_V - f$ curves for various powders using the same measuring conditions. Each powder has a particular characteristics curve. All the tested powders have common peaks at specific frequencies, and this can there-

fore be considered a feature of any solid particulate material under these measuring conditions, regardless of its composition or physical properties. The vibrational characteristics of the measuring system and the physical properties of the powders intermingle in a complex manner, as reflected in the value of the discrete peaks appearing at given frequencies. At this stage of the investigation, it remains impossible to explain satisfactorily why the peaks and valleys appear at specific vibration frequencies. In spite of this difficulty, it is at least possible to discuss the relative variations of the physical properties of different powder systems by comparing their vibrational characteristics curves.

3. 2 Vibrational characteristics of the powder mixtures

Figure 4 shows the influence of adding small amounts of a second component and the effect that the mixing method has on the beds' vibra-

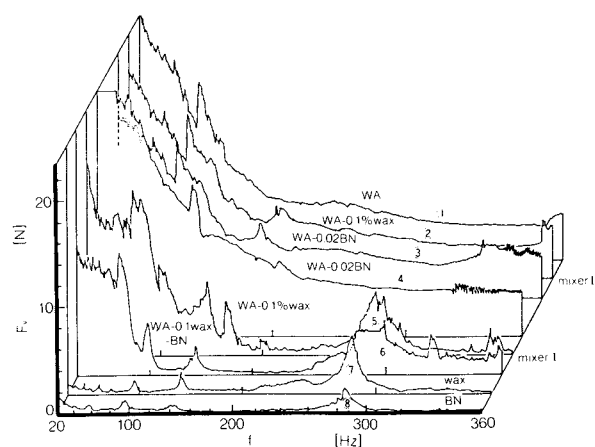


Fig. 4 Effects of additions and mixing methods on the patterns of the characteristics curve

tional characteristics. By comparing the $F_V - f$ curve of pure alumina (1) to those of its mixtures (curves 2 ~ 8), it can be seen how the addition of the second component always modifies the output curve, reflecting the adhesion of the minor constituent onto the surface of the alumina particles. The vibrational characteristics of the minor component itself also af-

fects the pattern of the mixtures characteristic curves. Both wax and BN show very low F_V values at almost every frequency, except for those where peaks appear. Therefore, the general tendency of the output curves for the mixtures alumina-wax and alumina-BN must be very similar to that of pure alumina, except at those frequencies where the minor component exhibits peaks. This figure also permits the comparison of the mixture properties as obtained using the two different mixers mentioned above.

Such comparison shows that mixtures prepared by mixer (I) (high speed mixer) have more variable patterns, especially for the alumina-wax mixture (curve 5) in which the coating effect is highly noticeable. For the mixture prepared by adding BN to the alumina-wax mixture, the vertically transmitted force F_V is smaller at every frequency than that of the alumina-wax mixture and, moreover, new peaks appear.

If only BN is added to alumina (4), the general pattern is similar to that obtained with the rotary-type mixer (discussed below); however, some of the peaks below 120 Hz are lost when using mixer (I).

For mixer (II) (rotary-type), although the addition of wax (2) and BN (3) results in variations in the curve, the basic pattern of the pure alumina curve (1) is preserved. The F_V values are globally lower than they are for pure alumina, but the peaks around 140 Hz, which correspond to the pure minor components, remain at the same value.

As mentioned above, both the addition of different components and the differences between the mixers account for the variations in the vibrational response curves.

3. 3 Influence of the concentration of additives

Figure 5 shows the $F_V - f$ curves of alumina-wax mixtures of different concentrations, prepared by the high-speed mixer. All these mixtures were obtained through 90-minutes of mixing under fixed operating conditions. The mixtures reached a temperature of 86°C and were subsequently cooled to room temperature, after which their vibrational characteristics were measured. Pure alumina was also agitated under the same operating conditions, and although the size distribution and the shape of

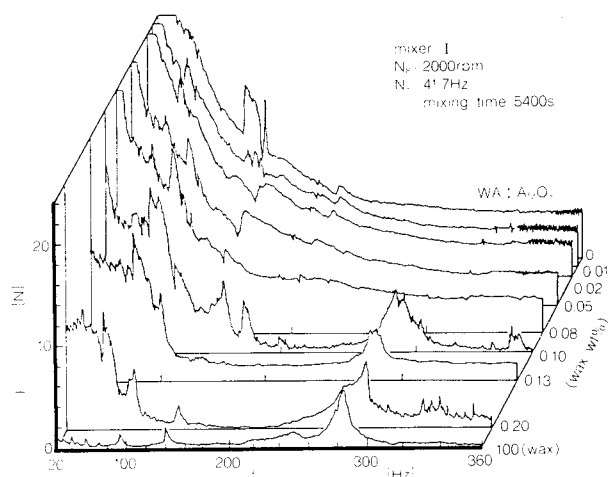


Fig. 5 Change in the patterns of the characteristics curve with wax concentration

the alumina particles before and after agitation were practically the same, the vibration characteristics suffered slight modifications (compare 1 in Fig. 4 – pure alumina before agitation, and Al_2O_3 in Fig. 5 – pure alumina after agitation). At low frequencies (below 80 Hz) F_V increased for agitated alumina, the peak at approximately 140 Hz was slightly modified, and at frequencies above 330 Hz a new phenomenon appeared – the oscillation of the F_V value. The differences observed between alumina before and after agitation are due to the modification of the particles' surface characteristics as a result of friction.

As the concentration of wax increases, the peak intensity at 140 Hz decreases; on the contrary, the peak at 60 ~ 70 Hz becomes sharper and more conspicuous. The above-mentioned oscillating phenomenon at high frequencies disappears for wax concentrations above 0.06%. For concentrations of approximately 0.10% the curve pattern clearly changes and preserves its shape through the remaining concentration ranges.

To investigate the extent to which the physical properties of alumina are modified as the wax content increases, we studied the variation in the difference between the transmitted vertical force for mixtures, F_V , and that corresponding to the reference powder (alumina), F_{V0} :

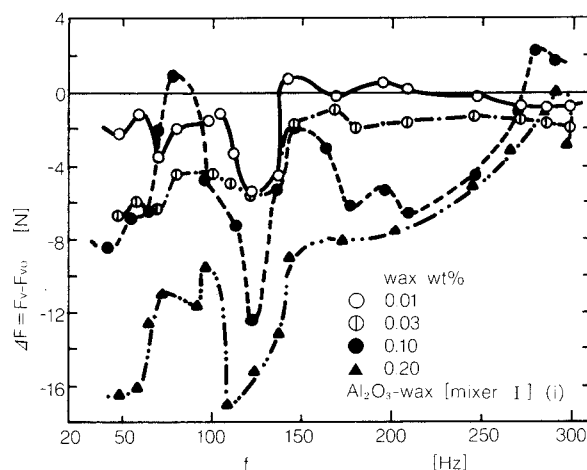


Fig. 6(i) Relationships between ΔF and f for different combinations of powder using mixer I: (i) alumina-wax

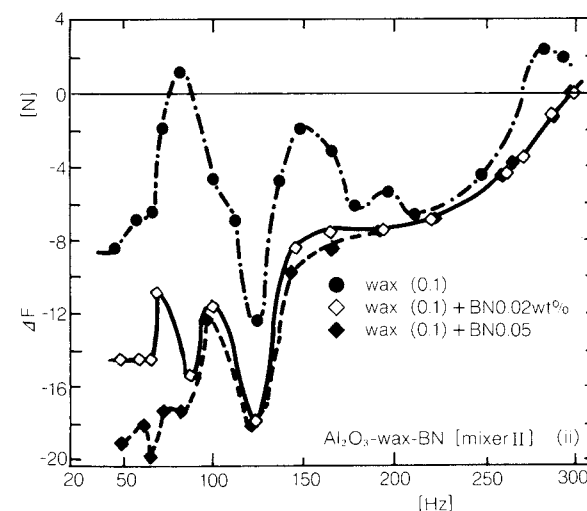


Fig. 6(ii) Relationships between ΔF and f for different combinations of powder using mixer I: (ii) alumina-wax-Boron Nitride

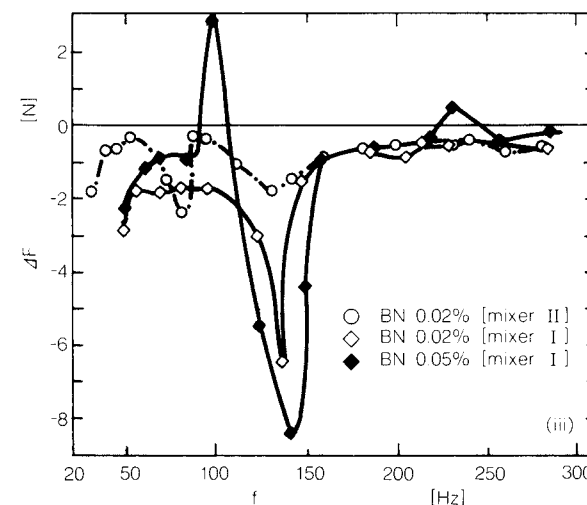


Fig. 6(iii) Relationships between ΔF and f for different combinations of powder using mixer I: (iii) alumina-Boron Nitride

$$F = F_V(f) - F_{V0}(f) \quad (1)$$

Figure 6 shows the relationship between F and f for i) alumina-wax mixtures, ii) addition of BN to 0.1% alumina-wax mixture, and iii) alumina-BN mixtures. F as a function of f varies depending on the minor component added and its concentration.

Case i) alumina-wax. As the wax concentration increases, the function $F(f)$ tends toward negative values. The value of F , however, is positive at certain frequencies, which means that the mixture's packing condition was such that the transmitted vertical force was greater than it was for pure alumina as a result of the reduced friction coefficient.

Case ii). The addition of BN to alumina-wax mixtures results in a further decrease in the value of F , especially at frequencies below 100 Hz.

Case iii). In this case, the 0.02% alumina-BN mixtures obtained by the two mixers are compared. For mixer II (rotary-type), the F_V curve of the mixture is slightly lower than for pure alumina; however, the pattern is almost the same. The patterns are clearly different when the mixture is prepared with a high-speed mixer. It is thus obvious that for a given powder system the type of mixer used exerts a strong effect on the mixing state (coating) of the resulting mixture. In other words, the state of adhesion of the BN particles onto the surface of the alumina particles depend on the shearing forces acting upon the powder.

3. 4 Influence of the mixing method on the variation ratio η

Next, we evaluated the relative variation η of the vertically transmitted force for those peaks (with large variation ΔF) as a function of the minor component concentration. The variation ratio is defined as

$$\eta = \frac{F_V}{F_{V0}} - 1 = \frac{\Delta F}{F_{V0}} \quad (2)$$

The relationship between η and wax concentration is shown in Fig. 7. The η ratio decreases as the concentration of wax increases and approaches a stable value at higher concentrations. This suggests that fine particles of wax progressively cover the surface of the alumina particles, and when the degree of coverage is high

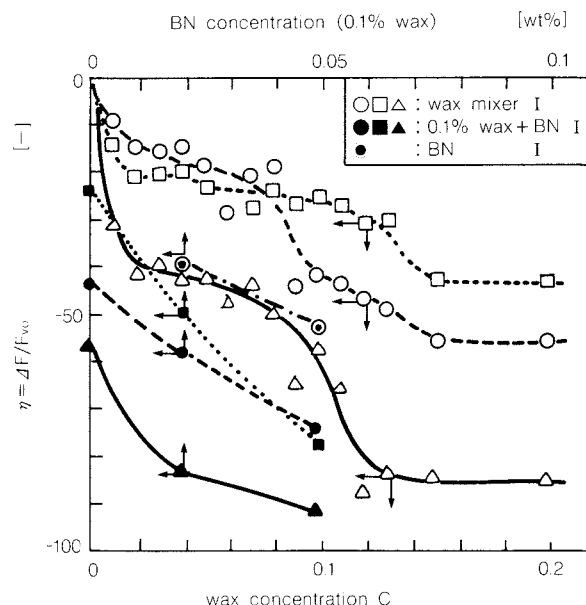


Fig. 7 Relative change of the vertically transmitted force, η , with concentration of added powder (mixer I)

enough or complete, η attains a stable value. This fact is even more clear when the variation ratio η is evaluated for the peaks appearing at 140 ~ 150 Hz, which seem to be more sensitive to variations in the physical properties of this particular powder system. For comparative purposes, the sliding friction coefficients of the alumina-wax mixtures were measured by the tilting plate method. It was found that the coefficient values were very close to each other (0.76 ± 0.03) and demonstrated no clear tendencies. When BN is added to wax-coated alumina, η also decreases with increasing concentrations of BN. Finally, when only BN is added to alumina, the tendency is similar, and the η values are close to those obtained for alumina-wax mixtures.

Figure 8 shows the effect that the type of mixer used has on the η - C relationship for alumina-BN mixtures and uses the peaks at 140 ~ 150 Hz to evaluate η . For concentrations larger than 0.004%, η decreases with increasing concentrations of BN. When mixer II (rotary-type) is used, η attains a minimum value at a BN concentration of 0.02% and then suddenly increases. Again, it is assumed that at this point the alumina surface has been completely covered by the fine BN particles. For higher concentrations, the excess fine particles do not adhere to the coarser particles, but

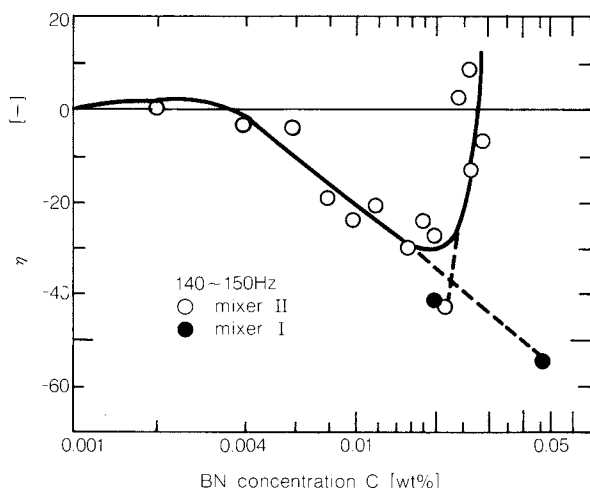


Fig. 8 Effect of the different mixing mechanisms on the coating of fine powder onto coarse particles

rather remain free, thus modifying the packing state of the powder bed. On the contrary, no minimum value for η is observed when mixer I (high-speed) is used. In this case, the shearing conditions created within the mixer permit further adhesion of the excess fine particles onto the coarser material. In fact, a sample with a concentration of 0.05% was withdrawn and studied, and it was found that there were practically no free BN particles, which means that almost all of them had adhered to alumina particles.

4. Conclusions

An apparatus was tested for detecting the force imparted by a vibrating powder bed onto a sensing sphere immersed in the bed, sweeping continuously at a certain range of vibration frequencies. The evaluation of this force for different samples permitted the detection of the relative variation of the physical properties of the powders.

The pattern of the curve that relates the vertically transmitted force to the vibration frequency depends on the type of powder and the mixing mechanism. The characteristics of the measuring apparatus itself also influence the

pattern of the output curve. It was shown that variations in the physical characteristics of the powder can be followed up by studying the peaks appearing at specific frequencies.

By comparing the vibrational response curves of the reference powder (alumina) to those of the mixtures of the reference powder and a minor component (wax and BN), it was shown that the measuring system was highly sensitive to changes in the curves' pattern, and new peaks appeared as a result of the presence of the minor component.

The method also permits the detection of differences existing in the mixing state (the coating of coarse alumina by fine particles of wax and/or BN) as a result of the type of mixer used.

This paper has reported on a comparative study on the peak intensities of a number of mixtures. The investigation is now being focused on how the characteristics curves are related to the physical properties of the powder.

Nomenclature

C	: concentration of fine powder	[wt%]
f	: frequency	[Hz]
F_V	: vertically transmitted force for the testing powder	[N]
F_{V0}	: vertical transmitted force for the reference powder	[N]
N_R	: rotary speed of vessel or impeller	[s ⁻¹]
N_V	: rocking speed of mixer	[s ⁻¹]
ΔF	: difference of the transmitted force	[N]
η	: ratio of the force defined by Eq. (2)	[-]

References

- 1) Satoh, M., S. Komura and K. Miyanami: *J. Soc. of Powder Technology, Japan*, **22**, 530 (1985).
- 2) Satoh, M., Y. Deguchi and K. Miyanami: *J. Soc. of Powder Technology, Japan*, **24**, 647 (1987).
- 3) Satoh, M., M. Marukusu, K. Miyanami, A. Naiki and S. Kondo: *J. Soc. of Powder Technology, Japan*, **25**, 139 (1988).
- 4) Satoh, M., T. Fujimoto and K. Miyanami: *J. Soc. of Powder Technology, Japan*, **24**, 462 (1987).

Current Status of the Mechanofusion Process for Producing Composite Particles[†]

Kouichi Tanno

*Department of Materials Science and Engineering,
Miyagi National College of Technology*

1. Need for Composite Particles

This article reviews the current status and future prospects of the mechanofusion process as an approach to producing composite particles. This article places special emphasis on the process used for particle formation.

Composite particles have been studied as a way to allow each component to express its inherent functions. These particles are used mainly in cosmetics, foods, and medicines, and some have already found commercial applications. However, other applications have received scant attention. In the area of characteristics of single-phase industrial materials, including structural and functional materials have been fully developed, and many researchers are interested in composite materials in which dissimilar materials are combined or joined to realize new functions or to improve characteristics of known materials^{1~6)}. Powder mixing is a common way to develop composite powders; but the process is inevitably accompanied by segregation during manufacturing, when particles of different powder characteristics are mixed. This makes it difficult to secure a uniform composition, one of the essential prerequisites for improved composite characteristics. Segregation is particularly noted in composite systems, such as metal-ceramics, where the components differ greatly in their respective powder characteristics. On the other hand, composite particles are characterized by each particle being a composite of dissimilar materials. Recently, composite particles have been studied extensively in view of their potential for realizing ordered mixtures⁹⁾ that consist of components of different particle size, shape, and density that are difficult to mix without causing segregation or to dissolve in each other

by the ordinary method. The other potential advantages are improved spraying in the nozzles improved sprayed structures, when spraying is adopted to handle them.

In addition, CVD- or PVD-based hard facing and other surface modification techniques have recently been developed to a stage where particles can be coated directly.

A variety of techniques have been studied to realize composite particles, including mechanical methods (such as mechanical blending), moving beds, and CVD- or PVD-based approaches¹⁷⁾. Of these, mechanofusion has been attracting special attention because of its potential for producing composite particles relatively easily and in large quantity^{10~16)}. Mechanofusion compresses mixed particles, and the resulting heat energy is used to coat the core particles with added particles (hereinafter referred to as "guest particles") to form the composite particles. The process has been applied mainly to metal-ceramic systems and in some cases has been developed to a commercial stage. The process by which composite particles are formed, however, is not fully understood.

The authors have demonstrated that mechanofusion works well when producing metal-ceramic composite particles. The coating layer is sufficiently dense and adheres quickly to the nucleus particles^{17~18)}. For the composite particles to be commercially viable, the coating layers must have uniform thickness, and the joining characteristics of the heterogeneous interfaces must be improved, by efficiently removing gases remaining in the void spaces in the particles that constitute the coating layers. Finally particles sinterability must be high. It is therefore essential to produce composite particles that satisfy these requirements. The authors have been working to develop such composite particles.

This article discusses the characteristics of

[†] Received June 7, 1990

* 48, Nodayama, Shiote, Medeshima, Natori, Miyagi 981-12
TEL. 022 (384) 2171

composite-forming, with special emphasis on the effects of the properties of the core particles, mechanofusion duration and rotation speed on the changes in the coating layer phases, such as these by agglomeration, condensation and solidification, and on the proposed composite particle forming process based on our results to-date. This article also gives an overview on devices that adapt to different atmospheres, including vacuums.

2. Requirements of Composite Particles

For composite particles to produce high-performance and highly reliable composite materials, they must satisfy the following requirements.

- 1) The components must be compounded at a specific ratio.
- 2) The structure of the coating layer, which significantly affects the sintering characteristics of the composite, must be accurately controlled.
- 3) There must be no void spaces in the interfaces between the core particles (guest particles) and the coating layer, and between the host particles that constitute the coating layers. These spaces contain gases that may degrade mechanical and electrical properties of the composite material.
- 4) Composite forming must be done using an apparatus that is free of impurities. This is particularly important when producing composite particles that contain metal.

In addition to the above requirements, it is necessary to keep the composite highly pure during forming. Most high-performance composite materials require high purity.

3. How Mechanofusion Works

Figure 1 illustrates the basic stages of mechanofusion. A mechanofusion apparatus consists essentially of a rotary vessel that supplies the starting powders for the composite particles, and the semi-cylindrical inner pieces and the scrapers provided in the rotary vessel. The starting powder is forced outward towards the vessel walls, and when the vessel begins to rotate, the powder remains along the walls and rotates.

Providing a sufficiently narrow gap between the inner piece and the inner wall of the rotary vessel allows the particles passing through this

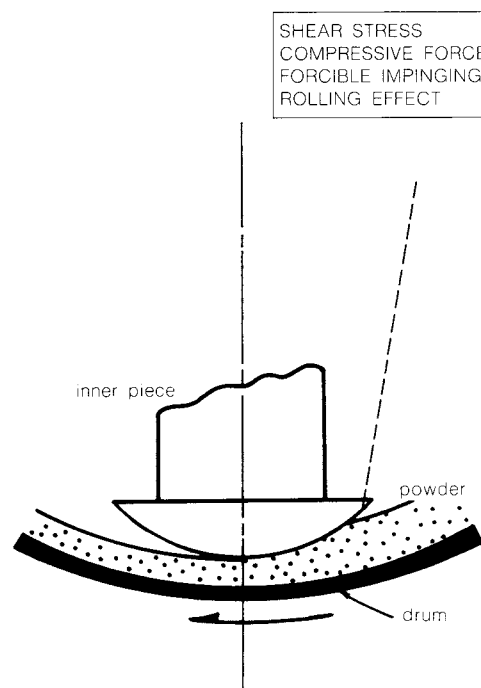


Fig. 1 Principles of mechanofusion

gap to violently collide against each other, thereby generating enough heat energy to fuse the particles together. The fused and condensed particles are coated on and adhered to the core particles by the rotary motion of the nucleus particles and by strong compressive forces acting on them. (The rotary motion is generated by friction between the particles.) This is the current explanation on how composite particles form.

The types of particles and the processing conditions used in this study are summarized below:

Core particles;

water-atomized stainless steel particles (SUS 316L)	: 3.0 μm
gas-atomized stainless steel particles (SUS 316L)	: 35.0 μm
gas-atomized Cu particles	: 35.0 μm
gas-atomized Pb-Sn particles	: 35.0 μm

Coating layer particles

(guest particles);

PSZ (containing 3 mol% of Y_2O_3)	: 0.3 μm
$\alpha\text{-Si}_3\text{N}_4$: 0.3 μm
Al_2O_3 particles	: 0.3 μm

Processing conditions;

rotating speed of the processing vessel	: 250 to 1500 r.p.m
processing time	: 5 to 300 min

4. Basic Parameters Affecting Formation of the Composite Particles

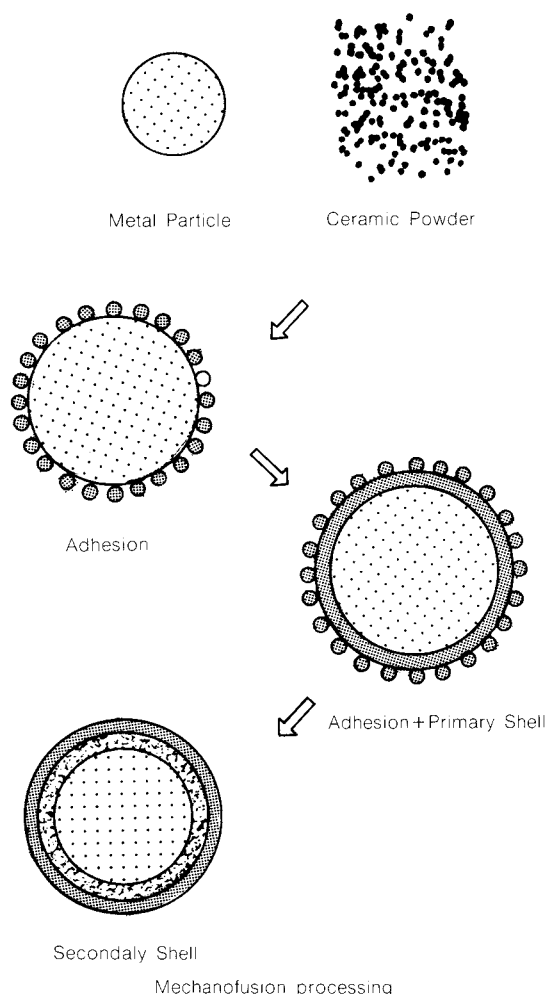


Fig. 2 Mechanofusion model

As shown in Fig. 2, mechanofusion adheres mechanically fine particles to core particles to form composite particles. This process makes it relatively easy to produce composite particles. However, the structure of the coating layers produced widely vary depending on the rotation speed of the compounding vessel, treatment time, atmosphere, and other processing conditions. This means that these conditions can be modified to produce composite particles of varying structures. The important processing parameters are summarized below.

4. 1 Effect of treatment time on composite forming

Figure 3 shows the effects of the mechanofusion treatment time on temperature at a depth of approximately 1 mm in from the inner

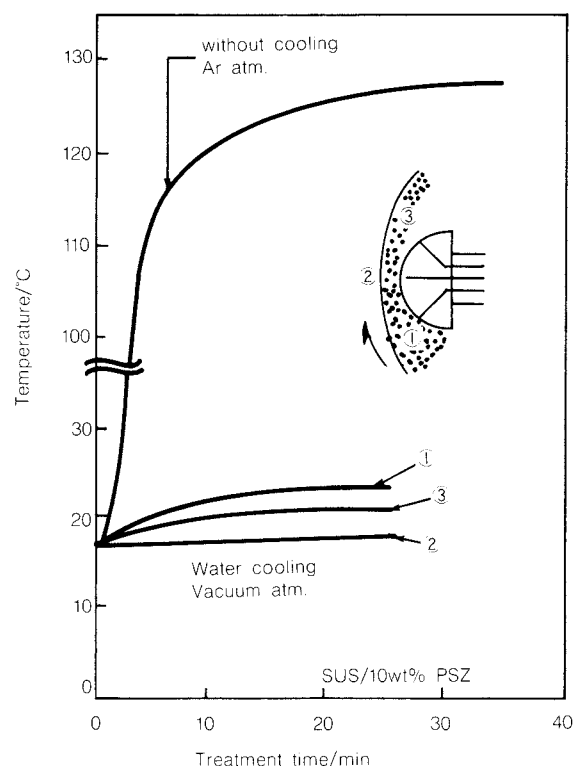


Fig. 3 Temperature change in the vicinity of the inner piece during mechanofusion

surface for cases with and without water cooling. The rotation speed was set at 16.6 Hz.

Temperature varied with rotation speed. When not water-cooled, temperature attained the highest level approximately 5 min. after the apparatus was started at the above rotation speed. The measured temperature represents a rough average, and actual local temperature on the particle surfaces was significantly higher when taking into account the effects of thermal conduction. It was observed that the core particles of Pb-Sn and Pb were fused in a short time of approximately 5 min. Indicating that local temperature was fairly high. Significant water-cooling effects were noted, because little temperature rise was observed at the measurement point in the water-cooled case.

Figure 4 presents the composite particles changing in outer appearance with treatment time. As shown, morphologies of the guest particles attached to the core particles were represented at first by irregular agglomerates. These particles then interacted gradually over the core particles, and were condensed through a sintering-like phenomenon. They finally

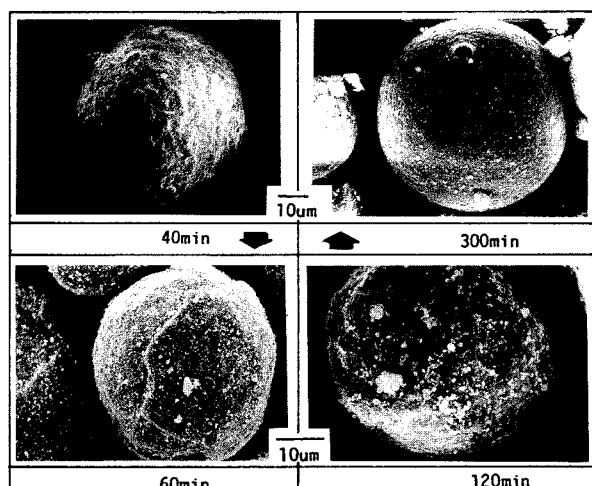


Fig. 4 Morphological changes of the composite particles with time, SUS 316L/PSZ, Rotating speed 16.6 Hz, Ar atmosphere

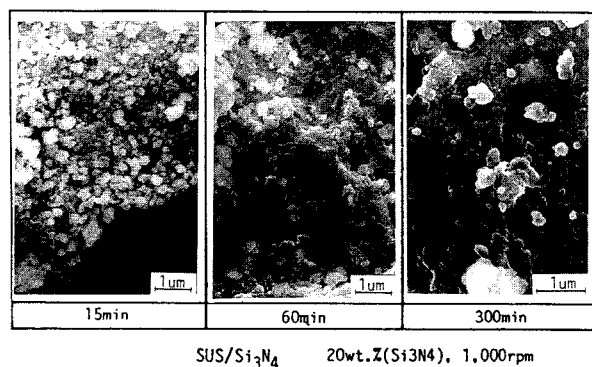


Fig. 5 Magnified SEM images of the coating layer surfaces

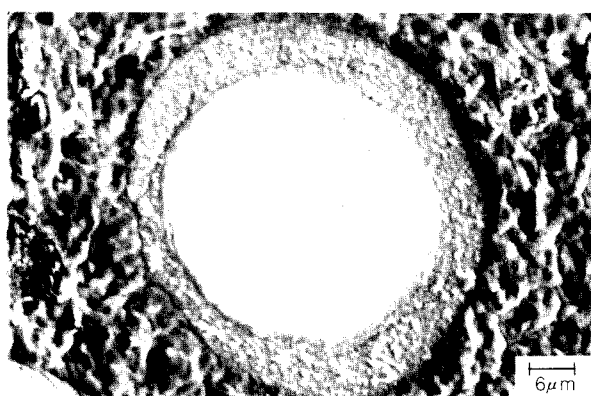


Fig. 6 Cross-sectional structures of particles constituting the condensed phase (SUS316L/PSZ)

formed the solidified coating layers covering the entire surfaces of core particles. Figure 5

presents the magnified SEM photographs of the coating layer surfaces, showing the conditions of the guest particles changing with time. Figure 6 presents the optical microscopic photographs of the composite particle cross-sections, showing that the condensed phase was partly formed in the coating layers. These results indicated that the changed phases by agglomeration, condensation, and solidification started not from the coating layer surfaces or the interfaces with the core particles, but from unspecified points within the coating layers, and from there propagated throughout the layers.

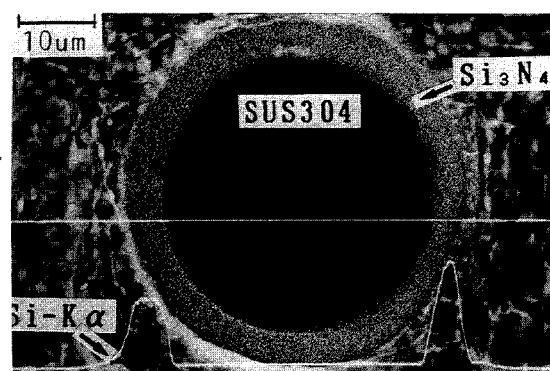


Fig. 7 Compositional analysis of composite particle cross-sections (Si-Kα analyzed line of SUS/Si₃N₄)

Figure 7 presents photographs produced by line- and surface-analysis with the aid of Si-Kα-rays for the cross-sections of the SUS/Si₃N₄-base composite particles. As shown, solid coating layers were formed in this system. X-ray diffraction analysis also indicated that the composite system became amorphous as treatment time increased.

4. 2 Effect of rotation speed on composite forming

Increasing the rotation speed increases the particles' kinetic energy producing more heat by particle-particle bombardment and compression. This naturally accelerates fusion. Figure 8 shows the morphological changes of the composite particles treated for 1.8 ks in a rotary vessel which was cooled with water to control fusion. No fusion was observed in the samples rotated at 8.3 Hz or less, and the particles remained dispersed. Irregular agglomeration was observed sporadically in the samples ro-

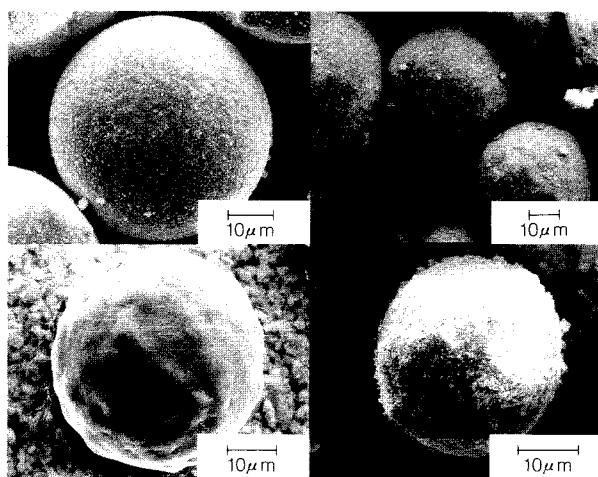


Fig. 8 Morphological changes of the composite particles under a vacuum during cooling, SUS316L/PSZ. 1.8 ks

tated at 16.6 Hz, indicating that weak agglomeration started between the guest particles at this rotation speed. However, SEM images did not clearly indicate interparticle condensation. The solidified phase was apparently formed at 26.6 Hz, though the system was cooled with water.

4. 3 Effect of the compounding ratio

Mechanofusion can potentially handle a wide range of compounding ratios, from 0 wt% to 100 wt%, though the conditions differ to some extent depending on specific gravity of the guest particles. A typical example is shown in Fig. 9. However, some guest particles were

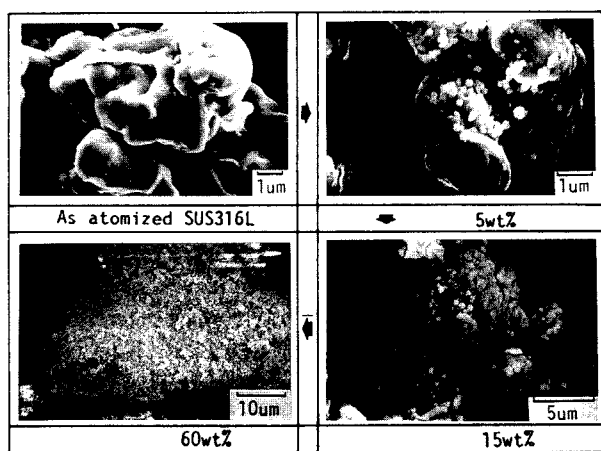


Fig. 9 Morphological changes of composite particles of different compositions, SUS316L(Water at.)/PSZ

found to be agglomerated with each other when their proportion exceeded 50 wt%. It is therefore necessary to develop compounding techniques further to handle agglomerated particles in such cases. Removing the agglomerated particles would be one approach.

4. 4 Effect of materials

Mechanofusion has been shown to work well with metal-ceramic and metal-metal composite systems, though success has not been achieved with ceramic-ceramic systems. It should be noted, however, that the coating layer conditions varied depending on the way the particles

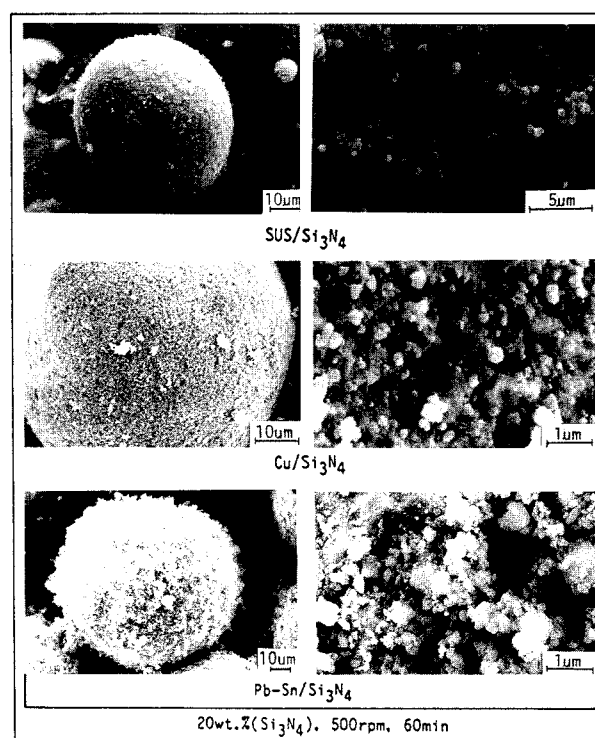


Fig. 10 Composite particles with core particles of different hardness
(a) SUS316L/Si₃N₄
(b) Cu/Si₃N₄
(c) Pb-Sn/Si₃N₄

interacted. Figure 10 shows sample results for core particles of different hardnesses (a) SUS/Si₃N₄, (b) Cu/Si₃N₄, and (c) Pb-Sn/Si₃N₄. The coating layers solidified quickly on hard core particles, but remained lightly agglomerated and did not solidify when the core particles were soft. This is suggested by Fig. 11, which shows particle cross-sections. The extent of agglomeration of the coating layer over the core particle of Pb-Sn was too weak to permit a

photograph of the particle cross-section.

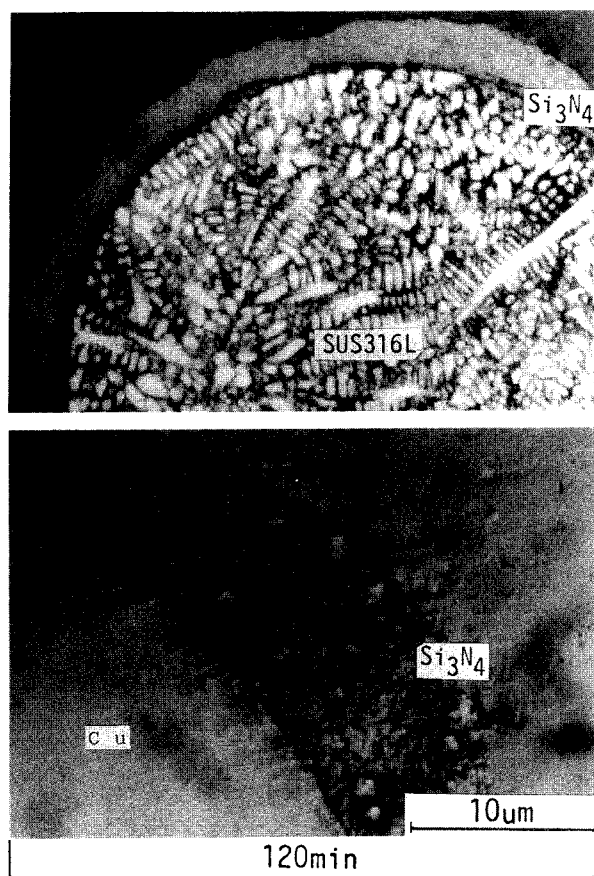


Fig. 11 Cross-sections of the composite particles shown in Fig. 10

Table 1 summarizes how composite conditions vary with treatment time using different combinations of core and guest materials for cases with and without water cooling. Coating layers varied significantly depending on the hardness of the core particles. It was also found that fusion was efficiently controlled when the vessel was cooled with water. These results in-

Table 1

	Samples	Treatment time/min						
		5	10	30	60	120	180	300
Ar gas	SUS/Si ₃ N ₄	A	C	S	S	S	S	S
	Cu/Si ₃ N ₄	A	A	C	C	C	S	S
	Pb-Sn/Si ₃ N ₄	A	A	C	C	C	C	C
	SUS/PSZ	A	C	S	S	S	S	S
	SUS/Al ₂ O ₃	A	C	C	C	C+S	C+S	C+S
Vacuum	SUS/PSZ	A	A	C	C	C	C	C+S
Water-cool	SUS/Si ₃ N ₄	A	A	C	C	C	C	C+S

A: Agglomeration C: Coagulation S: Shell structure

indicate that the coating layer of the composite particles can be greatly modified by selecting the right combination of rotation speed, treatment time, and treatment temperature.

Mechanofusion also works for producing

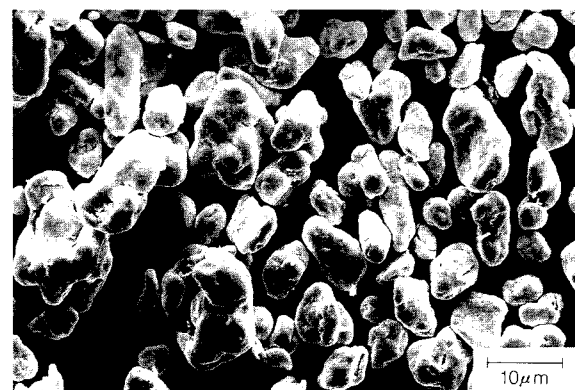


Fig. 12 Example of metal-metal (Fe/Cu) composite particles

metal-metal composite particles. Figure 12 shows an Fe/Cu composite particle as one example.

4. 5 Composite forming

Based on our current understanding, composite forming consists of the following steps:

- (1) First, a strong shear stress created in front of the inner piece acts on the agglomerated guest particles to divide them into mono-dispersed of smaller agglomerated particles.
- (2) The strong compressive and impact forces created in a narrow space between the inner piece and the rotary vessel force the guest particles to adhere to the core particle surfaces by mechanochemical reactions¹⁴⁾ at the interfaces. These reactions include the embedding of guest particles into the core particle surfaces (Fig. 13) and the resulting deformation of the core particle surfaces (Fig. 14).
- (3) The heat energy generated by the collision of particles against each other increases the temperature of the minute surfaces of the guest particles. This, coupled with the compressive force acting on the particles, causes reagglomeration of the particles. At the same time, friction between the particles causes the core particles to rotate, rolling the reagglomerated particles onto them



Fig. 13 Guest particles embedded in the core particle surfaces

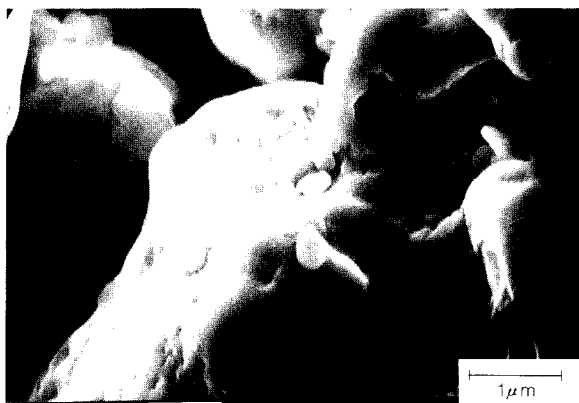


Fig. 14 Core particle surfaces deformed by the collision of guest particles



Fig. 15 Coating of the core particles using agglomerated guest particles

(Fig. 15) to form a coating layer of guest particles on each of the core particles.

(4) The guest particles are bonded to each other by sintering, and the sintering accel-

erates, spreading throughout the agglomerated guest particles through plastic deformation.

(5) The solidified layer propagates throughout the coating layer to form a shell encasing each of the core particles.

5. Mechanofusion Apparatus Working under a Vacuum

The authors have developed a new apparatus capable of satisfying the requirements described in Section 2 to produce composite particles suited for the development of new materials. This apparatus is characterized by its ability to adapt to different processing atmospheres,

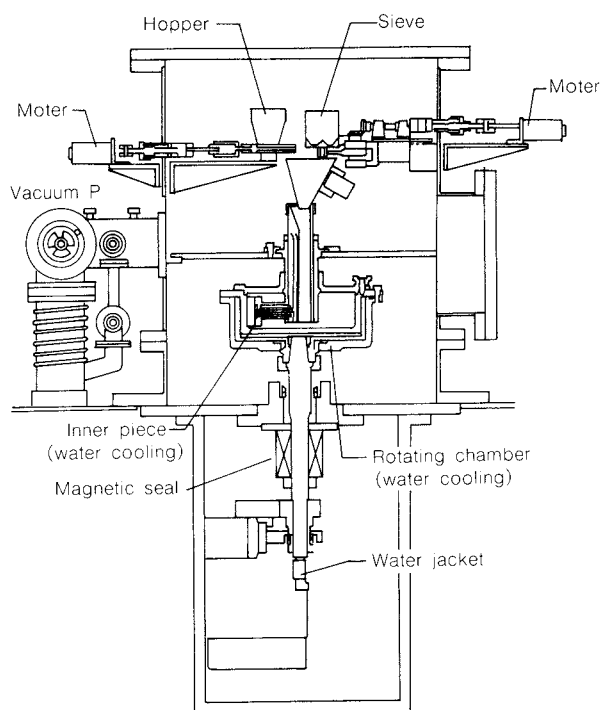


Fig. 16 Cutaway view of a mechanofusion apparatus that works under a variety of processing atmospheres

including vacuums. Figure 16 shows the apparatus.

The main mechanofusion devices for forming composite particles such as the rotating chamber and the powder feeder, are encased in a sealed vessel. The processing atmosphere — whether a vacuum, inert gas, or reducing gas — can be selected at will. The powder supply rate can be also freely controlled for both the core and guest particles.

Figure 17 shows the change in the pressure

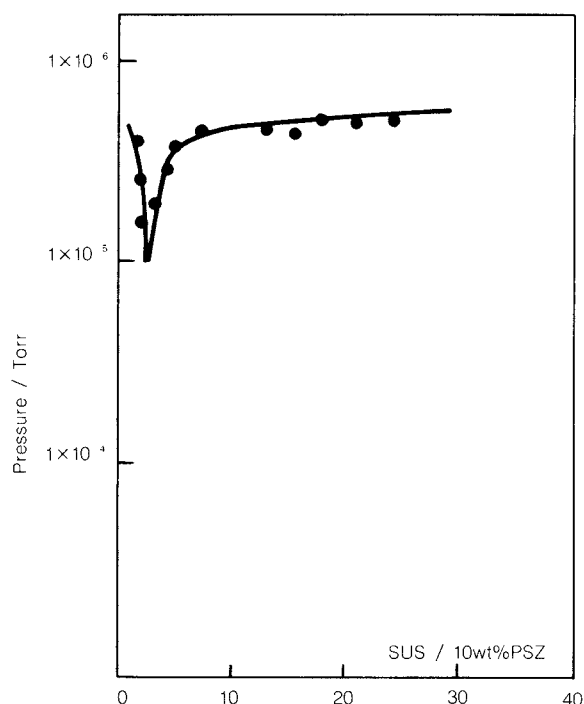


Fig. 17 Desorption of the absorbed gases during mechanofusion

of the sealed vessel with time, where the vessel containing the mixed powders was evacuated to 5×10^{-5} Torr to remove the residual gases between the particles. Mechanofusion was then started. The vacuum became sharply lower immediately after the treatment started because of desorption of the gases adsorbed on the particle surfaces. The newly developed apparatus allows you to remove the gases remaining in the interfaces between the nucleus particle and coating layer and between the guest particles that constitute the coating layer. When used in a vacuum, it also allows you to remove gases adsorbed on the particles that are desorbed as mechanofusion proceeds. Furthermore, if the atmosphere is switched to a reducing gas, the apparatus forms composite particles by compounding the nucleus and guest particles while keeping intact the new surfaces formed on the particle surfaces. Other processing atmospheres can be used as needed.

Operating under a vacuum greatly reduces the turbulence of the processing atmosphere by changing the gas flow within the processing vessel from one governed by viscous flow to a flow that is nearly molecular.

This makes it relatively easy to coat the core particles with guest particles. Figure 18 gives

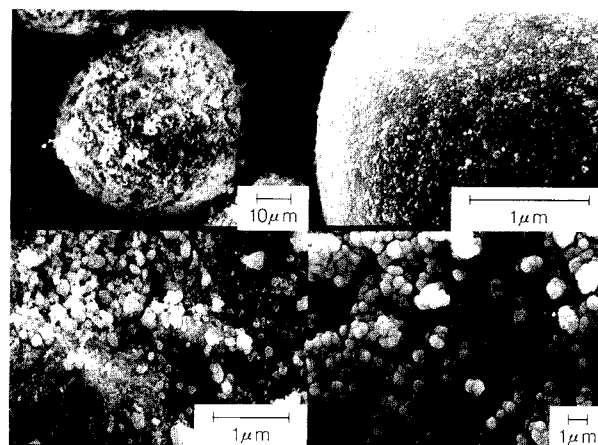


Fig. 18 Morphologies of composite particles not water-cooled in an Ar atmosphere versus those that have been water-cooled under a vacuum

SEM images of composite particles surfaces prepared in varying processing atmospheres. As can be seen from the results, the newly developed apparatus produces very pure, adhesive composite particles and will be useful for producing new materials.

The authors are now assessing sintering properties. Our results will be presented separately.

References

- 1) Katsumura, Mitsuda, Kobori and Suzuki: *Powder and Powder Metallurgy, (Japan)*, **36**, 1, 65 (1989).
- 2) Koiwa and Takada: *J. of the Japan Institute of Metals*, **27**, 7, 5253 (1988).
- 3) Ishida: *ibid.*, **25**, 5, 413 (1986).
- 4) Okamoto and Suganuma: *ibid.*, **25**, 5, 416 (1986).
- 5) Suga: *ibid.*, **25**, 5, 419 (1986).
- 6) Yamada and Kohno: *ibid.*, **25**, 5, 424 (1986).
- 7) Shinno: *New Ceramics (Japan)*, **5**, 51 (1989).
- 8) Niihara, Nakahira and Suganuma: *ibid.*, 51 (1989).
- 9) A. Hersey: *Powder Technol.*, **11**, 41 (1975).
- 10) Abe, Hirose and Kikuchi: *J. of the Society of Powder Technology, Japan*, **22**, 5, 10 (1985).
- 11) J. E. Gline and J. Wulff: *J. of the Electrochemical Society*, Oct., 385 (1951).
- 12) Horio *et al.*: *Proc. Japanese Symp., Plasma Chem.*, **1**, 213 (1988).
- 13) Tokoyama, T. and K. Urayama *et al.*: *Kona*, **1**, 53 (1983).
- 14) Koishi, M: *J. of the Society of Powder Technology, Japan*, **20**, 772 (1983).
- 15) Nomiyama, Sakakibara, Ozaki and Katahata:

- Powder and Industry, Japan*, **21**, 9, 88 (1989).
- 16) Murata: *ibid.*, **21**, 9, 93 (1989).
- 17) Tanno, K., T. Yokoyama and K. Urayama: *J. of the Society of Powder Technology, Japan*, **27**, 153 (1990).
- 18) Tanno, K., K. Urayama, T. Yokoyama and R. Watanabe: CIMTEC World Proceedings, (1990), Elsevier Applied Science, in print.

Fundamentals of Aerosol Filtration[†]

Hitoshi Emi

Department of Chemistry and Chemical Engineering,
Kanazawa University*

1. Introduction

Collection of dust by filtering air using cloth or filter paper is a very simple operation and has been used for a long period of time. It dates back to the ancient Roman era, when miners applied this concept to their masks. It is only recently, however, that filtration has become a branch of engineering; it started in the early 1920's after World War I, and the basis of aerosol filtration was founded by Langmuir in the 1940's¹⁾.

Air filtration is characterized by a wide selection of collection performance, i.e., filter media are available in a variety of shapes and sizes with specific properties depending on the particles to be removed. However, unlike electrostatic precipitator, filtration requires special attention on the pressure drop across filter medium and filter clogging, which inevita-

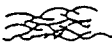
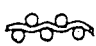


bly occurs when the filter is in service for a long time.

This article reports on the current research status of filtration technology. Not only fiber-packed beds but also granular beds which have been attracting much attention recently as a high-temperature dust collector, are reviewed with emphasis on their filtration mechanisms and efficiency.

2. Filter Structures and Filtration Mechanisms

Table 1 compares structures, characteristics and usage of various filter media, which are used in industrial process or for environmental protection purposes. Among them, air and bag filters are in high demand. The former is used for purifying air in a closed space, while the latter is widely used in industrial processes and to clean-up waste gases. Moving-bed filters and membrane filters, on the other hand, are used

Table 1 Structures of various filters

Filter	Structure	Void fraction	Thickness	Filter medium shape	Usage/purpose
Fiber bed		> 95%	0.5 ~ 50 mm	Fiber	Air filtration Clean room
Woven fabric		70 ~ 95%	1 ~ 5 mm	Fiber/yarn	Filtration in industrial processes High-concentration dust
Granular bed		35 ~ 50%	5 ~ 200 mm	Granule	High-temperature exhaust gas Moving bed
Membrane		5 ~ 90%	5 ~ 200 μm	Fiber/ porous media	High-pressure process gases Sampling

under extreme conditions, such as high temperatures and/or high pressure.

Common filter media, as shown in Table 1, include packed fibers, granular beds, cloths such as woven fabrics and felt, wire screens,

* 40-20, Kodatsuno 2-chome, Kanazawa 920
TEL. 0762-61-2101

† Received September 20, 1990

This review was originally printed in *Journal of Aerosol Research, Japan*, 4, 246-255 in Japanese, before being translated into English with the permission of the editorial committee of Japan Association of Aerosol Science and Technology.

and porous metals or ceramics. Filtration types are classified into two general categories; surface filtration in which particles are captured on a filter surface and depth filtration in which particles are collected in a filter. Typical media with surface filtration mechanisms are bag filters and those with the latter are packed beds of fibers and granules.

In surface filtration, inflowing particles are captured by interception or sieving effects, as illustrated in Fig. 1. The filtration efficiency by these mechanisms is very close to 100%. In

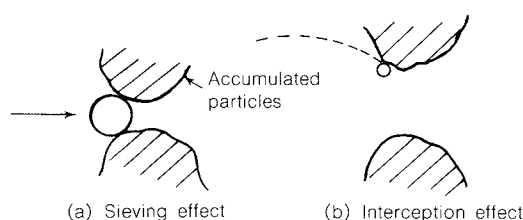


Fig. 1 Sieving and interception effects

depth filtration, on the other hand, the particle concentration decreases exponentially with bed thickness, as illustrated in Fig. 2. The material balance for the incremental thickness Δx is given by the following equation (see Fig. 2):

$$uAC - uA[C + (dC/dx)\Delta x] = S_c \eta_c u_0 CA \Delta x \quad (1)$$

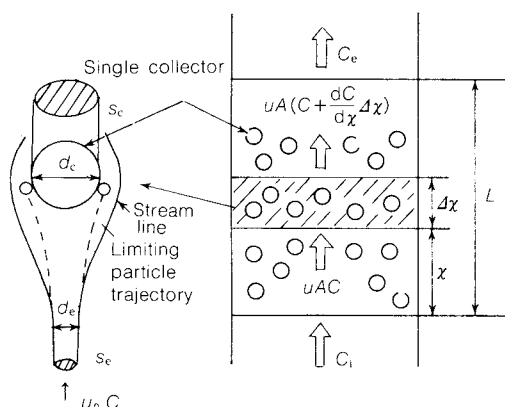


Fig. 2 Change of aerosol concentration in a packed bed and collection efficiency of single collector

Integrating Eq. (1) with $C = C_i$ at $x = 0$, and $C = C_e$ at $x = L$, yields:

$$\ln(C_e/C_i) = -S_c L \eta_c / (1 - \alpha) \quad (2)$$

where, u is the superficial velocity (m/s), u_0

the interstitial velocity [$u = u_0 (1 - \alpha)$], α the packing fraction (—), A the cross-section of the packed bed (m^2), S_c the sum of the projection areas of the single collector in a unit volume of the packed bed toward the flow direction (m^2/m^3):

$$S_c = \begin{cases} 4\alpha/\pi d_c & \text{for fibrous packed beds} \\ 3\alpha/2d_c & \text{for granular beds} \end{cases} \quad (3)$$

and η_c is the efficiency of a single collector, which is defined by:

$$\eta_c = S_e/S_c = \begin{cases} (d_e/d_c)^2 & \text{sphere, disc} \\ d_e/d_c & \text{cylinder, ribbon} \end{cases} \quad (4)$$

when all the particles flowing upstream into the cross-section S_e are completely swept away by the collector, as illustrated in Fig. 2.

For a given flow field around a collector, when inertial force and an external force (gravity, electrostatic force and so on) are the collection mechanisms, η_c can be obtained from limiting trajectory of particles which is calculated by integrating equation of particle motion, whereas for the particles in small size range ($d_p < 0.5 \mu m$) characterized by Brownian motion²⁾, η_c is obtained by solving the convective diffusional equation. η_c is generally a function of the dimensionless parameters listed in Table 2. These parameters, which appear as the coefficients in the dimensionless equation of motion and diffusional equation, are determined by the filtration conditions. An increase in these parameters leads to an increase in η_c .

3. Fibrous Packed Bed Filter

Fibrous filters have been used mainly to purify air closed spaces, e.g., living or working

Table 2 Dimensionless parameters governing collection efficiency of single collector

Name	Dimensionless numbers	Physical implication
Reynolds number	$Re = \rho u_0 d_c / \mu$	Fluid inertial force/viscous force
Packing fraction	α	Packing volume/bed volume
Stokes number	$St = C_c \rho_p d_p^2 u_0 / (9 \mu d_c)$	Inertial force/viscous resistance
Diffusional parameter (Reciprocal of Peclet number)	$D = D_B / (u_0 d_c) = 1/Pe$	Diffused quantity/convective quantity
Gravitational parameter	$G = C_c \rho_p d_p^2 g / (18 \mu u_0)$	Gravitation/viscous resistance
Electrostatic parameter	$K_E = F_E / (3 \pi \mu d_p u_0)$	Electrostatic force/viscous drag
Interceptional parameter	$R = d_p / d_c$	Particle size/collector size

ρ : fluid density (kg/m^3), ρ_p : particle density (kg/m^3), μ : fluid viscosity ($Pa \cdot s$), u_0 : interstitial velocity (m/s), d_c : collector size (m), d_p : particle size (m), F_E : electrostatic force (N), D_B : Brownian diffusivity ($C_c kT / 3 \pi \mu d_p$), (m^2/s) C_c : Cunningham slip correction factor (—), k : Boltzmann constant (J/K), T : temperature (K)

spaces. They have also been used to produce highly purified air in clean rooms, and to completely remove traces of radioactive aerosols in nuclear facilities.

3. 1 Estimation of single fiber collection efficiency

The filter media of air filters are mostly glass fibers. The void fraction of fibrous filters is much higher (above 95%) than that for granular beds (discussed later), and the average inter-

fiber distance is at least 8 times the fiber radius (at a void fraction of 95%). This configuration allows particles to flow deep into the packed bed, where they collide on the fiber surface under the influence of various forces, such as inertia, Brownian diffusion, interception and gravitation. Several researchers have proposed theoretical and empirical correlations to estimate the single-fiber collection efficiency for each filtration mechanism³⁾, Table 3 summarizes the most reliable correlations for the

Table 3 Correlations for single fiber collection efficiency

Collection mechanisms	Single fiber collection efficiency	Researchers	Remarks
Diffusion	$\eta_D = 2.9 h_K^{-1/3} Pe^{-2/3} + 0.624 Pe^{-1}$ $\eta_D = 2.7 Pe^{-2/3}$	Stechkina ²²⁾ Kirsch-Fuchs ²³⁾	Regular array, Theoretical Random and uniform packing Semi-empirical correlation
Diffusion and interception	$\eta_{DR} = \eta_D + \eta_R + f(Pe, R)$ $\eta_D = \begin{cases} 2.9 h_K'^{-1/3} Pe^{-2/3} + 0.624 Pe^{-1} \\ 2.7 Pe^{-2/3} \end{cases}$ $\eta_R = 1/2 h_K' [2(1+R)\ln(1+R) - (1+R) + 1/(1+R)]$ $f(Pe, R) = 1.24 h_K'^{-1/3} Pe^{-1/2} R^{2/3}$	Kirsch-Fuchs ²³⁾	Correlation of numerical results
Gravity	$\eta_G = G/\sqrt{1+G^2}$ $\eta_G = G/(1+G)$	Yoshioka <i>et al.</i> ²⁴⁾	Horizontal flow Downward flow
Inertia	$\eta_I = St^3/(St^3 + 1.54 St^2 + 1.76)$	Landahl-Hermann ²⁵⁾	$Re = 10$
Inertia and interception	$\eta_{IR} = (2 h_K')^{-2} I \cdot St + \eta_R$ $I = (29.6 - 28 \alpha^{0.62}) R^2 - 27.5 R^{2.8}$	Stechkina ²⁶⁾	$St \ll 1, Re < 1$

$$h_K = -1/2 \ln \alpha + \alpha - \alpha^2/4 - 3/4, \quad h_K' = -1/2 \ln \alpha - 0.5$$

single fiber efficiency.

Each correlation listed in Table 3 is a function of the dimensionless parameters in Table 2. Among the aerosol properties (ρ_p , d_p , ρ , and μ), filter properties (d_f and α) and operating conditions (u_0 and T) which determine these dimensionless parameters, the essential ones are the particle size d_p , filtration velocity u (or interstitial velocity u_0), fiber size d_f and filter packing fraction α . In particular, it is very important to assess the influence of d_p and u on η_c . The authors have drawn the η_c contours on the u_0 - d_p coordinates as shown in Fig. 3. These diagrams, drawn for a given combination of d_f and α , are practically very useful in estimating η_c for various operating conditions⁵⁾.

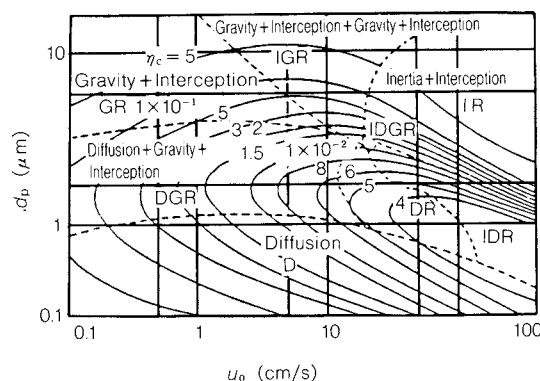


Fig. 3 The regions governed by individual collection mechanisms and contours of single fiber collection efficiency

3. 2 Relationship between filtration mechanisms and minimum collection efficiency

Figure 3 illustrates the regions governed by each filtration mechanism in d_p - u_0 coordinate system. This figure indicates that minimum efficiency exists at a certain d_p for a given u_0 , or vice versa. Figure 4 shows the experimental single fiber efficiency with the minimum effi-

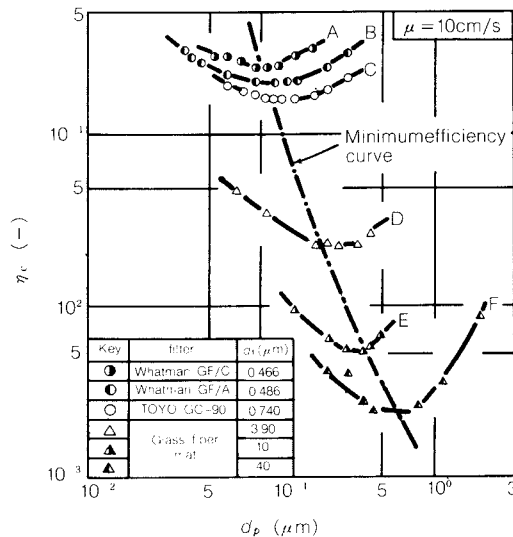


Fig. 4 Experimental single fiber collection efficiency of air filters with different sized fibers

ciency⁵⁾. These results are obtained for fibrous filters with the fiber size d_f ranging from 0.5 to 40 μm . The efficiency decreases as the fiber size increases. Each efficiency curve is concave against d_p -axis and the particle size $d_{p,\min}$ with the minimum efficiency increases as the fiber size d_f increases. This is because an increase in fiber size brings a smaller decrease in diffusion efficiency η_D than that in interception efficiency η_R . The efficiency curves A, B and C in Fig. 4 are those of HEPA or ULPA filters. Curve D corresponds to medium-performance filters, and curves E and F to filters for coarse particles.

The $d_{p,\min}$ also depends on the filtration velocity u ; the most penetrating particle size, $d_{p,\min}$ decreases as the filtration velocity u increases, for the same reason, as illustrated in Fig. 5, which plots the particle penetration P of a HEPA filter against the particle size.

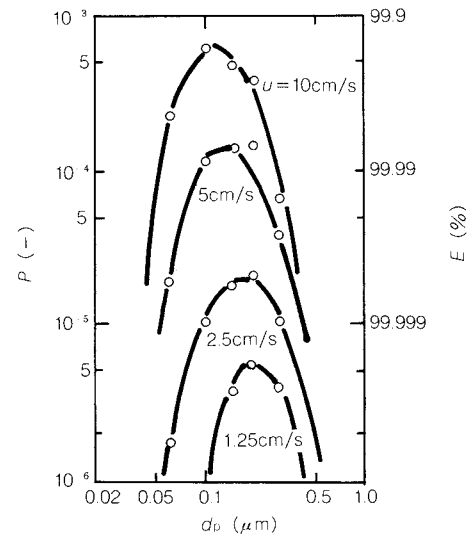


Fig. 5 Dependence of particle penetration of an ultra high performance filter on the filtration velocity (d_f : 0.76 μm , L : 0.395 mm, α : 0.075)

3. 3 Adhesion and bounce-off of particles

The aerosol filtration theory by inertia, diffusion and interception is based on the assumption that all the particles colliding with the fibers are retained on the fiber surface. This assumption, though almost valid for fine particles of several μm or less, is not valid for larger

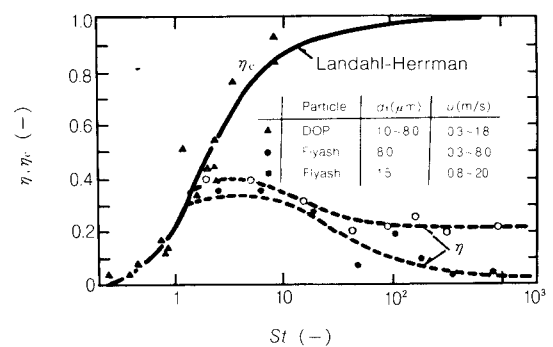


Fig. 6 Bounce-off of fly ash particles from stainless steel fiber surfaces

solid particles because probability of particle bounce-off increases with particle size. Figure 6 presents the experimental results of the particle bounce-off on the fiber surface⁶⁾, where the number, showing how the filtration efficiency

of fly ash (solid particles) and DOP (liquid particles) on stainless steel fibers of $8\ \mu\text{m}$ changes with particle size d_p and filtration velocity u . The DOP mists which do not bounce-off on the fiber surfaces, the collection efficiency are well represented by the theoretical correlation for inertial efficiency (refer to Table 3). For the fly ash particles, however, the observed efficiency deviates from the theoretical correlation at a large particle size or high filtration velocity (at a large Stokes number), and filtration efficiency η decreases with the Stokes number in large Stokes number region. In general, the filtration efficiency η is represented by the product of the impaction efficiency η_c and adhesion efficiency η_a , i.e., $\eta = \eta_c \cdot \eta_a$, and $\eta = \eta_c$ when $\eta_a = 1$. Referring to Fig. 6, $\eta_a = 1$ or $\eta = \eta_c$ for the DOP mists, whereas $\eta_a = \eta/\eta_c < 1$ for the fly ash particles.

The major forces responsible for the adhesion of fine particles on the walls are van der Waals, electrostatic and capillary forces. In systems which are not electrically charged and free of capillary van der Waals force (intermolecular force) is a dominant adhesion force. The theoretical report by Löffler *et al.*⁷⁾ studied the critical velocity of the particles at which they start bouncing off fiber surface, from the energy balances during the collision. Table 4 compares the critical bounce-off velocity estimated by Löffler *et al.* with the experimental velocity $v = u_c$ at $\eta_a = 0.5$ which are determined by plotting η_a against kinetic energy of particle $E_K = (1/2)(\pi d_p^3 \rho_p / 6)v^2$ for the data by Löffler *et al.* and other researchers²⁾. This table indicates that $1\text{-}\mu\text{m}$ particle bounce-off does not occur unless the flow velocity exceeds several m/s, although there is some uncertainty in both the experiment and the estimation.

Table 4 Estimated and observed bounce-off velocity (u_c)

$d_p\ (\mu\text{m})$	$u_c\ (\text{cm/s})$	
	Estimated	Observed
1	20 ~ 200	200 ~ 900
5	4 ~ 40	20 ~ 80
10	2 ~ 20	6 ~ 30

4. Electrostatic Air Filters

When particles and/or fibers are e

charged, electrostatic force is exerted between them. These electrostatic forces improve the filtration efficiency so much that it cannot be achieved by the previously mentioned mechanical mechanisms alone. These filters, which are referred to as electrostatic air filters, fall into two general categories; electrically charged and dielectric filters, depending on whether the filter medium is electrically charged or not. Table 5 outlines the five representative types of electrostatic air filters. Also shown in Table 5 are the correlations between the single fiber efficiency and the dimensionless electrostatic parameters.

Electret filters, which consist of permanently polarized fibers in particular, have been attracting much attention recently. The charged fibers are prepared by splitting an electret of polypropylene films into fibers or by making polypropylene fibers into an electret. The electret fibers made by the former method is characterized by a rectangular cross-section with a high charge density, but it is difficult to make fine fibers of $10\ \mu\text{m}$ or less. The latter

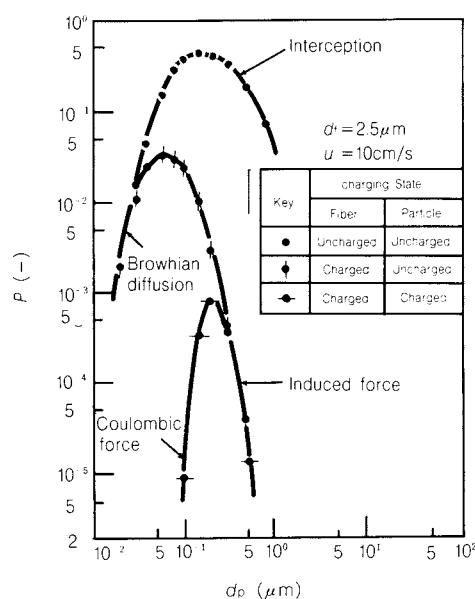
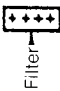


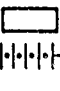


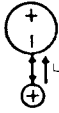


Fig. 7 Particle penetration of electret filters and uncharged filters

method can produce fibers with diameter of about $1\ \mu\text{m}$, but the charge density is not as high as that of the former method.

Figure 7 compares the penetrations of the same filter before and after the treatment to

Table 5 Types of electrostatic air filters and correlations for single fiber collection efficiency

Name	Filter type	Charging state		Electrostatic force	Dimensionless parameters	Correlations for single fiber efficiency	Researchers
		Particle	Fiber				
Charged filters		Uncharged	Charged	Induced force 	$K_I = \frac{\epsilon_p - 1}{\epsilon_p + 2} \frac{C_c Q^2 d_p^2}{3\pi^2 \epsilon_0 \mu d_f^3 u_0}$	$0.54 h_K^{0.60} K_I^{0.40} ; 1 < K_I < 100$	Brown ²⁷⁾ (Electret)
		Charged	Charged	Coulombic force 	$K_C = \frac{C_c q Q}{3\pi^2 \epsilon_0 \mu d_p d_f u_0}$	$0.59 h_K^{-0.17} K_C^{0.83} ; 0.1 < K_C < 10$	
Dielectric filters		Charged	Uncharged	Image force 	$K_M = \frac{\epsilon_f - 1}{\epsilon_f + 1} \frac{C_c q^2}{12\pi^2 \epsilon_0 \mu d_p d_f^2 u_0}$	$2(K_M/h_K)^{1/2} ; R \leq (h_K K_M)^{1/4}$ $R^2/h_K + K_M/R^2 ; R \geq (h_K K_M)^{1/4}$ $2.3 K_M^{1/2}$ (Empirical correlation)	Natanson ²⁸⁾
		Uncharged	External field	Dielectric polarization force 	$K_G = \frac{2}{3} \frac{\epsilon_p - 1}{\epsilon_p + 2} \frac{\epsilon_f - 1}{\epsilon_f + 1} \frac{C_c \epsilon_0 d_p^2 E^2}{\mu d_f u_0}$	$f(\epsilon_f, \alpha, K_G)$ (Numerical results)	Yoshioka <i>et al.</i> ²⁹⁾
		Charged	External field	Coulombic force 	$K_{EC} = \frac{C_c q \bar{E}^*}{3\pi \mu d_p u_0}$	$0.8 K_G^{2/3}$ (Empirical correlation)	Takahashi <i>et al.</i> ³⁰⁾
						$\frac{1}{1+K_{EC}} \left[\eta_R + K_{EC} \left\{ \frac{\epsilon_f - 1}{\epsilon_f + 1} \left(\frac{1}{1+R} + \frac{6}{p^6} \right) (1+R)^5 + (1+R) \right\} \right]$ where, $P = (2\pi/\sqrt{3\alpha})^{1/2}$	Kirsch <i>et al.</i> ³¹⁾
							Takahashi <i>et al.</i> ³⁰⁾

* $\bar{E} = E_0 \{1 - (\epsilon_f - 1)/(\epsilon_f + 1)\alpha\}^{-1}$, where E is average electric field in the bed, E_0 the electric field in the absence of fiber, ϵ_0 the space permittivity ($= 8.554 \times 10^{-12} \text{ F} \cdot \text{m}^{-1}$), ϵ_p and ϵ_f the dielectric constants of particles and fibers, q the particle charge (C), and Q the fiber charge ($\text{C} \cdot \text{m}^{-1}$).

make it into an electret filter. The filtration efficiency, which is 50% in the absence of an electrostatic force, is markedly improved to 99.9%, when singly charged particles are passed through an electret filter.

An electret filter can capture ultrafine particles at a very high filtration efficiency, but its efficiency tends to decrease as the particles accumulate on the surface, because the electrostatic charge is gradually reduced. This trend is more noticeable with organic mists, such as tobacco smoke and DOP particles. In the case of solid particles, on the other hand, the filtration efficiency tends to increase with dust load, because an increase in the mechanical efficiency by the accumulated particles prevails the decrease in electrostatic collection efficiency^{8,9)}

5. Granular Bed Filters

Granular beds have a higher packing fraction (around 60%) than that of fiber-packed beds. They are, however, inferior to fiber-packed beds in both filtration efficiency and pressure loss, because of large granule size (0.5 mm or more). These disadvantages left granular beds undesirable for a long period of time until a series of oil crises and the resurgence of coal-fired boilers in power plants brought them into the limelight as high-temperature dust collectors. The major advantages of granular beds are (1) durability at high temperatures, which stems from use of heat-resistant materials, such as sand, ceramics and a variety of metals as the filter media, (2) clogging of filter can be avoided by the use of moving-bed concept, and (3) granules can be recycled and reused, after removing the accumulated particles by sieve or fluidized bed. It is therefore possible for a moving bed to maintain stable operation with constant filtration efficiency and pressure loss.

Granules in a packed bed are in contact or very close to each other, thus making it very difficult to analyze the flow field, unlike in the case of fiber-packed beds. There are two models to describe the flow field in the granular bed, namely external flow model in which the flow passes around a single sphere and internal flow model (channel model) in which a variety of flow passages are assumed, as shown in Fig. 8. Most of the theoretical works on the granular bed filtration are based on the former model. Tardos *et al.*¹⁰⁾ assumed that the filtration effi-

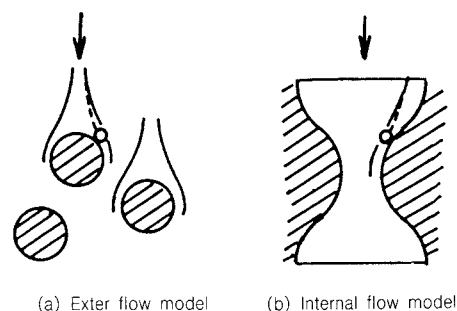


Fig. 8 Internal and external flow models for granular bed filter

ciency η_D of a single sphere in granular bed can be given by the product of the filtration efficiency η_{0D} of isolated sphere and the correction factor $g(\alpha)$ which is a function of packing density¹⁰⁾;

$$\eta_D = g(\alpha) \eta_{0D} \quad (5)$$

$g(\alpha)$ in the above equation is given in Table 6 for various cases. Table 7 summarizes the theoretical correlations for η_{0D} ¹⁰⁾.

For the inertial impaction of particles, D'Ottavio and Goren¹¹⁾, Gal *et al.*¹²⁾ and Pendse and Tien¹³⁾ obtained single sphere collection efficiency. These were recently reviewed by Jung *et al.*¹⁴⁾.

Table 6 Theoretical correlations for diffusional single sphere collection efficiency²⁾

Researchers	Flow	Diffusion efficiency η_D
Levich	Creeping flow	$4.03 Pe^{-2/3}$
Lochiel <i>et al.</i>	Boundary layer flow	$3.36 Pe^{1/6} Pe^{-2/3}$
Suneja	Potential flow	$3.027 Pe^{-1/2} + 2.0R$ (interception effect included)
Watts	Potential flow	$4.624 Pe^{-1/2} + 4.74 Pe^{-1}$

The authors have measured the initial filtration efficiency of the granular packed beds. The experiments covered the conditions of particle size d_p : 0.02 to 2.02 μm , filtration velocity: 0.4 to 120 cm/s, granule size d_g : 0.5 to 2.0 mm, packing fraction α : 0.574 to 0.667, and bed height L : 3.0 to 15.0. As a result, the following semiempirical correlations were obtained as a function of dimensionless parameters governing the filtration mechanisms. The correlation is based on the assumption that the filtration efficiencies by inertia, diffusion, gravi-

Table 7 Packing fraction functions $g(\alpha)^{10}$

Researchers	Flow	$g(\alpha)$	Applicable ranges	Remarks
Pfeffer <i>et al.</i>	Viscous flow (Happel flow)	$\left(\frac{2(1-\alpha)^{5/3}}{2-3\alpha^{1/3}+3\alpha^{5/3}-2\alpha^2} \right)^{1/3}$	$Re < 0.01$ $Pe \geq 1000$	Theoretical correlation
Tardos <i>et al.</i>	Viscous flow (Kuwabara flow)	$\left(\frac{1-\alpha}{1+\alpha-(9/5)\alpha^{1/3}-(1/5)\alpha^2} \right)^{1/3}$	$Re < 0.01$ $Pe \geq 1000$	Theoretical correlation
Sirkar	Low-Reynolds number flow (Tam flow)	$\left(\frac{2+1.5\alpha+1.5(8\alpha-3\alpha^2)^{1/2}}{(1-\alpha)(2-3\alpha)} \right)^{1/3}$	$Re \leq 1$ $Pe \geq 1000$ $\alpha < 0.67$	Theoretical correlation
Tardos <i>et al.</i>	Viscous flow (Kuwabara flow)	$1.07+3.43\alpha$	$Re < 0.01$ $Pe \geq 1000$	Numerical solution
Tan <i>et al.</i>		$1.1/(1-\alpha)$	$Re < 1$ $0.3 < \alpha < 0.65$	Empirical correlation
Wilson and Geankoplis		$1.09/(1-\alpha)$	$Re < 10$ $0.3 < \alpha < 0.65$	Empirical correlation

tation and interception are additive. They have proven to be applicable for various conditions. conditions.

$$\eta = \eta_D + \eta_G + \eta_I + \eta_R \quad (6)$$

$$\eta_D = A Sc^{f_1} \cdot Re^{f_2} \quad (7)$$

$$f_1 = -2/3 + Re^3/6(Re^3 + 2.0 \times 10^5)$$

$$A = 8.0, \quad f_2 = -2/3 : Re \leq 30$$

$$A = 40.0, \quad f_2 = -1.15 : 30 < Re < 100$$

$$A = 2.1, \quad f_2 = -1/2 : 100 \leq Re$$

$$\eta_G = G/(1+G) \quad (8)$$

$$\eta_I = St_{eff}^3/(St_{eff}^3 + 0.014) \quad (9)$$

$$St_{eff} = [1.0 + 1.75(1-\alpha)Re/150\alpha]St$$

$$\eta_R = 16R^{2-Re/(Re^{1/3}+1)^3} \quad (10)$$

where, subscripts D , G , I and R stand for diffusion, gravitation, inertia and interception. As shown by Eq. (7), the diffusion efficiency η_D is relatively insensitive to α , and it depends more on Re ; $\eta_D = 8.0Pe^{-2/3}$ with $Re \rightarrow 0$ (creeping flow) and $\eta_D = 2.1Pe^{-1/2}$ with $Re \rightarrow \infty$ (potential flow). Therefore, the exponents of the Peclet number coincide with those of the theoretical correlations shown in Table 6. Equation (8) is a purely theoretical correlation, and Eq. (9) is a correlation with the effective Stokes number proposed by Gal *et al.*¹²⁾. Sc ($= \mu/\rho D_B$) in Eq. (7) is a dimensionless number, known as the Schmidt number. Refer to Table 2 for the other dimensionless numbers in Eq. (6) to (10).

The authors have recently conducted experi-

ments at elevated temperatures of up to 300°C, and found that the observed results are well represented by these equations with the correction in air viscosity μ , air density ρ and Cunningham's slip correction factor at a high temperature¹⁶⁾. Though the dependence of collection efficiency on temperature varies with the test conditions, temperature rise generally leads to a decrease in the filtration efficiency and an increase in the pressure drop at a given mass flow velocity of air.

The collection performance of granular beds under dust loaded conditions has been studied by several researchers. Kimura *et al.* applied an interception model in fixed granular bed filtration¹⁷⁾ and analyzed distributions of collected particles in the bed^{18,19)}. Pendse *et al.* simulated the process of particle accumulation on the granule surface based on a channel flow model²⁰⁾. The moving beds are mostly used commercially. Particle accumulation in the moving bed differs significantly from that observed in fixed beds. For example, in the moving bed filtration it is necessary to consider the accumulated particle distributions in the moving direction (vertical direction to the air flow), and the reentrainment of collected particles by the movement of granules. Arashi *et al.*, taking these into consideration, proposed a model to predict the particle accumulation characteristics in moving beds from those in fixed beds²³⁾.

References

- 1) Langmuir, I.: OSRD Report. No. 865, (1942).
- 2) Emi, H: "Ouyou Earozoru Gaku", edited by K. Takahashi, Yoken-do, p. 141, (1984).
- 3) Iinoya, K.: "Shujin Souchi-no Seinou", Sangyo Gijutsu Center, pp. 777-222, (1976).
- 4) "Air Cleaning Handbook", edited by Japan Air Cleaning Association, Ohom-sha, p. 268, (1981).
- 5) Emi, H., C. Kanaoka and T. Ishiguro: Proc. of 6th Int. Symp. on Contamination Control, Tokyo, p. 219, (1982).
- 6) Ellenbecker, M. J., J.M. Price, D. Leith and M. W. First: EPA-600/9-80-039C, p. 171, (1980).
- 7) Löffler, F. and W. Muhr: *Chemie. Ing. Technik*, **44**, 510 (1972).
- 8) Kanaoka, C., H. Emi and T. Ishiguro: "Aerosols" (Ed. by Liu, Pui and Fissan), pp. 613-616, (1984).
- 9) Emi, H. C. Kanaoka, Y. Otani and T. Hayashi: Proc. of 7th Symp. on Air Cleaning and Contamination Control, p. 63, (1988).
- 10) Tardos, G.I., N. Abuaf and C. Gutfinger: *J. Air Pollut. Contr. Assoc.*, **28**, 354 (1979).
- 11) D'Ottavio, T. and S.L. Goren: *Aerosol Sci. Technol.*, **3**, 91 (1984).
- 12) Gal, E., G. I. Tardos and R. Pfeffer: *AIChE J.*, **31**, 1093 (1985).
- 13) Pendse, H. and C. Tien: *AIChE J.*, **28**, 677 (1982).
- 14) Jung, Y., S. A. Walata and C. Tien: *Aerosol Sci. Technol.*, **11**, 168 (1989).
- 15) Otani, Y., C. Kanaoka and H. Emi: *Aerosol Sci. Technol.*, **10**, 463 (1989).
- 16) Otani, Y., H. Emi and C. Kanaoka: *J. Aerosol Research, Japan*, **3** (4), 299 (1988).
- 17) Kimura, N., H. Mori, E. Murase, Y. Kasaoka and M. Shirato: *Kagaku Kogaku Ronbun-shu*, **13**, 780 (1987).
- 18) Mori, Y. and K. Iinoya: Proc. Int. Symp. on Powder Technol., Kyoto, p. 557, (1981).
- 19) Kimura, N., M. Kanamori, H. Mori and M. Shirato: *Kagaku Kogaku Ronbun-shu*, **15**, 119 (1989).
- 20) Pendse, H. and C. Tien: *J. Colloid Interface Sci.*, **87**, 225 (1982).
- 21) Arashi, N., K. Narato and H. Kuroda: *J. Soc. Powder Technol., Japan*, **25**, 739 (1988).
- 22) Stechkina, I.B.: *Dokl. Akad. Nauk SSSR.*, **167**, 1327 (1966).
- 23) Kirsch, A.A. and N.A. Fuchs: *Ann. Occup. Hyg.*, **11**, 299 (1968).
- 24) Yoshioka, N., H. Emi, C. Kanaoka and M. Yasunami: *Kagaku Kogaku*, **36**, 313 (1972).
- 25) Landahl, H.P. and R.G. Hermann: *J. Colloid Sci.*, **4**, 103 (1949).
- 26) Kirsch, A.A., I.B. Stechkina and N.A. Fuchs: *Kolloid Zh.*, **31**, 227 (1969).
- 27) Brown, R.C.: *J. Aerosol Sci.*, **12**, 349 (1981).
- 28) Natanson, G.L.: *Proc. Acad. Sci. USSR, Phys. Chem. Sect.*, **112**, 95 (1957).
- 29) Yoshioka, N., H. Emi, M. Hattori and Y. Tamori: *Kagaku Kogaku*, **32**, 815 (1968).
- 30) Takahashi, T. and A. Kanagawa: *Kagaku Kogaku Ronbun-shu*, **1**, 644 (1975).
- 31) Kirsch, A.A.: *J. Aerosol Sci.*, **3**, 25 (1972).

Motion Analysis in Tumbling Mills by the Discrete Element Method[†]

B. K. Mishra and R. K. Rajamani

*Department of Metallurgical Engineering
University of Utah**

Abstract

The media motion in a ball mill is simulated using a numerical algorithm known as the Discrete Element Method. The motion of the charge is modelling by considering the forces acting at each contact point during a collision and following the movement of individual balls as per Newton's law. First, experimental verification of the model is shown. Then a few simulated results are shown for some interesting cases. For the first time it is possible to get information about the distribution of energy in the collision between balls. Also the cataracting and cascading motion of charge in large mills can be simulated accurately with this simulation program.

Introduction

Grinding is an important unit operation in metal production from mined ores. Crushed ore in the size range of 1~3 centimeters is ground to a size finer than 72 microns. In almost all plants a tumbling ball mill is used for grinding. Importantly, this operation consumes a large amount of energy; the power cost may represent more than half the total processing cost. Therefore considerable attention has been focused on the breakage rates and energy consumption in tumbling mills. Our knowledge of comminution (the effect of operating variables on mill performance, modelling, simulation and control) has greatly widened, yet we face fresh problems that require both practical as well as theoretical solutions. One of the current problems is predicting the power draft of the mill. This would entail knowing precisely the distribution of forces during the tumbling motion of the balls. A good approach to the above problems clearly resides in the understanding of the dynamic motion of the balls within the mill, which is the genesis of the forces experienced by the particles to be ground.

Motion analysis of the charge of particulate material in a tumbling mill was reported, by

White¹⁾ and Davis²⁾, among others and has been reviewed by Rose and Sullivan³⁾. Although simplistic in nature, these works established the motion of the charge inside a ball mill approximately.

Once the charge motion was established, researchers took different approaches to predict the power draft of the mill. In one such approach, certain assumptions were made with regard to the dynamic charge: the entire mill charge composed of a single mass whose profile is determined by a line joining the toe and shoulder of the ball mass and the mechanical energy sustaining the mass at this position continuously. While the mill is at rest, the center of mass of the charge is on the vertical line passing through the center of the mill axis, but as the mill rotates the center of mass of the charge assumes a new position to the right of the vertical axis (for counterclockwise mill rotation). The torque required to maintain the charge in its offset position is then computed from the load and the offset distance from the mill center. The power draft is then related to the torque through the rotational speed of the mill.

The power-draft calculation described is quite simple, and hence the resulting analytical equations are widely used in the mineral processing industries. However, a host of factors like the profile of the charge, the natural angle

* 412 William C. Browning Bldg., Salt Lake City, Utah 84112 U S A.

† Received October 29, 1990

of response of the charge, frictional forces acting at the mill wall, the shape of the lifter bars, the size distribution of the ball charge, etc., influence power draft so much that the simple analysis begins to fail when higher accuracy is demanded. Liddell and Moys⁴⁾ have proved this point: none of the torque formulae could predict their carefully measured power draft of the 0.545-m \times 0.308-m mill. In their recent works Mishra and Rajamani⁵⁾ have shown that the center of gravity of the charge is not a fixed point in space; rather, it changes its position as the mill rotates. They have also shown⁶⁾ that the profile of the charge changes with the shape of the lifter bars. Therefore, any torque analysis treating the ball charge as a single mass is unrealistic.

The breakage rate of particles, wear rate of balls and liners, and power draft are known to be intimately related to the motion of the charge. Hence to accurately predict these quantities, motion of individual balls must be modelled. An analytical solution within the realm of classical mechanics is impossible. Therefore, the intention here is to explore some other avenues of fundamental inquiry, by means of which motion and collision of each and every ball in the ball charge can be tracked. Such an analysis is possible with the Discrete Element Method, which is a numerical tool for simulating multi-body collisions. In this analysis, the motion of the charge is treated as a multi-body collision problem, for which only the material properties with regard to impact must be known. The purpose of this paper is to present the results obtained through numerical simulation and discuss the trends in the results in comparison to physical experiments.

The Model

The Discrete Element Method (DEM) is a numerical scheme pioneered by Cundall and Strack⁷⁾ for simulating the behavior of systems of discrete interacting bodies. It has gained popularity over the past decade in several areas of science where behavior of particulate material had to be studied taking an alternate route to the continuum approach. This scheme allows finite displacements and rotation of discrete bodies, where complete loss of contact and formation of new contacts take place as the calculation progresses. The program DISC

developed by Corkum and Ting⁸⁾ implements the DEM algorithm for two-dimensional disc-shaped bodies; it has been used to study basic soil behavior and geotechnical problems. This code has been modified by Mishra⁹⁾ to simulate media motion in tumbling mills.

The numerical scheme adopted in the DEM formulation applies Newton's second law to the discs and force displacement law at the contacts. Newton's second law gives the motion of the discs resulting from the forces acting on it. The forces developing at the contacts are modelled by a pair of normal and tangential spring-dashpots at every contact point. The forces are found from the overlaps of the discs at the contact points by using a linear force displacement law; the contact forces are proportional to the amount and the rate of overlap between the discs. The provision of viscous-contact damping models the system realistically, because the coefficients of restitution for different contacts are used to compute the damping parameters. Also, friction damping occurs during sliding in any time step, when the absolute value of the shear force at any contact exceeds a maximum value found by the product of the normal force and the coefficient of friction.

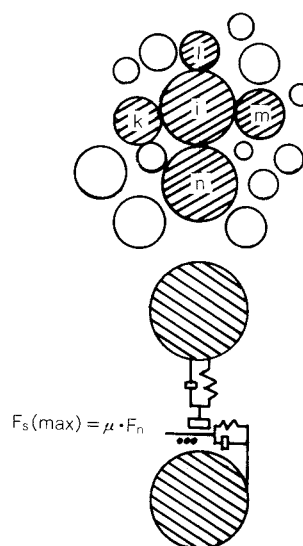


Fig. 1 Schematic representation of an assembly of discs and a contact showing the spring-dashpot arrangement.

As shown in **Fig. 1**, every disc is identified separately; they are allowed to overlap at the contact points; and the calculation is done for

each disc in turn. The relative velocity of the disc i with respect to other discs k , l , m , and n is determined for each contact. These relative velocities for every contact of disc i are resolved in the normal (along the line drawn through the disc centers) and shear direction, and the force calculation is then done for each contact in the following way:

$$\Delta F_n = K_n * dv_n * \Delta t$$

$$\Delta F_s = K_s * dv_s * \Delta t$$

$$\Delta d_n = C_n * dv_n$$

$$\Delta d_s = C_s * dv_s$$

where ΔF_n and ΔF_s are the incremental forces due to the springs, Δd_n and Δd_s are the incremental forces due to the dashpots, dv_n and dv_s are incremental velocities, K and C are the spring and dashpot constants, respectively, and Δt is the incremental time step. Then the contact forces on a disc are added to get the net out-of-balance force acting on it. The acceleration of disc i of mass m_i is given by

$$\ddot{x}_i = \frac{1}{m_i} \Sigma F_x,$$

$$\ddot{y}_i = \frac{1}{m_i} \Sigma F_y,$$

$$\ddot{\theta}_i = \frac{1}{I_{oi}} \Sigma M_o,$$

where \ddot{x} , \ddot{y} , $\ddot{\theta}$ are the accelerations in the x , y and θ directions, respectively, I_{oi} is the moment of inertia of disc i , and M_o is the total moment acting on the disc.

Then by integrating acceleration with a central difference scheme, the velocity and displacement are determined. Thus, by repeating this calculation for each disc, the new position of all the discs is determined, and, by repeating the entire set of calculation at successive time steps, the movement of the charge in the x , y -coordinate space is given.

Experimental Work

The majority of the experimental work was carried out in a small ball mill, and specialized equipment was used to determine material parameters. The principal aim of the experimental work is to verify the numerical simulations. The parameters needed for the numerical calculation are the coefficient of restitution, materi-

al stiffness and coefficient of friction. The material stiffness is determined by dropping the ball over a layer of particles situated on an anvil. A strain gauge embedded in the anvil records the strain waves. The analysis of the data gives stiffness.

Similarly in a pendulum experiment, the coefficient of restitution for the ball-ball collision is determined. Drop ball experiments are done to find the same for ball-wall collisions. These values of the coefficient of restitution are used to estimate damping parameters.

The coefficient-of-friction data are obtained from the results of the experiments done by Rose and Sullivan³⁾. The data used in the simulations are given in Table 1.

Table 1 Data used in simulations

Normal stiffness	418,400 N/m
Shear stiffness	278,930 N/m
Coefficient of friction	0.4
Coefficient of restitution:	
ball-ball impact	0.9
ball-wall impact	0.3
Mill diameter	0.3 m
Critical speed	76 rpm

Similar data have been used recently by Yokoyama *et al.*¹⁰⁾ for studying the movement of ball media in vibration mills.

For recording the motion of ball charge experimentally, a ball-mill/video-camera system was built. The video camera records events on a video tape, and a frame-grabber hardware transmits the image to the computer memory. Then a software program tracks the x , y -coordinates of the moving balls. In this manner the motion of the entire ball mass is compared with the simulation results. A schematic of this equip-

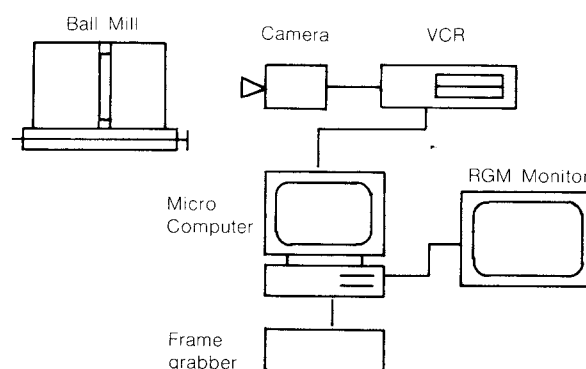


Fig. 2 Experimental apparatus

ment is shown in Fig. 2. The ball mill is a thin cylinder 1 centimeter thick and 30 centimeters in diameter, fitted with six equally spaced lifter bars. The discs are 3.4 centimeters in diameter and 0.8 centimeters thick. The discs are positioned in the mill, and a plexiglas end plate is bolted to the lifter bars. The plexiglas plate allows video recording of the charge motion. Thus, the experimental mill is made to correspond to the simulated mill.

Results

It is easy to calculate the trajectory of a

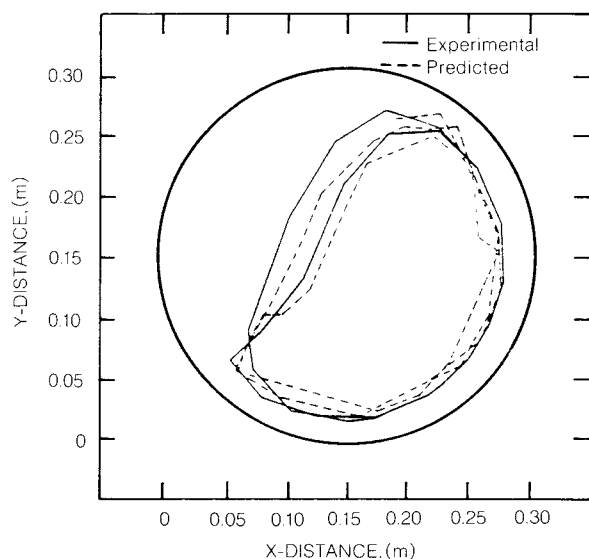


Fig. 3a Comparison of the measured and predicted trajectories of a ball residing close to the mill shell

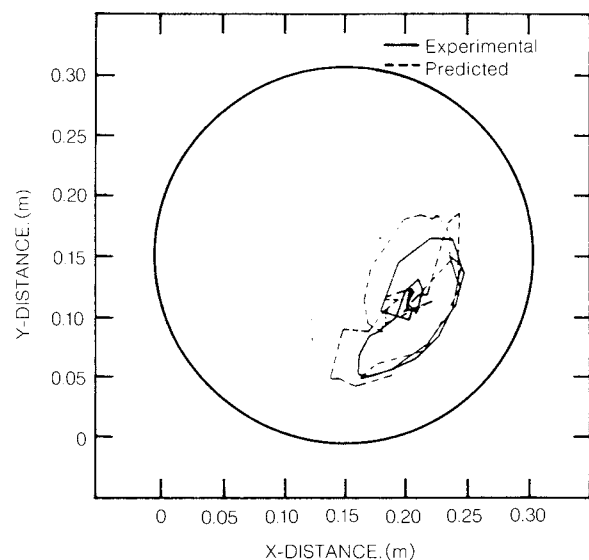


Fig. 3b Comparison of the measured and predicted trajectories of a ball residing on the outermost layer of balls

single ball; for two balls the trajectory calculation becomes slightly complex, and as the number of balls increases, it becomes impossible to calculate the individual trajectories. It is for this reason that in the literature many of the predictions are for a single ball. For the first time DEM enables tracking of all the balls no matter how many balls reside in the mill. **Figures 3a and 3b** compare the position of two arbitrary balls in an assembly of 24 balls; one of the balls resides close to the mill shell (**Fig. 3a**) while the other rests on the outermost layer of balls (**Fig. 3b**). The mill is filled with 24 balls of 3.4 centimeters diameter resulting in a 40 percent mill filling. Experimentally determined positions are compared against numerical simulation results for two revolutions of the mill. Even though collision events are stochastic in nature, the comparison is surprisingly close. It is difficult to say, however, that predictions would be equally good in the third revolution. Since the disc surface is rough, the actual trajectories deviate slightly from the theoretical, and as time passes these deviations build up to a large extent. It is believed that by correctly choosing the parameters the collision events can be simulated within the limits of acceptable error.

Even though the trajectories of individual balls become stochastic at longer periods of time, the mean tendency of the charge motion can be predicted with DEM. After a number of

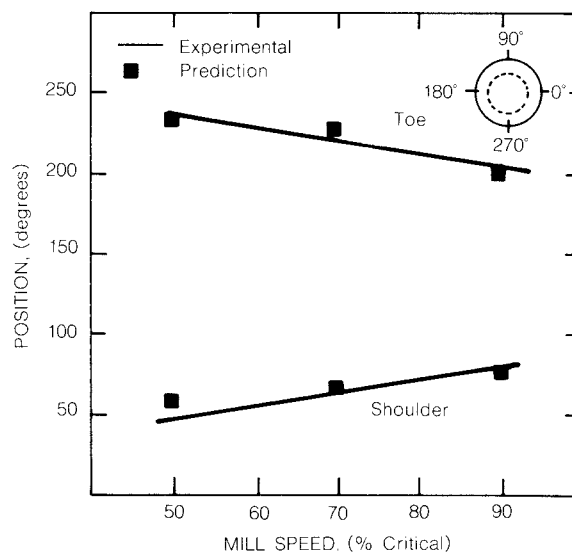


Fig. 4 Comparison of the measured and predicted toe and shoulder positions of the load at various speeds

revolutions the experimental profile of the charge can be compared with simulation. Usually the position of the shoulder and toe of the charge is referred to in the literature. Here “shoulder” means the point from which the balls leave the mill shell, after taking a circular path along the mill shell, and the “toe” is the point where the balls drop on the mill shell after being thrown out. The position of the toe and shoulder can approximately define the profile of the charge. Figure 4 shows the change in the angular toe and shoulder positions as the mill speed changes. It is seen here that the predicted positions are in agreement with the experiment. The trends are worth noting: With a lower mill speed the charge moves along the mill shell to a point where a component of the gravity exceeds the centrifugal force and lets the charge fall from the mill shell; from this point onwards, the charge moves in a parabolic path until it hits the mill shell. In contrast, at higher speeds, the outer layer of the charge begins to centrifuge; the angular toe position is lowered, while the angular shoulder position is

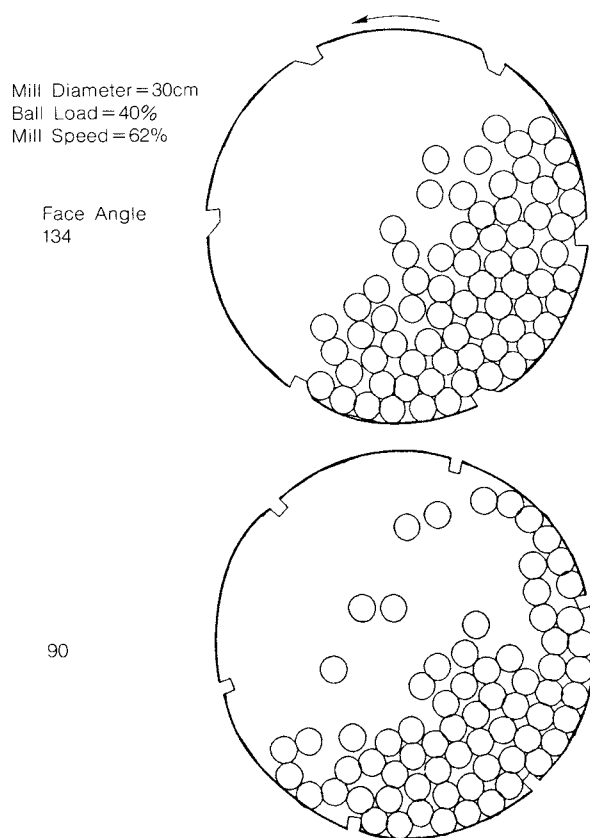


Fig. 5 Snapshots of motion of an assembly of balls depicting the difference in the profile of the load for two different lifter-bar geometry

raised. Therefore, to produce mostly cascading motion and very little cataracting of balls, the mill should be operated at an optimum speed. It is possible to ascertain this speed for any size mill with this simulation procedure.

After having built some confidence in the computer code, a few numerical experiments were carried out to compare the trends in the simulation results with actual observations. Lifter-bar shape tremendously influences the profile of the charge, but due to wear lifter-bar shape changes after prolonged hours of milling, causing a change in the ball trajectories; these changes in turn affect the power drawn. As an illustration, Fig. 5 shows snapshots of the charge profile as it evolves, for two different face angles of lifter bars — 134 degrees and 90 degrees. A comparison of power draft indicates that a 30-centimeter diameter mill, operating at 60 percent of its critical speed, 40 percent filling, with 90-degree face-angle lifter bars, draws twice as much power when compared to the same mill fitted with 130-degree face-angle lifter bars. How much of this extra power is utilized in particle breakage is not known.

It is possible to calculate the energy distribution of collisions in the ball charge. What makes this possible is the contact model using normal and tangential spring-dashpots. The frequency distribution of energy expended in various collisions reveals more diverse information about the behavior of the mechanical process. To il-

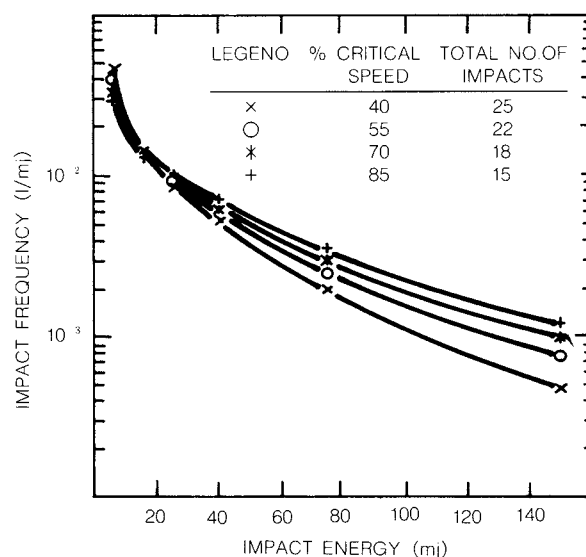


Fig. 6 Frequency distribution of energy between collisions for different mill speeds

illustrate this, a 55-centimeter diameter mill with 40 percent ball filling was simulated. **Figure 6** shows the frequency of impacts for a single ball during one revolution, as a function of impact energy, for different rotational speeds. It is seen that the number of impacts corresponding to small energy values is more than the number of impacts corresponding to that of large energy values. This happens when the cascading motion predominates the overall motion of the charge; this fact was readily noticed in the simulation-animation results which are not shown here.

It is important to know how the impact frequency corresponding to a given energy value changes with the rotational speed; with this information the particle breakage process can be

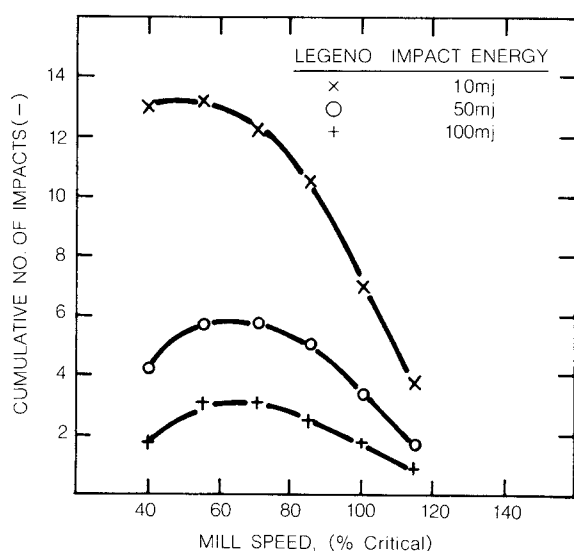


Fig. 7 Variation of cumulative number of impacts, corresponding to a given energy of impact, with mill speed

controlled. **Figure 7** shows the cumulative number of impacts greater than a given energy plotted against the rotational speed of the mill. The number of low-energy impacts (~ 10 mj) decreases with increasing rotational speed. The frequency of medium- (~ 50 mj) and high-energy (~ 100 mj) impacts increases with increasing rotational speed and subsequently decreases with speed. Also, low-energy impacts are greater in number than the high-energy impacts at any rotational speed of the mill. As the balls begin to centrifuge, the total number of impacts decreases. A combination of these impacts influ-

ences the mode of breakage of the material and the power draft. Also from the figure, it is safe to predict that the maximum in power draft of the mill would occur at about 70 percent of the critical speed. It is known that mill capacity is at its highest when the power draw is highest. For a given liner configuration and ball size distribution, it is possible to predict power draft with this DEM simulator.

The critical speed of the mill applies only to the outer layer of the balls, i.e., the ones which are in contact with the mill shell. This outer layer of balls cataracts, and the inner layers of balls then tend to cascade, as they would in a mill operated at a low speed. So, at any given time, some of the balls would be in flight (catracting) while others would not be. The proportion of these balls with respect to one another determines the frequency distribution of impacts. However, these energies of impacts cannot be determined experimentally, and one has to rely on numerical schemes as presented here. Rolf and Simonis¹¹⁾ measured the energies of impact in a carefully planned experiment. The balls were fitted with strain gauges and memory circuits and after going through collisions the information was transmitted to a computer for analysis. The simulated trends of energy frequency agree with Rolf's experimental findings.

Conclusions

An analytical description of multi-body collision is difficult, but the Discrete Element Method enables numerical simulation of ball charge motion. Currently, the simulation requires hours of supercomputer time, depending on the number of balls to be simulated. Published models describing the motion of the charge in a mill are invariably based on empiricism, and hence their use is limited. DEM simulation can give collision frequency and impact energy frequency. The collision frequency can be subdivided into ball-ball collisions and ball-liner (shell) collisions. Hence, with these frequencies, rates of both liner and ball wear and particle breakage can be modelled accurately.

The simulation results pertaining to two important aspects of ball motion are checked against laboratory experiments: First, the position of two arbitrary balls are tracked and found to match with the simulated trajectories,

and second, the toe and shoulder positions defining the profile of the charge as a whole as predicted by simulation agree with the experiments. Also the charge motion was simulated for two different shapes of the lifter bars. The snapshots of a charge motion depict the differences in the overall motion of the charge.

The key to any plant operation lies in a good understanding of the individual unit operations; ball mills in a concentrator are no exception. Very little is known about the processes taking place inside the mill due to the lack of sensors which can function in the harsh environment. Moreover, for process simulation, an adequate theory capable of describing the individual motion of balls is yet to emerge. As described here, it is possible to simulate multi-body collisions. Some simulations were carried out to study the impact process occurring within the mill. The low-energy impacts are far larger in number than high-energy impacts for all speeds. Furthermore, the number of impacts for a specified energy value reaches a maximum and then drops off as speed increases.

The results shown here, though in no way exhaustive, are quite fundamental in nature, and unveil the modes of charge motion and hence the mechanism of breakage. For the first time, the frequency distribution of energy of collisions is numerically calculated. This work is currently being pursued at greater lengths, to establish a mechanism of particle breakage with respect to the modes of charge motion. It will then be possible to predict the size distribution of the particles being milled. We believe that this work should open a new dimension of further investigation into comminution in ball mills.

Acknowledgement

This research has been supported by the

Department of the Interior's Mineral Institute program administered by the Bureau of Mines through the Generic Mineral Technology Center for Comminution under grant number G1175149.

The authors would also like to thank the Utah Supercomputing Institute which is funded by the State of Utah and the IBM Corporation for their support in this endeavor.

References

- 1) White, H.A.: *Journal of the Chemical Metallurgical, and Mining Society of South Africa*, Vol. 5, p. 290 (1904).
- 2) Davis, E. W.: *AIME Trans.*, Vol. 61, p. 250 (1919).
- 3) Rose, H. E. and R.M.E. Sullivan: *Ball, Tube and Rod Mills*, Chemical Publishing Co., New York (1958).
- 4) Liddel, K.S. and M.H. Moys: *S. Afr. Inst. Min. Metall.*, Vol. 88, p. 49 (1988).
- 5) Mishra, B.K. and R.K. Rajamani: Preprints of the 7th European Symposium on Comminution, p.555 (1990).
- 6) Mishra, B.K., R.K. Rajamani and W.G. Pariseau: Preprints of the S.M.E. Annual Meeting, Salt Lake City, Utah, U.S.A., Preprint No. 90-137 (1990).
- 7) Cundall, P. A. and O.D.L. Strack: *Geotechnique*, 29, p. 47 (1979).
- 8) Corkum, B.T. and J.M. Ting: Publ. 86-11, Univ. of Toronto, Canada (1986).
- 9) Mishra, B.K.: Ph.D. Thesis in Progress, University of Utah (1990).
- 10) Rolf, L. and W. Simonis: Preprints of the 7th European Symposium on Comminution, p. 543 (1990).
- 11) Yokoyama, T., K. Tamura and G. Jimbo: Proceedings of Second World Congress on Particle Technology, p. 455 (1990).

An XPS Investigation of Hydrothermal and Commercial Barium Titanate Powders[†]

C. C. Hung and R. E. Riman

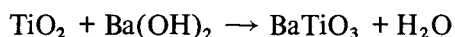
Department of Ceramics
Rutgers University*

Abstract

Hydrothermal and commercial barium titanate powders were examined for undesirable impurity phases. Compositional differences in the powder were evaluated using x-ray diffraction (XRD), x-ray fluorescence (XRF), and x-ray photoelectron spectroscopy (XPS). A barium-rich impurity phase, virtually undetectable by XRD, was detected via XPS. Barium impurity phase peaks were detected at binding energies @ 1.5 eV higher than those characteristic of barium in a barium titanate bonding state for both the Ba 3d and Ba 4d transitions. Simple curve-fitting techniques were used to quantify the percentage of barium in a barium titanate bonding state versus another barium bonding state for each set of doublets. The barium impurity bonding state accounted for 20–50 mol% of the barium detected by XPS.

1. Introduction

Submicron, crystalline barium titanate powders can be hydrothermally synthesized from inexpensive, aqueous slurries of barium hydroxide and titanium dioxide precursors at temperatures near the boiling point of water in an ambient atmosphere¹. The synthesis proceeds according to the net reaction:



To maximize conversion, an excess of barium hydroxide is necessary to force the reaction to go to completion. As in the processing of other chemically derived powders, a subsequent washing procedure is necessary following the synthesis of hydrothermal barium titanate to remove any excess reagent or other undesirable impurity phases from the product. In particular, excess barium hydroxide reagent must be removed to maintain a 1:1 Ba/Ti molar ratio and to prevent formation of barium carbonate upon contact with carbon dioxide in the atmosphere. However, excessive washing must be avoided, since a barium-deficient or titania-rich powder can result in excessive grain growth during firing². In addition, the hydrothermal slurries, which have a pH of 12–14 prior to

washing, must be neutralized to ease further processing.

This paper will focus on impurities in barium titanate powders as interpreted by x-ray photoelectron spectroscopy (XPS) and x-ray diffraction (XRD). To understand the effect of processing on the surface of the powder, XPS was used specifically because it gives direct measurements of surface atomic composition as well as surface chemical bonding information. Traditional methods of evaluating the chemistry of barium titanate powders establish a bulk barium/titanium atomic ratio by either x-ray fluorescence (XRF) or wet chemical analysis. However, these bulk methods cannot distinguish between the different phases of barium that may be present in the samples. In addition, bulk measurements may not reflect the true surface chemistry of the powder, especially in the case of high surface area, submicron powders where surface heterogeneities may be present. XRD is frequently used for phase analysis but is of limited value when amorphous phases or very small amounts of a phase are present, as is typical of a surface. Fourier transform infrared (FTIR) spectroscopy can be used to identify surface groups, but the data cannot be easily quantified.

The XPS technique uses low energy x-ray beams to ionize inner-shell electrons from the

* P.O. Box 909, Piscataway, New Jersey 08855-0909, U.S.A.

† Received October 29, 1990

surface of the sample (depths $< 50 \text{ \AA}$)³⁾. Chemical information is interpreted from the kinetic energy spectra of the photoelectrons collected. Photoelectrons of a specific kinetic energy range correspond to a specific electronic transition of a particular element. The binding energy of an atom is related to the kinetic energy of the ionized electron by the Einstein equation³⁾:

$$KE = h\nu - BE - \phi - W_c$$

where KE = kinetic energy of the ejected electron, $h\nu$ = x-ray excitation energy, BE = binding energy of the atom, ϕ = combined work function of the instrument and sample holder, and W_c = work required to overcome charging in the sample due to poor electrical conduction.

Elements exhibit binding energy peaks whose relative positions depend on the electronegativity of their surrounding atomic neighbors. These are the chemical shifts by which the bonding states of the element are identified. In the case of a phase mixture where more than one bonding state exists, the relative distribution of a particular element in each bonding state can be interpreted by curve fitting the binding energy peaks and computing the total peak area fraction for each bonding state. However, curve-fitting results are associated with a high degree of error, are not necessarily unique solutions, and thus might not have a physical meaning, especially when energy shifts approach the peak resolution of the instrument³⁾. Finally, different electronic transitions of the same element can reveal compositional information at two different depths if the difference in kinetic energy between the transitions is large enough. A depth composition profile of barium is possible because of the large difference in kinetic energy between the 3d barium peaks at 475 eV and the 4d barium peaks at 1160 eV. The 475 eV Ba 3d transition has a maximum escape depth of 10-20 \AA , which corresponds to the powder surface, while the 1160 eV Ba 4d transition has a maximum escape depth of 30-50 \AA , which corresponds more to the bulk region of the particle.

Peak identification for ceramic powders is especially difficult due to sample charging, which prevents assignments based on absolute binding energy. Rough and/or chemically non-uniform surfaces can cause differential charging effects that shift the energy peaks nonlin-

early. Referencing to the graphite C 1s peak or to the Au 4f peak is a standard technique for overcoming this problem³⁾. However, slight differences in values for the same material in different studies are common in the literature. Charging can also broaden peaks, leading to the false conclusion that multiple bonding states are present. Although the literature does not cite a Ba binding energy for barium titanate, XPS studies of barium and barium-containing compounds have been of recent interest due to ongoing research in the field of superconductors. Van Doveren and Verhoeven, in their work on XPS spectras of alkaline earth metals and their oxides, determined that the spin-orbital splitting between the Ba $4d_{5/2}$ and the Ba $4d_{3/2}$ doublet for Ba metal and single-crystal BaO samples ranges from 2.1 to 3.0 eV⁴⁾. Ford *et al.* have demonstrated how Ba 4d spectras of $\text{YBa}_2\text{Cu}_3\text{O}_x$ (123) superconducting samples can be successfully deconvoluted into two sets of doublets using Gaussian peaks and a Ba 4d spin-orbital splitting value of 2.47 eV⁵⁾. XPS studies by Ford and coworkers and Brow on 123 superconductors exposed to air demonstrated additional peaks at higher binding energies in the Ba 3d, O 1s, and C 1s spectra, but not in the Cu 2p and Y 3d spectras^{5,6)}. Furthermore, Brow shows that these high binding energy peaks correspond to a spectra of a known BaCO_3 sample with an O 1s peak at 531.4 eV, a Ba $3d_{5/2}$ peak at 780.1 eV, and a C 1s peak at 289.2 eV.

The binding energy shifts of barium can be explained by chemical bonding models. Barium is a highly electropositive element, and barium oxide compounds are nearly completely ionic. In these cases, the barium can be assumed to be in the 2+ state at all times. Chemical shifts are then primarily the result of local potential changes caused by different anion coordination⁷⁾. A higher coordination of negative ions would increase the local electron potential function, decreasing the measured binding energies of the photoelectrons. Assuming a perovskite-like structure for the 123 compound, the barium is 12-fold⁸⁾. In comparison, barium carbonate has 9-fold and barium hydroxide has only 8-fold coordination with oxygen ions^{9,10)}. The 123 would be expected to have the lowest binding energies, with the barium carbonate and hydroxide having increasingly larger binding

energies. Barium titanate has an oxygen coordination of twelve and is expected to have core photoelectron binding energies similar to 123 and thus lower than both barium carbonate and barium hydroxide.

2. Materials and Characterization

2. 1 Powder preparation

Both a commercially available oxalate-derived barium titanate and various hydrothermally synthesized barium titanate powders were studied under XPS. The commercial powder was a high purity grade barium titanate (Ticon HPB, Lot #716, TAM Ceramics, Niagara Falls, NY) made by an oxalate coprecipitation process, calcined to 850°C, and spray dried.

Three partially reacted hydrothermal powder batches were prepared for initial XPS studies, each by mixing 20 g of reagent-grade hydrous barium hydroxide (Fisher Chemical, Fairlawn, NJ) with 5 g of reagent-grade titanium dioxide (Fisher Chemical, Fairlawn, NJ) in ambient atmosphere for an initial Ba/Ti molar ratio of 1. A slurry of the powder and 30 ml of deionized, double distilled water was reacted without stirring in a 90°C oven in a sealed 60 ml teflon reaction vessel (Saville, Minneapolis, MN). The slurry from a different batch was taken out of the oven after 1, 4, 12, and 56 h. Each slurry was diluted with 100 ml of 1 M formic acid and vacuum filtered with 0.2 μ m pore polyvinylidene difluoride filter paper (Millipore Corp., Bedford, MA) until dry. The filter cake was oven dried in air at 90°C.

More fully reacted batches of hydrothermal powder with an initial Ba/Ti ratio of 1.1 were prepared for rinsing studies in a similar fashion by mixing 29 g of barium hydroxide with 6.7 g of titanium dioxide in sealed 90 ml teflon reaction vessels (Saville, Minneapolis, MN). After 72 h the slurry was vacuum filtered without dilution with 0.2 μ m pore polyvinylidene difluoride filter paper (Millipore Corp., Bedford, MA) until dry. To minimize reactions between the powder and atmospheric carbon dioxide and possible hydrothermal reactions in a drying oven, freeze drying (Dura-Dry, FTS Systems, Stone Ridge, NY) was employed instead of oven drying as before.

2. 2 Characterization

The hydrothermal and commercial barium

titanate powders were characterized by XRD, XRF, and XPS. Quantitative x-ray analysis (XRD) was performed via a matrix flushing method on an automated diffractometer (Model D-500, Siemens AG, Karlsruhe, FRG) using Ni-filtered Cu K-alpha radiation and operated at 40 kV, 30 mA, with zircon as the internal standard¹¹). The data were collected by means of a DACO (Siemens AG, Karlsruhe, FRG) microprocessor using a stepwidth of 0.04 degrees 2 θ and a measuring time of 2 s per step for the barium titanate peak and 10 s per step for the other minor peaks. Bulk XRF measurements of samples of the hydrothermal powder were conducted at E. I. du Pont de Nemours using wavelength dispersive spectroscopy in conjunction with a proprietary analysis method. Two replicate fused samples were examined for Ba, Sr, and Ti content. These same samples of hydrothermal powder were also examined by XPS.

For XPS analysis, powders were tightly packed into a shallow depression in an aluminum sample stub with a glass slide to avoid spurious signals from commonly used adhesives. The samples were then gradually degassed in the sample introduction chamber and placed into the high vacuum chamber of the XPS spectrometer (XSAM-800, Kratos, Ramsey, NJ) for examination. The electron signal was generated by nonmonochromated Mg K-alpha radiation produced from a Mg anode under 16 keV and 15 mA. The spectra were collected with a spot size of 2 mm \times 2 mm to minimize the signal from the sample stub using a hemispherical electron energy analyzer with a bias setting of 5.0 eV. Powders were found to contain barium, titanium, oxygen, and carbon peaks. However, only the barium 3d and 4d spectra were extensively analyzed and quantified due to poor peak resolution and high noise levels in the other spectra. The signal curves for the various barium bonding states were fitted by peak addition using Gaussian peak approximations and Shirley background reduction.

For the quantitative barium bonding state analysis, all the overlapping barium peaks were fitted by peak addition methods that incorporated an energy shift of 1.4-1.6 eV between each barium bonding state in the spectra and a rough $d_{5/2}$ to $d_{3/2}$ intensity ratio of 3:2. This interval and intensity ratio were determined by

extensive analysis of peak shift trends in over twenty different barium titanate samples as well as a barium carbonate standard. Because barium carbonate and barium hydroxide have similar coordinations, to simplify calculations these impurity phases were added together as one barium impurity state to be distinguished from the barium titanate bonding state in the powder. Since the area under each peak corresponds to the concentration of a particular bonding state, the percentage of total peak area under the barium titanate doublet was taken to correspond to the percentage of the total moles of barium detected by XPS in a barium titanate bonding state. This calculated number reflected the mole percent of barium detected in a barium titanate chemical bonding state for each sample. The percentages calculated from the above mentioned curve-fitting routines had an uncertainty of roughly ± 5 mol%.

3. Results and Discussion

In general for the XPS barium spectra, two sets of doublet peaks, each corresponding to a different chemical bonding state, were found

for both the 3d (Fig. 1) and 4d Ba transitions. The chemical shift between the bonding states ranged from 1.4-1.6 eV for both the Ba 3d and Ba 4d transitions. The Ba 3d peaks had an average full width half maximum (FWHM) of 2.2 eV, while the Ba 4d peaks were narrower, having an average FWHM of 1.5 eV. The spin-orbital splitting for the Ba 3d transition was found to be @15 eV, allowing separate windowing of each of the Ba 3d doublet peaks. The spin-orbital splitting for the Ba 4d transition, however, was found to be only @ 2.5 eV, which is in agreement with 123 work by Ford *et al.* Using methods discussed previously, analysis of the barium spectra identified the lower binding energy peaks as lattice barium titanate and the higher binding energy peaks as barium carbonate and/or barium hydroxide. Considering the aqueous thermodynamic stability of barium carbonate in contact with air, the presence of barium carbonate would be expected in these samples¹²⁾. As analyzed by XPS, barium titanate powders in contact with air apparently have a surface layer of barium carbonate or some other lower coordination barium impurity.

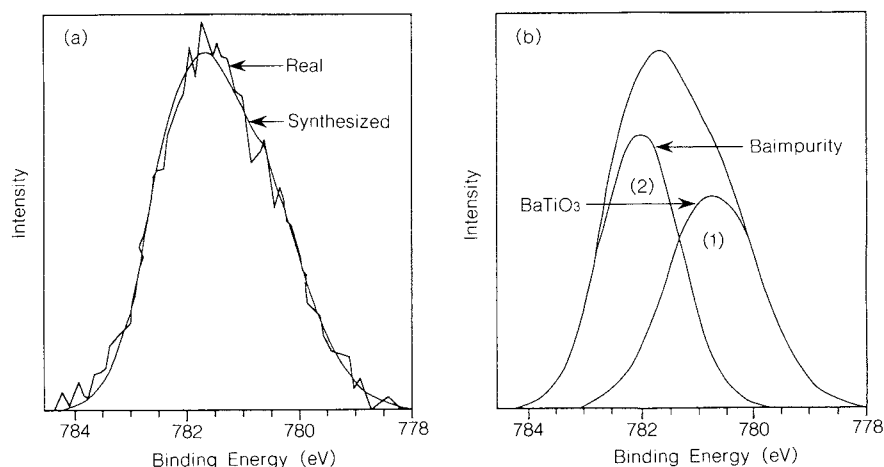


Fig. 1 A typical Ba 3d_{5/2} curve fit for Barium titanate
A. The real and synthesized signal curves.
B. The synthesized peaks: 1) BaTiO₃, Ba 4d_{5/2} peak, 2) BaTiO₃, Ba 4d_{3/2} peak, 3) Ba impurity, Ba 4d_{5/2} peak, 4) Ba impurity, Ba 4d_{3/2} peak

Support for our peak assignment analysis was provided by other experimental data. First, a wide variety of commercial and hydrothermal powders have all followed the same general trends described above. Second, XPS and XRD studies of the partially reacted hydrothermal samples showed that an increase in barium titanate bonding state detected by XPS corre-

sponded to an increase in crystalline barium titanate phase detected by XRD, as shown in Fig. 2.

Analysis of our XPS data provided information on a barium impurity phase faintly present or absent by other characterization methods (Table 1). A common characteristic of all the barium titanate powders analyzed with XPS

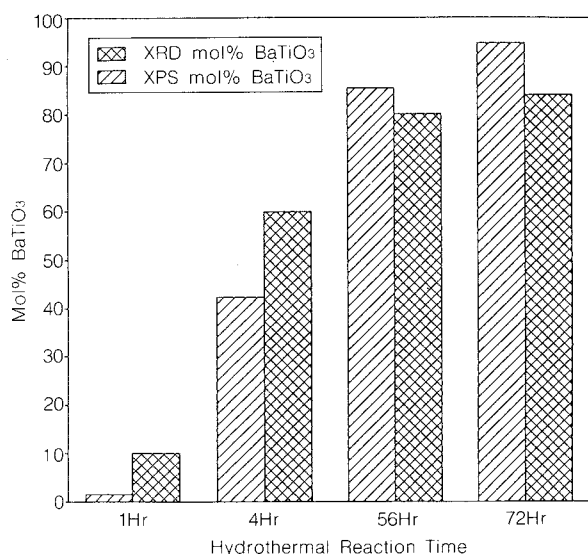


Fig. 2 Comparison between Ba 3d XPS data versus XRD data for several partially reacted hydrothermal barium titanate powders

was that the percentage of barium in a barium titanate bonding state was 80 mol% or less, with the barium impurity phase accounting for the rest of the barium signal. The @ 1 : 1 (BaO + SrO)/TiO₂ molar ratios detected by XRF and low impurity levels detected by XRD are typical of what one would expect if the impurity phases were amorphous or concentrated in the near surface region. Comparing hydrothermal powder batches 1 and 2, it is interesting to note that the XRF (BaO + SrO)/TiO₂ molar ratios, 1.016 and 1.021, inversely scale with the corresponding XPS Ba 4d data, 74 and 61 mol% BaTiO₃. These data indicate that as the powder became richer in barium, the additional barium was incorporated into an impurity phase.

XPS was also capable of resolving the spatial nature of the impurity phase. Comparison of

Table 1 Barium titanate powder characterization

Analysis method	As received commercial oxalate derived powder	Batch 1 hydrothermal powder	Batch 2 hydrothermal powder
XRD: BaCO ₃ (wt %)	1.45	0.539	0.731
TiO ₂ (wt %)	0.00	1.23	1.42
XRF#	1.001*	1.016	1.021
XPS (mol% BaTiO ₃): Ba 3d	53	50	47
Ba 4d	66	74	61

* XRF data from manufacturer
(BaO + SrO)/TiO₂ molar ratio

the Ba 3d and 4d data in **Table 1** reveals that consistently less barium in a barium titanate bonding state was detected for the Ba 3d transition than the Ba 4d transition. For instance, Batch 2 was found to have a bonding state proportion of 47 mol% BaTiO₃ for the Ba 3d transition, while this increased to 61 mol% BaTiO₃ for the Ba 4d transition. It is also interesting to note that the magnitude of the 3d barium titanate levels for the hydrothermal powders (approx. 47-50 mol% BaTiO₃) are within experimental error of the curve-fitting routine and thus are indistinguishable. The similarity of the 3d peaks and the contrasting nature of the 4d peaks described earlier suggest that the thickness of the impurity phase is greater than the escape depth of the Ba 3d electrons (< 20Å) but less than that of the Ba 4d electrons (< 50

Å). This impurity phase may be present either as a surface layer or as a barium impurity phase occluded within microporous regions of a porous barium titanate particle.

4. Conclusion

XPS studies have revealed that a barium titanate bonding state can be distinguished from a non-barium titanate bonding state on the basis of the barium peak shifts. The non-barium titanate bonding state has been assigned a peak located 1.5 eV higher in binding energy than the barium titanate peak for both the 3d and 4d barium transitions. Further studies have shown that barium titanate powders exposed to air have a significant amount of barium-rich surface impurity phases undetectable by XRD or XRF. Ongoing work with XPS is investigating

the effect of postsynthesis processing, such as rinsing procedures, on the surfaces of sub-micron barium titanate powders.

Acknowledgments

Funding for this work was provided by the National Science Foundation, the Center for Ceramic Research, and the New Jersey State Commission on Science and Technology. Special thanks to Dr. Donald Swanson for XRF work done at E. I. du Pont de Nemours Co., Inc., Jackson Labs, Dr. M. S. Hegde at the Indian Institute of Technology, Bangalore, India, and Dr. William Mullins at Purdue University, Lafayette, Indiana, for very helpful conversations regarding the XPS data and to Ms. K. Griffin for editorial assistance.

References

- 1) Peterson, J. H.: U.S. patent 2,216,655 (1940).
- 2) Jaffe, B., W. R. Cook, and H. Jaffe: "Piezoelectric Ceramics," p. 70, Academic Press, New York (1971).
- 3) Defosse, C. and P. G. Rouxhet: "Advanced Chemical Methods for Soil and Clay Minerals Research," NATO Advanced Study Institutes, Series C, **63**, 163, D. Reidel Pubs., Boston (1980).
- 4) Van Doveren, H. and J. A. Th. Verhoeven: *J. Elec. Spect.*, **21**, 265 (1980).
- 5) Ford, W. K., J. Anderson, G. V. Rubenacker, J. E. Drumheller, C. T. Chen, M. Hong, J. Kwo, and S. H. Liou: *J. Mater. Res.*, **4**[1], 16 (1989).
- 6) Brow, R. K.: "Research Update, 1988: Ceramic Superconductors II," p. 598, Am. Cer. Soc., Westerville, OH (1988).
- 7) Egelhoff, W. F., Jr.: *Surface Sci. Repts.*, **6**, 253 (1987).
- 8) Kingery, W. D., H. K. Bowen, and D. R. Uhlmann: "Introduction to Ceramics," 2d ed., p. 25, Wiley, New York (1976).
- 9) Speer, J. A.: "Carbonates: Mineralogy and Chemistry," *Reviews in Mineralogy*, **11**, 145, Mineral. Soc. of Am., Washington, DC (1983).
- 10) Wells, A. F.: "Structural Inorganic Chemistry," 4th ed., p. 519, Clarendon Press, Oxford (1975).
- 11) Chung, F. H.: *J. Appl. Cryst.*, **7**, 519 (1974).
- 12) Osseo-Asare, K., F. J. Arriagada, and J. H. Adair: "Ceramic Powder Science II: International Powder Processing Science Proceedings," **1**, 47, Am. Cer. Soc., Westerville, OH (1988).

Competition between Powder Metallurgy and Other Near Net Shape Processes: Case Studies in the Automotive and Aerospace Industries[†]

Narayan V. Nallicheri

*Project Manager, IBIS Associates, Inc.**

Joel P. Clark

*POSCO Professor of Materials Engineering, MIT***

Introduction

With increasing industry competition, development of new alloys, stiffer price competition, and rising energy and material costs, there has been a distinct trend to diverge from conventional forming technologies. The need to produce the final product in fewer processing steps with minimal material wastage has led engineers and component designers to develop and critically evaluate alternative processing routes which would be more cost effective, while maintaining the same high level of performance. Several techniques for manufacture to "net shape" or "near net shape" are being developed to meet present and future demands.

The fundamental incentive for the development of alternative fabrication processes is economic. The reduction and, at times, elimination of a large number of machining steps provides sufficient cost savings on a per part basis to warrant the use of net shape processes, even though they may entail extra capital equipment and/or special handling equipment¹⁾. An indication of the significance of net shape processes can be found in automobile industry statistics: approximately fifty pounds of precision formed parts are used in a typical American or European automobile, and about three times that amount in a Japanese automobile^{2,3)}.

The material selection problem faced by present day designers is also a problem of choosing the optimal processing route, especially since the choice of a particular material is tied to the manufacturing process employed. For example, a switch to steel from nodular iron for connecting rod also implies a change in processing from casting to forging.

Driven by the need to reduce the costs of

fabrication, and enhance material utilization rates, net shape and near net shape processes have been gaining in importance. These encompass not only the traditional casting and forging, but also exotic powder techniques such as hot isostatic pressing, and powder forging.

One of the key forces driving the shift towards near net shape production is the reduction of secondary machining or metal removal operations. The annual economic value of material removed, measured in terms of labor and overhead, is estimated at over \$125 billion in the U.S. alone⁴⁾. Considering the enormous economic value, it is apparent that any reduction in metal cutting operations will provide substantial economic savings for the manufacturing industry. To this end, there have been sizable efforts focused on improving the machining operation and in developing means to reduce, if not eliminate, the amount of machining required. Further, the field of machining has been aided by the development of a host of empirical relations relating the various cutting parameters in order to choose the optimum cutting conditions^{5,6)}.

There have been a large number of changes in the field of machining itself, spurred by the evolution of new materials, difficult to machine alloys, etc., and also by the need for higher precision. To meet these requirements there have been numerous advances in the cutting tool industry, such as the emergence of new material cutting systems and surface coatings aimed at enhancing tool life. Global competition, in conjunction with the difficulty associated with machining some high-temperature alloys and some composite materials, provides a constant incentive for the development of new tool materials and tool surface treatments aimed at extending metal removal rates. These advances serve to aid shifts in technology towards net shape. Figure 1 highlights the chron-

* 55 William St. Ste. 220, Wellesley, MA 02181, U.S.A.

** Rm 8-409, 77 Mass. Ave., M.I.T.; Cambridge, MA 02139, U.S.A.

† Received September 10, 1990.

ological order of advances in the cutting speed capabilities of tool materials. The improvements in cutting speeds progressively achieved over the years have been both through the introduction of new tool materials (solid line), and the use of coatings on existing tool materials (dashed line).

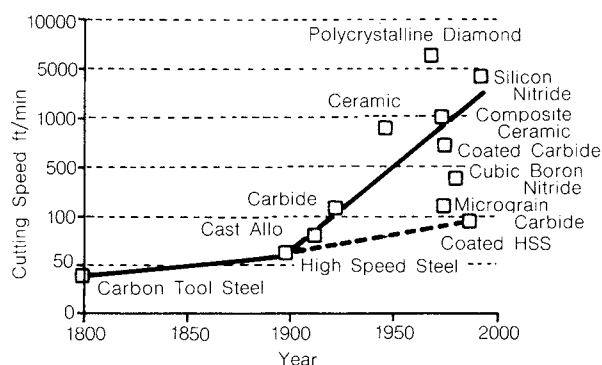


Fig. 1 Chronological development of tools with their cutting speed capability

The technologies summarized above are just a tip of the iceberg as far as the whole range of possible fabrication routes available for metals processing are concerned. There is an interdependence between the technologies themselves, to a limited extent, and between the primary fabrication routes and secondary routes, such as machining, to a larger extent. Although part of this shift towards near net shape technologies is material driven, a large fraction still stems from the economic advantages to be reaped by a shift in technology. The advent of these new technologies warrants active markets where possible applications can be found. The range of applicability depends on the level of economic savings offered by near net shape technologies, and on the performance characteristics obtainable. Further, a particular application may, at times, warrant the use of a high performance material due to performance requirements. A change in material may also be associated with a change in processing route. Thus competition between technologies may arise out of pure performance considerations based on the limitations of the current material/process.

The scenario outlined above is quite prevalent in the automotive industry where con-

tinual changes in engine designs place stringent requirements on the possible materials which may be used for their manufacture. The automotive industry, where large production volumes are typical, has been an optimal environment for the penetration of these technologies. The automotive industry is one of the largest users of formed parts, either cast, forged or stamped. In 1988, the automotive industry consumed a total of \$16.9 billion worth of steel stampings, 1.6 million tons of nodular iron castings, and approximately 21 lbs/auto of metal powder⁷⁾. Thus, from the point of view of introducing new net shape processing routes which may require high initial capital investments, it is preferable to have high production volume runs to obtain economies of scale, which are typical of the automotive industry. In the case of P/M, almost 70% of the end of metal powder can be traced to the automotive industry⁸⁾. Further, as mentioned above, the automotive industry is under continuous pressure to innovate and use lighter, stronger materials for its components. Figure 2 presents the trend of iron powder shipments used solely for P/M parts⁹⁾. The increasing trend clearly shows the enhanced used of P/M parts in automobiles. In fact, General Motors recently announced their intention to use at least 18-20 lbs of powder parts per automobile in the next few years¹⁰⁾.

The advent of new materials and near net technologies is not limited to the automotive industry alone. Table 1 tabulates the projected growth rate for RS materials in the U.S. The growth of these exotic materials is tied into the growth of the near net technologies associated with their processing¹¹⁾.

From the foregoing discussion it is apparent that there is currently a great deal of interest in the advent of near net shape technologies. The prime motivation for a shift in technology towards net shape is economic, though performance considerations are also of importance. The above discussion also suggests that there is a dual nature to the materials selection problem. Designers need to lay emphasis not only on the level of performance delivered by the component, but also on the costs of manufacture.

The drive towards more powerful, fuel efficient aerospace engines has been such that,

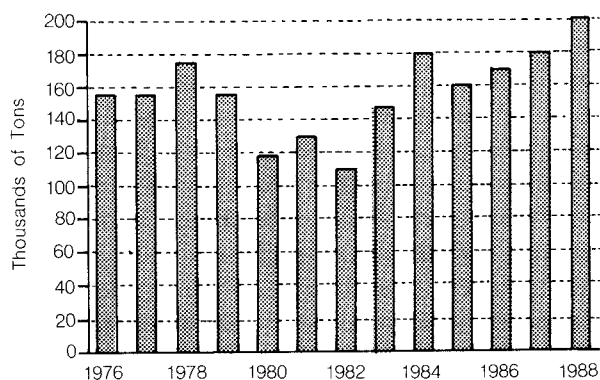


Fig. 2 Iron powder shipments for P/M parts

Table 1 Projected growth for RS materials in the U.S.¹¹⁾

	Average, Annual growth rate %	\$ (millions)	
		1988	1993
Metallic glasses	52*	10.0**	81.0**
Iron base alloys	10	62.0**	100.0**
Superalloys	7	54.0	76.0
Aluminum alloys	22	3.0	8.0
Titanium alloys	20	0.2	0.5
Ceramics	68	0.15	2.0

* - New technology, starting from small base

** - Numbers may be on high side

since the establishment of civil jet transport in the mid 1950's, specific fuel consumption has been halved, thrust has increased fifty fold, and engine thrust to weight ratios have been increased by a factor of ten. In addition to the proliferation of new materials, many of these improvements have been achieved by the exploitation of cost-effective near net shape manufacturing technology and by an increased understanding of the dependence of performance on manufacturing¹²⁾.

The use of nickel based superalloys for aircraft engine components has been on the rise. The successful application of these "super-alloys" is due to their creep strength and stability at elevated temperatures over long times. Nickel base superalloys owe their high temperature mechanical properties to the presence of gamma-prime precipitates, which are coherent and remain stable at high temperatures¹³⁾.

Aircraft turbine engines are manufactured worldwide by some 35 companies and consortia. A recent study by the Gorham Advanced Materials Institute predicts U.S. domination of this industry for the next ten years¹⁴⁾. How-

ever, the next decade will show an increasing competitiveness among consortia as designers, builders, and marketers of engines.

Currently, about 91% of the weight of an advanced gas turbine engine consists of either superalloys (41.5%), steel (26.5%), or titanium (23.5%), with the balance being made up of aluminum and small amounts of magnesium, polymers/polymer matrix composites, and refractory materials. Superalloys are expected to maintain their superiority in this market, and by 1998 the mix of materials used is expected to become 43% superalloys, 23.5% steel, and 22.5% titanium¹⁵⁾. A breakdown of the overall materials consumption is presented in Table 3, and in Fig. 3.

This attractive market potential for super-alloy materials makes it an active area of research, especially when considering the proliferation of gas turbine applications. The attractive high temperature properties offered by this class of materials makes it the obvious choice for certain applications. The traditional processing routes, casting and forging, are being replaced by powder metallurgical routes. This trend has been driven by the more stringent performance requirements needed in hostile engine environments. Currently, the two main near net shape processing routes, hot isostatic pressing and isothermal forging, have their roots in powder metallurgy.

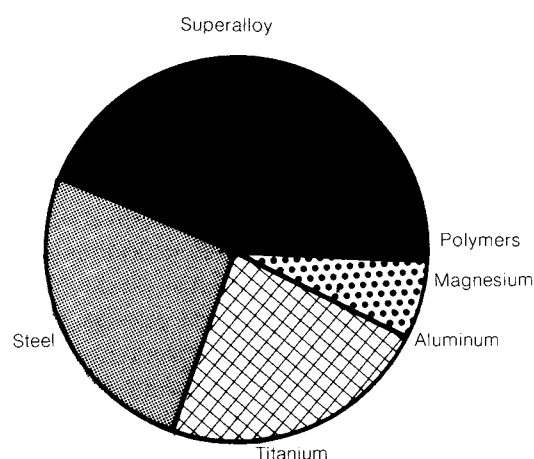


Fig. 3 Global materials consumption in aircraft gas turbine engines (1988-1998)

The low cycle fatigue (LCF) capability of current superalloys for disk applications is

largely limited by the presence of defects in the alloy. The defects in a typical René 95 alloy are determined by the processing route undertaken. As shown in Table 2, the largest defects in the as-hipped product are large reactive prior particle boundary defects. The inclusion of small ceramic particles during the melting and atomization stage of the cycle limits the fatigue capability of the thermomechanically processed disk. As evidenced by the data in Table 2, a shift in technology from hot isostatic pressing to isothermal forging from extruded bar has potential for improvements in LCF properties.

The mechanical properties of extruded compacts were higher than their hiped counterparts due to the fine grain size of extrusions. Because of heavy deformation occurring in the extrusion process, the size of the original powder particle did not significantly affect final grain size¹⁶⁾. Coarser particle size distribution results in larger grained compacts having lower tensile properties and increased stress rupture problems. Compaction by extrusion minimizes differences caused by original powder particle size distribution. It is this phenomenon that leads to an enhancement of final disk properties.

The problems associated with the larger scatter of low cycle fatigue properties in as-HIP consolidated René 95 have increased the use of isothermal forging techniques for final fabrication. This, in turn, has encouraged shear deformation methods such as extrusion for the forging stock in order to break up ceramic inclusions and to reduce overall defect size¹⁷⁾. The large particle size variation for the hiped product has deleterious results on mechanical and fatigue properties. As opposed to this, isothermal forging from an extruded bar results in a more uniform grain structure, because the extrusion process breaks down the individual grains to a fine structure. This leads to an enhancement of properties. Of course, it is possible to use a starting powder stock for hot isostatic pressing with a very close size distribution and cleanliness. This will result in enhanced properties of the isostatically pressed turbine disk. However, a close powder particle size distribution will result in low yields at the screening stage of the isostatic pressing operation, resulting in poor material utilization. This

will lead to an escalation of the amount of raw material required to process each component, thereby leading to enhanced cost.

It is evident from the foregoing discussion that while powder metallurgical processes, *viz.*, hot isostatic pressing and isothermal forging, are being preferred over conventional wrought techniques for this application, the exact choice depends not only on the economics of fabrication, but also on the technical ramifications of certain processing variables. This study was focused towards understanding the economic and technical forces underlying the use of these technologies. The automotive connecting rod and the aerospace turbine disk were

Table 2 Comparison of defect type vs size at LCF initiation site
HIP vs Extruded + iso-forge René 95¹⁸⁾

Temp (°F)	Total strain range %	Defect type*	Defect size, mils			
			HIP		Extruded + iso forge	
			Avg.	Max	Avg.	Max
1000	<0.75	1	6.7	36	4.8	9.8
		2	9.5	50	8.9	12.1
		3	18.7	242	None	None
		4	6.3	10.3	None	None
1000	>0.75	1	11.2	50	4.8	8.1
		2	13.1	111	7.1	16.0
		3	19.3	83.6	None	None
		4	5.3	6.8	1.0	1.5
750	0.75	1	7.5	9.1	4.1	8.7
		2	8.6	13.1	5.2	10.2
		3	6.4	6.4	None	None
		4	None	None	0.5	0.7

* 1 - Ceramics, 2 - Ceramic clusters,
3 - Prior particle boundaries, 4 - Voids

Table 3 Global materials consumption in aircraft gas turbine engines 1988-1998¹⁴⁾

Material	Millions of pounds
Superalloys	600.00
Steel	356.00
Titanium	321.00
Aluminum	75.00
Magnesium	10.00
Polymer/Polymer composites	13.00
Rubber/Elastomers	0.15
Total	1,375.15

used as cases to test the applicability of materials systems analysis at looking at material competitiveness.

Powder Metallurgy of Superalloys

The use of nickel base superalloys in engine disks has created widespread research interest, especially in the area of processing. Powder metallurgy (P/M), has increasingly become the process of choice, due to the flexibility it provides to tailor properties according to need. Further, P/M has been aided by advances in the field of rapid solidification, now capable of delivering fine uniformly sized powder with exotic non-equilibrium microstructures. The mechanical and fatigue properties are often tied closely to the size and size distribution of the raw powder used. This has led to research into the production of fine powder. A controlled inert gas P/M process has proven successful for producing fine grain, segregation-free material. Inert gas atomization requires the use of special controls, especially the control of oxygen and nitrogen content which degrade mechanical properties if present in quantities larger than a few hundred ppm. Further, the presence of certain tramp elements may be detrimental to processing, especially elements such as Cr, Al, and Ti which form oxides that are difficult to reduce. Likewise, the nitrides of Ti and Zr are detrimental as they do not dissociate in a vacuum melting furnace.

Conventional powder consolidation techniques are not readily applicable to superalloy powders because the powders are incompressible. Additionally, these powders do not sinter easily because they contain aluminum, chromium, and titanium, which oxidize easily at the sintering temperatures. Consequently, other techniques for powder consolidation which can apply high pressures at sintering temperatures, without triggering material problems, are required¹⁹⁾.

The superplastic behavior of superalloys was discovered at Pratt & Whitney, and led to the development of the gatorizing process²⁰⁾. However, it was found that gatorizing could not eliminate macrosegregation in as-forged alloys. Thus, gatorizing, more commonly known as isothermal forging, was applied to dense PM preforms. On an industrial scale, it has been applied to extruded PM billets. The superplastic deformation helps achieve forgings close to net shape, minimizing the amount of machining required and scrap losses. In order to

obtain a fine grain size (1-10 μm) stable at temperatures above half the melting point, the powder compacts are extruded at temperatures slightly below the recrystallization temperature of the alloys.

Hot isostatic pressing (HIP) is a technique used to consolidate powders to full density. HIP is a process by which an isostatic pressure is applied at high temperature, to metal powder placed within a container or die. The compact is compressed in a pressure vessel using argon gas. Pressures range from 20 to 300 MPa, and temperatures from 480°C for aluminum alloy powders to approximately 1700°C for tungsten powder²¹⁾. Processing temperatures are within the plastic range of the material being formed – high enough for diffusion bonding to occur, yet low enough to prevent undesirable microstructural changes. Heat transfer during isostatic pressing is highly efficient. At high pressures argon gas is denser than water. To ensure uniform heating, molybdenum resistance heating elements are located throughout the work zone²²⁾.

The first use of HIP was in the 1960's for diffusion bonding of clad nuclear fuel elements. Consolidation of beryllium metal powder to shape followed shortly thereafter. Since then, the size of units and use of the process has extended greatly. Uses now include the production of titanium and superalloys for the aerospace industry, net shapes in PM beryllium and niobium alloys and other refractory metals.

Isothermal forging and hot isostatic pressing have evolved into the dominant processes for this application over the past few years. An investigation geared towards understanding the key forces underlying the choice of either of these technologies would be invaluable, due to the fact that they form a class of emerging near net shape processes. As such, a competitive analysis based on cost was carried out in this study. The study used the technique of "Technical Cost Modeling" to estimate the manufacturing costs based on the given fabrication routes. Performance also plays an important role in the final choice of the processing route. Therefore, the ramifications of performance considerations on cost was also assessed.

Technical Cost Modeling

The importance of a systematic evaluation

of the costs of manufacturing cannot be over-emphasized. The approach used in technical cost modeling is to separate the different cost elements and estimate each one separately. This applies basic engineering principles, the physics of the manufacturing process, and clearly defined and verifiable economic and accounting principles. The models themselves are developed using a spreadsheet methodology. The use of a spreadsheet methodology to simulate the fabrication process is very helpful, because it provides a flexible environment for estimating the costs of manufacture using exotic materials and processes that are currently not in production, and because it is easy to use and offers visible parametrizing of the model.

A detailed account of the various cost elements are presented elsewhere. Interested readers may review the following references^{23),24)}.

Hot Isostatic Pressing

Based on the premise that isostatic pressing and isothermal forging have emerged as viable alternatives for the turbine disk application, it stands to reason that a detailed construct aimed at understanding the economic competitiveness of the above processes would be very helpful in making strategic decisions about the processes in the future. This paper undertakes such an evaluation using the technique mentioned above. Further, the economic implication of technical changes is also highlighted in this paper. A competitive assessment of a typical T700 turbine disk was carried out as a part of this study.

The T700 Turboshaft engine design includes four cooling plates and two isostatically pressed P/M René 95 disks. This engine is characterized by improved fuel consumption, extended operating life and simplified maintenance. As used in the U.S. Army Blackhawk helicopter, the T700 engine has accumulated well over 200,000 operating hours. The composition of René 95 used for turbine disk applications is presented below²⁵⁾:

Carbon	0.04-0.09%
Manganese	0.15% Max
Silicon	0.20% Max
Sulfur	0.015% Max
Phosphorus	0.015% Max.
Chromium	12.0-14.0%

Cobalt	7.0-9.0%
Iron	0.50% Max
Tantalum	0.20% Max
Columbium	3.30-3.70%
Zirconium	0.03-0.07%
Titanium	2.30-2.70%
Aluminum	3.30-3.70%
Boron	0.006-0.015%
Tungsten	3.30-3.70%
Oxygen	0.015% Max
Nitrogen	0.005% Max
Hydrogen	0.001% Max
Nickel	Remainder

The powder required for the isostatic pressing process is first screened to a-150 mesh size was (the size assumed in this study). Based upon the requirements of the turbine disk, the screened powder size distribution may need to be finer (around-270 mesh). The screening step of the operation is typified by low yields, especially if there are stringent controls on cleanliness and the final powder size distribution. The screened powder is then blended to homogenize different batches of atomized grades and loaded into a clean, evacuated container. This stem also serves as a vent for outgassing. The container is usually made of mild steel. The stem is joined to the container by gas tungsten arc welding.

The loaded container is outgassed by heating under vacuum up to about 700°F. The containers are placed in the HIP unit. The isostatic pressing was done at 2050°F, under a pressure of 30,000 psi for a minimum of 2 hours. Under this pressure, the heated container collapses, compacting the metal powder. At 2050°F the powder particles become plastic and coalesce to form a solid alloy. After pressing, the fully dense parts are heat treated as follows:

1. 2090°F, 1 hour, salt quench
2. Aged at 1600°F, 1 hour, air cooled
3. Aged at 1200°F, 16 hours, air cooled²⁶⁾.

Age hardening strengthens the material through precipitation of the gamma prime (Ni_3Al , Ti) and the heat treatment develops resistance to low cycle fatigue²⁷⁾. Mechanical properties of René 95 are influenced by the rate of cooling from the solutioning temperature. If quenched too rapidly, there is a danger of cracking the disk. If quenched too slowly, it

will not obtain the desired property level. It is for this reason that a salt bath solution and quench was used.

A hot isostatic pressing model was constructed to estimate the manufacturing costs based on the sequence of operations shown in Fig. 4. The set of assumptions used in the cost estimates is outlined below:

HIP - Assumptions

Finished Weight of Disk	4.5 lbs
Annual Production Volume	125 parts/year
Raw Material	René 95
Raw Material Cost	\$22/lb
Labor Cost	\$16/hr
Labor Overhead	40%
Labor Productivity	85%
Working Period	240 days/year

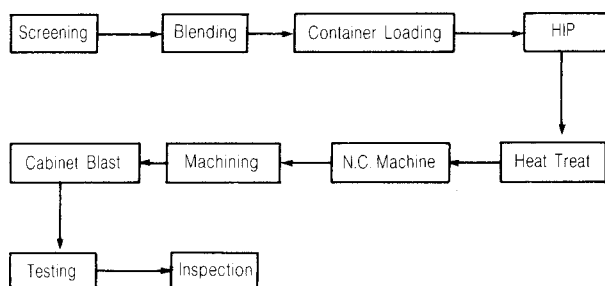


Fig. 4 Operation sequence for hot isostatic pressing of turbine disks

It was assumed that components other than turbine disk were made using the same equipment used to fabricate the disk. In other words the isostatic pressing facility was run in a non-dedicated fashion primarily due to the low production volumes. The powder yield during the screening operation is a very critical determinant of the total cost of the finished component. Figure 5 shows the breakdown of cost by processing step as estimated by the model, assuming a screening yield of 40%. Material cost is the most cost intensive factor in the total cost of the component. The high cost of container loading is a consequence of the high labor content. The breakdown of cost by factor and process is tabulated in Table 4.

Isothermal Forging

The alternative to hot isostatic pressing is isothermal forging of turbine disks. This process

Table 4 Breakdown of cost for hot isostatically pressed turbine disk

By Factor

	\$/part	Percent
Raw material	\$1,045.00	36.28%
Process material	\$27.39	0.95%
Labor	\$857.03	29.76%
Energy	\$12.70	0.44%
Scrap credit	(\$3.21)	-0.11%
Equipment	\$461.45	16.02%
Tooling	\$214.05	7.43%
Aux. equipment	\$18.03	0.63%
Maintenance	\$69.22	2.40%
Taxes	\$9.23	0.32%
Insurance	\$6.92	0.24%
Building	\$162.47	5.64%
Total	\$2,880.29	100.00%

By Process

	\$/part	Percent
Raw material	\$1,045.00	36.28%
Screening	\$247.32	8.59%
Blending	\$53.74	1.87%
Container loading	\$205.22	7.12%
Hipping	\$401.65	13.94%
Heat treating	\$69.36	2.41%
Tumblasting	\$3.49	0.12%
Machining	\$436.78	15.16%
Inspection	\$9.71	0.34%
Testing	\$245.55	8.53%
Building	\$162.47	5.64%
Total	\$2,880.29	100.00%

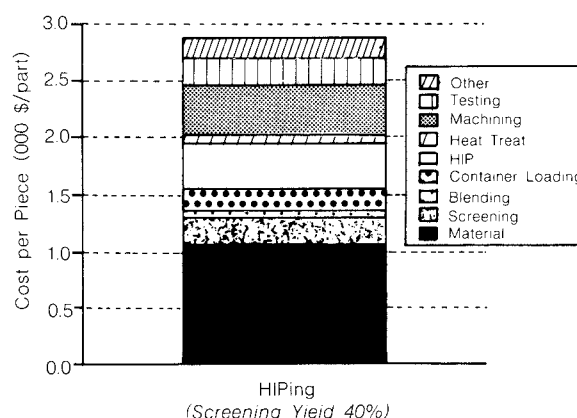


Fig. 5 Breakdown of cost by processing step for the hot isostatically pressed turbine disk

is also called gatorizing (as patented by Pratt & Whitney). The disks are forged from an extruded bar of René 95. The extrusion process

results in a more uniform, fine grain structure. The implications of this fine grain structure will be explained later in this paper.

The process involves heating stock to a temperature of about 2050°F and forging at a very controlled strain rate in dies heated to the same temperature. The best available die material is TZM molybdenum, an alloy that is very strong at the required forging temperature, but also one that oxidizes rapidly when exposed to air. Consequently, the isothermal forging press requires a vacuum chamber for the actual operation and sensitive temperature controls to ensure that the material being forged remains at the temperature where it is superplastic. Other system features unique to the isothermal forging press include a special vacuum furnace to bring the stock to forging temperature, transfer units for moving the forge mults from the furnace to the dies, and press controls that allow the programming of slow cross-head movements.

The sequence of processing steps is graphically shown in Fig. 6.

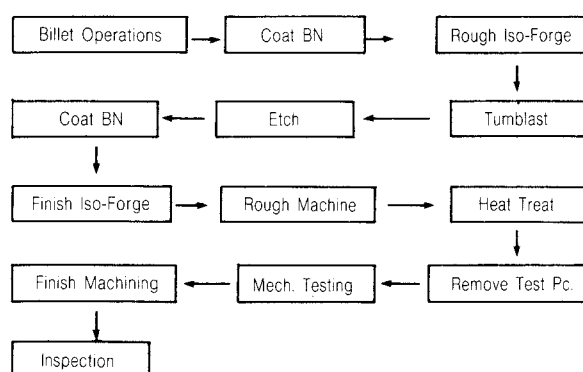


Fig. 6 Flowchart of operations for the case of the isothermally forged turbine disk

The billet operations mainly consist of cutting and grinding the billet down to the required size. The boron nitride coating prior to isothermal forging serves both as a lubricant and as a parting agent that prevents the adhesion of the forged disk to the die. Isothermal forging is achieved in two stages, the initial forge yielding a rough disk shape. After the forging, the component is etched using an etchant called "Heppenstal." The purpose of the etchant is to reveal surface flaws. This is actually a two bath etching process. Their compositions are listed

below:

Bath 1. $\text{HCl} + \text{HF} + \text{HNO}_2$

Bath 2. $\text{HCl} + \text{HNO}_3 + \text{Ferric Solution}$

It should be noted that the cost of disposing the etchant is a significant fraction of the total cost of the etchant²⁸. While the actual etchant is priced at \$1.25/gallon, it costs \$1.30/gallon to dispose of it.

The isothermal forging operation is accomplished using a pair of TZM Molybdenum dies. Under the assumed manufacturing scenario, the dies cost \$175,000/set and are replaced after 600 forgings.

The heat treating and testing operations were assumed to be similar to those in the case of hot isostatic pressing. Each forging was assumed to be individually tested for room temperature strength, high temperature strength, and stress rupture properties. The final inspection operations included Brinell hardness testing, surface etching to reveal surface flaws, and dimensional tolerance measurements.

The assumptions used in the model are listed below:

Isothermal Forging - Assumptions

Finished Weight of Disk	4.5 lbs
Annual Production Volume	125 parts/year
Raw Material	Extruded René 95 Bar
Raw Material Cost	\$31/lb
Labor Cost	\$16/hr
Labor Overhead	40%
Labor Productivity	85%
Working Period	240 days/year

The breakdown of cost by processing step, as estimated by the model, is graphically presented in Fig. 7. Isothermal forging accounts for almost half of the total cost of the finished component, because of the high cost of the equipment and the TZM dies. Table 5 presents a breakdown of total cost by factor and process. Unlike the case of hot isostatic pressing, material costs were a far smaller fraction of total cost. This reduction is a consequence of the material yield increase associated with the process.

Competitive Analysis

Figure 8 presents a breakdown of cost by factor for the two competing processes. In the

Table 5 Breakdown of cost for isothermally forged turbine disk

By Factor

	\$/part	Percent
Raw material	\$589.00	14.05%
Process material	\$11.86	0.28%
Labor	\$705.67	16.83%
Energy	\$9.80	0.23%
Scrap credit	(\$1.24)	−0.03%
Equipment	\$1,127.45	26.89%
Tooling	\$1,356.84	32.36%
Aux. equipment	\$1.33	0.03%
Maintenance	\$169.12	4.03%
Taxes	\$22.55	0.54%
Insurance	\$16.91	0.40%
Building	\$183.49	4.38%
Total	\$4,192.78	100.00%

By Process

	\$/part	Percent
Raw material	\$589.00	14.05%
Billet operations	\$133.76	3.19%
BN coating	\$11.51	0.27%
Isothermal forging	\$2,033.89	48.51%
Etching	\$23.86	0.57%
Heat treating	\$86.88	2.07%
Tumbling	\$15.44	0.37%
Machining	\$715.37	17.06%
Inspection	\$11.79	0.28%
Testing	\$387.78	9.25%
Building	\$183.49	4.38%
Total	\$4,192.78	100.00%

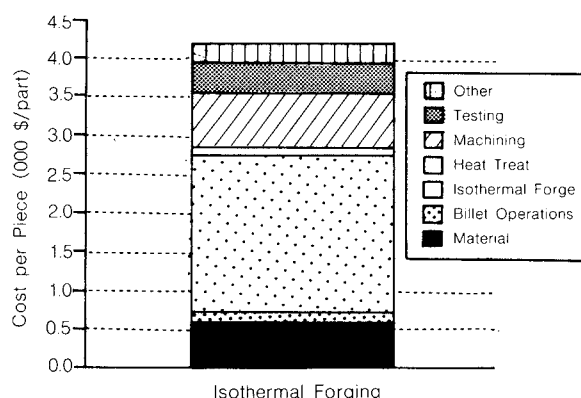


Fig. 7 Breakdown of cost by processing step for the isothermally forged turbine disk

case of hipping, the breakdown is presented for two different screening yields. The close dependence of final cost on the screening yield is clearly shown. Low screening yields, while re-

sulting in a tighter powder size distribution, lead to very high material cost. Molybdenum TZM dies, being expensive and difficult to machine result in high tooling costs. The isothermal forging press, costing nearly \$7,000,000, results in a very high per piece equipment cost.

Figure 9 presents a graphical representation of the sensitivity of cost to annual production volume. The HIP costs are presented for three different screening yields. The results show economies of scale because the fixed costs are distributed over higher volumes leading to a smaller contribution on a per piece basis. The spike in the curve at a volume of around 500 parts/year is due to the requirement of an additional set of tools. As can be seen, the break-even point shifts to higher production volumes with increasing HIP screening yields.

In other words, at low screening yields (say 10%) the hipped turbine disk is less expensive at volumes below 50 parts/year. At all volumes above this, changing to isothermal forging is economically advantageous. As opposed to this, if the yield were to increase to 15% at the

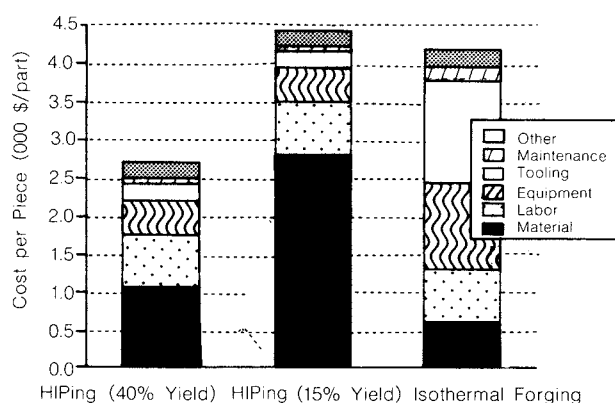


Fig. 8 Breakdown of cost by factor for the turbine disk

screening stage of the hot isostatic pressing operation, the break-even point would shift to 110 parts/year. Thus, while low screening yields result in a closer control in the powder size distribution leading to a concomitant enhancement of fatigue and mechanical properties, it also results in highly elevated costs. The original motivation for resorting to a powder process was to reduce final costs by minimizing material input. This is defeated because a coarse particle size distribution leads to poor LCF properties.

Figure 10 presents the variation of the cost of the isostatically pressed turbine disk with screening yield. The base case isothermal forging cost refers to the cost as estimated by the isothermal forging model using the set of assumptions listed above. It can be seen that at screening yields below about 16%, isothermal forging presents cost benefits over hot isostatic pressing. As screening yields increase, isostatic pressing becomes progressively less expensive. However, there is an adverse effect on properties at high screening yields. This leads to the conclusion that although isostatic pressing does present a feasible alternative and has been used in the past, production with adequate performance is not a feasible solution, especially when isothermal forging presents an attractive cost effective alternative.

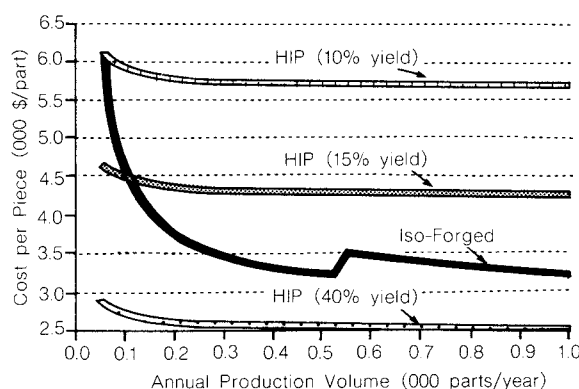


Fig. 9 Variation of cost with production volume for the case of the turbine disk

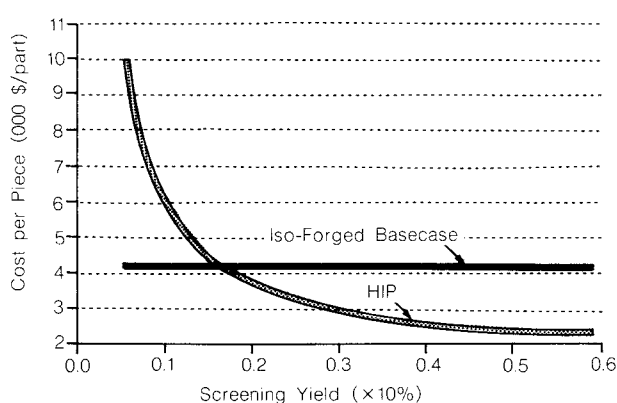


Fig. 10 Variation of HIP cost with screening yield

Based on the premise that isothermal forging is the most feasible alternative for this application, it stands to reason that efforts be directed

to reduce the cost of fabrication. Referring to Fig. 6, it can be seen that tooling is a sizable chunk of the final total cost of the component. Thus, any reduction in the cost of the TZM die set would aid in reducing the total fabrication cost.

Figure 11 presents a set of scenarios presenting the sensitivity of cost to production volume at different die set costs. The figure shows that a reduction in the cost of the TZM dies from \$175,000 to \$25,000 results in a 30% reduction of total cost at volumes around 100 parts/year.

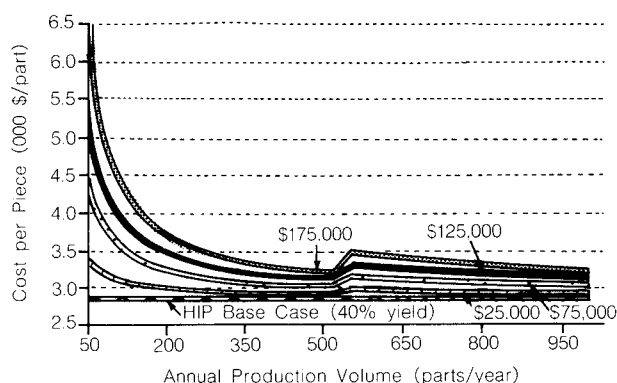


Fig. 11 Variation of total cost with volume at different TZM die costs for the iso-forged turbine disk

Case Study: Material Alternatives for Automotive Connecting Rod

Conventional forging has traditionally been the processing route of choice for this application. Of late, powder forging has emerged as a key process for this application. Powder forging yields a high density component with properties akin to those of conventional hot forging. Although this technology emerged in the early seventies, it has not been exploited as completely as one would have expected. However, Ford Motor Company has been using powder forged connecting rods ever since 1987, and production recently crossed the 10.0 million mark.

Further, in the case of conventional forging, the rods and caps have been forged and machined separately. Powder forging, on the other hand, undertakes a single piece forging operation. There seems to be no real technical reason as to why the rods and caps cannot be forged as a single piece by conventional forging as well.

Based upon these considerations, the three

processing routes for the manufacture of the automotive connecting rod and cap were evaluated: steel forging a one piece rod, forging the rod and cap separately, and powder forging a one piece rod.

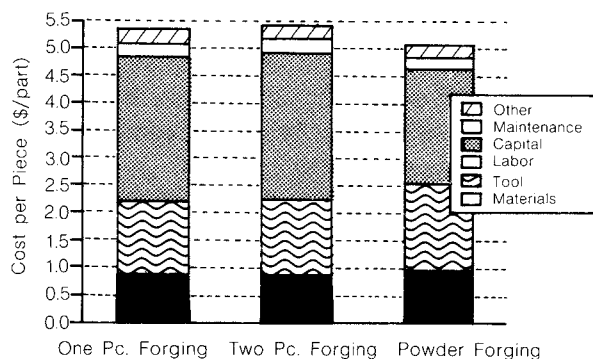


Fig. 12 Breakdown of cost by factor for the connecting rod & cap

The costs of production and their breakdown by factor are presented graphically in Fig. 12. There are several critical features to note:

Table 6 Breakup of cost by factor for the connecting rod & cap

Fully machined cost

	Combined forging	Separate forging	Powder forging
Variable costs	\$2.49	\$2.48	\$2.10
Fixed costs	\$2.91	\$3.02	\$2.96
Total costs	\$5.40	\$5.50	\$5.06

Fully machined cost

	Combined forging	Separate forging	Powder forging
Processing cost	\$2.06	\$2.16	\$2.94
Machining cost	\$3.34	\$3.34	\$2.12
Total costs	\$5.40	\$5.50	\$5.06

	Combined forging	Separate forging	Powder forging
Material	\$0.89	\$0.87	\$0.96
Labor	\$1.48	\$1.49	\$1.06
Tooling	\$1.31	\$1.37	\$1.57
Capital	\$1.21	\$1.25	\$1.06
Maintenance	\$0.24	\$0.24	\$0.21
Other	\$0.26	\$0.27	\$0.21
Total	\$5.40	\$5.50	\$5.06

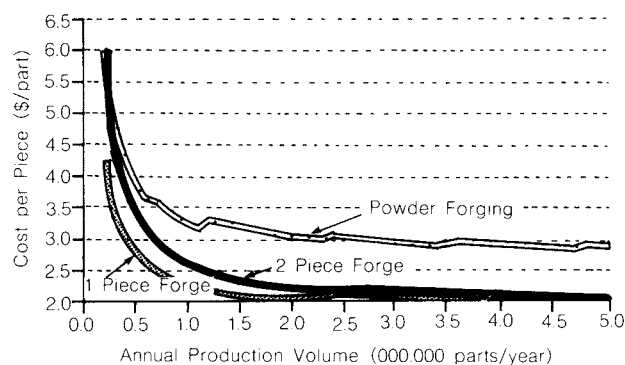


Fig. 13 Variation of cost with volume for the unmachined connecting rod & cap

- The breakdown clearly depicts the cost advantages of powder forged connecting rods over the competing processes, in spite of the high material costs.
- Forging the rod and cap as one single piece offered a cost savings over a two piece forging.
- The high cost of forging can be attributed not only to the amount of machining required, but also to the fact that expensive, dedicated equipment is required.

The fabrication costs estimated by the different models for the four cases are presented in Table 6. Powder forging is clearly less expensive than the other alternatives. Combined forging offers cost savings over separate forging due to lower fixed costs because of the elimination of a separate line to forge them separately.

Although these are point estimates, it is possible to use the cost model to evaluate the sensitivity of these costs to critical assumptions. Sensitivity with respect to volume was evaluated and is graphically presented in Figs. 13 and 14. The sensitivity of the unmachined component cost to production volume is of particular importance when evaluating a high capital, near net shape alternative to a low capital, machining intensive process. In particular, the perception of cost effectiveness can be adversely affected if the consumer of a semi-finished part is not familiar with machining differences between alternatives and their cost consequences. For example, a process which may look cost effective to a consumer who buys less expensive as-formed parts may actually entail enough in-house machining that the final part cost exceeds that which would be incurred using a

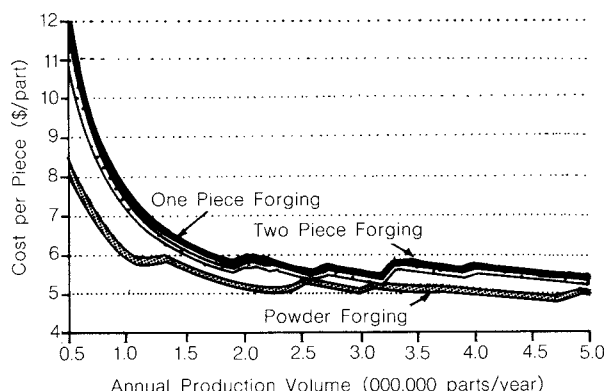


Fig. 14 Variation of cost with volume for the fully machined connecting rod & cap

more expensive, but nearer to net shape part.

At the base case production volume of 3,000,000 parts/year, powder forging yields the most cost effective component. Figure 13 clearly shows that, in the unmachined state, the powder forged rod and cap are more expensive than the conventional rod and cap. This is attributed to the high capital cost and the cost per pound of raw powder, which is almost double the cost of bar stock. Further, it is also evident that forging the rod and cap as one piece offers savings at all volumes considered up to 5,000,000 parts/year over the other two cases.

As opposed to this, as seen in Fig. 14, powder forging offers cost savings over conventional forging at all volumes up to 5,000,000 parts/year. Powder forging offers a near net shape product, unlike the conventionally forged rod and cap. This is clearly evidence by the cost savings accrued in the machining step of the operation. Thus, while powder forging was more expensive than the conventionally forged rod and cap in the unmachined state, it offers significant savings over the conventional rod and cap in the fully machined state. This is a classic example of the cost savings accrued by a shift towards a near net shape technology.

The cost difference between a two-piece and one-piece conventional forging is about 9 cents/part, which is too small to detect within the scale of the graph in Fig. 14. A primary factor influencing materials choice in this application is the issue of tooling requirements for machining of these rods. It became apparent that, once a commitment to tool a line for machining a rod and cap of a given material had been

made, it was virtually impossible to reverse the choice of material for the rod and cap, even though an alternative might offer some attractive features. Further, increases in tensile and fatigue strength served only to improve the design margin of safety in the engine. An interesting feature was the fact that, although a stiffer rod may be beneficial up to a certain limit by reducing vibration, further increases may actually be detrimental, since they can lead to increases in crank loading.

Based upon the preceding cost analyses, the powder forged rod seems to be well positioned to substitute for conventionally forged rods. However, there is considerable skepticism as to the cost effectiveness of these rods and caps. As was pointed out in the section on cost analysis of connecting rods and caps, as-forged rods are cheaper than as-forged powder rods, while in the finished state the reverse is true. At present, the machinability of powder forged rods is an issue of some concern and there seems to be a lack of comprehensive information in this area. Since it is the machining step which provides the cost benefit of powder forged rods, uncertainty in this area is almost guaranteed to slow introduction of this material technology.

Further, there is the issue of tooling expenditures on existing facilities to be considered when deciding a possible shift from conventional forging to powder forging. In the event of setting up of a new facility for connecting rods, it is quite apparent that opting for a powder forging route as opposed to conventional forging offers substantial cost savings.

The possibility of a combined forging as opposed to a two piece forging was analyzed in the preceding sections. Stemming from the cost minimizing drive in decision making, it follows that a shift to a one piece forging would improve cost effectiveness. In fact, this practice is being followed for some V-8 connecting rods and caps.

Cold forging of caps also offers the possibility of forging closer to net shape and better forging detail, reducing cost by reducing the number of machining steps. In situations where the rod and cap are forged separately, cold forging could improve cost effectiveness.

This outlines the major issues of concern for connecting rods and caps. While powder forging does not seem to be a potent threat to exist-

ing facilities, it should be borne in mind that the industry is becoming more aware of the cost effectiveness of this processing route. Thus, for the case of green field facilities, it is likely that powder forging will be seriously considered, provided that both forging and machining be conducted by the same source (since the major cost advantages come about only in the machining stage of the operation).

Discussions indicated that powder forging is the only commercially acceptable alternative to forged connecting rods in higher performance engine applications. While more exotic material alternatives do exist and are in use, they are restricted to specialty platforms or long term development programs.

To restate the primary conclusions of the utility analysis of connecting rods and caps:

1. The automotive industry is giving increased consideration to powder forged rods and caps.
2. The critical limitation to P/M competitiveness in this application is the lack of comprehensive, reliable process information, especially machining information.
3. The economic advantages of powder forging can be best exploited by fabricators who both forge and machine the component.
4. Manufacturers who are currently tooled to handle conventionally forged rods and caps can more cost effectively manufacture connecting rods from one piece forgings, rather than forging the rod and the cap separately.
5. Steel forging shops must enhance forging detail, reduce trim scrap, and move toward increased use of forging presses. Better dimensional control and the reduction of process scrap can go far to improve the economics of forging.

Conclusions

This paper has highlighted the growing importance of near net shape processes in metals fabrication. The economics of near net forming has been treated using the very useful tool of cost modeling.

The connecting rod and cap offers a classic example of the cost savings to be accrued from opting for a near net shape production route. The cost of powder forged rods and caps is

high in the unmachined state, due to the high cost of powder and capital equipment. However, they offer significant cost savings over the conventional forged rod and cap in the fully machined state, due to the fact that powder forging results in a near net shape component, which does not require extensive machining. Thus, the savings are accrued in the machining stage of the operation. While powder forging has the highest degree of acceptability at the moment due to its low cost, it is evident that redesign of the component resulting in weight savings would further enhance this acceptable rating due to cost savings.

The case of the turbine disk presents an interesting situation of competition between alternate net shape technologies. While isostatic pressing can potentially provide low cost turbine disks, it requires high material yields in the screening stage of the operation, which in turn leads to wide range of particle size distribution and degraded mechanical and fatigue properties. On the other hand, isothermal forging offers an alternative route to fabricate the component having acceptable performance. An isostatically pressed disk with performance characteristics equivalent to that of an isothermally forged disk, requires low screening yields, increasing cost dramatically. Thus, isothermal forging or *gatorizing* offers an optimal set of characteristics for commercial use in this market. Efforts to reduce the cost of the isothermally forged disk should be focused towards reducing the cost of the TZM dies. The underlying assumption in the above analysis is that the level of testing required is the same in both cases.

Isothermal forging has a promising future if one could exploit the tremendous savings in material utilization possible. In the aerospace industry, this accounts for a significant fraction of the total cost of fabrication. Parts with pronounced circular geometry are particularly well suited for isothermal forging due to the fact that the symmetry of the component aids in prolonging the die life. Smaller size and lower complexity makes it easier to forge the surfaces to net shape. In large forgings over about 150 sq.in. plane area, net surface forging becomes increasingly difficult because of the manufacturing tolerances on die dimensions, variability in material properties, and varia-

tion and non-uniformity of die temperatures²⁹⁾. Research geared towards reducing the high cost of TZM tooling or using alternate tool materials would also help enhance the economic position of this process.

References

- 1) McGee, S.W. and F.K. Burgess, "Identifying Cost Effective P/M Applications", *International Journal of Powder Metallurgy and Powder Technology*, Vol. 12, No. 4.
- 2) *Production to Near Net Shape*, American Society of Metals Source Book, Ed. C. J. Van Tyne and B. Avitzur, American Society of Metals, Metals Park, Ohio, 1983.
- 3) Van Dommelen, H.M.: "Net Shape Forming", Private Report.
- 4) Koster, W.P.: "Machining-Forecast '90", *Advanced Materials & Processes*, Vol. 137, Issue 1, January 1990, pp. 67.
- 5) Boothroyd, G.: *Fundamentals of Metal Cutting and Machine Tools*, McGraw Hill publications, 1975, pp. 142-163.
- 6) *Machining Data Handbook*, American Society of Metals Publications, "Economics in Machining and Grinding", pp. 1-41.
- 7) *Predicasts: Basebook 1987*, Predicasts, Issue No. 112, July 15, 1988.
- 8) Industry News, *International Journal of Powder Metallurgy*, Vol. 22, No. 3, 1986, pp. 138-139.
- 9) Johnson, P.K.: Metal Powder Industries Federation, Private Communication, August 1989.
- 10) *Metalworking News*, March 5, 1990, pp. 1.
- 11) Froes, F.H.: "Powder Metallurgy", *Advanced Materials & Processes*, Vol. 137, Issue 1, January 1990, pp. 56.
- 12) Driver, D.: "Near Net Shape Manufacture of Aero Engine Components", *Metals & Materials*, August 1988, pp. 492-497.
- 13) Driver, D.: "Developments in Aero Engine Materials", *Metals & Materials*, June 1985, pp. 350-352.
- 14) "High Performance Materials Demand in Aircraft Gas Turbine Engines: Market Forecasts, Technology Assessments and New Business Opportunities, 1988-1998", Gorham Advanced Materials Institute.
- 14) "High Performance Materials Demand in Aircraft Gas Turbine Engines: Market Forecasts, Technology Assessments and New Business Opportunities, 1988-1998", Gorham Advanced Materials Institute.
- 15) Private Communication, Netcast, Investment Casting Institute, January 1990.
- 16) Baker, J.F. and E.H. VanDerMolen, "Effects of Processing Variables on P/M René 95", *Superalloys Processing*, Proceedings of 2nd International Conference, September 18-20, 1972, Champion, Pennsylvania, pp. AA1-AA25.
- 17) Gessinger, G.H.: "Mechanical Properties of dispersoid free P/M superalloys", *Powder Metallurgy of Superalloys*, Butterworths, 1984, pp. 153.
- 18) Ross, E.W., D.R. Chang, R.A. Sprague and P.J. Linko: "Superalloys in 2001", *Advanced High Temperature Alloys - Processing & Properties*, Nicholas J. Grant Symposium, Ed. S.A. Allen, R.G. Pelloux & R. Widmer, American Society of Metals, 1986, pp. 152.
- 19) Gessinger, G.H. and M.J. Bomford: "Powder Metallurgy of Superalloys", *International Metallurgical Review*, Vol. 19, 1974, pp. 51-77.
- 20) Pratt & Whitney, U.S. Patent No. 3519503.
- 21) Gane, N.: "Developments in Powder Metallurgy", *Materials Forum*, Vol. 13, 1989, pp. 81-100.
- 22) Hanes, H.D. and J.M. McFadden: "HIP'ping of Castings: An Update", Asia Pressure Systems Monograph.
- 23) Nallicheri, N.V., J.P. Clark & F.R. Field: "A Technical & Economic Analysis of Alternate Manufacturing Processes for the Connecting Rod", Proceedings, International Conference on Powder Metallurgy, Pittsburgh, May 1990.
- 24) Bush, J.V. and F.R. Field: "Technical Cost Modeling", *Blow Molding Handbook*, eds. Donald & Dominick V. Rosato, Hanser Publishers, 1989, pp. 839-870.
- 25) Happ, M.B. and P.S. Clemente, "HIP of René 95", *U.S. Army Manufacturing Technology Journal*, Vol. 4, No. 4, 1979, pp. 41-44.
- 26) Eisen, B.: Crucible Compaction Metals, Private Communication, January 1990.
- 27) Lasday, S.B.: "Hot Isostatic Pressing of Heat and Alloy Corrosion RESistant P/M Alloy Components for Aerospace and Petroleum Industries", *Industrial Heating*, June 1983.
- 28) Zecco, J.: Wyman Gordon, Private Communication, December 1989.
- 29) Kulkarni, K.M.: "Isothermal Forging-From Research to a Promising New Manufacturing Technology", *Production to Near Net Shape Source Book*, American Society of Metals, 1983, pp. 157.

Compositional Variation in Multiphasic Compacted Powders[†]

Thomas P. Meloy (*Benedum Professor*)

Sigrun Drescher (*Visiting Scholar*)

Particle Analysis Center, WVU *

Abstract

For well mixed compacted powders such as those used in the Pharmaceutical and food industries, the assay variation in the composite particles is a bell shaped Gaussian curve with a mean assay of the bulk powder being compacted and a standard deviation proportional to the ratio of the powder to particle size raised to the 3/2 power divided by the volume fraction locked. With increasing compacted particle size, the standard deviation grows smaller. The Ferrara point, for these larger particles, becomes the peak of the Gaussian curve and differs in location from the Ferrara point of the smaller particles.

Introduction

God is against those that wish to store well mixed powders for later use. As soon as a batch of well mixed powders is placed in a container, segregation begins. Any form of energy – vibration, pressure variation, movement – will cause particles within the mixture to move, causing separation to occur. While the separation will never approach completion, it will soon be sufficient to change the powder—at least on the microscopic level—from a well mixed to a well segregated powder. While this segregation problem in stored well mixed powders is universal, compaction, immediately after mixing, is the widely used solution.

When a well mixed powder is pressure compacted immediately after mixing, the powder particles are bound together by a mechanical bond preventing resegregation. During the compaction process, secondary larger composite particles are created composed of a number of smaller powder particles. These larger composite particles are known as “locked particles.” Assuming ideal random mixing of the powder prior to compaction, the compositional variations, locking profile, in the larger composite particles depends on two variables: 1) the size of the larger composite particles made by compacting the well mixed powder and 2) the size

of the powder particles. This monograph considers the problem of the locking profile as a function of these two particle sizes.

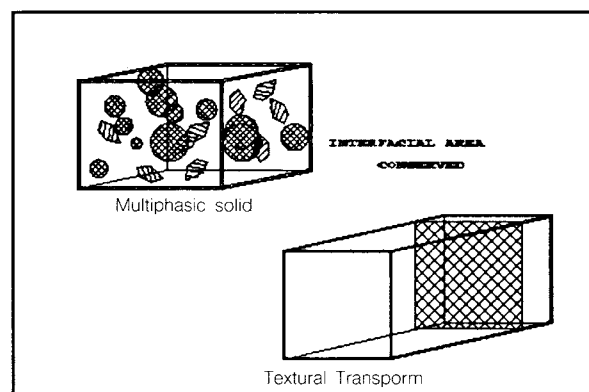


Fig. 1 Upper left solid transformed to lower left – a Textural Transform.

Composite particles, those particles composed of two or more phases or grains are called “large locked particles.” For large locked particles, the extant statistical work by Meloy *et al* (1989) uses chaos to order Textural Transforms. Locking profiles for fragments or particles smaller than the inclusions have been derived by King (1985), Barbary (1985), Schonert (1985), Lin *et al* (1984) Meloy (1984), Meloy *et al* (1985, 1986, 1987, 1989).

Although the thrust of this study is the compositional variation of large locked particles, it is informative to look at the work done on

* Morgantown, WV 26506, USA

† Received September 10, 1990

small locked particles. In contrast to a large locked particle where the inclusions are small compared to the particle size, in small locked particles, the particle is small compared to the inclusion or powder size.

To obtain the frequency distribution of small locked particles, one makes the Textural Transform (chaos to order transform) shown in Fig. 1. The chaotic arrangement of the inclusions (upper left) is transformed into an orderly solid, the Textural Transform (lower right). Three properties are conserved in this transform: 1) the total interfacial area between the two phases—the *hatched area*, 2) the volume of the continuous phase—to the *left of the interfacial plane*—and 3) the total volume of the dispersed phase—to the *right of the interfacial plane*.

For small locked particles to obtain the percent of material locked—the locking profile, one finds the volume frequency distribution of the two phases as a function of the relevant variables (Meloy *et al*, 1988). For small locked particles, the volume frequency distribution is a function **not** of the particle size but the **particle shape**.

Figure 2, half the volume frequency distribution of the two phases, shows how the slope of the curve varies from a flat plane for a locking shape factor of 1, to a deeply sided U-shaped curve for a locking shape factor of 3. Rods have a locking shape factor of 1; spheres, 1.5; flat diamonds, 2; and double ended tetrahedra, 3. Most powder particles have a shape factor of

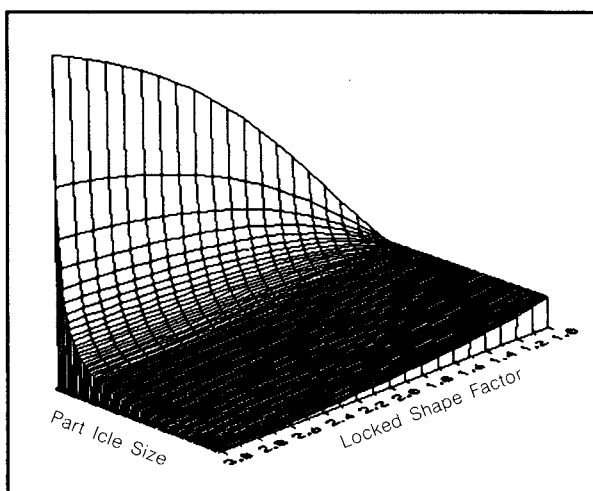


Fig. 2 One half of a locking profile as a function of particle shape

2.5 ± 0.5 .

As may be seen in Fig. 3, where the full volume frequency distribution curve may be seen, for locked particles that are blocky—those with a locking shape factor of 2.5 or greater, most of the particles have a composition close to that of a pure particle. There are few locked particles having a composition of 30% to 70%.

The locking profile of small locked particles is not sensitive to the relative particle to inclusion size ratio, but it is sensitive to the particle shape. By contrast, for large locked particles, it is expected that the reverse will be true; that the locking profile will be independent of particle shape but sensitive to particle size.

Model

Consider a powder mixture of two different powder ingredients: one the active ingredient and the other the binder or inactive ingredient. These two powders are put in continuous blender and, after the blender has stabilized, a batch of the powder is removed and immediately compacted under pressure. This compacted solid, usually a sheet, is subsequently broken into a particle size distribution of larger composite particles.

Since there is always a size distribution of the composite particles, it is assumed that the smaller composite particles, those whose size is within an order of magnitude or less of the larger powder particle size. Fines are removed because these smaller particles may segregate causing local inhomogeneities. Thus the locked particles are always significantly larger than the powder particles.

When the well mixed powder is compacted under pressure, a relatively large flat solid is formed. This flat solid is subsequently comminuted or broken into relatively large fragments—large compared to the powder particles (all the smaller locked particles are removed). As mentioned, for the purpose of this study, these composite fragments are large compared to the powder particles. In this paper the comminution-locking model used is the same Interfacial Area Conservation, IAC, model used in the referenced papers. The IAC model assumes: i) homogeneous comminution of the solid, ii) both the fragments and inclusions are randomly distributed in the compacted powder, and iii) that the intergranular area between phases

is conserved during comminution. Finally, more for the readers ease of understanding, the particles and inclusions will be assumed to be spheres.

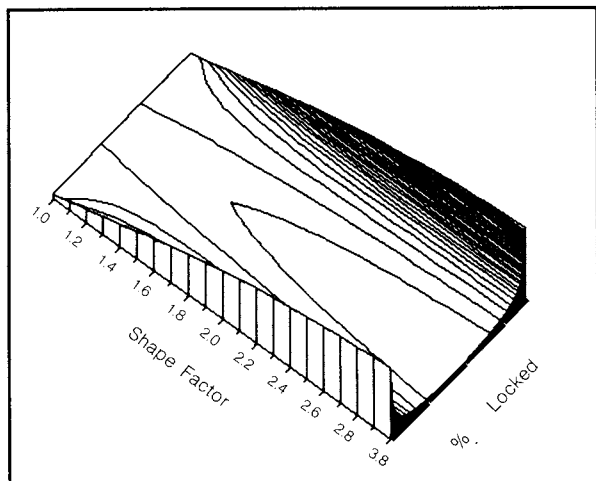


Fig. 3 Most small locked particles have a composition close to that of the pure material

When a composite fragment is much larger than the largest inclusion (powder particle), the fragment is likely to contain a number of active ingredient inclusions. On average, the large locked particle fragments will have an assay of the active ingredient phase close to that of the bulk powder mix from which it was formed. As the particle fragments become larger, they will tend to contain a larger number of active ingredient inclusions and, from a statistical view point, have an assay close to that of the bulk powder. The purpose of this work is to derive how the active ingredient locking profile of the larger composite particle varies with increasing particle size, or to be more precise, the increasing ratio of the locked particle size to active ingredient particle size. This work has important implication in pelletizing and especially pharmaceutical pill making.

Three characteristics of the compositional locking profile sought, are postulated but not assumed. First, because the larger composite particles will have a large number of inclusions in them, these particles will have, on average, the assay of the well mixed bulk powder. Second, because the assay of the large composite particles is made up of a large number of different randomly distributed active ingredient inclusions, the mean of these composite parti-

cles will be normally distributed about the assay of the well mixed powder batch. Third, the distribution about the well mixed powder mean will have a standard deviation which, along with the system mean, defines the distribution sought. Since, for the larger particles, the mean assay and the normal distribution are literally given, therefore the main task is to find: how the standard deviation varies as a function of composite and powder particle size.

Standard Deviation about the Mean

In the larger particles the assay varies from particle to particle because, in particles of the same size, there may be a different number of active ingredient inclusions or active ingredient inclusions of different sizes. More inclusions or larger inclusions may increase the inclusion assay and conversely fewer or smaller inclusions can decrease the assay. The key problem is to simultaneously find a way to handle both variations in the number and size of the active ingredient inclusions.

To handle the variation in the number of inclusions of a given size about the mean, the classical approach will be used. If N is the mean number of inclusions in a composite particle, it will be assumed that the standard deviation about the mean number of inclusions is:

$$\sigma = \sqrt{N} \quad (1)$$

Where σ is the standard deviation.

While Eq. 1 is valid for the variation in the number of inclusions in a particle regardless of the inclusions size, it is not valid for estimating the volume standard deviation when the particle sizes vary. One large inclusion can profoundly effect the composite particle's volume assay, while 10 small additional inclusions may have little or no effect. An active ingredient inclusion, 10 times the size of another inclusion, has a 1000 times its mass of the latter. Therefore (below) a method will be developed to handle the standard deviation for all inclusion sizes.

This new method, referenced above: 1) computes the number of active ingredient inclusions of a given size locked particle, 2) computes the standard deviation due to these mono sized inclusions and 3) then sums the volume standard deviations (variance) over all sizes of inclusions to find the true standard deviation

for the given size locked particle. This proposed method assumes that there is a continuous, known size distribution of inclusion (powder) sizes. From the volume size distribution, the frequency distribution of the number of inclusions as a function of inclusion size is computed. For a given inclusion size, the standard deviation for the locked particle is calculated. This number standard deviation is then converted to the volume of active ingredient inclusion of the given size to get the volume standard deviation of the active ingredient in the locked particle. The overall volume standard deviation is then calculated by first taking the sum of the variance for all inclusion sizes and then taking the square root of the overall variance, thereby obtaining the given size locked particle's volume standard deviation of the active ingredient.

Let $G(y)$ be the cumulative volume fraction size distribution of inclusions in the compacted powder where y is the size of the active ingredient inclusions and x is the size of the locked particle. Moreover, let $V_p(x)$ be the volume of a locked particle of size x , let $V_i(y)$ be the volume of the an inclusional particle of size y , V_t be the total volume of the compacted powder, V_a be the total volume of the active ingredient in the compacted powder, and V_{fl} the volume fraction of the active ingredient in the compacted powder. Thus $V_{fl} = V_a/V_t$.

For simplicity, it will be assumed that both the inclusions (powder particles) and the locked particles are spheres. Therefore their respective volumes are: $V_i = (\pi/6)y^3$ and $V_p = (\pi/6)x^3$. If all the inclusions were of size y , then the number of inclusions in a particle with a volume V_p would be proportional to V_p/y^3 and thus σ , the number standard deviation, is:

$$\sigma = \sqrt{k \frac{V_p(x)}{y^3}} \quad (2)$$

While for large particles Eq. 2 is a valid for the **number** of inclusions in the locked particle, it is not a valid basis for estimating the **volume** of the active inclusions. Near the surface in any locked particle, there is a zone, depending on the size of the inclusion, in which only part of the inclusions are present in the particle – the remainder of the inclusion volumes being in one or more other locked particles. Let these two zone be called: the interior volume and the

transition volume. Were the locked particle a sphere, then the volume of these two zones would be respectively: $(\pi/6)[x-y]^3$ and $(\pi/6)[3x^2y - 3xy^2 + y^3]$. For simplicity in the derivation, it will be assumed that the locked particle is enough large, $x \gg y$, so that the transition zone may be neglected.

Equation 2 is the number standard deviation, what is needed is the normalized number standard. Substituting for V_p and dividing Eq. 2 by the number of particles one obtains:

$$\sigma_n = \frac{1}{\sqrt{k \frac{x^3}{y^3} V_{fl}}} \quad (3)$$

The term σ_n is a function of both x and y . Rearranging Eq. 3 yields:

$$\sigma_n(y, x) = \sqrt{K' \frac{(y/x)^3}{V_{fl}}} \quad (4)$$

Since one adds variances not standard deviation, one must obtain the variance. The variance is the square of the standard deviation. Thus:

$$\sigma_n^2(y, x) = K' \frac{(y/x)^3}{V_{fl}} \quad (5)$$

What is needed is not the number standard deviation but the volume standard deviation, σ_v . When all the particles are of the same size then $\sigma_n = \sigma_v$. If one multiplies the right hand side of Eq. 4 by $dG(y)/dy$, the volume of active ingredient of exactly size y , one obtains the derivative of the volume variance, σ_v , or:

$$\frac{d\sigma_v^2(y, x)}{dy} = \frac{(y/x)^3}{V_{fl}} \frac{dG(y)}{dy} \quad (6)$$

Integrating both sides and rearranging:

$$\sigma_v^2(y, x) = K \int_0^y \left[\frac{(y/x)^3}{V_{fl}} \right] dG(y) dy \quad (7)$$

To complete the integration, an expression for $G(y)$ must be obtained. For many ground products an approximation to the volume fraction size distribution is:

$$G(y) = \left[\frac{y}{y_0} \right]^m \quad (8)$$

where y_0 is the largest size particle on the powder and m is the slope of the functions straight

line on a log-log plot.

From Eq. 8, the derivative of $G(y)$ is:

$$dG(y) = \frac{m}{y_0^m} y^{m-1} \quad (9)$$

Substituting Eq. 9 into Eq. 7 and turning the mathematical crank, one obtains for σ_v :

$$\sigma_v(y_0, x) = \sqrt{\frac{m/(m+3)}{V_{fl}}} \left(\frac{y_0}{x}\right)^{3/2} \quad (10)$$

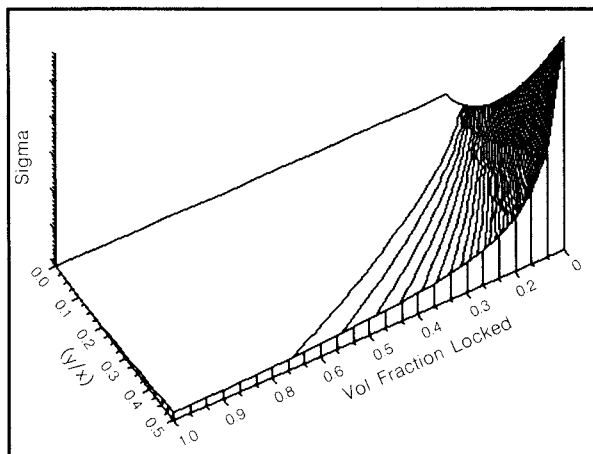


Fig. 4 Sigma is small for large V_{fl} and small y_0/x values

If the compacted powder's volume fraction locked is V_{fl} then the mean value assay also is V_{fl} . Thus the locking profile, H , for a locked particle significantly larger than the inclusions, is a Gaussian distribution with a mean at V_{fl} and the standard deviation given by Eq. 10.

$$H(\% \text{locked}) = \frac{K}{\sigma_v \sqrt{2\pi}} e^{-\frac{(y-V_{fl})^2}{2\sigma_v^2}} \quad (11)$$

Results

There are three variables in the Eq. 10: 1) the ratio (y_0/x) , the volume fraction locked and the slope of the size distribution curve. As may be seen from Fig. 4, the standard deviation is sensitive to the ratio of y_0/x because this term is raised to the 3/2 power. In Fig. 5 one may see that the σ_v is less sensitive to the volume fraction locked. For most powders m is about 0.8 ± 0.1 . Because of the square root, over the range of m , .7 to .9, σ_v varies no more than ten percent.

From Eq. 9 it may be seen that the active ingredient standard deviation decreases with in-

creasing particle size and decreasing inclusion size. In Fig. 5, the three dimensional graph, is a plot of the particle size ratio, $(y_0/x)^{3/2}$, vs the volume percent of the active ingredient in the locked particle vs the volume frequency distribution. The peak of the curve is at V_{fl} , the mean value of the active ingredient in the bulk powder. For a give size ratio, the curve, being a normal distribution about the mean - V_{fl} , is

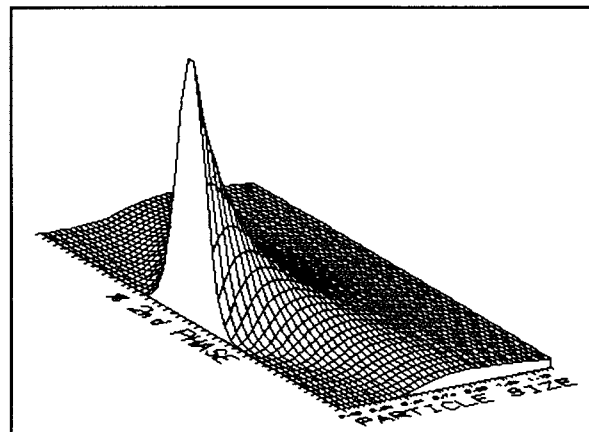


Fig. 5 As σ_n , sensitive to the ratio of $(x/y)^2$ and V_{fl} , grows smaller, the composition variation decreases See Fig. 4.

symmetrically distributed about the mean. These locking profiles of large locked particles are different from the locking profile of small locked particles seen in Fig. 1 and 2.

Note how quickly the width of the locking profile narrows with the increasing ratio of the locked particle to powder particle size. In the normal distribution, $1/\sigma^2$ appears in the exponent, hence the sensitivity to variations of the value of σ . Large locked particles have an active ingredient assay that has little variation.

In Fig. 5, for each locked particle to inclusion size ratio, the locking profile has the same area under the curve. In the larger (y_0/x) ratios - large σ_v values, the frequency distribution has low values near the mean but at the edge of the plot far from the mean, the value of the frequency distribution is still appreciable. This significant value of the frequency distribution for the smaller locked particles may be seen as the height of the curve above zero in the lower right hand corner of Fig. 5.

Discussion

In the above derivation, the quintessential

assumption stated that the standard deviation could be expressed by the square root of the number of inclusions. This assumption is valid for the Poisson distribution which assumes that the average number of inclusions is close to zero. Since one is working with an inclusion size frequency distribution, the mean number of inclusions for any one size is zero. Thus the assumption that the number standard deviation is the square root of N is valid for this derivation.

The postulate, made at the beginning of the paper, that the volume locking profile was normally distributed, is a valid assumption because this distribution is made up of the sum (integration) of a large number of inclusion size distributions. In the limit, the sum of samples taken from any shape distribution, is itself normally distributed. Since the mean of the volume fraction of inclusions for the larger particles is normally distributed, only two parameters are needed to define the curve: the mean and the standard deviation. Both these parameters have been defined and thus the curve is defined.

It is believed that the Ferrara point is a new significant parameter in the characterization of locked particles and, in of itself, a new particle shape parameter. For the smaller locked particles the Ferrara point is defined at the 50% point on the locking profile. As may be seen in Fig. 3, at this 50% point the surface, though continuous, has a crease in it, the trace of the Ferrara point. This is not the case for the larger locked particles.

In these larger locked particles, the Ferrara point shifts to the peak of the Gaussian curve. As the particle size ratio increases from the inclusions being larger than the locked particle to being smaller, the Ferrara point shifts from a trough with an assay of 50% to a peak with an assay of the mean value of the material.

As the locked particles increase in size, the sharpness of the Gaussian curve increases because the standard deviation in Eq. 10 becomes smaller with increasing locked particle size. By the same reasoning as the average inclusion size decreases, there are more inclusions of smaller size and this causes the error standard deviation to decrease. If the standard deviation is normalized with respect to the compacted powder's inclusion volume assay, then the Ferrara value

is a measure of the homogeneity of particles of a given size. Figure 5, constructed from the above information, shows how the Gaussian curve peaks as the particle size increases.

Because of the way the Ferrara point was originally defined, for these larger particles the Ferrara point is again an invariant with both the mass and volume locking profiles pass through it. As was the case for the smaller particles, the Ferrara point is relatively free from density variations and end effects and thus is an excellent point for characterizing the locked particle locking profile.

It was assumed that $y \ll x$ and therefore the transition zone could be neglected. Actually a case may be made that there is little difference in the transition zone because the missing volume appears from particles in another fragment but not counted in the given fragment. The proof is more complex.

From a practical point, larger locked particles have a relatively uniform assay but the smaller locked particles don't. When handling compacted particles, smaller particles must be discarded. This is true of the original small compacted locked particles as well as those small particles generated by the handling of the larger compacted particles. Moreover, removing the fines from the surface of the larger locked particles might be suggested for critical tests.

Because the equations derived above were based on a model that made certain assumptions, the above model's predicted results are the ideal case. In the model it was assumed that there is no differential attrition of the locked particles such that the softer phase is selectively removed from the particle surface. Moreover it was assumed that the original powder was ideally mixed and compacted in the ideally mixed state. Thus in actual practice, it would be better to use a safety factor of 10% for the inclusion to particle size ratio to handle the uncertainties in the uniformity of powder production.

In practice one would specify the value of σ_v and the V_f and from Eq. 10 find the value of the locked particle size. Smaller locked particles would be returned to the blender circuit for reprocessing. Even after long storage there would be no significant change in the uniformity of the locked particles. However there may be some attrition of the locked particles creat-

ing smaller particles.

When using the stored locked particles, the smaller particles caused by attrition must be discarded. These attrited particles, being small, have a wide variation in the compositional profile and, like the original powder will segregate readily.

Because the compositional variations were done for the general case, there is a degree of uncertainty for specific mixing-compacting systems. For these systems, the methods used here may be refined and even correlated with experience. One major assumption has been a blender that mixes perfectly – an assumption that is not always true.

Conclusions

The volume locking profile for locked particles larger than the inclusions has been derived. It is a Gaussian or normal distribution curve with its mean at the compacted powder's volume inclusion value and a normalized standard deviation inversely proportional to the square root of the particle size. At the peak of the curve is the Ferrara value, in stark contrast to its former position and value at the center of the deep U-shaped curves for locked particles smaller than the inclusion size.

1. For large composite (locked) particles, the compositional variation is a symmetrical peaked normal distribution curve.
2. The sharpness of the peak grows with increasing locked particle size.
3. The sharpness of the peak grows with decreasing inclusion size.
4. The sharpness of the peak increases with increasing volume percent locked.
5. The slope of the powder size distribution curve has a small effect on the sharpness of the peak.
6. The smaller locked particles must be discarded at the time of compaction – not stored.
7. Moreover, before using the larger com-

pacted locked particles, the secondary smaller locked particles must also be discarded.

8. A safety factor of 10% of the locked particle size is recommended to handle non uniform mixing problems.
9. It is relatively easy to specify and then obtain the correct active ingredient frequency distribution for a given set of conditions.

References

- Barbery, G. (1985): "Nouvelle Methode pour Caracteriser la Liberation Minerale par Analyses d'Images au Moyen de Mesures dans l'Espace a une et deux Dimensions. Theorie et Exemple d'Applications", XV IMPC, Cannes, June 2-9, V 1, pp. 20-31.
- Hartfeld, G., M. Marktscheffel and K. Schonert (1985): "Application of MHS – Separation in Liberation Analysis", XV IMPC, Cannes, June 2-9, V 1, pp. 88/97.
- King, R. P., N. Birtek and A.H. Juckes (1985): "Prediction of Dense Medium Cyclone Performance for Beneficiation of Fine Coal", XV IMPC, Cannes, June 2-9, V1, pp. 258-272.
- Lin, C. L., J. D. Miller, J. A. Herbst, J. E. Sepulveda and K.A. Prisbrey (1984): "Prediction of Volumetric abundance from two dimensional mineral images", 2nd Int. Cong. App. Mineral, Los Angeles.
- Meloy, T. P. (1983): "Analysis and Optimizing of Mineral Processing Circuits – Circuit Analysis", Int. J. Min. Process., V 10, pp. 61-80.
- Meloy, T. P. and N. N. Clark: "Liberation of Target Material from Locked Particles: A Theoretical Analysis", 15th Annual Meeting of Fine Particle Society, Orlando, July 1984, Abstracts, p. 16.
- Meloy, T. P. (1984): "Liberation Theory – Eight, Modern, Useable Theorem", Int. J. Min. Process, V 13, pp. 313-324.
- Meloy, T. P. and N. N. Clark (1985): "Theoretical Study of Locked Particle Comminution", XV IMPC, Cannes, June 2-9, V1, pp. 12-20.
- Meloy, T. P. and N. N. Clark: "Generalized Locking Profile for Angular Particles – Locked Particle Theory" Particle Characterization, Vol 3, 1986, pp. 63-67.
- Meloy, T. P., G. Ferrara, U. Preti and G. Schena (1989): "Locked Particle Standard Deviation for Two Phase System, Powder Technology, 59, pp. 109-115.

Ultrafine Grinding in an Annular Ball Mill[†]

Osawaru A. Orumwense and Eric Forssberg

Division of Mineral Processing

Lulea University of Technology*

Abstract

The influence of stirring speed, solids concentration, media density and size on grinding in a CoBall mill is described. The relationship between the product size and the process parameters was determined. It was observed that the product fineness is dependent on the balance between energy input and the ease with which the slurry-media (grinding bed) can be fluidized. It was found that the capacity and energy requirements are the decisive factors in optimizing the process parameters. Media colour, wear rate and separation problems would exert appreciable influence on the choice of grinding media. Very fine particles can be produced at a high throughput under optimal grinding conditions, but the associated rapid rise in temperature may be a hindrance in some applications.

1. Introduction

The increasing demands for finely ground materials and the high energy requirements in ultrafine grinding operations have given impetus to the development of effective grinding devices. The conventional ball mill, due to its characteristic high energy consumptions and long grinding times, is not efficient for ultrafine grinding purposes. Research efforts during the past decades in the area of equipment design have culminated in the availability of a number of grinding mills such as stirred ball mills, centrifugal/vibration mills and fluid energy mills.

The three equipment groups embody a variety of designs or configurations, but the basic principles within each group unchanged. Fluid energy mills are known to be the least economic of the three groups due to their relatively high energy consumption. They are suitable for grinding flaky minerals and for applications where high purity is essential^{1,2)}.

The media mills, on the other hand, differ from one another in their effectiveness. It is not uncommon to find in the literature that the stirred ball mill is more efficient than the vibration mill^{3,4)}. Distinction must, however,

be made between the high grinding rate and, the relatively high energy consumption of stirred ball mills, as against the lower grinding rate and the lower energy consumption of vibration mills. It is clear that not all types of vibration mills can compete favourably with stirred mills, but those having a characteristically small mean grinding path may surpass them in energy utilization.

This investigation deals with fine grinding of dolomite in an annular CoBall mill which belongs to the stirred ball mill group. The aim has been to study the effects of stirring speed, solids concentration, media size and energy input on the mill performance.

2. Experiment

Dolomite of size grade *E* with an approximate mean size of 57 μm (as determined with the Malvern Master Sizer) obtained from Ernström Mineral AB, Sweden, was used as received in the grinding experiments. The CoBall or annular ball mill, model MSM-18, manufactured by Fryma Maschinen AG of Switzerland, was used. The mill is equipped with a 6.8 kW motor and a Mohno feed pump with a nominal power rating of 0.18 kW. The grinding chamber consists of a stator with a toroidal base and an involuted conical rotor. The design of the stator and rotor leaves the

* 951 87 Lulea, Sweden

† Received November 2, 1990

mill with a 3.5 to 6.5 mm grinding gap. Consequently, the centrifugal velocity effect is minimized, and the radial dependent kinetic energy is effectively utilized⁵⁾. The slurry outlet and media separation mechanism are located or situated at the mill top, adjacent to the rotor. The mill is equipped with a water cooling jacket which has a maximum inlet pressure of 2 bar. A schematic representation of the mill grinding chamber is shown in Fig. 1.

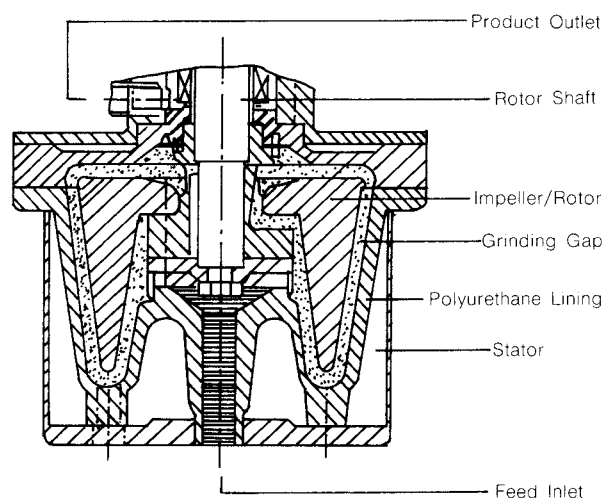


Fig. 1 Cross-sectional view of the grinding chamber of CoBall mill

The rotor circumferential speed was varied in the range of 10 to 16 m/s by changing the belt pulley on the drive motor. The mill was filled with media to approximately 70% of the effective volume. Three media size fractions, consisting of alumina balls of $-2 + 0.85$ mm, zirconia balls of $-1 + 0.65$ mm and of $-0.75 + 0.425$ mm diameter were used. The pulp density was varied between 8 to 36% volume solids. The tests were run batch-wise but with a continuous recirculation of the slurry, and samples were taken at predetermined time intervals. The feed inlet pressure was set at 1 bar and the outlet temperature at a maximum value of 100°C. The mill motor power draft was read from a three-phase kilowatt-hour meter. The product particle size distribution was analyzed by making use of an X-ray sedimentometer Sedigraph 5000 D, and the specific surface area measured using a Ströhlein area meter which is based on the single point BET method.

3. Results and Discussion

3. 1 Rotor circumferential speed

The effect of the stirring speed on the product size distribution and the specific surface area was studied in conjunction with the other operation parameters. The difference in the product characteristics attributable to the rotor speed is greatly influenced by the media size and the grinding time or energy input level used for evaluation. Generally, the higher the stirring speed, the higher the energy usage. In other words, the higher the impeller speed, the

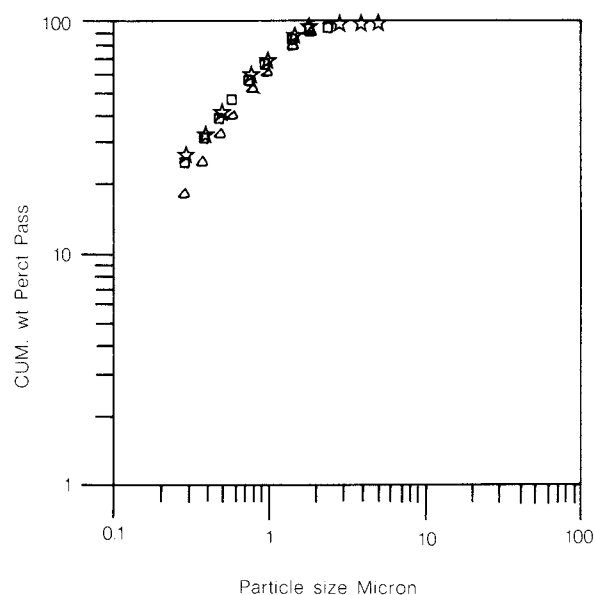


Fig. 2 Product size distribution with impeller speed as a parameter, Δ 10, \square 13 and \star 16 m/s

finer the product size as depicted in Fig. 2. Stanczyk and Feld⁶⁾ also made a similar observation in their work on stirred ball mills. The magnitude of the difference is reduced by long grinding times or high energy input levels. Where very fine grinding media are employed, the product fineness may be grossly impaired by media wear.

When the effect of stirring speed on the product fineness is assessed at a constant energy input, the order of fineness may be reversed. This method of evaluation was adopted by Mankosa *et al.*⁷⁾ in their studies on stirred ball mills. This is so because the residence or the grinding time is proportionately reduced in relation to the rate of energy input. The effectiveness of the resultant higher grinding forces due to a high rotor speed is dependent on the grinding time and the dispersion state of the

mill feed. The magnitude of the difference also depends on pulp density, media size and energy input level. Similarly, when a comparison is made based on the specific energy, the lowest stirring speed would appear to be the most economical setting, as low specific energy is often utilized under such circumstances. The plot of the product's median size against the energy input in Fig. 3 depicts those results.

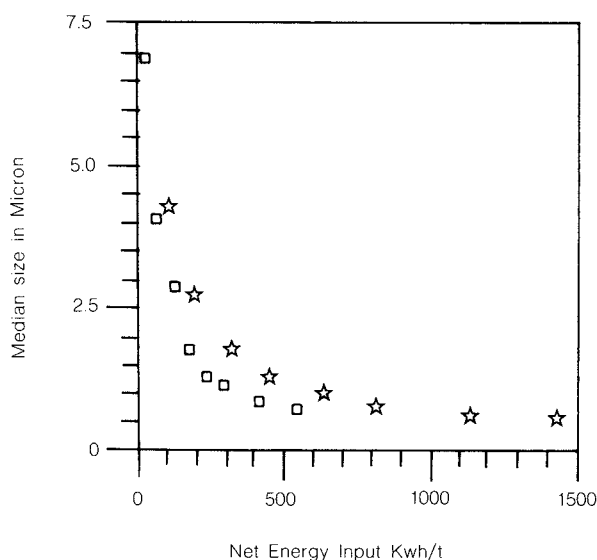


Fig. 3 Product median size as a function of the net energy input with the stirring speed as parameter, \square 10 and \star 16 m/s

The slurry temperature increases with increasing rotor speed. Although the effect of temperature is difficult to quantify, it is expected that a temperature increase either enhances grinding by reducing the apparent slurry viscosity, or impedes grinding by drying up the slurry through rapid evaporation of water. However, Stanczyk and Feld⁶⁾ reported that a temperature rise slightly improves grinding.

3. 2 Pulp density

The solids content of a mill feed is an important parameter in wet grinding operations because of its direct relationship with the mill capacity, ease of attaining the desired product fineness, and operating costs or energy consumption. This seems to be much more pronounced in ultrafine wet grinding operations, where the required product fineness often necessitates the use of a very low solids content as classification is seldom employed.

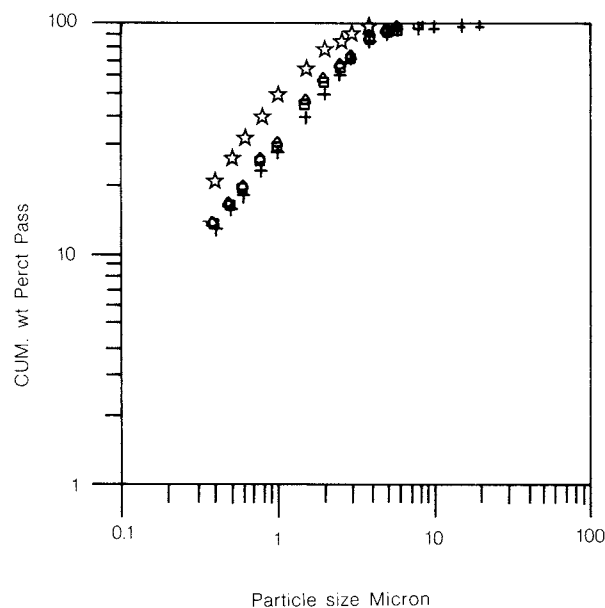


Fig. 4 Product size distributions with solids concentration as a parameter, \star 8%, \square 13%, \triangle 26% and $+$ 36% volume solid

The effect of pulp density is shown in Fig. 4. It can be seen that the product fineness increases with decreasing solids content, despite the fact that the difference between 13 to 36% volume solids appears to be small. While the products in general become coarser as the pulp density increases, the magnitude of the difference is reduced at long grinding time intervals. This depends of course on how the slurries have been prepared. If the change is made by mere water dilution as it is the case for the 26% and 36% volume solids in the given figure, there will be almost no difference in the product fineness provided the slurry volume is not very large. The major difference in such a case is that the less dense slurry can be subjected to grinding for a longer period. Reduced fluidity and the cushioning effect of fines are some of the causes of decreased product fineness.

The use of viscosity modifiers in such instances, allows more energy input by way of extended grinding times as would water dilution, and in addition, dispersion of particles in batch operations. Similar to the observation on the use of dispersants⁸⁾ in vibration mills, the ground products were found to be slightly coarser in the presence of grinding aids. This phenomenon can be attributed to the drop in the apparent viscosity of the slurry resulting in the sedimentation of the coarse particles and

the lubrication effect of dispersants.

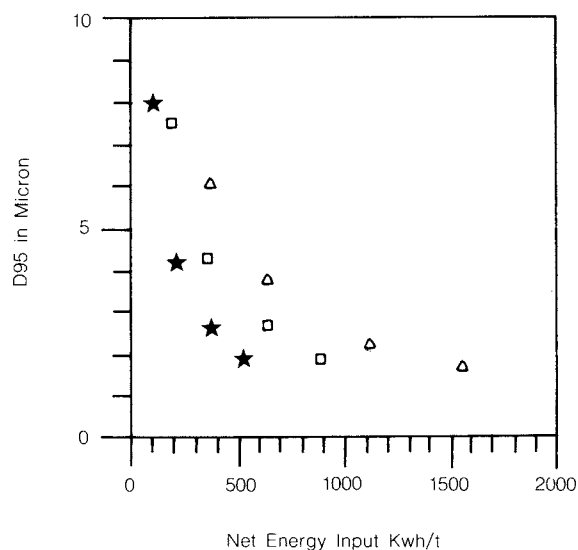


Fig. 5 Product size (d_{95}) as a function of the net energy input with the pulp density as parameter, Δ 8%, \square 13% and \star 26% volume solids

When the effect of the slurry solids content is compared in terms of energy input as in Fig. 5, a better result is obtained with a high pulp density, as a relatively lower specific energy is utilized. However, a high pulp density is associated with such problems as a rapid increase in viscosity and a low unit output, as a relatively longer time is required to attain a desired size. On the other hand, the use of a very low pulp density constitutes an ineffective mode of operation as it involves high media wear, high energy concentration, and consequently high wastage. In mills having small grinding chambers, this would also result in a short residence time and hence coarser products. Pulp density is known to be greatly influenced by the material characteristics and media size, since the larger the media size, the higher the solids content that can be employed. In addition, the process-related parameters such as the operational characteristics of the mill and pump can also be a hindrance.

It is known that as the particle size decreases, the particle number concentration or viscosity increases, and the slurry exhibits a pseudo-plastic or Bingham plastic behavior. The consequence of this in a stirred mill is that the resultant slurry agitation is turbulent when near the impeller, and stagnant or laminar in other

parts, especially when far from the impeller⁹). This phenomenon, and the resilient nature of fine particles, are the main causes of the decrease in particle breakage, as the viscosity or slurry density increases. As the solids concentration or apparent viscosity of the slurry increases, the power draft of the stirring mechanism rises asymptotically. This rapid rise in power draft often results in the drive motor becoming overloaded, causing occasional operational difficulties. Thus, the relationship between the slurry pulp density and the stirrer motor power draft places a restriction on the pulp density that can be employed.

3. 3 Media size

Figure 6 shows the influence of the media

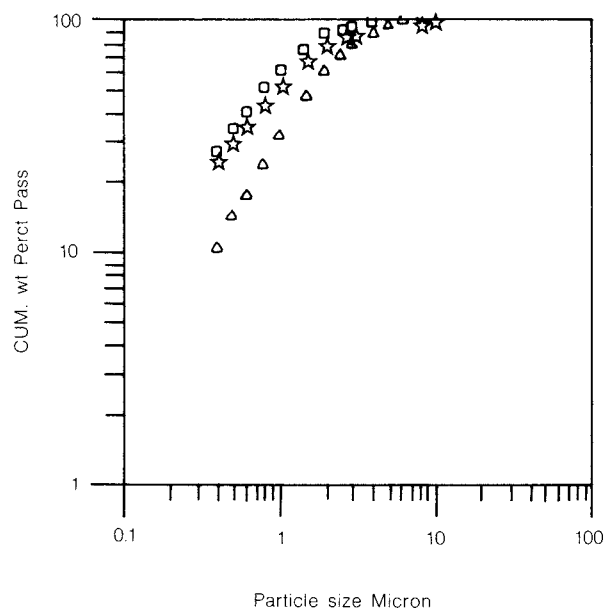


Fig. 6 Product size distribution with grinding media size as parameter, Δ 0.59 mm, \square 0.83 mm and \star 1.42 mm media diameter

size on the product size distribution. The product size becomes finer as the media size decreases. This trend is upheld until the media size becomes too small to effectively nip the feed particles. A similar trend can be discerned in terms of the product's specific surface area, as depicted in Table 1. Besides the increased probability of particle capture arising from the use of fine media sizes, the corresponding increase in fluidity results in reduced energy input. The high dispersion implies intense compressive and torsional stresses³), and conse-

quently high particle breakage. The mass of

Table 1 Product characteristics and ball wear as a function media size

Media material	Media size mm	Product			Ball wear g/kWh
		d_{95} μm	spec. surf. m^2/g	$-1 \mu\text{m}$ kg/kWh	
Zirconia	$-0.75+0.43$	1.40	14.996	1.139	380.87
Zirconia	$-1.00+0.65$	1.20	19.196	0.657	5.24
Alumina	$-2.00+0.85$	1.60	17.133	0.529	6.24

material finer than $1 \mu\text{m}$ produced per unit energy input decreases as the media size increases (under identical grinding conditions) as is evident in Table 1. This must, however, be combined with the wear resistance to give a complete overview of the cost-effectiveness of the respective ball sizes. Media choice is without doubt more crucial to the success of ultra-fine grinding than is usually assumed.

Conley⁵⁾ has suggested a media to feed size ratio in the range of 7:1 to max. 20:1 as being the optimum range for effective operation of stirred ball mills. Although this range is consistent with the observation here, the lower limit of the media-feed size ratio is about 10:1, possibly due to the grinding mechanism. Mankosa *et al.*¹⁰⁾ found that maximum breakage occurs with a media-feed ratio of 20:1. Our results show that the media-feed ratio should be less than this value. From a theoretical viewpoint, the grinding efficiency will be improved if the media – feed ratio can be maintained as the particle size decreases. However, this is a very cumbersome task in practice as media wear and separation problems become pronounced.

3. 4 Media wear

Media wear necessitates frequent replacement of the grinding media. In coarse grinding operations, the average media consumption is known to be in the range of 0.1 – 1 kg/t, and the resultant media replacement costs can be as high as 40% of the total milling costs¹¹⁾. The replacement costs will be much higher in ultra-fine grinding operations. Besides this, wear is generally a source for product contamination.

The media consumption observed in the present work is given in Table 1. It is evident that media wear resistance deteriorates with decreasing media size. The high wear rates of the

finest media size fraction is due to ball breakage, poor separability of the smallest balls, and the relatively low specific energy associated with the use of small balls. The high breakage observed with the finest grinding media is partly due to the tendency of the relatively larger balls to grind the smallest ones, and possibly due to some manufacturing defects of the balls. Media wear arises from the combined effects of attrition and impact forces, which are the characteristic grinding mechanisms of the process. Media wear is influenced by the grinding method, stirring speed, and by the media and material characteristics – shape, size, and hardness. The results of Stanczyk and Feld⁶⁾ show that spherically-shaped media are more resistant to wear than angularly-shaped media. It can be inferred from the same work that the media hardness or the specific gravity is secondary in importance to media shape in terms of wear resistance. Similarly, the higher the media density, the higher the power required for fluidization.

3. 5 Product size and process parameters correlation

The product's median size and d_{95} have been correlated with the various process parameters by the method of least squares and the following relation was obtained:

$$di = aE^b d_B^c N^e \rho^f \quad (1)$$

The correlation coefficients are greater than 0.95, and the standard deviations are less than 10%. Therefore, the parameters account reasonably well for the observed product size. The coefficients of the model are given in Table 2.

Table 2 Coefficients for all regression equations

	a	b	c	e	f	st.dev.	R adj.
d_{50}	4.941	-0.804	0.371	0.971	-0.476	0.057	0.960
d_{95}	17.561	-0.966	0.476	1.180	-0.742	0.080	0.946
E	0.175	0.818	0.855	1.998	0.878	0.110	0.936
P	0.121	1.896	0.807	0.369		0.100	0.830
S	0.474	0.508				0.087	0.857
d_{95}	197.198	-0.689				0.172	0.754

The process parameters influence the product size in the following decreasing order: rotor speed, energy input, solids concentration, and grinding ball diameter. While the stirring speed and the ball size have a direct power relation

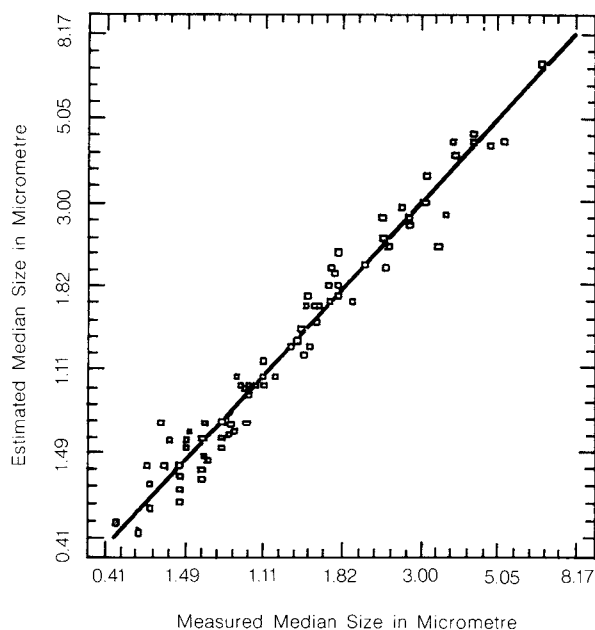


Fig. 7 The relationship between estimated and measured product median size

with the product size, energy input and pulp density on the other hand show an inverse relationship. The median size estimated by Eq. 1 is plotted against those measured experimentally in Fig. 7.

3. 6 Energy consumption

The power characteristics of stirred ball mills have been determined to be similar to those of turbine-agitated mixers from tests using pure water, a glycerol – water mixture, and very fine solids slurries in the absence of grinding media^{12,13}). Usually, stirred ball mills are operated at such a high speed that the characteristic fluid motion is turbulent. Thus, the mechanical power from theory is independent of the Reynolds number, and is given by the following relation as:

$$P = k \rho_1 N_1^3 D^5 \quad (2)$$

However, tests with coarse feed and those in which the grinding media size^{4,12}) have been considered, exhibit gross deviations. Thus, the consideration of a stirred ball mill as being similar to mixers is at best a first approximation, and provides a means for correlation with an established theory. The Reynolds number for the operation range of the CoBall mill used here lies within the values of 6×10^5 to 1×10^6 with pure water. Therefore, turbulent flow evi-

dently prevails. The power draft is observed to increase with increased solids concentration and media size, while the product fineness shows an opposite trend. This is because more energy is utilized or wasted in keeping the solids in suspension under such conditions. Numerical correlation of the process parameters with the net energy consumption by the method of least square yields the following relation:

$$E = a T^b d_B^c N^e \rho^f \quad (3)$$

The coefficients and standard deviations of the equation are given in Table 2. The high correlation coefficients and the low standard deviations imply that the net energy consumption is well accounted for by the model parameters. The parameters in decreasing order of importance are: stirring speed, solids concentration, media (diameter) size, and grinding duration. Although the grinding media density was expected to play a vital role, its exclusion from the above model exerts no significant effect on the correlation coefficient and standard deviation.

Therefore, the net energy consumption was converted to net power draft, and further numerical evaluations were made with the grinding time held constant, to see if a model similar to that given by Sepulveda³) would be obtained. The model so obtained is as follows:

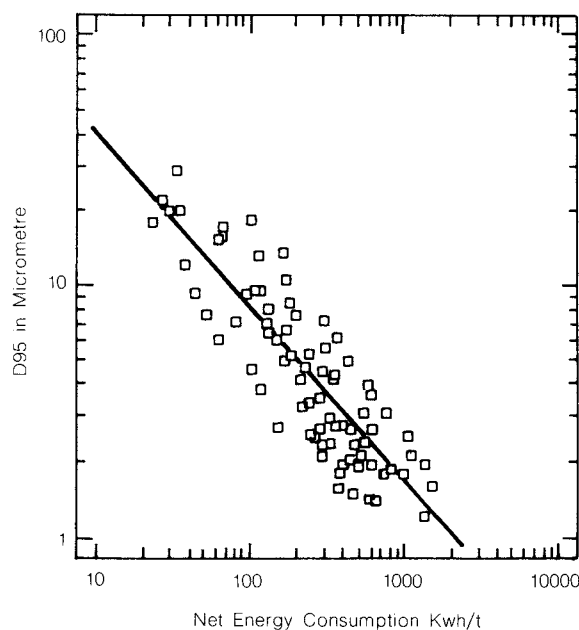


Fig. 8 Product size (d_{95}) as a function of the net energy consumption

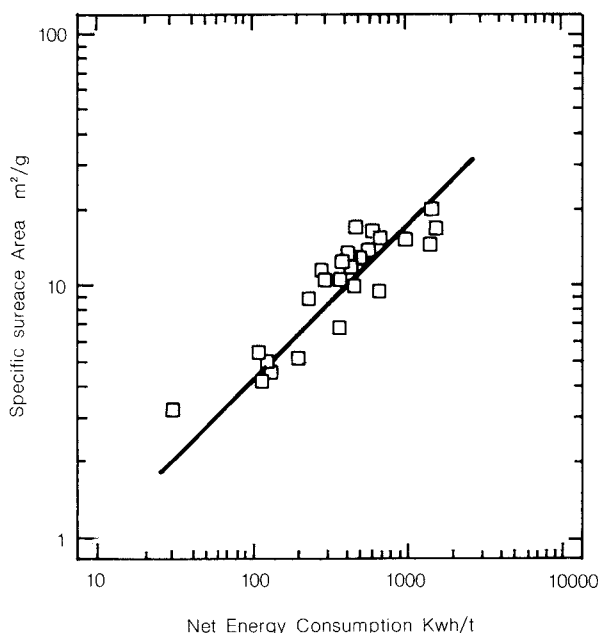


Fig. 9 Specific surface area of the product as a function of the net energy consumption

$$P \text{ (kW)} = a N^b d_B^c \rho^e \quad (4)$$

Thus, it seems likely that the effect of media density is well accounted for by the media size, and the former need not be included in the model. Net energy consumption as used here, is defined as the difference in electrical energy to drive the mill rotor with and without loads.

The product's top size, represented by the size corresponding to 95% passing, and the product's specific surface area respectively, are plotted as a function of the net energy input in Fig. 8 and 9. The straight lines in the figures were drawn by using the following regression equation:

$$d_{95}, S = a E^b \quad (5)$$

The regression coefficients for the equation are given in Table 2. The scatter of points in both figures arises due to the fact that the product fineness or the grinding effectiveness depends more on the way that the grinding energy is applied than on its magnitude. Thus, excessive concentrations of grinding energy, which is a typical feature of high stirring speeds and a low slurry density, often represent a time-effective but an energy-ineffective mode of operation. This situation is illustrated in Fig. 5, where the product size (d_{95}) is plotted against the net energy input. It can be seen

that as the pulp density increases to a certain extent, a low specific energy is utilized to obtain a specified size. It should be borne in mind that the scatter in Fig. 9 arises from varying just one single parameter. In a situation where the effects of a number of parameters are superimposed as in Fig. 8, the variations in the product size acquires a different magnitude.

4. Conclusions

The CoBall mill would be suitable for ultra-fine grinding operations with a high throughput, if properly operated. However, the tendency of the temperature to rise rapidly may be a limitation in its use for the grinding of heat sensitive materials.

The mill power consumption and the product fineness are influenced by the stirring speed, solids concentration, grinding media size, and hardness. The process parameters can either be tuned to maximize unit output or to minimize specific energy consumption, as desired.

The product fineness is enhanced when the media to feed size ratio is within the range of 10:1 to 20:1. Grinding is inferior above and below this range.

The suitability of a particular media type and size should be assessed in terms of the associated specific energy, wear rate, and colour. The performance of the media at the pulp density of interest in the case of wet grinding should be checked since the former is greatly influenced by the solids content.

Although the wear rate of zirconia balls is relatively low, the yellowish colour poses severe contamination problems, and so they may be unsuitable where a high product brightness is required, as in coating applications.

Acknowledgement

This work was partially supported by the Swedish Mineral Processing Research Foundation.

Nomenclature

a, b, c, e, f, k	: constants
d_i	: product size – median size and d_{95} [μm]
d_B	: grinding media (diameter) size [mm]
d_{95}	: product size corresponding to 95% passing [μm]
D	: impeller diameter [m]
N_1	: impeller rotation [Hertz]

N	: impeller circumferential speed	[m/s]
E	: net energy consumption	[kWh/t]
P	: impeller power draft	[kW]
T	: grinding time	[minutes]
S	: specific surface area	[m ² /g]
ρ	: solids content	[kg]
ρ_1	: slurry pulp density	

References

- 1) Nied, R.: The Fluidized Bed Counter Jet Mill – Recent Findings and New Applications. *Aufbereitungs-Technik* (1982) 5, p. 236/242.
- 2) Ramanujam, M. and D. Venkateswarlu: *Studies in Fluid Energy Grinding*. *Powder Technology*, 3 (1969) 2, p. 92/101.
- 3) Sepulveda-Jimenez, J. L.: A Detailed Study on Stirred Ball Mill Grinding. Ph. D. Dissertation, Metallurgy Department, University of Utah, Salt Lake City, Utah, USA, 1981.
- 4) Stehr, N. and J. Schwedes: *Investigation of the Grinding Behaviour of a Stirred Ball Mill*. *German Chemical Engineering*, 6 (1983), p. 337/347.
- 5) Conley, R. F.: Attrition Milling of Industrial Minerals. Conference Processing of the Ultrafine Grinding and Separation of Industrial Minerals, Malgahan, S. G. ed., New York; SME-AIME, 1983, p. 37/48.
- 6) Stanczyk, M.H. and I. L. Feld: Investigation of Operating Variables in the Attrition Grinding Process. US Bureau of Mines RI 71681, 1968, p. 28.
- 7) Mankosa, M. J., G. T. Adel and R. H. Yoon: *Effect of Operating Parameters in Stirred Ball Mill Grinding of Coal*. *Powder Technology*, 59 (1989), p. 225/260.
- 8) Orumwense, O. A. and E. Forssberg: *Comparison of Dispersants in Vibration Milling of Dolomite*. *Aufbereitungs-Technik*, 31 (1990), 5, p. 257/265.
- 9) Uhl, V.W. and J. B. Gray: *Mixing – Theory and Practice*, Vol. 111, Academic Press Inc., London, 1986.
- 10) Mankosa, M. J., G. T. Adel and R. H. Yoon: *Effect of Media Size in Stirred Ball Mill Grinding of Coal*. *Powder Technology*, 49 (1986), p. 75/82.
- 11) Wills, B. A.: *Mineral Processing Technology*, Fourth Edition, Pergamon Press, England, 1988.
- 12) Sadler, L. Y., D. A. Stanley and D. R. Brooks: *Attrition Mill Operating Characteristics*. *Powder Technology*, 12 (1975), p. 19/29.
- 13) Stanley, D. A. *et al.*: *Attrition Milling of Ceramic Oxides*, *American Ceramic Society Bulletin*, 53 (1974) 11, p. 813/829.

Experimental Investigation of Silo Stresses under Consideration of the Influence of Hopper/Feeder Interface[†]

Dietmar Schulze and Jörg Schwedes

Institute of Mechanical Process Engineering
Technical University Braunschweig*

Abstract

With the data gathered from an experimental silo, operating with two different kinds of bulk solid (cohesive limestone powder and free-flowing plastic pellets), it is shown to what great extent the geometry of the transition from hopper to feeder influences flow profile and thus the stress pattern within the hopper. The optimal geometry for achieving mass flow and even withdrawal of a bulk solid over the entire outlet area depends on the bulk solid's flow properties and, in the case of the cohesive limestone powder, must be closely adhered to, as the flow pattern of this particular bulk solid is very sensitive to any deviations.

Furthermore, it is shown how the load acting on the feeder can be ascertained. While the power required of the feeder for bulk solid removal in the discharging condition can be satisfactorily calculated from Jenike's theory, some well-known analytical methods available for the filled condition of the silo provide results which are too imprecise. The assumption of hydrostatic conditions in the hopper leads to stress values which are several times greater than those actually measured in the experimental silo. With the help of the empirically based equations, DIN 1055, Part 6, one can find acceptable solutions for the order of magnitude and for the tendency of the stresses acting on the hopper walls. How one might determine the load on the feeder from these solutions needs further looking into.

Through basic physical considerations, the dependency of the force required for removal of a bulk solid from under the outlet on the vertical load acting on the feeder, was found to be of a simple nature, from which an upper limit can be calculated. This was confirmed by measurements made on the experimental silo.

1. Introduction

In order to achieve mass flow, avoiding arching and pipe formation, a silo must be designed to suit the bulk solid it is to hold, the properties of which can be determined in shear tests^{1,2,3)}. The outlet of a silo is usually provided with a feeder which serves to regulate withdrawal of the bulk solid. It should be adapted to the outlet so as to remove the bulk solid from its entire cross-sectional area.

The form of the feeder and the geometry of the adjoining outlet play a decisive role here. This is demonstrated for the case of a belt conveyor illustrated in Fig. 1.1. A horizontally

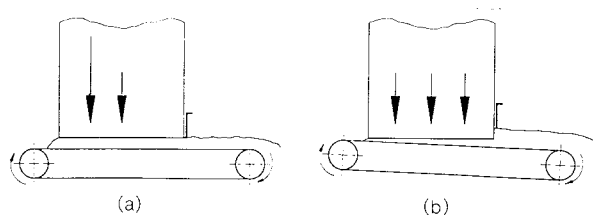


Fig. 1.1 Influence of feeder geometry on flow profile

mounted belt conveyor beneath a horizontal, rectangular outlet often leads to bulk solid being removed predominantly from the rear end of the outlet (Fig. 1.1a). By inclining the lower edge of the feeder or installing a slide gate on its front side, one can effect bulk solid removal from the whole area of the outlet (Fig. 1.1b)^{4,5)}.

* D-3000 Braunschweig, Volkmaroder Str.415, Germany

† Received November 2, 1990

In order to remove material from under the outlet, the feeder must be in a position to move the bulk solid against the forces of stress containing it, that is, to overcome the forces of internal friction. As would be expected, these forces depend on the properties of the bulk solid itself, on the stress acting in the outlet and, consequently, on the stress in the silo as a whole. On the other hand, the feeder itself influences conditions within the silo – for example, by uneven removal of material, leading to dead zones or to regions with unequal flow. It is clear that not only the feeder is influenced by conditions in the hopper, but that these conditions themselves are influenced by the action of the feeder.

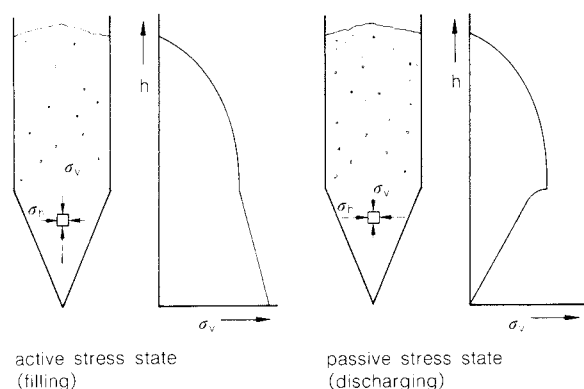


Fig. 1.2 Active and passive stress fields within the silo

In a silo, two basic stress conditions can be distinguished which lead to different loading of the feeder. In Fig. 1.2, the so called “active stress field”, present just after filling the silo, is shown on the left, while on the right the “passive stress field” developed during discharging is illustrated. Under conditions of active stress, the largest principal stress along the axis of the silo acts in a vertical direction, while the smaller principal stress acts horizontally. When the silo is discharging, due to converging in the hopper, the bulk solid is compressed in a horizontal direction, which results in the largest principal stress along the silo axis shifting to a horizontal direction. Under active stress in the hopper section, an increase or a decrease in the largest principal stress in vertical direction is possible, depending on the geometry of the hopper and on the properties of the bulk solid, whereas under conditions of passive stress, the largest principal stress is proportional to the local hopper diameter. For this reason, the ver-

tical stress at the level of the outlet is generally less under conditions of passive stress than under conditions of active stress.

When considering the form and capabilities of a suitable feeder, apart from the requirement of ensuring mass flow, one must find answers to the following questions regarding the two types of stress field mentioned above:

- How does the stress field in the hopper and in particular the stress of the bulk solid on the feeder itself depend on the properties of the bulk solid and on the geometry of the silo?
- How does the power required of the feeder in order to remove the material depend on the properties of the bulk solid and on the vertical stress?
- What form should the connection between hopper and feeder have in order to ensure that material is removed from the entire area of the outlet?

In the literature, one finds initial attempts at describing these relationships, whereby, however, the influence of the feeder on the conditions of stress is not taken into consideration and furthermore, they are usually only applied to cohesionless bulk solids. In order to cast more light on the matter and to seek answers to the above questions, measurements were made on an experimental silo. Using the obtained results the aforementioned attempts at description were checked for their validity and usefulness in practice.

2. Experimental Set-up

The experimental silo, which was set up specifically to answer the stated questions, was given a plane geometry (length in the direction of conveyance 800 mm, width 600 mm, height of vertical section 3700 mm) and provided with a belt conveyor suspended under the outlet slit. The silo stands on four legs, connected with diagonal struts, thus forming a stable, self-sufficient structure. The walls are made of perspex (thickness 20 mm) supported by diagonal struts to prevent bulging.

In order to vary the silo's geometry, it was possible to alter the positions of both the vertical and hopper walls. The different combinations of adaptable walls enabled the construction of silo geometries with an outlet diameter between 100 and 300 mm and a hopper slope

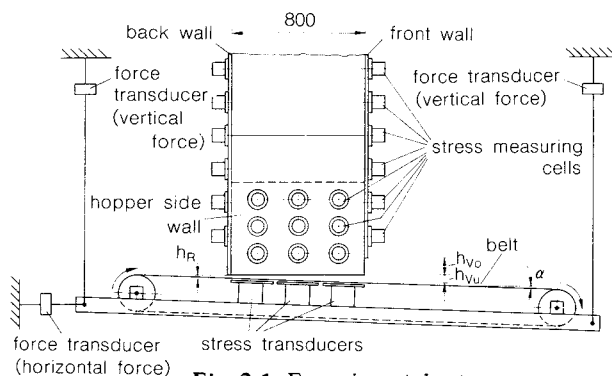


Fig. 2.1 Experimental set-up

ranging from 10° to 40° against the vertical.

Besides these factors, those shown in Fig. 2.1 can also be varied:

- h_{Vu} Distance between belt and lower edge of hopper side walls (below front wall)
- h_{Vo} Distance between lower edge of front wall and lower edge of hopper side walls
- h_R Distance between belt and lower edge of hopper back wall
- α Inclination of belt to horizontal, lower edge of hopper side walls

By varying these factors – as already intimated – discharge behaviour can be influenced: according to the factors chosen, the bulk solid will be removed from across the outlet either evenly or unevenly. Furthermore, Fig. 2.1 shows the individual gauges employed in the experimental set-up. The belt conveyor is suspended from steel cables attached to force transducers for measuring the vertical force acting on the conveyor belt. Force transducers are also built into the belt conveyor for measuring the horizontal forces arising during operation.

A total of 25 stress measuring cells developed at the Institute of Mechanical Process Engineering^{6,7)} were fitted into the silo walls. They served to record the normal and shear stresses acting on the silo walls, and were positioned mainly in the region of the hopper. Below the conveyor belt, in the area under the outlet, three further force transducers were installed for measuring the forces acting on the belt. Besides a few signal amplifiers and chart recorders, data were fed into a computer-controlled data recording unit consisting of three multi-channel digital amplifiers with a total of 130 channels and a PC.

As experimental bulk solids, cohesive limestone powder (mean particle size $x_{50} = 5.3 \mu\text{m}$) and plastic pellets ($4 \text{ mm} < x < 6 \text{ mm}$) were

chosen. The bulk density, ρ_b , the effective angle of internal friction, φ_e , and the wall friction angle, φ_x , of the mentioned bulk solids are listed in Table 2.1.

Table 2.1 Flow properties, measured in a Jenike Shear Tester at major consolidation stresses $\sigma_1 = 10 \text{ kPa}$ (limestone powder) and $\sigma_1 = 6 \text{ kPa}$ (plastic pellets)

Bulk solid	ρ_b [kg/m ³]	φ_e [°]	φ_x [°]
Limestone powder	1200	38	26
Plastic pellets	535	20	10

3. Experiments

3. 1 Investigation of stresses acting within the hopper and on the feeder

Measurements of filling stresses were made with hopper slopes Θ ranging from 10° to 40° in order to discover the relationship between the measured stresses and the hopper slope. The data obtained were compared with the results of well-known attempts to describe filling

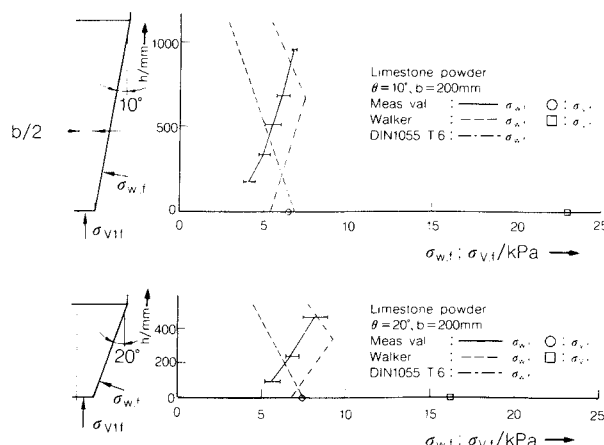


Fig. 3.1 Normal stresses on the hopper wall for $\Theta = 10^\circ$ and $\Theta = 20^\circ$ (limestone powder)

stresses in silos. In Fig. 3.1 for the examples $\Theta = 10^\circ$ and $\Theta = 20^\circ$, the measured pattern of normal stress on the hopper wall, as well as the vertical stress at the level of the outlet are shown. In addition, the stress patterns obtained from the well known analytical models of Walker⁸⁾ and Walters⁹⁾ and from the DIN 1055, Part 6 equations¹⁰⁾, which are based on empirical relationships, are shown. According to Walker and Walters, there is a certain hopper slope Θ , which in the case under consideration would be lower than 10° , above which a hydrostatic increase in stress in the hopper is

assumed. One will note when comparing it to the experimental data that this model leads to vertical stresses which are too large, and that also the tendency and the order of magnitude of the normal stresses acting on the hopper walls is not correct. The overcalculated vertical stresses lead to an overestimation of the feeder load and of the power required of it to remove the bulk solid from under the outlet. This model is nevertheless recommended and used by many authors^{3,5,9,11}, since there is no simpler model at present which will predict the stresses acting in a hopper and because in respect of the load acting on the feeder, one wants to be on the safe side. The degree of overestimation of the feeder load decreases with increasing hopper slope angle Θ .

The stress patterns calculated from the empirically based DIN 1055, Part 6 show a better correlation with the experimental data in respect of the order of magnitude and tendency. However, DIN 1055 offers no indication of how to calculate the vertical stress acting at the level of the outlet.

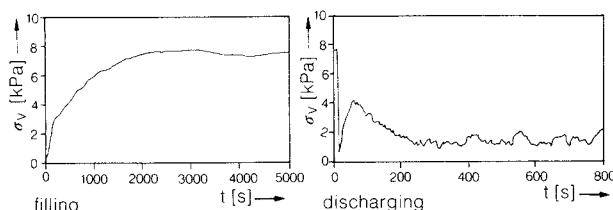


Fig. 3.2 Vertical stress σ_v at the outlet vs. time (limestone powder)

The course of the changes in vertical stress acting on the belt conveyor during filling is shown on the left in Fig. 3.2. One recognizes a typical course of events, whereby the stress initially rises sharply before reaching a final value which is independent of the height of the charge. In this case, the final vertical stress acting on the middle of the belt conveyor after filling was 7.7 kPa. When discharging is initiated, the vertical stress on the belt conveyor changes as shown on the right in Fig. 3.2. As soon as the belt conveyor is turned on the vertical stress drops sharply, increases somewhat, drops again, and finally settles at a constant average value. The fluctuations in stress are the result of what is going on in the hopper during discharging, eg. shear bands which descend with the bulk solid and arches which after for-

mation immediately collapse, both resulting in a fluctuating load on the feeder.

The sharp fall in vertical stress observed immediately after beginning discharging is due to the time required for the cohesive bulk solid to change from a resting state to one of movement. Once it has gained motion, the vertical stress increases again. At the same time, the stress field within the hopper changes from that characteristic of the filling condition (active stress field) to that of the discharging condition (passive stress field), which soon leads to the vertical stress dropping again to a constant average value.

Similar experiments using plastic pellets as the experimental bulk solid show a sharp fall in vertical stress after initiating discharge, too. However, contrary to the behaviour of the limestone powder, the passive stress field here has developed and the average value of the vertical stress remains constant, i.e. there is no further increase in vertical stress after the sharp fall.

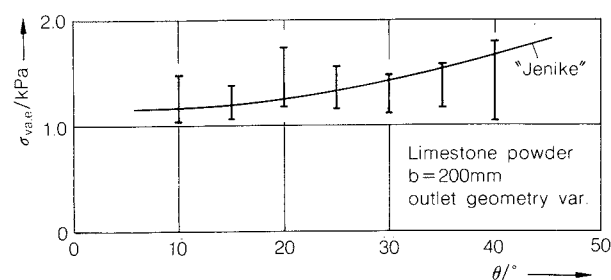


Fig. 3.3 Vertical stress at the level of the outlet (observed values and values calculated according to Jenike)

Jenike³⁾ developed a theory for describing conditions during discharging in terms of a so-called "passive stress field", with which the vertical stress acting on the feeder can be calculated. Figure 3.3 shows the measured values for vertical stress and those calculated according to Jenike at the level of the outlet $\sigma_{v,e}$ for various hopper slopes Θ . The values of vertical stress given are the mean values over the entire outlet cross-section. One will notice that the calculated values correspond well with the order of magnitude observed in the experiments. The fluctuation in the experimental data results from the influence of the outlet geometry, which will be described in chapter 3.3.

3. 2 Estimation of the power required by the feeder

In order to calculate the force required of a discharging device, the relationship between the vertical stress σ_v acting on the feeder under the outlet and the force necessary to move it

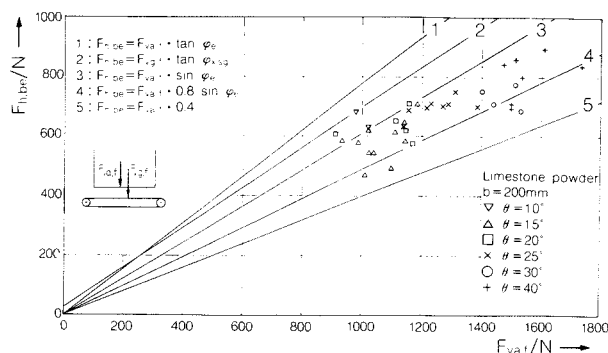


Fig. 3.4 Horizontal force required for removing bulk solid in relationship to the vertical force acting on the feeder

must be known. Fig. 3.4 shows the measured values of the vertical force, $F_{va,f}$ (the vertical stress multiplied by the cross-sectional area of the outlet), for various hopper geometries, and the force $F_{h,be}$ required for withdrawal of the bulk solid at the initiation of discharging. During discharging, the bulk solid must be removed horizontally under the acting vertical stress, whereby, as in shear tests, the bulk solid is subject to shearing forces. By taking the effective angle of friction φ_e , which describes the internal friction of the bulk solid during steady flow, to describe the relationship between the vertical force and the necessary horizontal force for removal, and assuming that the bulk solid is sheared directly beneath the lower edge of the hopper where the vertical stress $\sigma_{va,f}$ is effective, one obtains the straight line curve shown in Fig. 3.4 (Eq. 3.1).

$$F_{h,be} = F_{va,f} \tan(\varphi_e) \quad (3.1)$$

This relationship is valid on condition that the bulk solid is actually removed by the feeder, which will be the case with a rough belt or a plate reclaimer, when the angle of friction between the conveyor belt and the bulk solid is about as great as the effective angle of friction. In the experimental set-up, the angle of friction between the conveyor belt and the bulk solid $\varphi_{x,sg}$ was about 34° and somewhat smaller than the effective angle of friction φ_e , which was

38° . In this case, the maximum possible force with which a bulk solid can be removed is equal to the maximum force of friction which the conveyor belt can exert on the bulk solid, giving a maximum horizontal force of removal of:

$$F_{h,be} = F_{vg,f} \tan(\varphi_{x,sg}) \quad (3.2)$$

The vertical force $F_{vg,f}$ effective on the conveyor belt is greater by the weight of the bulk solid between the lower edge of the hopper and the conveyor belt than the vertical force $F_{va,f}$ at the level of the outlet. Therefore, any curve will cut the abscissa not at the origin but at a point shifted to the left by an amount proportional to the weight of this bulk solid. This curve represents an upper limit for all the measured values.

In the literature, one finds various relationships applied to the upper limit of the force $F_{h,be}$ required of a feeder at the initiation of discharging, which are included in Fig. 3.4. These relationships are as follows:

Johansen¹²⁾ and McLean and Arnold¹³⁾:

$$F_{h,be} = F_{va,f} \sin(\varphi_e) \quad (3.3)$$

Rademacher¹⁴⁾ and Manjunath and Roberts⁵⁾:

$$F_{h,be} = F_{va,f} \cdot 0.8 \sin(\varphi_e) \quad (3.4)$$

Reisner¹⁵⁾ and Bruff¹⁶⁾:

$$F_{h,be} = F_{va,f} \cdot 0.4 \quad (3.5)$$

These relationships were established empirically and, in the case under consideration, sometimes led to too low an estimation of the power required of the feeder.

As already shown, the vertical stress $\sigma_{va,f}$ effective after filling drops sharply at first, before finally taking on the passive stress field. For this condition, a similar diagram can be drawn showing the relationship between the horizontal force and the vertical force. For the relationship between these two forces the same is valid as shown for initiation of discharging.

3. 3 Influence of the hopper/feeder interface

As shown in principle in Fig. 1.1, the geometry of the hopper/feeder interface influences the velocity field inside the silo. To investigate this interrelationship, the particle velocity at the silo walls during discharge, was measured by marking the position of single particles on

the outside of the perspex silo walls at regular time intervals. For the experiments, plastic pellets with a particle size between 4 mm and 6 mm were used. With the data gathered from those experiments, the velocity distribution over the silo walls was calculated by use of an

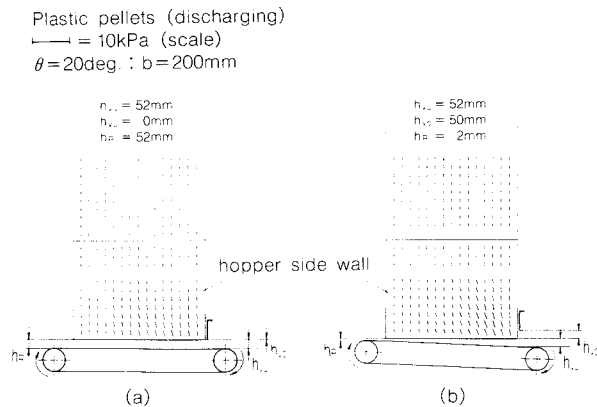


Fig. 3.5 Velocity distribution on hopper side wall (Plastic pellets)

interpolation method. **Fig. 3.5** shows the measured velocity vectors at one of the hopper side walls during discharge for two different geometries of the hopper/feeder interface. The length and direction of each vector line represent the magnitude and the direction of the velocity at that point. The geometry (a), shown on the left of **Fig. 3.5**, yields a relatively even velocity distribution, the geometry (b) on the right side a

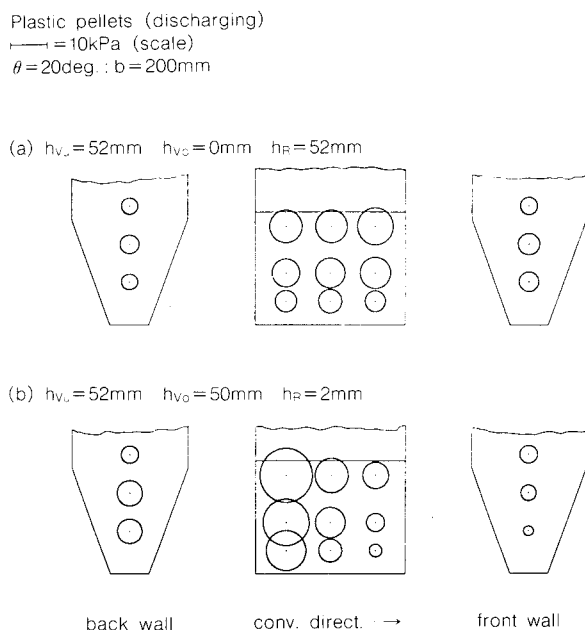


Fig. 3.6 Normal stress (σ_w) distribution on hopper walls (Plastic pellets)

very uneven one. The stress distributions corresponding to the shown velocity vectors are presented in **Fig. 3.6.a** and **b**. On the left in the figure is the back wall, on the right is the front wall, and in the middle is a hopper side wall, all represented schematically. The circles represent the normal stresses acting perpendicularly to the wall at these points, which are proportional to the lengths of the radii and correspond to the scale shown in the top left hand corner. In the case of the geometry producing the more uneven velocity distribution (b), the stresses acting on the hopper side, back and front walls are also more uneven than those associated with the more even velocity distribution. This observation agrees with similar measurements and calculations made on silos characterized by funnel flow, where it was also found that the stresses in regions of flow were less than in the dead zones^{17,18}. Apparently, stresses in the slowly downward moving regions increase, while in faster flowing regions they are decreased. The uneven stress distribution can be explained qualitatively by a simple model. The cause of the change in wall stress is the shear stress between the two regions flowing at different velocities. The shear stress acts on the slower moving region in the direction of gravity and on the faster moving region in the opposite direction. Thus there is an extra downward force acting on the slower flow region which must be taken up by the adjacent hopper side walls, leading to an increase in hopper wall stress. The faster moving region, on the other hand, is supported by the slower moving region, leading to a reduction of stress in the hopper wall adjacent to the faster moving region.

With the investigated plastic pellets, the uneven distribution of stress, starting from a stress pattern of the fully charged silo, took form shortly after initiating discharge. In **Fig. 3.7**, the course of the non-dimensional wall stress S at various positions on the hopper wall (A to F), as well as on the conveyor belt (G), over the non-dimensional time T are presented for the geometry shown in **Fig. 3.5.b** and **3.6.b**. The non-dimensional stress S and the non-dimensional time T are defined as follows:

$$S = \sigma_w / (\rho_b g B) \quad (3.6)$$

$$T = t / (V_{Tr} / Q) \quad (3.7)$$

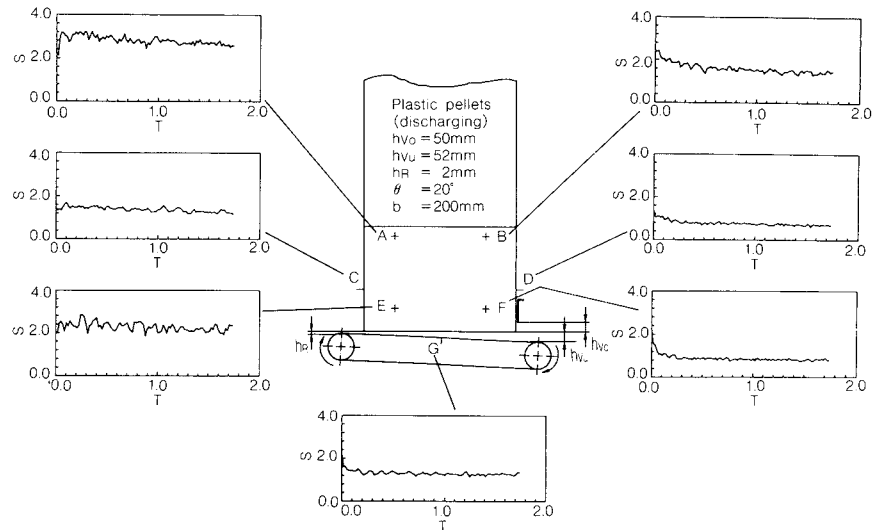


Fig. 3.7 Stress variation vs. time (plastic pellets)

where:

σ_w	wall normal stress	[Pa]
ρ_b	bulk density	[kg/m ³]
B	width of the vertical section of the experimental silo, $B = 0.6$ m	[m]
g	acceleration due to gravity	[m/s ²]
t	time	[s]
V_{Tr}	hopper volume	[m ³]
Q	volume flow rate	[m ³ /s]

The non-dimensional time $T = 1$ is the time needed to discharge a volume of bulk solid equal to the hopper volume V_{Tr} . From the stress-time curves presented in Fig. 3.7, it can be seen that all of the shown stresses fluctuate around a stationary mean value. The fluctuations are typical for hopper stresses during discharge. They result from shear bands moving downwards with the bulk solid. The mean

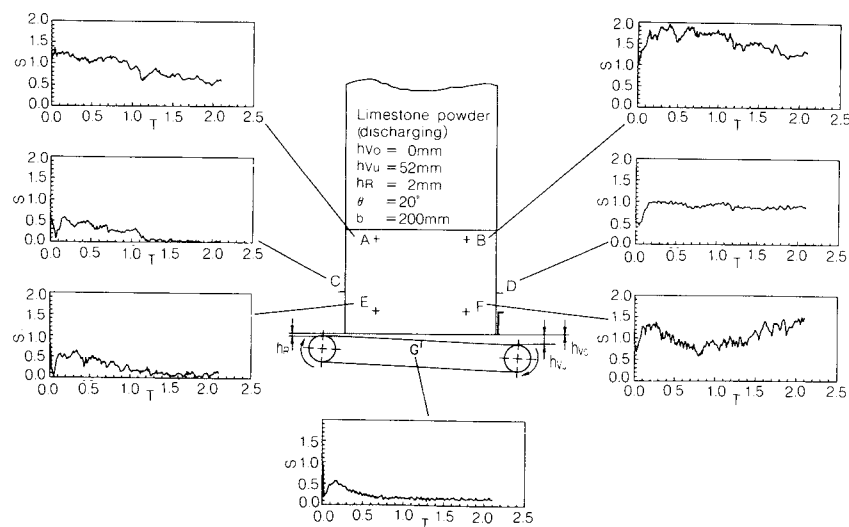


Fig. 3.8 Stress variation vs. time (limestone powder)

values of the stresses S remain almost constant with time after a short initial period of $T = 0.1$ to $T = 0.2$, where the stress field is changing from the active to the passive state.

Figure 3.8 shows stress-time curves for the

limestone powder. In this particular case, the geometry of the hopper/feeder interface was such, by choosing a small height h_{Vo} , that the bulk solid in the rear part of the outlet slit flowed more quickly than that in the front part,

which resulted in very different stresses on the rear and front walls. In contrast to the curves measured with plastic pellets, stresses were found to vary with time over longer periods; some of them still change at $T > 2$. Qualitative velocity measurements carried out by inserting thin rods through holes in the hopper walls, showed a decrease in velocity near the front wall with time until the velocity at the front wall was zero ($T \approx 2 \dots 3$). Velocity equal to zero at the front wall is equivalent to the formation of a dead zone in this region.

Comparing the stress-time curves gathered from measurements with plastic pellets and limestone powder, the following points become clear:

- Uneven removal of a bulk solid causes an uneven velocity field and, hence, an uneven stress distribution.
- The uneven velocity field and stress distribution develop after a short period of time ($T = 0.1 \dots 0.2$) in the case of plastic pellets, a virtually incompressible bulk solid, and remain almost constant. In the case of the compressible limestone powder, the velocities and stresses change over evidently longer periods of time ($T > 2$).

The geometry depicted in Fig. 3.8 with $h_{Vo} = 0$ yields an uneven outflow of the bulk solid and an uneven stress distribution. By choosing greater outlet heights h_{Vu} and/or h_{Vo} , one can achieve an even outflow velocity over the entire area of the outlet, which in turn evens out the stresses acting on the hopper walls. A further increase in h_{Vo} leads to more bulk solid passing through the front part of the outlet, whereby the stresses measured in the front part

of the silo are less than in the rear part. The stresses acting on the hopper side walls follow the same tendency as those acting on the vertical hopper walls under conditions of different outlet heights.

Figure 3.9 shows the stress σ_w on the hopper walls for various outlet heights h_{Vo} (h_{Vu} and h_R are constant) during discharge (limestone powder, hopper slope $\Theta = 30^\circ$, outlet width $b = 200$ mm). In the figure, the back wall is on the left, the front wall is on the right, and in the middle is a hopper side wall, all represented schematically. The circles represent the normal stresses acting perpendicularly to the wall at these points, which are proportional to the length of the radii and correspond to the scale shown in the bottom left hand corner. It is evident that even a relatively small change in the outlet height h_{Vo} has a very strong influence on stress formation in the hopper. Where there is a strong flow of bulk solid, the stress is less, while where flow is weak or has come to a standstill, stress increases. The stress pattern which arises when a bulk solid is withdrawn unequally from across the outlet deviates, particularly at the front and back wall of the silo, from that predicted by Jenike's theory, so that one must question its validity under such conditions.

In this particular case, the optimal outlet height h_{Vo} , which serves to evenly withdraw the material, seems to be in the range of $h_{Vo} = 44$ mm to $h_{Vo} = 38$ mm, this is a total outlet height ($h_{Vo} + h_{Vu}$) of between 96 mm and 90 mm. Deviations of a few mm from this optimum cause an unequal velocity and stress distribution (see Fig. 3.9).

Optimal geometry depends largely on the flow properties of the bulk solid. The optimal geometry found for limestone powder causes an uneven velocity and stress distribution in the case of plastic pellets, and vice versa.

Taking a look at the stresses acting on the hopper walls during discharging (see Fig 3.8), one notices that it is only after a certain amount of time – in this case after the hopper content has been discharged about 2 to 3 times – a stable pattern of stress is established. Only now is it possible to say whether or not the chosen silo geometry effects an even discharge across the outlet, and thus an even pattern of stress on the silo walls. Dead zones in the front

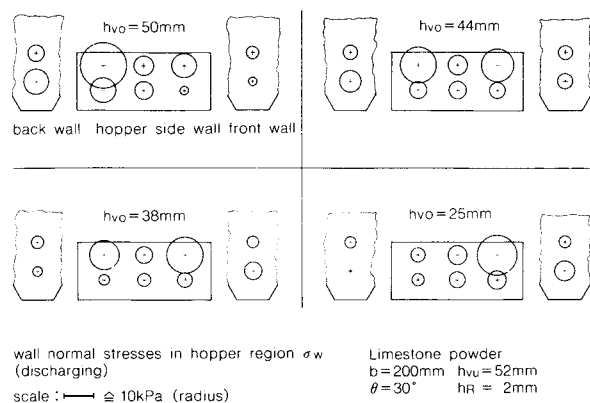


Fig. 3.9 Hopper wall stresses σ_w for various outlet heights h_{Vo}

and rear part of the silo sometimes only arise after a considerable time, which seems to be dependent on the 'difference' between the chosen geometry of the hopper/feeder interface and the optimum geometry. In Fig. 3.10, the stress distribution on the hopper side wall at various non-dimensional times T is shown. The geometry is very close to the optimal geometry; h_{Vo} is only about 6 mm greater than the optimal value of h_{Vo} . The non-dimensional time $T = 0$ corresponds to the filling stresses (active stress field). After switching on the feeder, the passive stress field develops. From Fig. 3.10, it can be seen that the hopper stresses

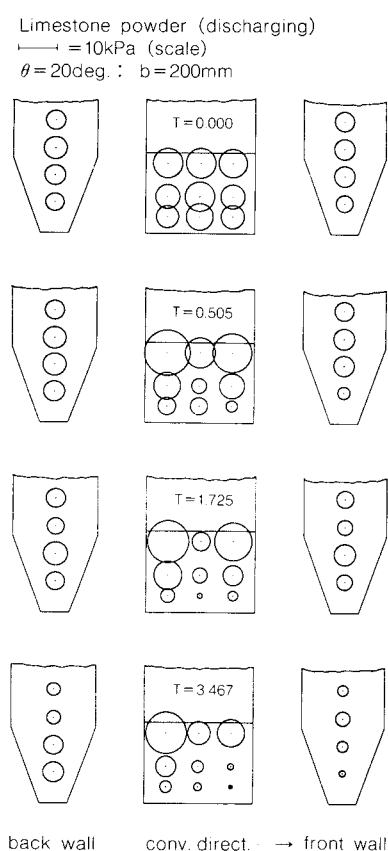


Fig. 3.10 Hopper wall stresses at various non-dimensional times T (limestone powder)

remain quite even until $T = 0.5$ (i.e. discharge of a volume equal to 50% of the hopper volume). With greater values of T (e.g. $T = 1.725$ and $T = 3.467$, Fig. 3.10), stress distribution becomes more and more uneven. In contrast to these results, the hopper stresses shown in Fig. 3.8, due to a geometry with a great divergence from the optimal geometry, are uneven from the very beginning of discharge (e.g. non-di-

mensional stress S at points E and F , Fig. 3.8).

In this respect, a cohesive bulk solid like limestone powder behaves differently from a non-cohesive one such as plastic pellets, where a stable stress pattern is established very soon after discharge initiation. The cause of the limestone powder's behaviour is its compressibility: locally differing stresses lead to the limestone powder being variously compressed, which in turn influences the stress pattern, which again influences the compression, and so on.

The results of the measurements in respect to achieving an even withdrawal of a bulk solid can be summarized as follows.

- Optimal geometry is dependent on the bulk solid's flow properties.
- The range of geometric values which ensure even withdrawal is narrow.
- In the case of cohesive limestone powder, the velocities and stresses in the hopper vary during discharge over relatively long periods of time. Therefore, a geometry similar to, but not identical with the optimal geometry causes uneven withdrawal only after discharge of a greater amount of bulk solid. A geometry very different from the optimum causes uneven withdrawal after a relatively short period of time.

The question is how can even withdrawal of bulk solid be ensured. The results of the measurements show the difficulties in determining the optimal geometry, especially in the case of the cohesive limestone powder. Furthermore, as one can imagine, optimal geometry is influenced by changes in the flow properties, e.g. due to changes in particle size or humidity.

One possible solution is to force the bulk solid to flow out evenly. For this purpose, a

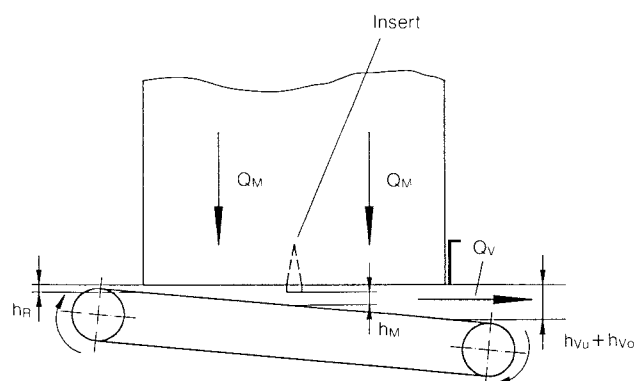


Fig. 3.11 Hopper with insert

hopper/feeder interface geometry was chosen which caused withdrawal from the rear end of the outlet. In addition, an insert was fixed in the outlet slit perpendicular to the conveying direction half way between the front and back wall (Fig. 3.11). The distance h_M between the lower edge of the insert and the belt was adjusted so that the volume flow rate Q_M below the insert was half as much as the flow rate Q_V below the front wall. Due to the insert, the volume flow rate in the front half of the silo was equal to that in the rear half, i.e. Q_M .

Limestone powder (discharging)
 — 10kPa (scale)
 $\theta = 15^\circ$; $b = 200\text{mm}$

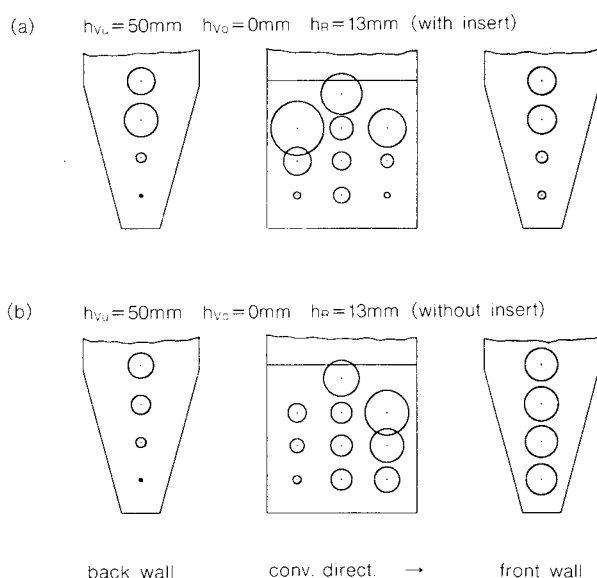


Fig. 3.12 Hopper wall stresses when using an insert (a) and without an insert (b) (limestone powder)

Measurements carried out with a well adjusted insert show an even stress distribution and no occurrence of dead zones, even after discharge over long periods of time (Fig. 3.12.a). To show the influence of the insert, Fig. 3.12.b shows the wall normal stresses for the same hopper/feeder interface geometry without the insert. The measured stresses show a large change in magnitude in horizontal direction. By use of the insert, two outlet slits are simulated, both with a length to width ratio of about 2. Obviously, it is easier to achieve even withdrawal with smaller length to width ratios. This easily understandable relationship agrees with Rademachers¹⁴⁾ recommendations to choose a length to width ratio for the outlet

slit of no more than 2 or 3. But, following Jenike's³⁾ method for silo design, the length of an outlet slit should be at least 3 times the width, and, in many practical applications, slit lengths of more than 3 times the width are necessary. Therefore, the use of inserts to ensure uniform withdrawal seems to be a reasonable solution. When using such inserts, it has to be ensured that they do not cause flow obstructions like dead zones or stable arches.

Nomenclature

b	: outlet width	[m]
B	: width of the vertical section of the experimental silo	[m]
F_h	: required horizontal force of the feeder	[N]
F_{va}	: vertical force, acting at the hopper outlet	[N]
F_{vg}	: vertical force, acting on the feeder	[N]
g	: acceleration due to gravity	[m/s ²]
h	: height	[m]
h_R	: distance between belt and lower edge of hopper back wall	[m]
h_{Vu}	: distance between belt and lower edge of hopper side walls (below front wall)	[m]
h_{Vo}	: distance between lower edge of front wall and lower edge of hopper side walls	[m]
Q	: volume flow rate	[m ³ /s]
S	: non-dimensional stress	[-]
t	: time	[s]
T	: non-dimensional time	[-]
V_{Tr}	: hopper volume	[m ³]
α	: inclination of belt to horizontal, lower edge of hopper side walls	[°]
ρ_b	: bulk density	[kg/m ³]
σ_h	: horizontal stress	[Pa]
σ_v	: vertical stress	[Pa]
σ_{va}	: vertical stress at the hopper outlet	[Pa]
σ_{vg}	: vertical stress acting on the feeder	[Pa]
σ_w	: wall normal stress	[Pa]
φ_e	: effective angle of internal friction	[°]
φ_x	: wall friction angle	[°]
$\varphi_{x,sg}$: wall friction angle (conveyor belt)	[°]
Θ	: hopper slope angle measured against the vertical	[°]

Indices:

f	: filling
e	: discharging
be	: beginning discharging

References

- 1) Schwedes, J.: Fließverhalten von Schüttgütern in Bunkern, Weinheim 1968.
- 2) Schwedes, J.: *Chem.-Ing.-Tech.*, **48** (1976), 4, 294/300.
- 3) Jenike, A.W.: Bull. No.123, Engng. Exp. Station

- Univ. Utah, Salt Lake City, 1970.
- 4) Bridge, D.T. and J.W. Carson: Powder and Bulk Solids 12th Annual Conf., Rosemont, IL, 1987.
 - 5) Manjunath, K.S. and A.W. Roberts: *Bulk Solids Handling*, 6 (1986), 769/775 and 903/911.
 - 6) Schulze, D. and C. Lyle: *Reports in Applied Measurements*, 4 (1988), 2, 34/38.
 - 7) Schulze, D. and C. Lyle, J. Schwedes: *Chemical Engineering & Technology*, 12 (1989), 318/323.
 - 8) Walker, D.M.: *Chem. Eng. Sci.*, 21 (1966), 975/997.
 - 9) Walters, J.K.: *Chem. Eng. Sci.*, 28 (1973), 779/789.
 - 10) DIN 1055, T. 6: Lasten in Silozellen, 1988.
 - 11) Benink, E.J.: Flow and Stress Analysis of Cohesionless Bulk Materials in Silos Related to Codes, Ph.D.-Thesis, Univ. Twente, The Netherlands, 1989.
 - 12) Johanson, J. R.: Storage and Flow of Solids, Three Day Working Seminar Notes, Australian Mineral Found., Adelaide, July 1976.
 - 13) McLean, A.G. and P.C. Arnold: *J. Powder and Bulk Solids Technology*, 3 (1979), 3, 25/28.
 - 14) Rademacher, F.J.C.: *Bulk Solids Handling*, 2 (1982), 2, 281/294.
 - 15) Reisner, A. and M. v. Eisenhart-Rothe: Bins and Bunkers for Handling Bulk Materials, TransTech Publications, Clausthal-Zellerfeld, 1971.
 - 16) Bruff, W.: Industrisiloer, Ingeniorforlaget A/S, 1974.
 - 17) Eibl, J. and U. Häußler: *Beton- und Stahlbetonbau*, 5 (1986), 136/138, and 7 (1986), 189/193.
 - 18) Motzkus, U.: Belastung von Siloböden und Auslauftrichtern durch körnige Schüttgüter, Ph.D.-Thesis, Techn. Univ. Braunschweig, Federal Republic of Germany, 1974.

Chemical Vapour Precipitation of Silicon Nitride Powders in a Laser Reactor[†]

R. A. Bauer, F. E. Kruis, P. van der Put,
B. Scarlett and J. Schoonman

Faculty of Chemical Technology and Materials Science
Delft University of Technology*

Abstract

The Laser Chemical Vapour Precipitation (L-CVP) of Si_3N_4 powders from mixtures of halogenated silanes and NH_3 has been studied. The reactant gases were mixed at varying position in the laser beam, thus preventing low temperature reactions. The Si_3N_4 was collected and separated from the waste product, NH_4Cl , by electrostatic precipitation. A major problem in utilizing SiHCl_3 and SiCl_4 is their poor absorption of radiation from CO_2 -lasers. SF_6 and SiF_4 have been explored for possible use as an inert sensitizer. Silicon can be prepared from SiH_2Cl_2 without the use of a sensitizer. The diameter of the Si_3N_4 particles is typically between 15 nm and 110 nm dependent on the process conditions.

1. Introduction

This paper concerns the preparation of fine ceramic powders, specifically silicon nitride, by chemical vapour precipitation. The eventual quality of a ceramic product is dependent upon the properties of the powder before it is compacted and sintered. The morphology of the powder is usually specified through its particle size distribution and the degree of agglomeration of the powder. Chemical Vapour Precipitation, CVP, is an attractive route to prepare powders of very fine particle size, less than 1 μm . The eventual particle size is dependent upon the nucleation rate and growth of the aerosol particles which, in turn, can be controlled mainly by the temperature profile in the reactor. However, when using conventional heating sources, not only is the lower limit of the particle size restricted, but also the degree of agglomeration increases with decreasing particle size due to a long residence time at conditions of temperature and high number density.

The alternative use of a laser beam as the source of heat has been investigated and re-

ported by several laboratories^{1,2,3}. In this paper, we summarize our experience with this novel and promising technique. Exciting the gas mixture thermally by laser radiation increases the heating and cooling rates enormously, whilst the process temperature is not restricted by the reactor construction material. The excitation of the reactants can be made selectively by separate reactant injection^{4,5} and by matching the laser frequency with the absorption bands of one of the reactants. This introduces flexibility and an additional variable to control the reaction mechanism.

The success of the technique is also dependent upon the choice of reactants. Most previous research has concerned the production of silicon nitride, Si_3N_4 , from a reaction of silane, SiH_4 , and ammonia, NH_3 . The silane is strongly absorbent of the light emitted by a CO_2 -laser which has a wavelength of 10.6 μm . In this process it is difficult to obtain a stoichiometric product, an excess use of silicon has often been reported. We have based our investigations on the alternative use of chlorinated silanes, SiHCl_3 and SiCl_4 , for this process which are potentially commercially more attractive and safer. They have, however, a much lower absorption coefficient of the CO_2 -laser radiation. This problem can be overcome by the addition of a

* P.O. Box 5045, 2600 GA Delft, The Netherlands

[†] Received November 2, 1990

third gas which acts as a sensitizer, for example SF_6 or SiF_4 . Whereas SF_6 absorbs strongly the $10.6\ \mu\text{m}$ radiation (10P20 line) of CO_2 -lasers, SiF_4 absorbs only at $9.4\ \mu\text{m}$ the 9P42 line of a CO_2 -laser. The wavelength of a tuneable laser can be adjusted to optimize the absorption by particular reactants. Another interesting alternative is to excite the ammonia instead of the silicon containing precursor. The use of alternative precursors and of sensitizers does lead to more complex reaction products and can lead to contamination of the product if it is not collected at high temperatures.

It is clear that the process has great potential for numerous variations in reactants and in reactor design. In this paper, CO_2 -laser light absorption by NH_3 at atmospheric pressure was used to form Si_3N_4 powder, starting with absorbing and non-absorbing chlorinated silanes.

2. Experimental Procedure

A schematic diagram of the apparatus is

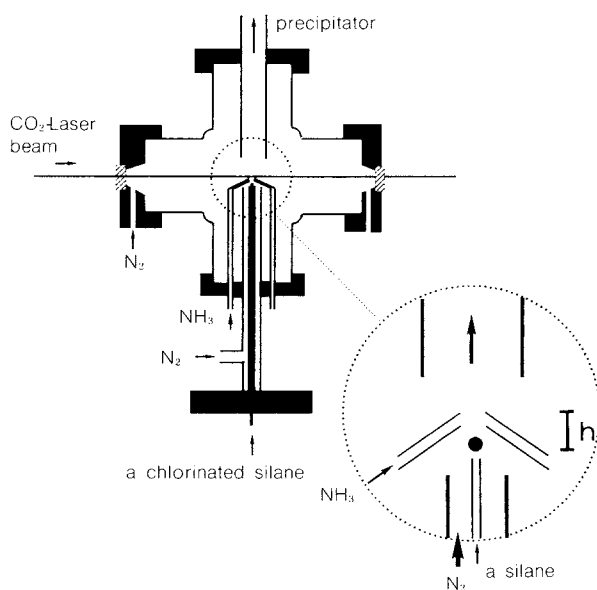


Fig. 1 Schematics of the reactor and the nozzle with the used gases

shown in Fig. 1 and a photograph in Fig. 2. The reactants are introduced through separate nozzles immediately below the laser beam. The sudden rise in temperature and subsequent cooling cause a chemical reaction and condensation of aerosol particles within a stable flame. A picture of a typical flame is shown in Fig. 3.

The reactor was constructed of stainless steel and the laser was introduced through two KCl

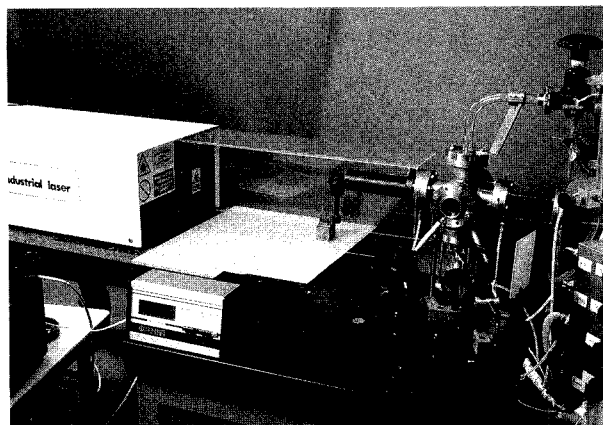


Fig. 2 Photograph of the laser reactor



Fig. 3 Laser reaction flame produced by excitation of SiH_2Cl_2

windows which were flushed with N_2 (467 sccm). The reactor was operated at atmospheric pressure. A 200 W cw CO_2 -laser, with a wavelength tuneable between $9.166\ \mu\text{m}$ and $10.886\ \mu\text{m}$, was partially focused with a ZnSe lens, of focal length 30 cm, to a spot 1.5 mm in diameter and shone orthogonally to the stream of the reactants.

The gas inlet nozzle consisted of four jets which directed the ammonia onto a central jet of the chlorinated silane. The gases were mixed in or above the laser beam to avoid low temperature reactions since they react at low temperature to form solid silicon diimide, $\text{Si}(\text{NH})_2$. The concentric inlets could be adjusted in both the horizontal and vertical directions. The plan view of the different configurations tested are shown in Fig 4. Normally configuration A was used.

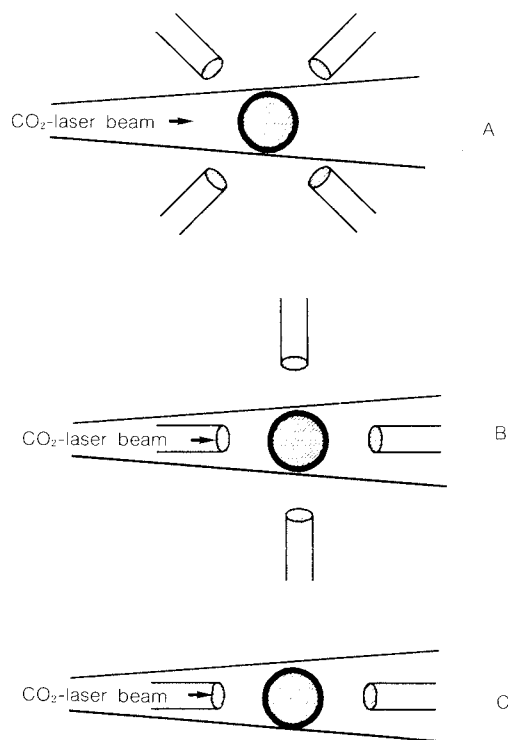


Fig. 4 Nozzle configurations

When NH_3 was the excited gas, configuration C gave the best results because in this case the highest temperature was recorded. An arrangement which exchanged the reactant flows, with the NH_3 gas coming through the middle and the SiH_2Cl_2 gas from the outside inlets, produced poor results. In that case, only with low reactant flows was a stable flame observed and the powders produced were also very poor since they contained a relatively large amount of imide. The reaction products were confined to a small, well-defined reaction zone by a concentric N_2 gas flow. The gas and particle stream was fed into a horizontal electrostatic precipitator (ESP) which separated the Si_3N_4 powder from the NH_4Cl . The potential of the central wire electrode was about +20 kV, whilst the

external cylindrical counter electrode was earthed. This cylindrical counter electrode was placed outside the pyrex collection tube in order to prevent electrode corrosion by the product gas stream. The temperature of the ESP furnace was maintained at 570 K during operation to achieve optimum collection. The powder collected was subsequently heated to 770 K, under vacuum, for fifteen hours in order to remove the remaining traces of NH_4Cl . This temperature is low enough to avoid a reaction of imides, if present, to nitrides. In order to measure the flame temperature, a 2-color pyrometer in combination with a spectrometer was used, as shown in Fig. 5. The setup con-

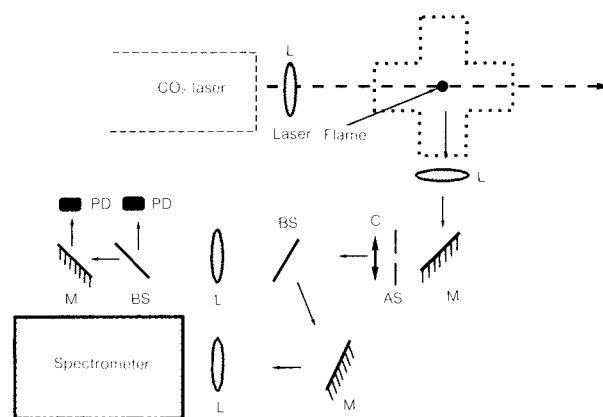


Fig. 5 Arrangement of spectrometer and 2-colour pyrometer

sisted of a pair of mirrors to scan the flame. One lens was used to focus the flame onto the aperture stop, and behind this stop another lens was used to focus the light, split by a beam splitter, onto two hotodiode detectors. Band-pass filters were used to define the wavelength of the light received on the detectors. The light beam was chopped in order to be able to use lock-in amplifiers for phase sensitive detection of the small emission signals. The radiation emitted from an ideal black body at temperature T is given by the Planck function,

$$I_{B\lambda} = \frac{2c^2 h}{\lambda^5 (e^{\frac{hc}{k\lambda T}} - 1)} \quad (1)$$

The temperatures were calculated¹⁰⁾ from the intensity ratio of two different wavelengths I_λ , corrected for the extinction of the particles:

$$R = \frac{I_1}{I_2} = \frac{\lambda_2 I_{B\lambda_1}}{\lambda_1 I_{B\lambda_2}} \quad (2)$$

Some of the light is fed to a spectrometer, equipped with a photomultiplier and a Si/PbS-photodiode detector. The lock-in amplifiers

were also used to amplify the signals from the detectors. The spectra were recorded in a small computer.

The powders were analyzed using IR-spectroscopy, and characterized by X-ray diffraction (XRD), and electron diffraction in a transmission electron microscope (TEM). The amount of nitrogen in the powders was determined by decomposing the samples in LiOH at 950 K and measuring the amount of NH_3 released⁷⁾. The particle sizes and the state of agglomeration were measured from transmission electron micrographs. In Fig 6 are shown examples of spherical particles of 100 nm, the required product, whereas Fig. 7 shows an example of a heavily agglomerated product. The critical factors in this technology are so to control the reaction, condensation and agglomeration rates that particles of the required size are eventually produced.

3. Experimental Results

3. 1 Absorption of CO_2 -laser radiation

All reactants and sensitizers show luminescence if CO_2 -laser radiation is being absorbed. The excited molecules have been shown to be in an thermal equilibrium state at pressures above 10 m Bar⁸⁾. To determine the wavelength dependence of the laser heating, the intensity of the luminescence from reactants and sensitizers in the reactor was measured in the conditions used during synthesis. The luminescence is shown to be mostly thermal. Using SiH_2Cl_2 , a yellow flame was observed if radiation of one of the 10P or 10R lines around the $10.4\text{ }\mu\text{m}$ region of the CO_2 -laser was focussed onto the reactant flow. This luminescence varied little with the wavelength radiated by the laser. The 9P and 9R lines of the CO_2 -laser were not absorbed. Using either SiHCl_3 or SiCl_4 no luminescence was observed using any line. NH_3 showed emission if the reactant was excited by radiation of several lines of the CO_2 -laser. When using the 9R30 line especially strong emission was observed in the reaction zone. Less prominent emission was observed using the 9R16, 10P32 and 10P34 lines of the CO_2 -laser. SF_6 is a well-known^{9,10)} sensitizer used in IR-laser chemistry and is known to absorb the 10P20 line of CO_2 -lasers strongly. SiF_4 is also used as sensitizer if SF_6 is not inert in the prevalent condition¹¹⁾.

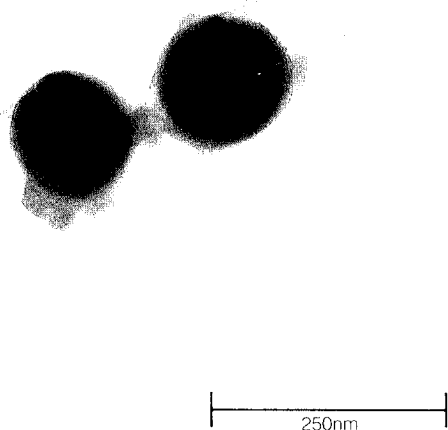


Fig. 6 TEM photograph of Si_3N_4 particles of 100 nm from NH_3 and SiH_2Cl_2



Fig. 7 TEM photograph of agglomerated Si_3N_4 particles

When SiF_4 was injected into the reactor strong emission was observed using the lines around 9P42 of the CO_2 -laser.

3. 2 Silicon particle formation

SiH_2Cl_2 was used in the L-CVP of silicon powders. A yellow, thermal flame developed in the reactor due to laser excitation with the 10P20 laser line and decomposition of SiH_2Cl_2 followed by nucleation of elemental silicon. Dark brown powders of amorphous and crystalline silicon were produced, which were fairly monodisperse. The mean particle diameter of the amorphous powders was 30 nm and that of the crystalline powders was 100 nm. The product contained small amounts of chlorine impurities as observed with EDX. A few minutes after starting the deposition experiments, the reaction flame stabilized and long production times could be maintained. The spectra recorded revealed only a smooth curve, indicating black body radiation. The calculated temperature was about 1770 K. The capacity of the electrostatic collector limited the experiments to one hour. As shown above, dichlorosilane is clearly capable of absorbing sufficient power from an untuned CW industrial laser to dissociate completely, and to produce ultra-fine silicon powders at atmospheric pressures.

Utilizing SiHCl_3 or SiCl_4 as reactant with either SF_6 or SiF_4 did not result in particle formation. In both cases a blue flame was observed. Spectroscopy showed a broad band around 450 nm in the SF_6 experiment and three narrow bands around 440 nm in the SiF_4 experiment which can be attributed respectively to S_2 and SiF radicals.

3. 3 The influence of the process conditions on the Si_3N_4 formation from excited SiH_2Cl_2

Using 50 sccm of SiH_2Cl_2 and 110 sccm of NH_3 the height of injection of the NH_3 into the reaction zone was changed. By injecting the NH_3 below the laser beam the maximum temperature, between 2400 and 2600 K, was measured at the area where the NH_3 flow entered the central SiH_2Cl_2 flow. It seems likely that laser light absorption by the $\text{Si}(\text{NH})_2$ particles formed caused this high temperature. Strongly agglomerated particles were formed during synthesis at low NH_3 injection height. The particle size

distribution is also relatively wide. The diameter calculated from BET surface measurements is similar to the primary particle size as observed with the electron microscope. The particles were shown to be amorphous by X-ray and electron diffraction in the TEM. IR-spectroscopy revealed the silicon nitride particles to contain a considerable amount of imide impurities. The amount of nitrogen (around 33%) was close to the stoichiometric value for Si_3N_4 (40%).

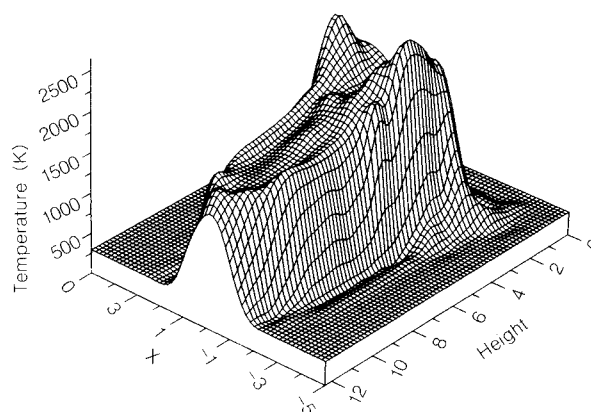


Fig. 8 Temperature profile of laser reaction flame

When NH_3 was injected into the laser beam the temperature was maximal in the area between the central and the concentric outlets. This is illustrated in Fig. 8. Whereas the measured temperature in this area was similar to the previous experiment, the synthesized particles were larger and less agglomerated than those obtained in the previous experiment. Several of the particles contained a small amount of crystalline silicon as indicated by X-ray diffraction and electron diffraction. Several of the particles appeared to contain crystalline silicon cores. IR-spectroscopy revealed only a small number of N-H bonds. The nitrogen content of the particles was lower than in the previous experiments. Thus the powders were shown to consist mainly of silicon nitride with a minor contamination of imides and silicon. In addition to spherical particles a large number of fibers were observed as is shown in Fig. 9. The fibers were distorted and conically shaped with a spherical tip and were also amorphous.

When NH_3 was injected above the laser beam the region with the highest temperatures comprised the injection area of NH_3 in the upper part of the flame. The temperature was much



Fig. 9 TEM photograph of amorphous fibers from NH_3 and SiH_2Cl_2

lower than in the previous experiments; between 1600 and 1700 K. In these experiments larger spherical and egg shaped particles were formed. The agglomeration grade was relatively low and the particle size distribution was narrow. The equivalent diameter calculated from BET measurements was smaller than the diameter observed with TEM. The particles may be porous which is probably caused by the nitridation. The majority of the particles had large crystalline silicon cores as detected by XRD and electron diffraction on the TEM but their exterior was amorphous. IR measurements revealed the relative number of Si-N bonds to be very high. Using EDX, no chlorine could be detected in these powders and the amount of nitrogen was quite low (18%). This indicated that only the outside of the particles had been converted to amorphous silicon nitride.

3. 4 Excitation of NH_3 for the synthesis of Si_3N_4

Exciting NH_3 with the 9R30 line resulted in a flame consisting of three regions, as shown in Fig. 10. Where the CO_2 -laser beam crossed the

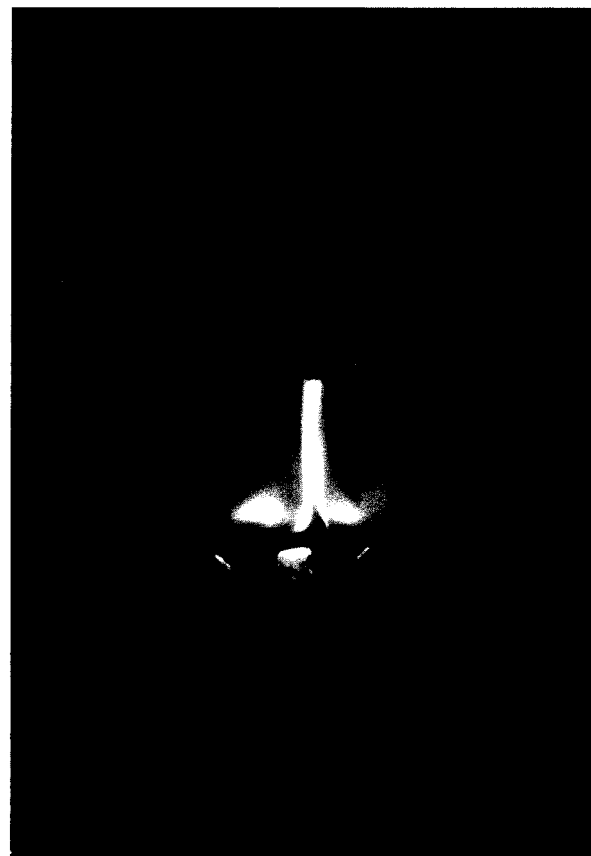


Fig. 10 Laser flame produced by excitation of NH_3

NH_3 injection, spectral measurements showed a discrete spectrum agreeing with that of the NH_2 -radical spectrum. Directly above the central inlet, where SiH_2Cl_2 entered the system, no emission was observed. In the boundary layer between these regions a strong emission was observed. Measurements showed a continuous spectrum, due to black body radiation from the particles formed. Comparing this spectrum with the Planck formula (1), corrected for scattering (2), a temperature of around 2220 K was calculated. The powder characteristics are shown in Table 1. In another experiment a flow of only 20 sccm SiHCl_3 was used as the silicon source whilst the other experimental conditions were unchanged. In this experiment the yellow emission from the area close to the NH_2 emission was much stronger. Spectral analysis of this emission, lying between 350 and 850, showed a continuous spectrum with a black body temperature of 1770 K. The powder collected was also white. IR-measurements showed a much less prominent Si-NH absorption shoulder at 1200 cm^{-1} on the Si-N

Table 1 Process conditions and powder characteristics of the formation of Si_3N_4

Reactant	SiH_2Cl_2	SiH_2Cl_2	SiHCl_3	SiHCl_3	SiHCl_3	SiCl_4	SiCl_4	SiCl_4
Laser line	10P20	9R30	10P20	9P42	9R30	10P20	9P42	9R30
Excited gas	SiH_2Cl_2	NH_3	SF_6	SiF_4	NH_3	SF_6	SiF_4	NH_3
Reaction temperature (K)	2520	2220		2070	1770			
d TEM (nm)	20	26	30	40	40	30	15	15
d SF3 (nm)	100	142	148	129	99			
d BET (nm)	19	14		20	14			
Fibers	many	none	none	none	none	none	none	none
Color powder	light brown	almost white	white	white	white	white	white	white
IR absorption NH-band (1200 cm^{-1})	very weak	very weak	strong	weak	very weak	moderate	strong	very strong

band at 1100 cm^{-1} . The powder was amorphous to electron diffraction in the TEM. The particle size was around 40 nm, larger than the particles made from SiH_2Cl_2 . Using SiCl_4 a weak flame was observed. The relative amount of imide in the product was very high. Transmission electron micrographs showed a mixture of larger ($d = 200\text{ nm}$) and small particles ($d = 15\text{ nm}$). The larger particles showed great resemblance to particles formed in a low temperature reaction between SiCl_4 and NH_3 ¹². Thus little Si_3N_4 has been formed from excited NH_3 and SiCl_4 .

3. 5 Exciting a sensitizer for the synthesis of Si_3N_4

If reactants do not absorb laser radiation sufficiently other strong CO_2 -laser absorbing gases can be used to act as an energy transfer media. For an untuned CO_2 -laser SF_6 is often used as a sensitizer because of its strong absorption around $10.6\text{ }\mu\text{m}$ and its relatively inert character. At low SF_6 flow rates (below 10 sccm) a thermal flame color (yellow white) was always observed. However, at a high SF_6 flux (30 sccm) a blue fluorescence could be seen beyond the reaction flame core. Similar fluorescence has been observed^{9,10} and ascribed to fluorescence of sulphur particles^{13,14} formed during decomposition of the laser excited SF_6 . This decomposition occurs in the presence of hydrogen, or hydrogen containing compounds. This latter observation is corroborated by the presence of minor amounts of sulphur in the product. When less than 10 sccm SF_6 was used

with 20 sccm SiHCl_3 or SiCl_4 and 80 sccm of NH_3 , all the powders contained a considerable amount of sulphur. The particles formed were amorphous and contained a considerable amount of imides as well as Si-N bonds. The slight activity of SF_6 prevents the synthesis of Si_3N_4 with low contamination.

In these cases SiF_4 is preferred as a sensitizer. For this sensitizer a tuneable laser set at around $9.7\text{ }\mu\text{m}$ can be used. The powders produced with a small amount of SiF_4 (10 sccm) contained fewer Si-NH bonds compared to the SF_6 experiments. Using SiHCl_3 as the silicon source the product contained mostly Si_3N_4 according to IR-spectroscopy. All the powders were amorphous to electron diffraction. The particle sizes of the product from SiHCl_3 were around 40 nm compared to 15 nm of the particles formed from SiCl_4 .

4. Thermodynamic Calculations on the Chemical Vapor Deposition of Si_3N_4 and Si from Chlorinated Silanes

Thermodynamic calculations are a useful tool in understanding a specific CVP system and thus to optimize the process conditions. A thermodynamic analysis should be completed before the kinetic effects are considered. Furthermore, kinetic models often include a thermodynamic term. In the case of the homogeneous nucleation of ceramic powders, for example, the supersaturation, which is the driving force for the process, must be known.

The main limitations to the validity of these thermodynamic calculations result from the in-

accuracy or lack of the thermodynamic data and, of course, from the assumption that equilibrium is achieved. Concerning the thermodynamic data, a small change in the heat of formation of a major species can change the deposition efficiency considerably. It has been pointed out by several workers, especially Walsh¹⁵⁾ and Ho¹⁶⁾, that some literature study is needed before attempting calculations, since standard tables such as JANAF¹⁷⁾ and CATCH¹⁸⁾ might not contain the latest results. We used the JANAF values of the heat of formation, except for the chlorosilanes, for which the values of Farber¹⁹⁾ were used, and for the silicon subchlorides, for which 158.9 kJ/mol (SiCl) and -326.4 kJ/mol (SiCl₃) were used. This set of values was tested on the experimental results of Woodruff²⁰⁾.

The result of this work is presented in form

of a CVP phase diagram, which depicts which solid phases would deposit as a function of experimental variables such as temperature and input gases. These diagrams show the phase boundaries and also the deposition efficiency of the Si₃N₄ and Si phases. Kingon²¹⁾ made some CVD-diagrams of the Si-H-Cl-N system, but only up to 1800 K, and using old JANAF values. In this work, temperatures up to 2600 K were used, in accordance with our experimental results. The calculations were carried out using the SOLGASMIX-PV program and also a control program which searches for phase transitions within 0.2% accuracy. One CVP-diagram takes several hours on a Compaq 386/25, making tens of thousands equilibrium calculations.

In Fig. 11 CVP-phase diagrams for 4 silane/
NH₃ systems are depicted. The pressure is 1

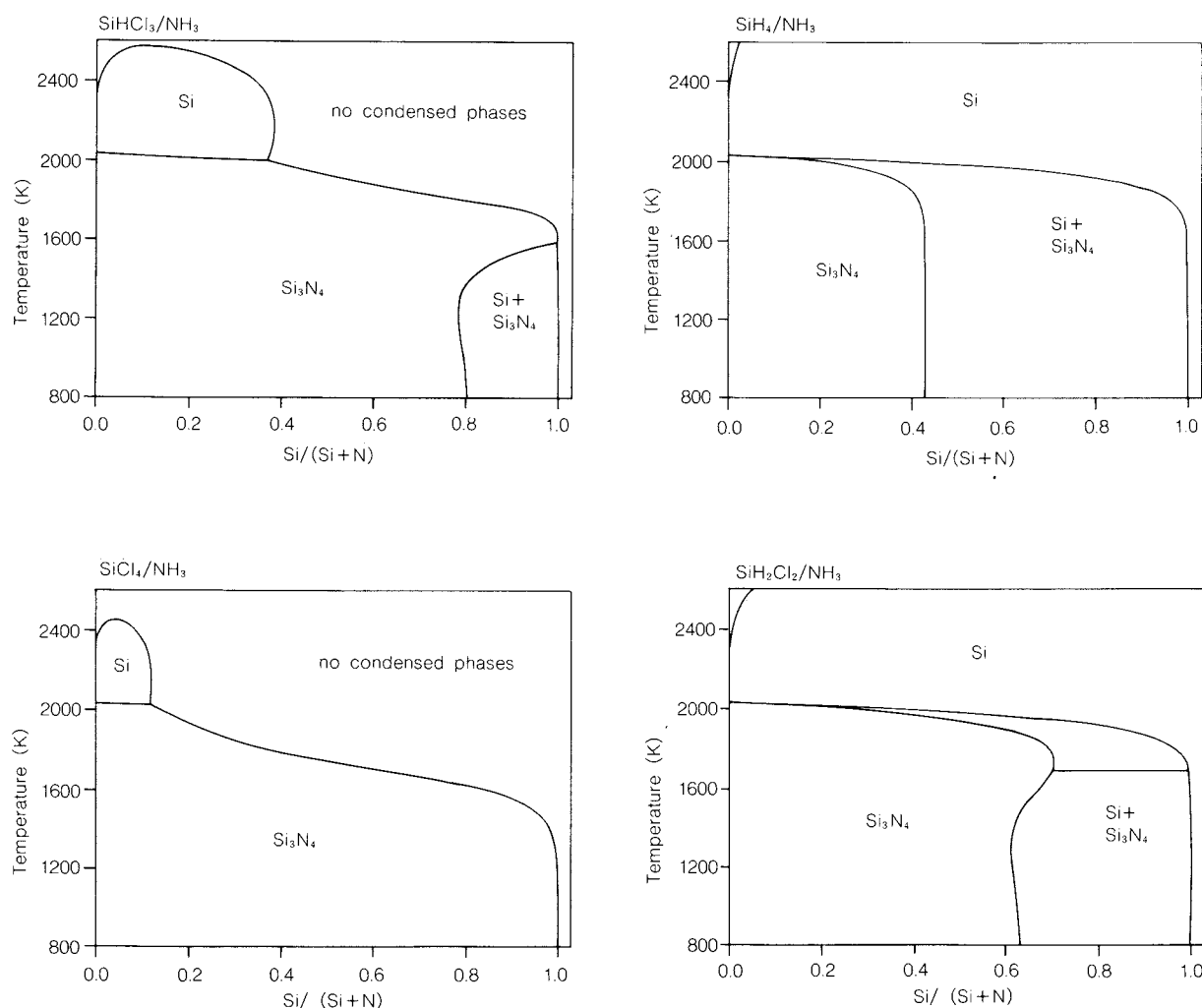


Fig. 11 CVP phase diagrams

Bar. $\text{Si}/(\text{Si}+\text{N}) = 0.1$ means, for example, an input of 1 mol (chlorinated) silane and 9 mol NH_3 . From the diagrams it is clear that the higher the chlorine content of the silane, the smaller the deposition efficiencies but also the smaller the regions of co-deposited Si and Si_3N_4 . This is confirmed by the higher nitrogen content of the powders produced with SiHCl_3 , compared with SiH_2Cl_2 . An important result is that, in the SiHCl_3 and the SiCl_4 systems, there is a large region at higher temperatures where there are no condensed phases. This is confirmed by the experimental failure to make silicon from SiHCl_3 and SiCl_4 .

5. Conclusions

It has been shown that Si_3N_4 powder can be formed from SiH_2Cl_2 by exciting NH_3 using the strongly absorbing 9R30 CO_2 -laser line at $9.4\ \mu\text{m}$ or by using a sensitizer such as SF_6 or SiF_4 . SiF_4 is shown to be more inert in the conditions used and produces less contamination. A stoichiometric product, without fibers, is formed from SiH_2Cl_2 compared to using the 10P20 line at $10.4\ \mu\text{m}$. SiH_2Cl_2 can also be excited directly without another absorbing media. The injection height of NH_3 in the laser is, in this case, a major process variable. It is very difficult to use SiCl_4 as the silicon source to produce Si_3N_4 powder with CO_2 -laser synthesis, because of the unfavorable energetic properties of this substance. The use of phase diagrams is a powerful tool in interpreting the CVP process and is, in any case, a necessary precursor to Kinetic calculations.

Acknowledgment

This research is financed partly by the Netherlands Ministry of Economic Affairs in the framework of the Innovation Directed Research Programs (IOP). The authors are grateful to DSM for financial support.

7. References

- 1) Cannon, W.R., S.C. Danforth, J.H. Flint, J.S. Haggerty and R.A. Marra: "Sinterable Ceramic Powders from Laser-Driven Reactions: I, Process Description and Modeling", *J. Am. Ceram. Soc.*, **65**, [7], 324-30 (1982).
- 2) Cannon, W.R., S.C. Danforth, J.S. Haggerty and R.A. Marra: "Sinterable Powder from Laser-Driven Reactions: II, Powder Characteristics and Process Variables", *J. Am. Ceram. Soc.*, **65**, [7], 330-35 (1982).
- 3) Symons, W. and S.C. Danford: "Synthesis Characteristics of Laser Synthesized Silicon Nitride Powder", pp. 249-256 in *Advances in Ceramics*, Vol. 21, eds. G.L. Messing, K.S. Mazdiyashi, J.W. McCauley and R.A. Haber: American Ceramic Society, 1987.
- 4) Bauer, R. A., F. E. Kruis, P. Van der Put, B. Scarlett and J. Schoonman: "Laser-Synthesis of Low Agglomerated Submicrometer Silicon Nitride Powders from Chlorinated Silanes", submitted to *J. Am. Ceram. Soc.*
- 5) Bauer, R.A., F.E. Kruis, J.G.M. Becht and J. Schoonman: "Laser-Synthesis of Low Agglomerated and Narrow Sized Submicrometer Silicon Nitride Powders from Chlorinated Silanes", pp. 1.28-1.32 in *Euro-Ceramics*, Vol. 1, Processing of Ceramics, eds. G. de With et al., Elsevier Sc. Publishers LTD, 1989.
- 6) Flower, W.L.: "Optical Measurements of Soot Formation in Premixed Flames", *Combustion Science and Technology*, **33**, 17-33 (1983).
- 7) Puxbaum, H. and A. Vendl: "Zur Relativkonduktometrischen Bestimmung von Stickstoff in einigen Siliciumnitridhaltigen Werkstoffen" (For Relative Conductometric Determination of Nitrogen in several Silicon Nitride containing Components), *Fresenius Z. Anal. Chem.*, **23**, 134-7 (1977).
- 8) Losev, V.V., V.F. Papulovskii, V.P. Tychinskii and T.A. Fedina: "Luminescence of Ammonia and Ethylene under the Action of the radiation of a laser with a wavelength of $10.6\ \mu\text{m}$ ", *Khimiya Vysokikh Energii*, **3**, [4], 331-334 (1969).
- 9) Steinfeld, J.I: "Laser-Induced Chemical Reactions: Survey of the Literature, 1965-1979", pp. 243-267 in *Laser-Induced Chemical Processes*, ed. J.I. Steinfeld, Plenum Press, New York, 1981.
- 10) Shaub, W.M. and S.H. Bauer: "Laser-Powered Homogeneous Pyrolysis", *Intern. J. Chem/Kinet.*, **7**, 509-529 (1975).
- 11) Olszyna, K.J., E. Grunwald, P.M. Kreehn and S.P. Anderson: "Megawatt Infrared Laser Chemistry", *Tetrahedron Lett.*, **19**, 1609-1612 (1977).
- 12) Bauer, R.A., R. Smulders, J.G.M. Becht, P.J. van der Put and J. Schoonman: "Laser-Chemical Vapor Precipitation of Submicrometer Silicon and Silicon Nitride Powders from Chlorinated Silanes," *J. Am. Ceram. Soc.*, **72**, [7], 1301-304 (1989).
- 13) Ronn, A.M: "Laser Induced Sulfur Particulate Formation," *Chem. Phys. Lett.*, **42**, [2], 202-204 (1978).
- 14) Lin, S.T. and A.M. Ronn: "Particulate Formation by Infrared Laser Dielectric Breakdown," *Chem. Phys. Lett.*, **56**, [3], 414-418 (1978).
- 15) Walsh, R.: "Thermochemistry of Silicon-containing Compounds," *J. Chem. Soc. Faraday Trans. 1*,

- 79, 2233-2248 (1983).
- 16) Ho, P., M.E. Coltrin, J.S. Binkley and C.F. Melius: "A Theoretical Study of the Heats of Formation of SiH_n , SiCl_n , and SiH_nCl_m Compounds," *J. Phys. Chem.*, **89**, 4647-4654 (1985).
 - 17) JANAF Thermochemical Tables, ed. Chase, NBS, Washington, 1985.
 - 18) Pedley, J.B. and B.S. Iseard: CATCH Table for Silicon Compounds, Univ. of Sussex, 1972, 1976. Available from NTIS, No. AD 773 468.
 - 19) Farber, M. and R.D. Srivastava: "Mass Spectrometric Determination of the Heats of Formation of the Silicon Subchlorides $\text{SiCl}(\text{g})$, $\text{SiCl}_2(\text{g})$ and $\text{SiCl}_3(\text{g})$ ", *J. Chem. Soc., Faraday Trans. 1*, **73**, 1672-1680 (1977).
 - 20) Woodruff, D.W. and R.A. Sanchez-Martinez: "Experimental Study of Equilibrium Conditions in the Si-H-Cl System," *J. Electrochem. Soc.*, **132**, [3], 706-708 (1985).
 - 21) Kingon, A.I., L.J. Lutz and R.F. Davis: "Thermodynamic Calculations for the Chemical Vapor Deposition of Silicon Nitride," *J. Am. Ceram. Soc.*, **66**, [8], 551-558 (1983).

Emission Control of Particles and Gaseous Pollutants with a High-Temperature Granular Bed Filter[†]

W. Peukert and F. Löffler

*Institute of Mechanical Process Engineering and Mechanics
University Karlsruhe**

Abstract

The combined collection of fine dusts and the sorption of gaseous pollutants at high temperatures have been experimentally and theoretically investigated. The results of the fractional separation efficiency measurements and the experimentally determined breakthrough curves have revealed that excellent SO₂ and HCl sorption characteristics exist under conditions which also yield high particle collection efficiencies. New concepts have been developed to describe the measured fractional collection efficiency curves in the inertia dominated size range, which are based on particle trajectory calculations using a simple flow model. During the sorption, conversions of over 80% can be achieved when using a reactive bed consisting of pellets agglomerated from fine limestone particles. The application of such beds in a counter-current mode can even yield solid conversions of nearly 100%. The mathematical prediction of the conversion time behaviour under differential conditions and the breakthrough characteristics in a fixed bed are in reasonable agreement with the experimentally measured data.

1. Introduction

The application of granular bed filters for hot gas cleaning has become an increasingly popular topic. The use of reactive bulk media additionally opens up the possibility of combining the filtration with a process which extracts specific gases by means of catalytic conversion or sorption within the bed. The industrial realization of such simultaneous particle collection and gas sorption processes will then offer small and average-sized plants a technique with which hot flue gases can be effectively cleaned, even at temperatures of up to 1000°C, whilst functionally exploiting the waste heat involved.

The particle collection behaviour is characterized by means of systematic fractional separation efficiency and pressure loss measurements in dependence of the chief operational parameters. The sorption process of gaseous components is characterized with the aid of experimentally determined conversion time curves under differential conditions, and by the

evaluation of breakthrough curves of the acidic gaseous components SO₂ and HCl using an integral reactor. The investigations were conducted at temperatures of up to 800°C.

2. Results of the particle collection measurements

Systematic separation efficiency measurements at room temperature for particles in the size range between 0.01 μm and 10 μm have allowed the influence of the chief filtration parameters (e.g. filter face velocity, filter thickness, type and size of the bed grains and the electrostatic charging of the up-stream particles) to be extensively quantified. The influence of the filtration duration is of decisive importance to the assessment of such a filter's operational behaviour. In general, it may be assumed that the separation improves with the quantity of dust collected. Nevertheless, unfavourable operation (filter medium grain size $d_K \geq 1$ mm, filter face velocity $u_o > 0.2$ m/s), in conjunction with high dust concentrations can lead to a breaching which consequently causes the filtration characteristics to deteriorate.

* D-7500 Karlsruhe 1, Germany

† Received November 2, 1990

rate enormously. In view of both the separation and the pressure-loss (and hence energy consumption), the room-temperature collection would appear more favourable at low filter face velocities ($u_o < 0.1$ m/s) and with small bed grains ($d_K < 0.5$ mm)¹⁾. This is demonstrated in Fig. 1, in which the mass-specific penetration E_3 , calculated from the measured fractional efficiencies, and the inlet particle

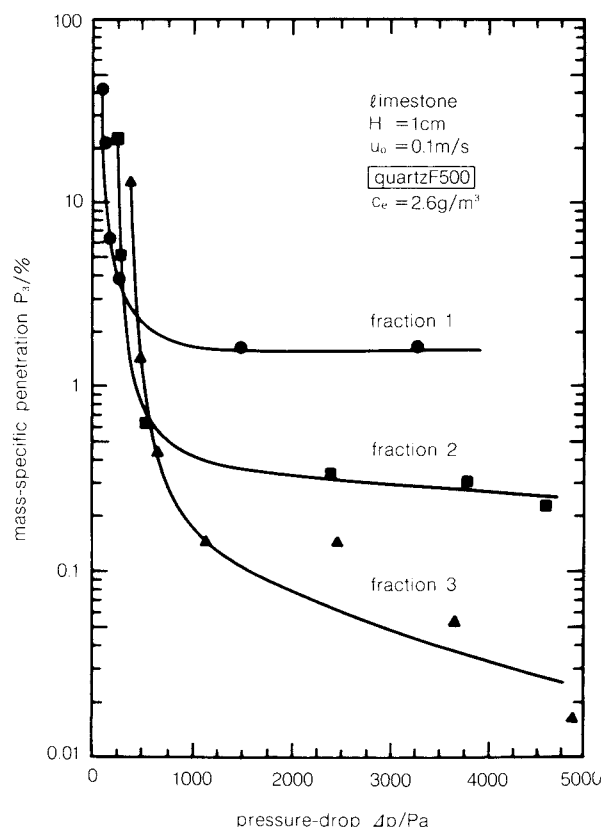


Fig. 1 Penetration as a function of the pressure drop for three grain fractions (limestone) at a filter face velocity of $u_o = 0.1$ m/s (temperature $T = 20^\circ\text{C}$). Fraction 1: 10 mass-% $d_K = 0.29$ mm; 90 mass-% $d_K = 0.7$ mm; Fraction 2: $d_K = 0.29$ mm; Fraction 3: 10 mass-% $d_K = 0.12$ mm; 90 mass-% $d_K = 0.29$ mm

size distribution has been plotted for three different filter medium grain sizes as a function of the measured pressure drop. One can observe that after a short run-up period, the finest grain bed shows the highest total separation efficiency for any specific pressure loss and thus, the lowest emission values.

The influence of the temperature on the particle collection has been investigated up to temperatures of 800°C . Theoretically, the transport conditions for extremely small particles

($x < 0.5$ μm) improve towards the grain's surface with increasing temperature as a result of the increasing particle diffusion coefficient. Conversely, a poorer collection performance is to be expected with increasing temperature for larger, inertia-dominated particles ($x > 0.5$ μm) due to increasing drag forces, since the dynamic viscosity of the fluid increases with the temperature, hence impairing the transport. This anticipated theoretical temperature influence was verified for particles in the inertia dominated regime by experimentally determined grade efficiency curves²⁾.

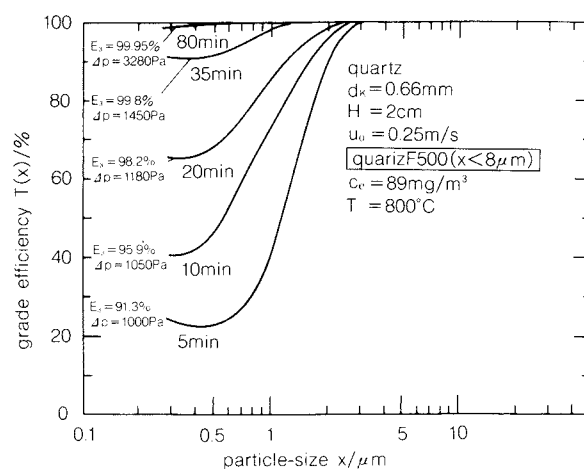


Fig. 2 Temporal behaviour of a quartz bed (grain size $d_K = 0.66$ mm) at a temperature of 800°C and a filter face velocity of $u_o = 0.25$ m/s

The high-temperature, long-term filtration influence (and therefore the effect of the filter loading) is demonstrated in Fig. 2. In addition to the fractional separation efficiencies, this graph also incorporates the mass-specific total separation efficiency E_3 calculated from the grade efficiency and the raw gas particle distributions, together with the pressure loss Δp , measured for each respective dust loading. Despite relatively coarse bed grains ($d_K = 0.66$ mm) and a comparatively high filter face velocity ($u_o = 0.25$ m/s), the fractional separation efficiency increased extremely rapidly, to remain at nearly 100% for all particle grades.

At ambient temperatures, similarly good collection characteristics could only be attained from bed grains smaller than 0.3 mm with significantly lower filter face velocities. The more favourable dynamic behaviour at higher temperatures is to be traced back to an improved adhesion to the individual surfaces of

the grains. Under such conditions, a dense dust layer forms on the filter's surface in a manner similar to the dust cake of a bag filter, so that even for substantially higher operational raw gas dust concentrations of $c_e = 2.6 \text{ g/m}^3$, clean gas values of less than 1 mg/m^3 may be achieved under standard conditions. As a result, the filter face velocity of granular bed filters may be substantially increased at higher temperatures. This will allow the filter area to be correspondingly reduced, cutting both the filter unit's required floor space and investment costs, although at the expense of higher pressure losses.

3. Theoretical calculation of grade efficiencies

Model concepts already exist with which the separation curves for dusts within the diffusion range may be adequately predicted³⁾, provided that the influence of the deposited dust mass may be neglected (i.e. for short filtration periods). In the inertia range, however, this is only possible with extensive restrictions. As a result, a new model concept has been developed which describes the collection process as a combination of fluid flow through the pores of the filter bed and stagnation flow around a spherical collector. With the aid of particle trajectory calculations, fractional separation efficiencies could be calculated which, in practice, are in good agreement with measured efficiencies. This is demonstrated in Fig. 3 for a limestone bed and particle sizes between $0.01 \mu\text{m}$ and $10 \mu\text{m}$. In addition to the measured fractional separation efficiencies (dots), the curves of Tardos⁴⁾ and Goren⁵⁾ have been included,

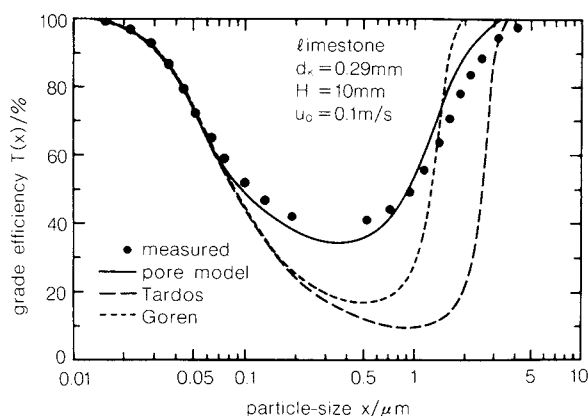


Fig. 3 Comparison between the measured (dots) and the calculated separation efficiency curves (full lines) at room temperature for a limestone bed with a grain size of $d_K = 0.29 \text{ mm}$ and a filter face velocity of $u_0 = 0.1 \text{ m/s}$

together with the results yielded by the pore model. The calculated grade efficiencies coincide not only at ambient conditions with the measured data, but also exhibit a reasonable agreement with the experimentally determined curves at elevated temperatures. In contrast, however, the theoretical description of the filtration kinetics is extremely sophisticated, and has not yet been accomplished.

4. Results of the Sorption of SO_2 and HCl

The investigations into the sorption of SO_2 and HCl have verified that the operational conditions relevant to the particle collection will also yield an effective pollutant gas sorption. The sorbents used incorporated raw limestone and pellets agglomerated from fine limestone dust. The size of this parent dust proves to be a key parameter for the achievement of high solid conversion rates and hence, maximal

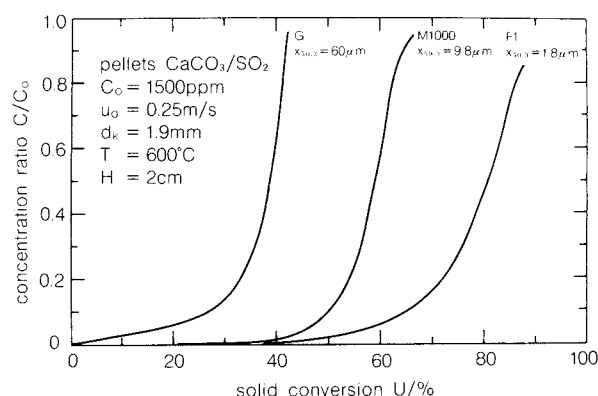


Fig. 4 Influence of the parent grain size $x_{50,3}$ on the penetration behaviour of SO_2 for three different limestone pellet beds (pellet size $d_K = 1.9 \text{ mm}$) at a filter face velocity of $u_0 = 0.25 \text{ m/s}$ (air as carrier medium)

sorbent exploitation. Figure 4 exemplarily illustrates breakthrough curves for SO_2 for various parent grain sizes through granular beds of limestone pellets (agglomerated using a rotary disk unit to a size of $d_K = 1.9 \text{ mm}$), as functions of the solid conversion calculated from the temporal progress of the clean gas SO_2 concentration, using a mass balance.

The sorption can be observed to improve with decreasing mass-specific parent grain size $x_{50,3}$. The most important aspect is that the breakthrough curves initially possess extremely flat trends which only increase at higher specific conversions. Therefore, should one wish to reduce the SO_2 gas concentration by 80% (inlet

gas concentration $C_o = 1500$ ppm) then, in the case of the finer fraction F_1 , 70% of the solids may be converted before an effective filtration ceases after 7 hours of operation.

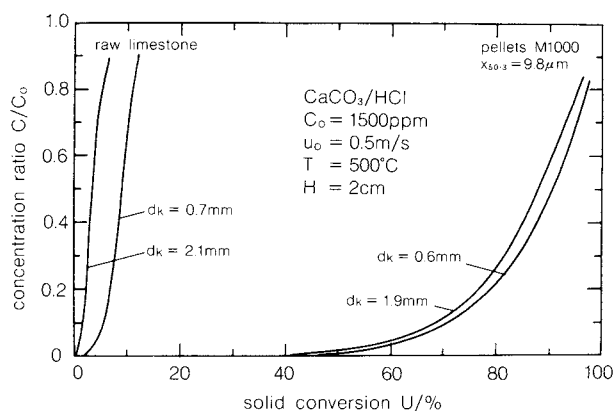


Fig. 5 Influence of the grain size on the breakthrough behaviour of HCl through granular beds of raw limestone and limestone pellets at a temperature of 500°C (air as carrier medium)

The actual size of the pellets themselves is only of subordinate relevance. This becomes evident from Fig. 5, which illustrates the breakthrough characteristics of HCl through beds of two different raw limestone fractions and agglomerated pellet sizes. In this instance, the pellets were fabricated from limestone M 1000 powder ($x_{50.3} = 9.8 \mu\text{m}$) and the filtration was conducted at 500°C. In the case of the raw limestone, it is evident that the attainable solid conversions are by no means adequate for industrial purposes. This does not stem from a financial assessment (since in comparison with other sorbents such as $\text{Ca}(\text{OH})_2$, limestone is indeed a cheap raw material), but rather from the problems involved in disposing of the residues.

At temperatures of around 500°C, a comprehensive sorbent exploitation may be attained by utilizing limestone pellets, which offer average solids conversions of over 90%. As a result of the low porosity of raw limestone ($\epsilon_s = 9.5\%$), the diffusive transport into the grain is not only impaired from the beginning of the reaction, but ceases completely at low conversion ratios due to the formation of product layers. The limestone pellets, however, possess a larger, more easily accessible internal surface, so that an almost total reaction can occur. Even at high solid conversions, the large pore volume of the pellets ($\epsilon_s = 45\%$) still warrants a diffu-

sive transport into the core of each sorbent particle.

The theoretical description of the single grain sorption kinetics (differential conditions) for HCl is accomplished by means of an elementary shrinking-core model⁶⁾. The sulfation reaction, however, requires the application of a model which also takes into account the pellets' internal pore radius distribution⁷⁾. The layout of a granular bed filter depends on the solution of the mass balance for the packed bed reactor, which may be accomplished using two different mathematical procedures. One can either solve the partial differential equation under consideration of the axial dispersion using a finite difference method, or apply the method of characteristics, in which axial dispersion is neglected. Since both approaches deliver nearly identical solutions, the influence of the axial dispersion can be excluded. The comparison between measured and calculated breakthrough curves for both HCl and SO_2

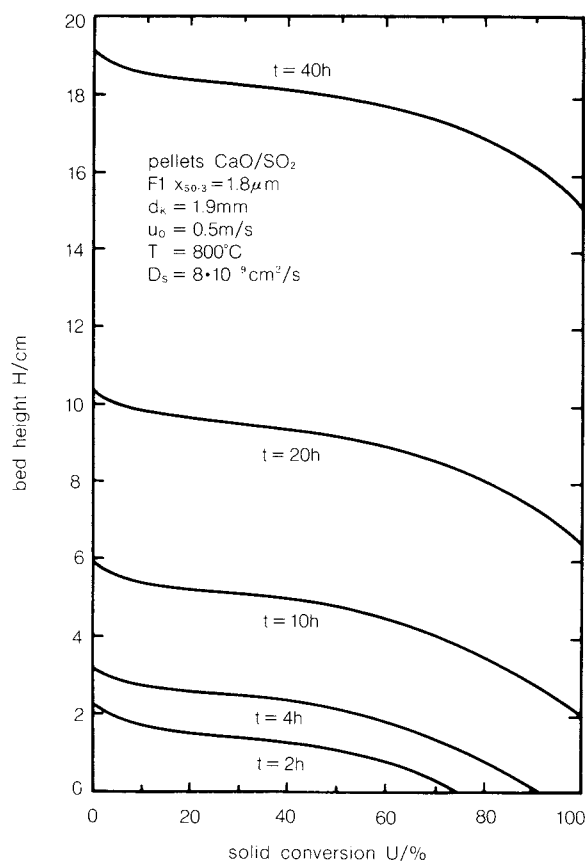


Fig. 6 Calculated solid conversion profiles during the reaction of SO_2 using CaO pellets at a filter face velocity of $u_o = 0.5$ m/s (raw gas inlet from below)

yield an adequate conformity⁸⁾.

The calculated solid conversion profiles within a 20-cm-deep CaO pellet bed for SO₂ (inlet concentration $C_o = 1500$ ppm) is demonstrated in Fig. 6. The kinetic parameters for the reaction model (i.e. reaction rate constant and the gas diffusion coefficient through the product layer) were implemented with those values with which both the temporal single grain solid conversion behaviour (measured under differential conditions), and the breakthrough characteristics (measured in an integral reactor) could be described.

The operational life of even relatively thin beds is in the order of many hours. In spite of the fact that the CaSO₄ product layer which forms during the reaction progressively retards the reaction, the solids may nevertheless be practically totally converted. The steep solid conversion profiles allow non-converted bed substance to remain available to the reaction, attaining low emission values. The counter-current application of this technique hence gives access to an unique possibility of being able to practically totally exploit the sorbent of a dry flue-gas cleaning process. This is especially important with respect to the increasing necessity of minimizing industrial waste.

A comparison between the results of the particle collection and the sorption of the gaseous components has revealed that the sorption of

the gases is indeed possible under similar operational conditions to the filtration of the dispersal phase. The mutual influences between the sorption and the particle collection, incited by bed structure modification through the chemical reaction or the lodging of inert dust, are generally insubstantial. This has been verified by means of separation efficiency measurements with both fresh and fully exhausted pellets, and from measured breakthrough curves through beds loaded with inert quartz dust.

References

- 1) Peukert, W. and F. Löffler: *Staub-Reinhaltung der Luft*, 48 (1988), 10, 379-386.
- 2) Peukert, W. and F. Löffler: 1. European Symposium "Separation of Particles from Gases", 19-21, April 1989, Nürnberg, Germany.
- 3) Tardos, G., C. Gutfinger and N. Abuaf: *AIChE Journal*, 22 (1976), 6, 1147-1150.
- 4) Gal, E., G. Tardos and D. Pfeffer: *AIChE Journal*, 31 (1985), 7, 1093-1104.
- 5) d'Ottavio, T. and S. Goren: *Aerosol Science and Technology*, 2 (1983), 91-108.
- 6) Ishida, M. and C. Y. Wen: *AIChE Journal*, 14 (1988), 2, 311-317.
- 7) Christman, P. and T. Edgar: *AIChE Journal*, 29 (1983), 3, 388-395.
- 8) Peukert, W.: Die kombinierte Abscheidung von Partikeln und Gasen in Schütttschichtfiltern, Dr.-Thesis, Universität Karlsruhe

Information Articles

The Symposium on Powder Technology

The Party of Powder Technology (Japan) held its 1st Hosokawa symposium on Powder Technology and the 24th symposium on Powder Technology on August 22 and 23 (1990) respectively, at the Sunshine Prince Hotel in Tokyo. The former symposium, which was limited to 70 participants, consisted mainly of discussions that focused on "Mechanofusion."

The limited attendance allowed all the participants to gain a deep insight on the subject. The latter symposium consisted of five lectures on the main theme of "The Powder Technology in New Material Production," to which approx. 250 participants enthusiastically listened. The titles of the lectures are listed below.

The 1st Hosokawa Symposium on Powder Technology What is Mechanofusion? – Function and Application

Lecture and discussion

Organizer: Prof. Genji Jimbo (Nagoya University)

- | | |
|---|--|
| <ul style="list-style-type: none"> • Mechanism of synthesizing composite powder by mechanofusion • Synthesizing process of metallic/ceramic composite powder by mechanofusion treatment • Synthesizing composite material of Al-Li system superplastic alloy and SiC • Mechanical alloying (MA)
– MA effect in mechanofusion – • Role of mechanofusion in superconductive oxide • Compositing process of Al-Ni by mechanofusion technique • Synthesizing conductive composite powder by mechanofusion and its evaluation • Discussion | <p>Mamoru Senna
(Keio University)</p> <p>Kouichi Tanno
(Miyagi National College of Technology)</p> <p>Kei Miyanami
(University of Osaka Prefecture)</p> <p>Shoichi Ochiai
(The Nishi-Tokyo University)</p> <p>Makio Naito
(Hosokawa Micron Corp.)</p> <p>Tohei Yokoyama
(Hosokawa Micron Corp.)</p> <p>Keijiro Terashita
(University of Osaka Prefecture)</p> |
|---|--|

The 24th Symposium on Powder Technology

Session I Application of mechanofusion to new materials

Chairmanship: Masafumi Arakawa (Former Kyoto Institute of Science)

- | | |
|---|---|
| <ul style="list-style-type: none"> • Mechanochemical phenomena in mechanically synthesizing fine composite powder • Application of Mechanofusion for metals and superconductive oxide | <p>Mamoru Senna
(Keio University)</p> <p>Tohei Yokoyama
(Hosokawa Micron Corp.)</p> |
|---|---|

Session II Powder Technology in producing functional materials

Chairmanship: Kei Miyanami (University of Osaka Prefecture)

- | | |
|---|--|
| <ul style="list-style-type: none"> • Powder technology in producing superconductive materials • Powder technology in toner for electrophotography • Microcapsuling technology in synthesizing composite powder | <p>Masanobu Awano
(Government Industrial Research, Nagoya)</p> <p>Noboru Kutsuwada
(Nippon Institute of Technology)</p> <p>Yoshiko Nakahara
(Government Industrial Research, Osaka)</p> |
|---|--|

Public Meeting Concerning Powder Technology Recently Held

The Second World Congress PARTICLE TECHNOLOGY and the First KONA Award

The Second World Congress held at the Kyoto International Conference Hall from Sept. 19 to 22, 1990 ended in great success with more than 700 experts and authorities including 161 oversea visitors in the field of powder technology from 27 countries all over the world. This Congress followed the first one that took place in Nürnberg, West Germany in April, 1986.

The Congress was organized by the Society of Powder Technology, Japan in association with VDI-Gesellschaft Verfahrenstechnik, West Germany and Fine Particle Society, USA, under the leadership of the chairmen of the Organizing Committee, Profs. G. Jimbo, K. Leschonski and K. Beddow. It was sponsored

by the Association of Powder Process Industry and Engineering, Japan, Japan Management Association and International Fine Particle Research Institute (IFPRI) and supported by more than twenty organizations.

At the opening ceremony in the morning of the first day of the Congress, three plenary lectures were given by Prof. G. Jimbo, Prof. R. Pfeffer and Mr. L. J. Ford after the welcome addresses by the guests and hosts. In the successive technical sessions, fifteen keynote lectures were given by prominent speakers in each specific field and 250 scientific/technical reports have been presented in oral or paper concurrent sessions in seven rooms classified into the following areas:

	number of reports
1. Mechanical powder properties	22
2. Particle characterization	36
3. Storage and conveying	30
4. Production of fine particles	47
5. Dispersion and classification	23
6. Mixing and kneading	8
7. Design and modification of powders	26
8. Mechanical and physical separation	20
9. Reactor design	17
10. New processes and products	21
Total	250

On the occasion of this Congress, the KONA Award was established to stimulate the research activity of younger powder scientists in the world, under 35 years of age. In the luncheon time on the second day of the Congress, the KONA Award was given to the winner, Prof. C.S. Campbell of University of Southern California, USA, with a scholarship of one million yen by the President of Hosokawa Micron Corporation, Mr. M. Hosokawa. In addition to the KONA Award, the following awards were pre-

sented during the Congress: Iinoya Award to Prof. K. Leschonski, Hausner Award to Prof. G. Jimbo, IP Award to Prof. K. Higashitani and Award for Excellence in Particle Technology Research to Prof. O. Molerus.

During the Congress period, three courses of works-visit were arranged to Shimadzu Corp., Murata MFG. Co. and Shigaraki Ceramic Cultural Park and catalogues of powder processing equipments as well as books related with powder technology were exhibited by ten companies.

KONA Award Established and the Commemorative Presentation by the KONA Awardee

Hosokawa Micron Corporation, since its early days, has enthusiastically sponsored industry-university joint activities in various fields. For example, Hosokawa Micron has established the Hosokawa Micromeritics Laboratory (1958), started the publication of "Funsai," a technical journal (also 1958), founded the Party of Powder Technology, Japan (1968), and sponsors "KONA" journal. Thus, Hosokawa Micron has contributed significantly to the improvement in powder technology, not only in Japan but also in the world.

Now Hosokawa Micron Corp. have established the "KONA Award" system. This award has two aims: first, to spur innovation in powder technology throughout the world, and second, to support brilliant young scientists who is promising to become leading figures in the field.

For the first KONA Award, the Award Committee of the Second World Congress has selected Dr. Charles S. Campbell, Associate Pro-

fessor of the University of Southern California, USA for his outstanding achievement in the areas of dynamics of particle flow, fluidization mechanisms in slurry flow, and mechanics/heat-transfer relationships for particle flow. Mr. M. Hosokawa, president of Hosokawa Micron Corporation, presented him with the KONA Award at a luncheon on September 20, 1990, at the Second World Congress PARTICLE TECHNOLOGY, held at the Kyoto International Conference Hall.

A commemorative presentation by KONA Awardee was held September 22 at Hosokawa Micron's R&D Center in Hirakata, with about sixty outstanding scientists and researchers, from twelve countries, in attendance.

Following the presentation, the participants enjoyed a casual tour of Hosokawa Micron's R&D section, a sightseeing trip to Uji Byodoin Temple in Kyoto, and an evening reception hosted by Mr. M. Hosokawa at the Kyoto Grand Hotel.



Academic publication concerning powder technology in Japan (1989)

Journal of the Society of Powder Technology, Japan Vol. 26 (1989)

Title	Author(s)	Page
• The Effects of the Filler Concentration and the Preforming Pressure on the Physical Properties for the Composite Material of PTFE – Polyaramid-Fiber	M. Satoh, Y. Tsuda, T. Nakanishi, K. Miyanami, S. Abe and Y. Samura	4–11
• A Consideration of the Mechanism of Particle Shape Separation by a Rotating Conical Disk with a Spiral Scraper	K. Yamamoto, T. Tsukada and M. Sugimoto	12–22
• Heat of Immersion of Various Si_3N_4 Powders	K. Inoue, R. Shoji, A. Tsukada and M. Arakawa	23–26
• Measurements of the Angle of Repose of Rice Granules Under Ambience in Air and in Water	Y. Fujio and Y. Kawai	27–32
• The Effect of Powder Feeding Conditions on Initial Porosity in the Interference Region between Two Feeding Points	I. Hanaoka, K. Kuramitsu and K. Makino	72–76
• Acoustic Emission from the Shear Flow of Granular Materials	J. Hidaka, N. Kinboshi and S. Miwa	77–84
• Interpretation of the Relationship between Energy and Size Reduction on the Basis of the Fractal Concept	T. Suzuki and T. Yano	99–102
• Preparation of Fine Particles of Superconducting Oxides by Aerosol Reactor	K. Okuyama, M. Adachi, K. Arai, Y. Kousaka, N. Tohge, M. Tatsumisago and T. Minami	146–150
• The In-situ Measurements of Ultra-Fine Oxide Particles Formed in a Flame	K. Ueyama, K. Tanaka, H. Kawazoe, A. Iino, Y. Matsuda and S. Furusaki	151–156
• Submicron Ceramic Powder Synthesis by a Fluidized Bed of Microcontainer Particles	M. Tsukasa, J. Naito, T. Masuda and M. Hirio	157–162
• Electrostatic Separation of CVD Ultrafine Particles as High Temperature	H. Yamamoto	163–168
• Electrostatic Formation of a Ceramic Membrane with Fine Pores	H. Yamamoto, T. Nomura and S. Masuda	169–173
• Synthesis of Composite Fine Particles in the Gas Phase	S. Endoh, K. Okuda, J. Koga, S. Matsumoto and K. Takeuchi	174–178
• Parameters of Acoustic Emission During the Compact of a Powder	J. Hidaka, S. Miwa and T. Kinboshi	238–244
• The Effect of Filling Methods on Frictional Force for a Rod Inserted in a Bin	R. Moriyama	245–249
• The Fractal Dimension in a Randomly-packed System of Uniform-sized Spheres, Simulated by Four Different Algorithms	M. Suzuki and T. Oshima	250–254
• Flow Characteristics in Horizontal Pneumatic Conveyance at Low Air Velocities (Part I) – Solid Flow Patterns –	M. Ochi and K. Ikemori	255–259
• Three Dimensional Shape Analysis of Pebbles and Its Characterization	T. Shibata, I. Akashi and K. Yamaguchi	316–321
• The Use of a Prism-Shaped Insert to Prevent Bridges in Existing Coal Bunkers	H. Tsunakawa	328–333
• The Electrification Mechanism of the Surface of Alumina Powders During Crushing	Y. Fujihara and Y. Yoshimura	334–339

Title	Author(s)	Page
• Development of the Micro Feeder for Fine Particles	H. Seno and T. Kondo	340–344
• An Experiment on Impact Grinding under Reduced Pressure	I. Aoki, T. Yamasita, T. Fujimoto and T. Matsuyama	396–400
• An Analysis of the Selection Function for Mills using Balls as Grinding Media – In the Case of Vibration Mill –	S. Nomura, K. Hosoda and T. Tanaka	401–405
• A Consideration of Ultrafine Grinding – Effect of a Binary Mixture of Balls Having Considerable Difference in Sizes –	Y. Kanda, Y. Abe and T. Oyamada	406–410
• The Grinding of Silica Sand by a Coaxial Circular Multi-vessel Type Beads Mill	K. Matsumoto, H. Nishizawa and M. Naito	417–423
• The Release of Enzymes and Protein from Baker's Yeast Disrupted by an Agitator Bead Mill	K. Matsumoto, S. Ito, H. Ohya and M. Naito	424–429
• Separation of Unburned Carbon from Fly Ash by a Dry Shaking Table	E. Abe, H. Hirose and N. Yamada	484–490
• Vertical Plug Conveyance – Falling Particles and the Motion of Plugs –	H. Ueno	491–496
• Nano-mechanics – Dynamics of Granular Assemblies with Non-linear Contact Interaction	H. Okamoto	497–504
• The Maximum Crushing Capacity of a Wood by Friction Mill	H. Endoh	505–507
• Data Base of Plug Conveying	Y. Tsuji	508–511
• Study on Deashing of Coal by the Oil Agglomeration Process – Influence of Growth of Agglomerates and Washing on Deashing Efficiency	H. Takase and M. Sugimoto	552–557
• Thermophoresis Velocity of SiO ₂ Ultra-Fine Particles in a Flame	K. Ueyama, K. Miyazawa, H. Kawazoe, A. Iino, Y. Matsuda and S. Furusaki	558–565
• A New Apparatus for Measuring Zeta Potential of Individual Powder Samples in an Aqueous Solution Containing Plural Samples	M. Tsunekawa, N. Habata, T. Takamori and E. Ogata	569–572
• Some Characteristics of Fly Ash Particles	S. Toyama, M. Nakamura, H. Mori, S. Sakurai, H. Yoshida and N. Kuroda	573–577
• Characterization of a Particle by a Pair of Shape Indexes	M. Sugimoto, N. Yokota and H. Nakazawa	624–656
• The Estimation of Packing Characteristics by Centrifugal Compaction of Ultrafine Particles	M. Mizuno, A. Fukaya and G. Jimbo	657–636
• A Study of the Aggregated Structure of Fine Particles in a Slurry	M. Arakawa, K. Hirota, T. Kimura, H. Kobayashi, Y. Okuda and H. Murata	637–631
• The Surface-treatment of Ceramic Powders through Pulverization in a Reaction Atmosphere with a Ball Mill (1) – The Surface-treatment of Quartz Powder –	H. Utsugi, A. Endo, N. Suzuki, Y. Kimura and Y. Go	632–674
• The Effect of Powder Properties on the Dry Impact Blending Preparation Method	H. Honda, T. Matsuno and M. Koishi	659–662
• The Shear Test of Iron Ore Pellets during Reduction at an Elevated Temperature	S. Mizukami, M. Matsukura and H. Murata	663–650
• Effects of the Preparation Processes for Powders on the Physical Properties of PTFE-Carbon Fiber Composite	M. Satoh, F. Hamano, T. Oshima, S. Shimamoto, K. Miyanami and T. Ikeda	651–644

Title	Author(s)	Page
• The continuous Kneading of a Composite Electric Conductive Material and Its Evaluation – Relationship between Electric Conductivity and Dispersion Characteristics According to Kinds of Fillers –	P. Lyoo, K. Terashita, M. Mitsui and K. Miyanami	645–689
• Study of the Movement of Granular Particles Uniform in a Moving Bed	N. Arashi, T. Komuro and O. Kanda	712–716
• Mixing and Drying Characteristics of a Multisectional Fluidized Bed	S. Hayashi, K. Kubota, T. Yoshimura, E. Goto and T. Fukunaga	717–723
• The Angle of Repose in a Synthesized Field of Gravitational and Centrifugal Force	H. Ohya, M. Yamamoto, T. Kokubo and H. Sakamoto	724–728
• Grinding Rate of Wood Crushers	H. Endoh	781–787
• Electric Potential Profile in the Neighborhood of a Surface Composed of Different Kinds of Materials and Aerosol Particle Deposition	H. Yoshida, T. Ninomiya and H. Masuda	770–775
• The Collection Performances of High Gas Velocity Filtration for a Moving Granular Bed	M. Hirota, R. Kitai, H. Tajiri and T. Oshima	776–780
• Flow Characteristics in a Horizontal Pneumatic Conveyance at Low Fluid Velocities (Part II) – Solid Particle Velocity and the Velocity Ratio of Particles to Fluid –	M. Ochi	781–787
• Imbibition into Unsaturated Granular Bed	K. Atsumi, K. Miyai, Y. Asada and T. Makino	828–831
• Particle Growth in a Tumbling Fluidized Bed Coater	E. Abe and H. Hirose	832–838
• Relationships between Maximum Holdup and Dimensions of Impact Mill	H. Endoh	839–842

Funsai (The Micromeritics) No. 34 (1990)

Title	Author(s)	Page
• Fine Grindings of Limestone by Tumbling Ball Mill – Influence of Air Humidity Sorption during Grinding –	A. Suganuma, Y. Fujii T. Hamada	4–9
• Measurements of Size Distribution of Separate Spherical Particles by Video System	K. Shinohara, T. Ishihara	10–18
• Effective Thickness of a Contact “Point” in the Solid Reaction Model of Particulate Matters	Y. Hao, T. Tanaka, A. Shimizu	19–24
• The Analysis of Asperity Particles	T. Shibata, T. Aida, I. Akashi and K. Yamaguchi	25–32
• Weight Control of a Hopper – Application of Self-tuning Control –	K. Wada, M. Ebisu, N. Hayano	33–38

Kagaku Kogaku Ronbunshu Vol.15 (1989)

Title	Author(s)	Page
• Predictions of Dead Zone Boundaries of Bulk Solids in Two-Dimensional Gravity Flows	K. Motono, S. Nomura and T. Tanaka	83–90
• Synthesis of SiC Ultrafine Particles by Thermal CVD Method	M. Sadakata, H. Baba, M. Sato and T. Sakai	91–97
• Power Consumption of Horizontal Gas-Solid Mixed-type Polymerization Reactor with Two Parallel Axes	T. Tenda, S. Komori and Y. Murakami	98–104
• Dust Load Distributions in Fibrous Mat and Granular Bed Filters	N. Kimura, M. Kanamori, H. Mori and M. Shirato	119–125
• Influence of Agglomerate Size on Drainage of Packed Bed of Coal Agglomerates	H. Takase and M. Sugimoto	238–245
• Effect of Mill Shape on Vibration Ball Milling	M. Hasegawa, T. Honma and Y. Kanda	343–348
• Evaluation of Kneading and Dispersion of Magnetic Powder	K. Terashita, K. Miyanami, K. Sakamoto and T. Horikoshi	747–753
• Fluidization Characteristics of Tapered Bed	H. Toyohara and Y. Kanamura	773–780
• The Effects of Fluidizing Gas Humidity on Gas-Solid Stirred Fluidized Bed Operation	T. Takahashi, S. Kaseno and J. Fukui	781–787
• Development of Continuous Vacuum Dryer for Highly Viscous Liquid Food	E. Kumazawa, Y. Saiki, K. Ido and M. Okazaki	938–945
• Light Scattering Properties of Prolate Spheroidal Aerosol Particles	S. Okuda, H. Takano and J. Hirose	954–962
• Flow Patterns and Mixing Characteristics of Particles in a Horizontal Gas-Solid Agitated Vessel with Paddle Blades on Double Parallel Axes	T. Tenda, M. Takao, S. Komori and Y. Murakami	985–991
• Vibro-Fluidization of Very Fine Particles	S. Mori, T. Haruta, A. Yamamoto, I. Yamada and E. Mizutani	992–997
• Vapor-Phase Synthesis of SiC Ultrafine Particles from $\text{SiH}_4/\text{C}_2\text{H}_2$ Premixed Gas	M. Sadakata, H. Baba, M. Sato and T. Sakai	1019–1025

Journal of the Society of Materials Science, Japan Vol.38 (1989)

Title	Author(s)	Page
• Thermal Spraying over Particulate-filled Epoxide Resins	Y. Itoh, H. Kashiwaya and S. Asai	1446–1451
• Continuous Kneading of Composite Conductive Plastics with Stainless Steel Fiber Filling and Its Evaluation	K. Terashita, M. Mitsui, D.J. Lyoo and K. Miyanami	1452–1457
• Countermeasure for Electrostatic Safety in Filter-Bag	M. Nakagome, T. Hara, Y. Kawaguchi and M. Masaki	37–44
• Charging of Powders in Liquids and Electrical Resistance of Dispersion	Y. Fujihara	219–229
• Destruction of Yeast Cells by Pulsed High Voltage Application	M. Hayamizu, T. Tenma and A. Mizuno	322–331
• Computer Simulation Analysis of Electrostatic Discharge in Electronic Equipment Systems	H. Higuchi, M. Maeda, K. Yamaguchi and N. Takahashi	431–438
• Development of Two Types of In-Situ Dust Resistivity Measuring Apparatus	N. Kogure, M. Shirahase, H. Yoshiyama and I. Tamori	496–502
• Dust Sensor	M. Kajimaki, Y. Nakajima and H. Yamamoto	503–508

Hosokawa Micron Corporation presents two new products.

□ **Atmosphere-Conversion Type Mechanofusion System AM-20FV for production of high-purity composite particles**

Hosokawa Micron Corp. has developed the Atmosphere-Conversion Type Mechanofusion System (AM-20FV), intended for the production of high-purity composite particle. This system is capable of processing particles with Mechanofusion technique into composite form in a vacuum as high as approximately 10^{-5} Torr, or of freely selecting atmospheric conditions of inert gas.

Applications

- To improve characteristics in a composite sintered compact
- New flame-spraying powder material
- Study of mechanical alloying
- Development of functional material

Features

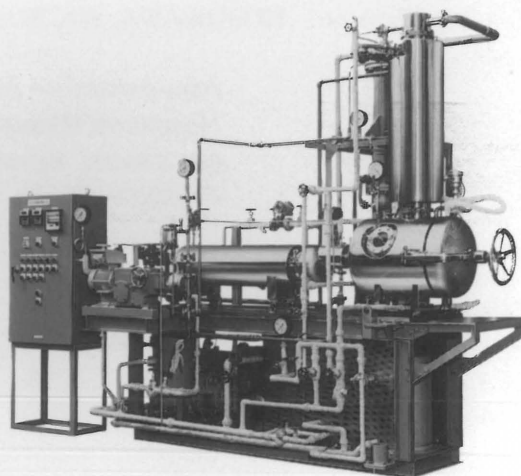
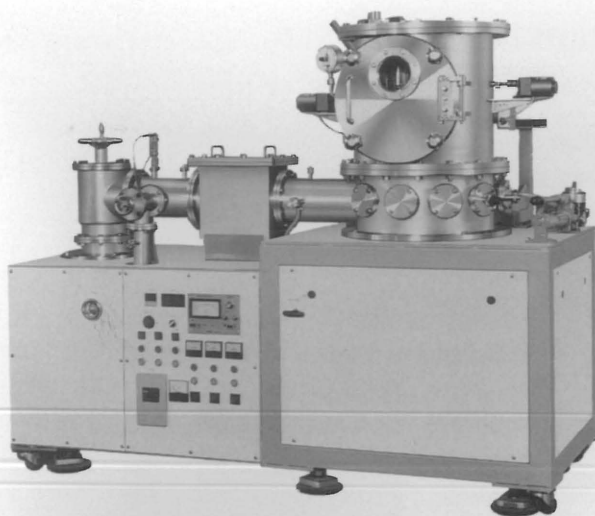
- Capable of manufacturing high-purity composite powder materials with new properties
- Capable of processing particles into composite form even in a vacuum as high as approximately 10^{-5} Torr
- Possible to select freely process environment such as argon, nitrogen gas and oxygen
- Capable of improving particle fluidity and of achieving precise mixing and dispersion of particles
- Easy handling, operation, and cleaning

□ **Crux Vacuum Drying System**

Crux Vacuum Drying System is the unique system of drying which is designed for continuous drying at a relatively high temperature with a short retention time, yielding the required result. Crux System has been used very successfully by many manufactures, for ceramics, electrical materials, chemicals, pharmaceuticals, pigments and others.

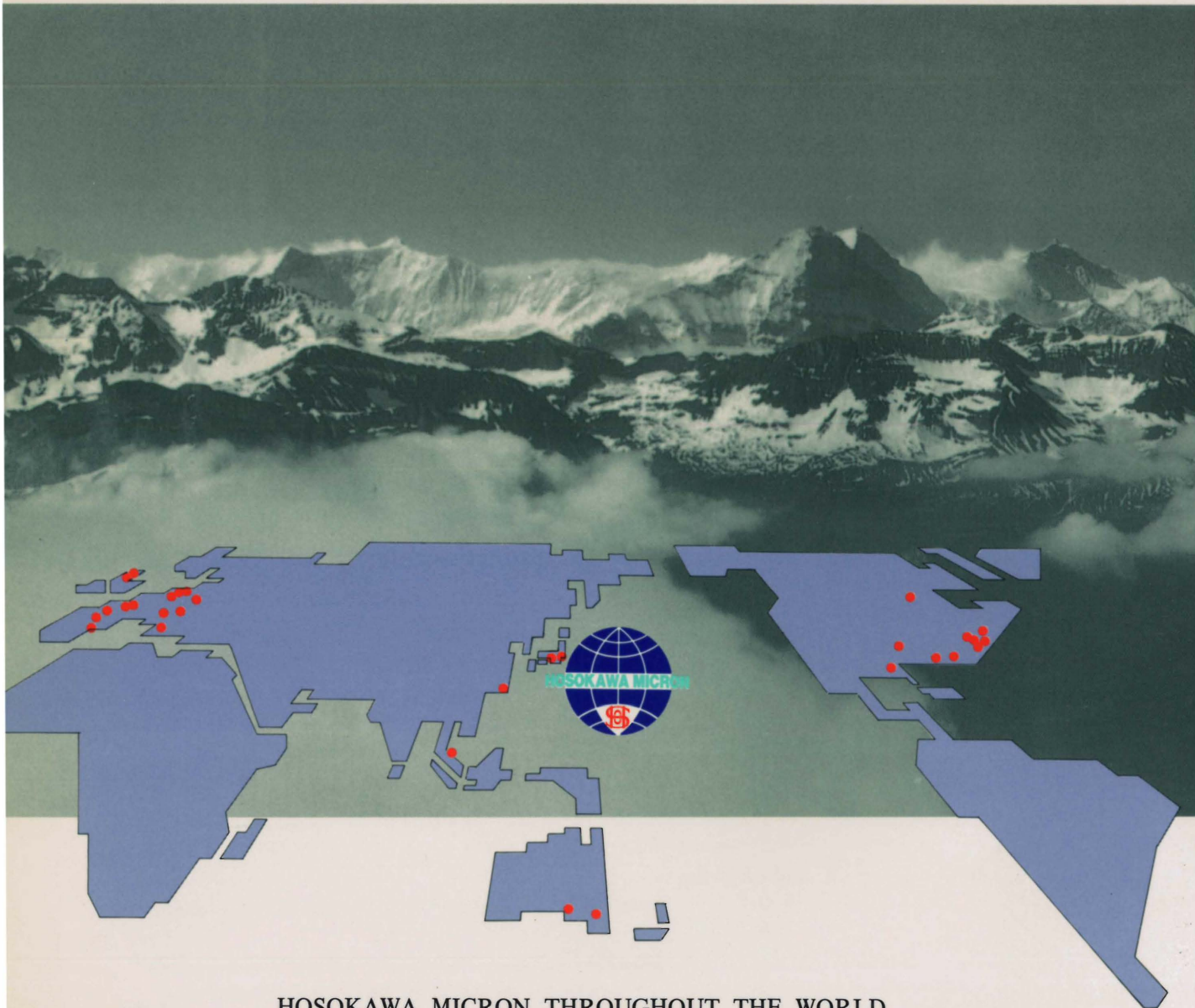
Crux system has many features as follow:

- Crux completely separates the feed (solution or slurry) into powder and solvent in one continuous process.
- The solvent can be recovered almost completely by a closed system at low cost.
- The dried powders with little secondary aggregation can be obtained.
- Be capable of surface modification and micro encapsulation.
- The difficult-to-process feed such as tar-like distillation residues can be processed in many cases, and volatile components in the feed can be recovered almost completely.
- Hazardous solvent are safely removed with an excellent recovery ratio.



HOSOKAWA MICRON

LEADERS OF POWDER PROCESSING TECHNOLOGY, ENVIRONMENTAL SYSTEMS, FILTER MEDIA AND PLASTIC PROCESSING SYSTEMS.



HOSOKAWA MICRON THROUGHOUT THE WORLD

Asia/Australian Block

Hosokawa Micron Corporation

5-7, 3-chome, Hommachi, Chuo-ku, Osaka 541, Japan

Telephone: 06-263-2555 Fax: 06-263-2552

Americas Block

Hosokawa Micron International Inc.

780 Third Avenue, New York, NY10017, U.S.A.

Telephone: 212-826-3830 Fax: 212-826-6612

European Block

Hosokawa Micron International BV.

World Trade Center, Strawinskylaan 249,
1077XX Amsterdam, Holland

Telephone: 020-73-5551 Fax: 020-76-2061